

SANDIA REPORT

SAND2012-7816

Unlimited Release

Printed September 2012

Modeling Thermal Abuse in Transportation Batteries

Richard P. Muller, Randall T. Cygan, Jie Deng, Amalie L. Frischknecht, John C. Hewson, Michael P. Kanouff, Richard Larson, Harry K. Moffat, Craig M. Tenney, Peter A. Schultz, Gregory J. Wagner

Prepared by
Sandia National Laboratories
Albuquerque, New Mexico 87185 and Livermore, California 94550

Sandia National Laboratories is a multi-program laboratory managed and operated by Sandia Corporation, a wholly owned subsidiary of Lockheed Martin Corporation, for the U.S. Department of Energy's National Nuclear Security Administration under contract DE-AC04-94AL85000.

Approved for public release; further dissemination unlimited.



Sandia National Laboratories

Issued by Sandia National Laboratories, operated for the United States Department of Energy by Sandia Corporation.

NOTICE: This report was prepared as an account of work sponsored by an agency of the United States Government. Neither the United States Government, nor any agency thereof, nor any of their employees, nor any of their contractors, subcontractors, or their employees, make any warranty, express or implied, or assume any legal liability or responsibility for the accuracy, completeness, or usefulness of any information, apparatus, product, or process disclosed, or represent that its use would not infringe privately owned rights. Reference herein to any specific commercial product, process, or service by trade name, trademark, manufacturer, or otherwise, does not necessarily constitute or imply its endorsement, recommendation, or favoring by the United States Government, any agency thereof, or any of their contractors or subcontractors. The views and opinions expressed herein do not necessarily state or reflect those of the United States Government, any agency thereof, or any of their contractors.

Printed in the United States of America. This report has been reproduced directly from the best available copy.

Available to DOE and DOE contractors from

U.S. Department of Energy
Office of Scientific and Technical Information
P.O. Box 62
Oak Ridge, TN 37831

Telephone: (865) 576-8401
Facsimile: (865) 576-5728
E-Mail: reports@adonis.osti.gov
Online ordering: <http://www.osti.gov/bridge>

Available to the public from

U.S. Department of Commerce
National Technical Information Service
5285 Port Royal Rd.
Springfield, VA 22161

Telephone: (800) 553-6847
Facsimile: (703) 605-6900
E-Mail: orders@ntis.fedworld.gov
Online order: <http://www.ntis.gov/help/ordermethods.asp?loc=7-4-0#online>



Modeling Thermal Abuse in Transportation Batteries

Richard P. Muller¹, Randall T. Cygan², Jie Deng⁴, Amalie Frischknecht⁵, John C. Hewson⁶,
Michael P. Kanouff⁴, Richard Larson⁴, Harry K. Moffat⁷, Craig M. Tenney³, Peter A. Schultz¹,
Gregory J. Wagner⁴

¹Advanced Device Technologies, ²Geosciences Research and Applications, ³Geochemistry,
⁴Thermal/Fluid Science and Engineering, ⁵Computational Materials Science and Engineering,
⁶Fire and Aerosol Sciences, ⁷Nanoscale and Reactive Processes,

Sandia National Laboratories
P.O. Box 5800
Albuquerque, New Mexico 87185-1322

Abstract

Transition from fossil-fueled to electrified vehicles depends on developing economical, reliable batteries with high energy densities and long life. Safety, preventing premature or catastrophic failure, is of paramount importance in battery design. The largest gaps in our technical understanding of the safe operation of electrical energy storage devices involve the fundamental mechanisms, energetics, and inefficiencies of complex processes that occur during battery operation that can lead to thermal runaway: charge transfer, charge carrier and ion transport, both in the bulk and at various interfaces, and morphological and phase transitions associated with Li-ion transport between cathode and anode. We have developed a suite of modeling tools to consider phenomena related to battery safety, thermal management, and the onset of thermal runaway in transportation-based secondary Li-ion batteries, rooted in a first-principles description of the governing atomistic processes at the electrode-electrolyte interface, propagating chemical information through multiple scales to a continuum-scale description of thermal transport and failure capable of addressing a variety of operational and thermal excursion conditions. These tools enable the identification of potential safety and stability issues of new battery designs prior to experimental realization.

ACKNOWLEDGMENTS

This work was motivated by, and has benefitted greatly from, conversations with members of the Sandia Power Sources Technology Group, including Pete Roth, Chris Orendorff, Terry Aselage, and Tom Wunsch. We have also greatly benefitted from conversations with Kevin Leung, Laura Frink, Frank van Swol, Bob Spotnitz, Mark Orazem, Bob Kee, Yue Qi, Steve Harris, Grant Smith, Sreekanth Pannala, John Turner, Kendra Letchworth-Weaver, Tomas Arias.

CONTENTS

1	Introduction	12
2	Modeling Research and Development	21
2.1	Overview	21
2.2	Single Phase Quantum DFT Mechanisms	22
2.2.1	Bond Breaking Reactions	22
2.2.2	Mechanisms for SEI Formation	26
2.3	Electrode-Electrolyte Interfacial Modeling	29
2.3.1	Modeling an Electrochemical System	29
2.3.2	Bulk DFT simulations of materials – lithium manganese oxides	30
2.3.3	Electrostatic boundary conditions in periodic DFT calculations	33
2.3.4	Modeling bulk surfaces and solid-liquid interfaces with charge with supercells	36
2.3.5	Fluids-DFT Overview	38
2.3.6	A model for the electrode-electrolyte interface	45
2.3.7	Method and code verification, and application to a double layer system	47
2.3.8	Future Development	52
2.4	Mechanisms for Chemical Diffusion in Materials	54
2.4.1	Simulation of Bulk Diffusion of Li Ions	54
2.4.2	Analysis of molecular clusters in simulations of lithium ion battery electrolytes	58
2.5	Modeling Passivation Layer Growth and Decomposition	72
2.5.1	Comsol Modeling of SEI Growth	74
2.5.2	Kinetic Monte Carlo Modeling of SEI Growth	75
2.5.3	Phase Field Modeling of SEI Growth	81
2.6	Cell Modeling	97
2.6.1	Transport models for electrolytes	98
2.6.2	Electrode transport	120
2.6.3	Electrode reactions	122
2.6.4	Cantera's Setup of Electrochemistry	125
2.6.5	Formulation of the Kinetics in Terms of Elementary Steps	130
2.6.6	Enthalpy Formulation of the Heat Equation	139
2.6.7	Darcy's flow Equation for flow and Changes in Electrode Porosity	140
2.6.8	Modular Architecture for 1D Electrode Model	142
2.6.9	Summary of the Equations System Solved by the 1D Electrode Model	144
2.6.10	Calculation of Source terms – Need for integrated source terms	145
2.6.11	Models for the Electrode Object	147
2.6.12	Multiple Plateau Regions	154
2.6.13	Algorithms for Handling Births and Deaths of Phases	156
2.6.14	Diffusion Models based on Point Defect Thermodynamics models for solid phases: Lattice Phases	159
2.6.15	Electrode model with Distributed Treatment of Diffusion	161
2.6.16	Initial DAE problem	163
2.6.17	Root finder used within the 1D code	164
2.6.18	Numerics of Linkage between the 1D electrode Code and the Electrode object	165
2.6.19	CanTrilBat Progress	176

3	Conclusions and Ongoing Work	179
4	References	180
	Appendix A: Electrostatic free energy in tramonto	187
	A.1. A note about units	187
	A.2. Poisson-Boltzmann Limit	188
	A.3. Tests of Electrostatics in Tramonto	190
	4.1.1 A.3.1. Pressure from electrostatic terms.....	190
	4.1.2 A.3.2. Sum rules.....	191
	4.1.3 A.3.3. PB Limit	191
	4.1.4 A.2.2.1. Problem 1: small surface charges	191
	4.1.5 A.2.2.1. Problem 2: large surface charges.....	192
	A.3.4. RPM model	193
	A.3.5. SPM model.....	193
	Distribution.....	198

FIGURES

Figure 1:	Schematic of a cylindrical battery cell, showing the arrangement of the anode, cathode, and separator elements in the spiral coil.	12
Figure 2:	Schematic of Li intercalation into graphite during battery charging.....	13
Figure 3:	Schematic of Li intercalation into a metal-oxide material during battery discharge. The electrons that accompany the Li^+ ions reduce the oxidation state of the metal atom after discharge.....	13
Figure 4:	Commonly used Li-ion battery electrolyte materials, including ethylene carbonate (EC), propylene carbonate (PC), dimethyl carbonate (DMC), and methyl ethyl carbonate (MEC).....	14
Figure 5:	Thermal ramp data (left, from Ref (Doughty 2005)) and DSC data (right, from Ref (Abraham, Roth et al. 2006)) for thermal abuse of Li-ion Batteries.....	14
Figure 6:	Heat release from different cathode materials, taken from Ref (Roth 2008).	15
Figure 7:	Hypothetical structure of the SEI layer.	16
Figure 8:	Computational model for thermal abuse of Li-ion batteries (top), compared to experimental results (bottom), from (Hatchard, MacNeil et al. 2001).	18
Figure 9:	Comparison of fits (left, red, purple, blue lines) using Dahn autocatalytic functional form shows poor agreement with data (left, green points), regardless of activation barrier; in contrast, using a more sophisticated reaction-diffusion functional form (right, red lines) shows much better agreement to data (right, green points).	19
Figure 10:	Hierarchy of multiscale modeling approaches used to understand and predict battery safety.	21
Figure 11:	Energies (kcal/mol) for breaking the indicated bonds in EC (left) and DMC (right), computed using B3LYP/6-31G**++ (black) and MP2/6-31G**++ (red) levels in the gas phase.	23

Figure 12: Energies (kcal/mol) for breaking the indicated bonds in EC (left) and DMC (right), computed using B3LYP/6-31G***++ in a solvation dielectric corresponding to a 50:50 EC/DMC mixture (blue).....	24
Figure 13: Energies (kcal/mol) for breaking the indicated bonds in EC ⁻ computed using B3LYP/6-31G**++ in the gas phase (black) and in a solvation dielectric corresponding to a 50:50 EC/DMC mixture (blue).	25
Figure 14: Energies (kcal/mol) for breaking the indicated bonds in ring-opened EC (left) and ring-opened EC ⁻ (right) computed using B3LYP/6-31G**++ in the gas phase (black) and in a solvation dielectric corresponding to a 50:50 EC/DMC mixture (blue).....	25
Figure 15: Reactions leading to the formation of organic SEI compounds, primarily EDC. B3LYP/6-31G**++ energies in kcal/mol computed using a dielectric representing a 50:50 EC/DMC mixture.....	27
Figure 16: Reactions leading to the formation of inorganic SEI compounds, primarily Li ₂ CO ₃ . B3LYP/6-31G**++ energies in kcal/mol computed using a dielectric representing a 50:50 EC/DMC mixture.....	28
Figure 17: Conceptual model of a lithium-ion battery.....	29
Figure 18: Illustration of the local level structure on the Mn atom in the Li _(0,1,2) Mn ₂ O ₄ compound.....	31
Figure 19: The supercell approximation.....	33
Figure 20: Slab supercell model for a vacuum surface, and electrode-electrolyte interface	36
Figure 21: Sketch of the SPM model near a hard surface, showing cations (red), anions (green), and neutral solvent (blue).....	40
Figure 22 Density profiles as a function of distance from a positively charged surface calculated using the SPM model in c-DFT (left) and using the Poisson-Boltzmann model (right), for the same set of model parameters.	43
Figure 23: Two-dimensional projection of a f-DFT calculation of the charge density of negative ions between two flat surfaces at constant potential, with a positively charged spherical atom on the left.....	44
Figure 24: Conceptual model for a DFT description of the double layer.....	45
Figure 25: Test system for double layer boundary conditions in DFT supercell.....	47
Figure 26: Coupled slab DFT and fluids DFT calculations. Top, electronic density from SeqQuest. Bottom, ion densities (relative to their bulk values) from Tramonto, for the electronic surface charge density of 0.03/Å ² represented in the top figure. The moment of the ion charge density is located 2.16Å from the surface. The contact density of Li ⁺ is 131 ρ _b	51
Figure 27: The challenge of a three-dimensional interface	52
Figure 28: Schematic representation of crystalline diffusion and the role of extended defects and grain boundaries as they relate to diffusion mechanisms. Modified from (Watson and Dohmen 2010).....	55
Figure 29: Schematic representation of an Arrhenius plot showing the transition between intrinsic diffusion processes at high temperature and the extrinsic region at lower temperature where the activation energy is lower and is equivalent to the migration enthalpy.	57
Figure 30: Ethylene carbonate (EC), dimethyl carbonate (DMC), and hexafluorophosphate (PF ₆ ⁻).	58

Figure 31: Self-diffusion coefficients versus time for 1.0 M LiPF ₆ in EC (top), DMC (middle), and EC/DMC (bottom) solvents at 300 K and 400 K.	61
Figure 32: Ideal Nernst-Einstein (uncorrelated) ionic conductivity versus time for 1.0 M LiPF ₆ in EC, DMC, and EC/DMC solvents at 300 K and 400 K.	62
Figure 33: As in Figure 31, except true (correlated) ionic.	63
Figure 34: Pair correlation functions $g(r)$ versus separation r for Li ⁺ with solvent carbonyl oxygens (Li-O), PF ₆ ⁻ (Li-P), and other Li ⁺ (Li-Li) for 1.0 M LiPF ₆ in EC, DMC, and EC/DMC solvents at 300 K and 400 K. “EC/dmc” and “ec/DMC” denote coordination of Li with EC and DMC, respectively, in mixed EC/DMC solvent systems.	64
Figure 35: Neighbor autocorrelation function (acf) versus time for Li ⁺ with solvent carbonyl oxygens (Li-O), PF ₆ ⁻ (Li-P), and other Li ⁺ (Li-Li) for 1.0 M LiPF ₆ in EC, DMC, and EC/DMC solvents at 300 K and 400 K. A “neighbor” is defined as an atom closer than the minimum after the first peak of the corresponding $g(r)$ in Figure 34.	67
Figure 36: Common cluster topologies formed by Li ⁺ (black) neighboring with PF ₆ ⁻ (green) or solvent carbonyl oxygen atoms (EC = blue, DMC = red). Lines represent neighbor pairing. Node size is proportional to the frequency with which a cluster topology was observed. The systems are composed of 0.1 M LiPF ₆ in EC, DMC, or EC/DMC at 300 K and 400 K.	69
Figure 37: As in Figure 36, except 0.3 M LiPF ₆	70
Figure 38: Snapshots showing all Li ⁺ ions (purple), all P atoms (orange) from PF ₆ ⁻ , and only solvent carbonyl oxygen atoms (red) neighbored with a Li ⁺ . The systems are 1.0 M LiPF ₆ in pure EC and DMC at 300 K. The blue box outlines the periodic simulation cell. Note that some clusters may span periodic boundaries.	71
Figure 39: Schematic of COMSOL model regions and their interfaces.	74
Figure 40: Example geometry lattice for KMC simulation. Each site is labeled with a material identifying its location in the anode/SEI/electrolyte structure.	75
Figure 41: KMC simulation results at a nondimensional time of $t = 200$ for two different values of the tunneling length ℓ_c : (a) $\ell_c = a$, (b) $\ell_c = 2a$, where a is the unit cell size. In both figures, the light blue sites represent the carbon anode, red are the organic SEI, green are inorganic SEI, and blue are the IHP sites where surface reactions take place.	80
Figure 42: Average SEI layer thickness for two different values of the tunneling length ℓ_c : (a) $\ell_c = a$, (b) $\ell_c = 2a$	80
Figure 43: Distribution of (a) phase field, (b) concentrations of species, (c) charge density and (d) electric potential at equilibrium state.	86
Figure 44: Concentrations of species at (a) 80 μ s and (b) 240 μ s; Distribution of (c) charge density and (d) electric potential at different time.	87
Figure 45: SEI thickness as a function of time.	88
Figure 46: (a) SEI growth and (b) distribution of electric potential at time 80 μ s under different electron diffusivity; (c) SEI growth and (d) distribution of electric potential at time 240 μ s with different SEI formation reaction rate.	89
Figure 47: (a) SEI growth and distribution of (b) electric potential, (c) Li ⁺ concentration and (d) e ⁻ concentration at time 240 μ s with different initial Li ⁺ and e ⁻ concentration in SEI.	91

Figure 48:	Distribution of (a) electric potential and (b) charge density at equilibrium state with different $\Delta\phi_0$	92
Figure 49:	(a) Distribution of electric potential at time 80 μs with different $\Delta\phi_0$; (b) Charge density distribution at different time when $\Delta\phi_0$ is (b) -0.05 V and (c) -0.15 V.	93
Figure 50:	Distribution of electric potential at (a, b) time 0 and (c, d) time 80 μs under different applied current density. (b) and (d) illustrate the electric potential distribution in the region enclosed by the rectangular box shown in (a) and (c), respectively.	94
Figure 51:	(a) Overpotential as a function of applied current density at different time; (b) Evolution of exchange current density during SEI growth.....	95
Figure 52:	(a) SEI growth under different temperature; (b) SEI thickness as a function of temperature at different time.....	96
Figure 53	XML format for the electron phase within Cantera for molten salt systems	127
Figure 54	Modular Approach to construction of the Domain: Volume Domains are sandwiched between Surface Domains, on which boundary conditions and tie conditions are applied.....	142
Figure 55	Node-centered Control volume implementation within each domain. Most variables are located at the nodes. Control volume faces are located at the midpoint between nodes. Axial velocities are located at the control volume faces.	143
Figure 56	Schematic of the electrode model for Pseudo-State state diffusion involving phase transformation.	151
Figure 57	Variations of the constant current curves as the exchange current density is varied. 50 amp current at various exchange current densities assuming infinitely fast diffusion. In this version the reaction's rate of progress is proportional to the inner surface area.	153
Figure 58	Variations of the constant current curves as the exchange current density is varied. 50 amp current at various exchange current densities for a fixed value of the diffusion coefficient of 1.0E-8.....	153
Figure 59:	Phase blue disappears on going from $t = t_n$ to $t = t_{n+1}$, while phase red appears on the outside. Two cases may occur depending on whether red nucleates before blue disappears. In the text, the inner blue region will be called S1 (solid#1). The green region will be called S2, and the red region will be called S3. After blue disappears, green will be S1, and red will be S2.	154

TABLES

Table 1:	Results of DFT structural calculations for lithium manganese spinels, a_0 in \AA (u_O). ..	32
Table 2:	Average number of solvent carbonyl oxygen atoms within first coordination shell of Li^+ for all combinations of solvent, temperature, and LiPF_6 concentration used in this study. "EC/dmc" and "ec/DMC" denote coordination of Li with EC and DMC, respectively, in mixed EC/DMC solvent systems.....	65
Table 3:	As in Table 2, except for coordination of PF_6^- ions with Li^+	65
Table 4:	As in Table 2, except for coordination of Li^+ ions with Li^+	66
Table 5:	Initial concentrations X_i in bulk phases	85

NOMENCLATURE

ARC	Accelerating Ramp Calorimetry
B3LYP	Becke-3-Lee-Yang-Parr density functional
BATLab	Sandia Battery Abuse Testing Laboratory
CSTR	Continuously stirred tank reactor
DAE	Differential algebraic equation
DFT	Density functional theory
DMC	Dimethyl carbonate
DSC	Differential Scanning Calorimetry
DOE	Department of Energy
EC	Ethylene carbonate
EDC	Ethylene dicarbonate
GAFF	Generalized Amber Force Field
GCS	Guoy-Chapman-Stern
GGA	Generalized Gradient Approximation
IHP	Inner Helmholtz plane
KMC	Kinetic Monte Carlo
LMCC	Local moment countercharge
MEC	Methyl ethyl carbonate
MP2	Moller-Plesset second order perturbation theory
MD	Molecular dynamics
OHP	Outer Helmholtz plane
PB	Poisson-Boltzmann
ROEC	Ring-opened ethylene carbonate
PBE	Perdew-Burke-Ernzerhoff density functional
PC	Propylene carbonate
SEI	Solid Electrolyte Interphase
SPM	Semi-primitive model
SNL	Sandia National Laboratories

1 INTRODUCTION

Vehicle electrification is widely seen as a method to reduce US dependence on foreign oil as well as carbon emissions related to transportation. Li-ion batteries, in particular, are playing an increasingly important role in the electrification process because of the energy density they allow compared to other battery chemistries. However, Li-ion batteries have also been associated with safety issues; driven to high enough temperatures, Li-ion batteries can undergo “thermal abuse”, generating large amounts of heat and often catching fire. The Sandia Battery Abuse Testing Laboratory (BATLab) has played an important role in assessing the risks and understanding the processes that lead to thermal abuse in a variety of battery chemistries, among them Li-ion.

The fact that an automobile component can catch fire and release energy is itself nothing new. Gasoline itself is flammable and can catch fire. However, we understand the safety margins associated with gasoline engines. For example, if the ambient temperature is 25° warmer, we don’t associate that with an increased risk of automobile gasoline fires. In contrast, we don’t understand the analogous effects of temperature on battery chemistries. Furthermore, the internal combustion energetics are more-or-less converged, whereas we anticipate that battery chemistry will change substantially over the next 5-10 years in attempts to obtain increased capacity, lower cost, lower weight, and other modifications to make batteries more practical for transportation. We would like to be able to make similar assessments of safety margins for all Li-ion chemistries, those that exist as well as those that have only been conceived. Moreover, a mechanistic understanding of *why* the battery has failed is often much harder to obtain than is the mere observation that a battery has failed. It is because of these needs that we sought to develop a predictive simulation capability to understand battery abuse.

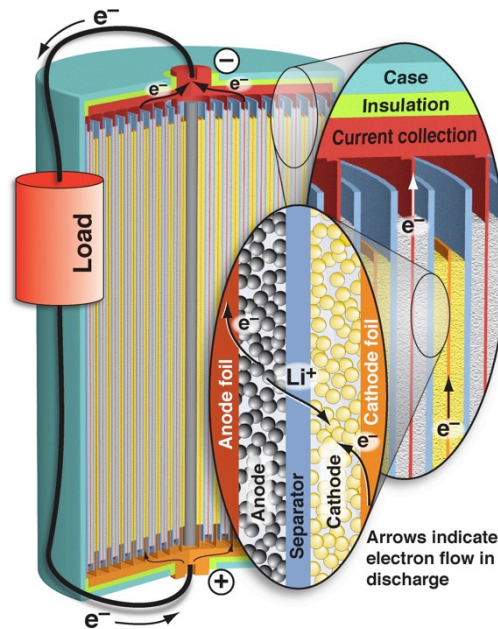


Figure 1: Schematic of a cylindrical battery cell, showing the arrangement of the anode, cathode, and separator elements in the spiral coil. Figure by Bob Kee.

Figure 1 shows a schematic drawing of a Li-ion cylindrical cell: shown is the anode or negative electrode, a separator and electrolyte region, and a cathode or positive electrode. When the battery is fully charged, the Li-ions reside in the anode. As the battery discharges, the ions move through the electrolyte from the anode to the cathode; the electrons, which can't pass through the insulating electrolyte region, pass through an external wire. Because the Li-ions are energetically more stable in the cathode materials than the anode materials, one can extract work from the electrons in the external circuit as they accompany the Li-ions to preserve charge balance during the discharge process. Not shown between the anode and the electrolyte regions is the solid electrolyte interphase (SEI) layer, a thin (50 nm) passivating layer that forms from decomposed electrolyte molecules during the initial charging cycles of the battery, and prevents lithiated anode material from reacting with additional electrolyte molecules. A passivating layer also forms on the cathode, but it is smaller and less critical to the battery's performance and degradation, and we will not consider the cathode SEI layer in this report.

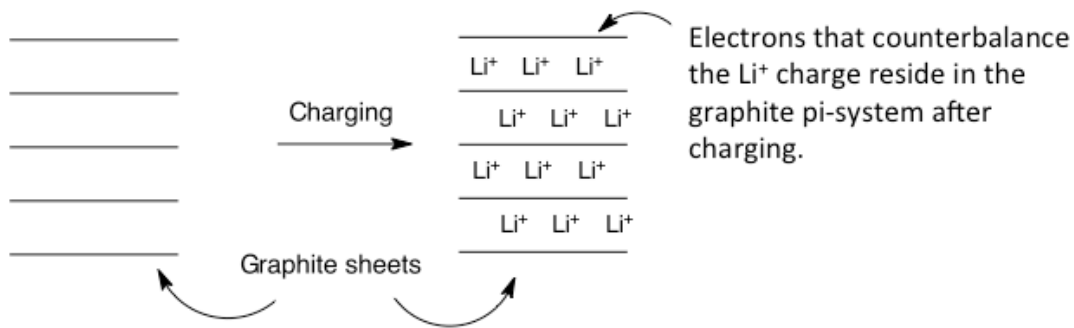


Figure 2: Schematic of Li intercalation into graphite during battery charging.

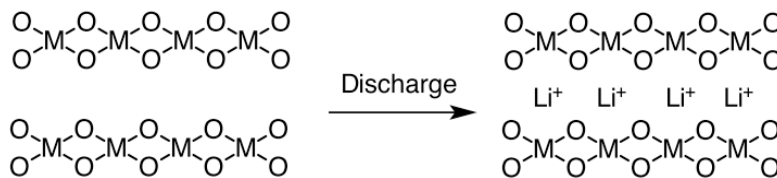


Figure 3: Schematic of Li intercalation into a metal-oxide material during battery discharge. The electrons that accompany the Li^+ ions reduce the oxidation state of the metal atom after discharge.

In a typical transportation battery, the anode consists of one of a number of forms of graphitic carbon materials, which intercalate Li^+ between the graphite sheets. The cathode consists of a number of different metal oxides (LiCoO_2 , LiMn_2O_4) or metal phosphate (LiFePO_4), among other compounds. FIG X1a shows Li^+ ions intercalated in graphite or a metal oxide.

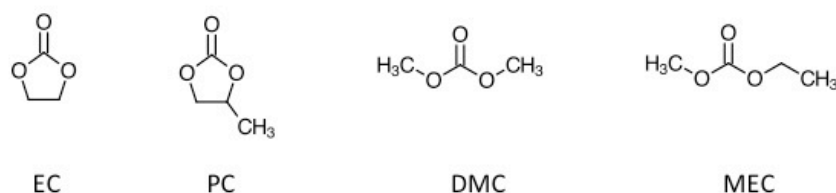


Figure 4: Commonly used Li-ion battery electrolyte materials, including ethylene carbonate (EC), propylene carbonate (PC), dimethyl carbonate (DMC), and methyl ethyl carbonate (MEC).

The electrolyte is a mixture of organic carbonate compounds (Figure 4), which have high Li^+ conductivities, typically a 50:50 mixture of ethylene carbonate (EC) and dimethyl carbonate (DMC). EC is chosen because it forms stable SEI layers, and DMC is chosen because it keeps the EC/DMC mixture liquid at relevant operating temperatures. The compound PF_6^- is typically used as a negatively-charged counterion to balance the positive charge introduced as Li^+ is transported through the electrolyte.

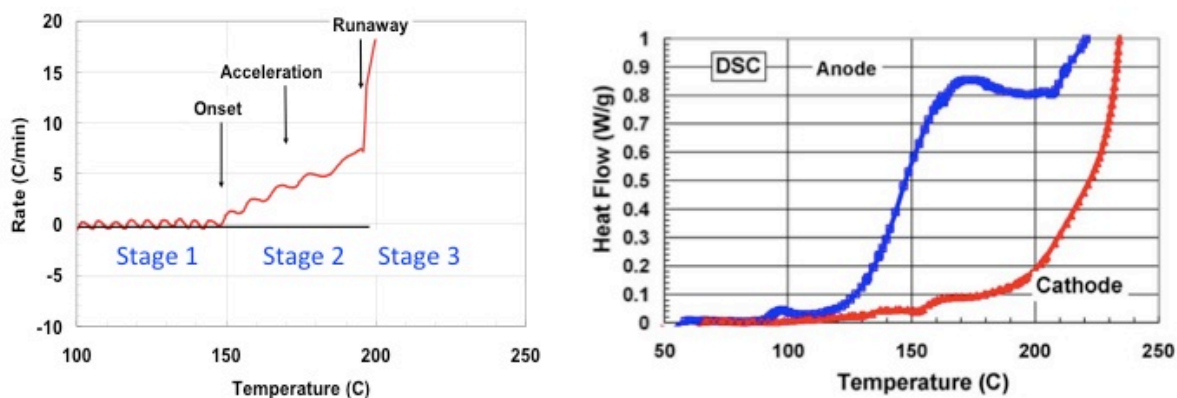


Figure 5: Thermal ramp data (left, from Ref (Doughty 2005)) and DSC data (right, from Ref (Abraham, Roth et al. 2006)) for thermal abuse of Li-ion Batteries.

Figure 5 shows one type of data collected by the BATLab, in this case thermal ramp data on the left (Doughty 2005), and differential scanning calorimetry (DSC) on the right (Abraham, Roth et al. 2006). The thermal ramp experiment consists of putting a battery cell in a temperature-controlled cell, heating it to different temperatures, and monitoring the heat production rate. In examining the ARC data, one sees several different regimes. Below 150 C (“stage 1”) the battery produces no additional heat. Between 150 and 190 C (“stage 2”) the additional ambient temperature enables chemical reactions in the battery that begin to produce heat, and the battery responds roughly linearly to the ambient temperature. Above 190 C (“stage 3”), the battery is in

full thermal runaway, and the rate of heat release is much more than linear; it is in this latter stage that the battery often produces enough heat to catch fire.

The DSC data provides additional resolution. In a DSC experiment, the battery cell is opened, and part of the anode electrode, with some of the electrolyte, is put in one compartment, and part of the cathode, again with some electrolyte, is put in another compartment. The apparatus is again held at different temperatures, but this time the amount of heat flow required to keep each compartment at a constant temperature is measured. In this way, separate information from the anode and the cathode thermal decomposition may be collected. Examining the DSC data in FIG X2 shows that at 125 C the anode is already showing a thermal response to the accelerated temperature, even though the ramp data doesn't show a cell-level response at this temperature. At around 150 C the cathode also begins showing a response, and both compartments are showing large heat fluxes by 200 C.

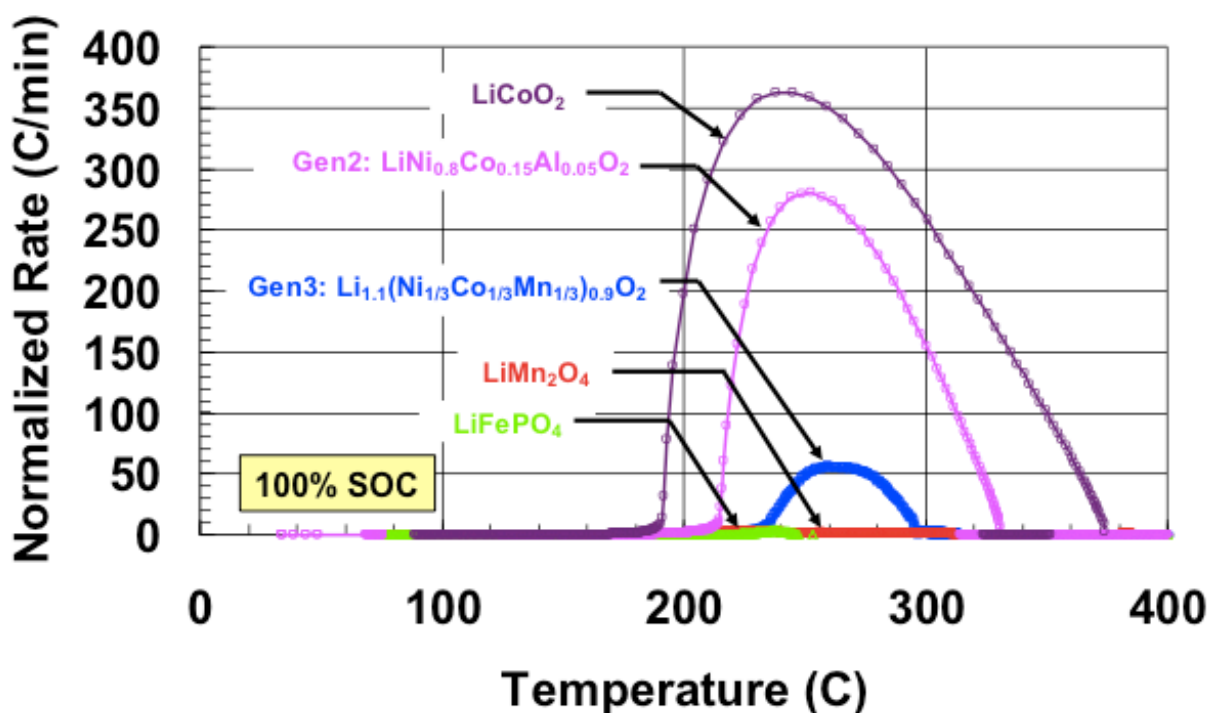


Figure 6: Heat release from different cathode materials, taken from Ref (Roth 2008).

The picture that arises from the above calorimetry data is one in which at lower temperatures the SEI passivation layer either starts to break down, exposing the electrolyte to lithiated carbon. The exothermic reactions that form the SEI layer itself are again possible, and form more SEI type product, generating heat in the process. At low total reaction rates, this heat can be dissipated (stage 1 in Figure 5). Beyond this point, however, the battery heats enough to accelerate the heating process (stage 2 in Figure 5). When the heat reaches a sufficient point, phase changes are possible in the cathode that change the cathode stoichiometry, for example, one that takes



The resulting oxygen species can cross the cell and further decompose the anode SEI layer. When the anode SEI decomposition reactions and the cathode phase change reactions are both occurring and reinforcing each other, thermal runaway (stage 3, Figure 5) can occur.

The role of cathode oxygen release is reinforced by the data shown in Figure 6, which shows a normalized rate coefficient for heat release from the cathode at various temperatures. The original CoO_2 layered compound, as well as more recent improvements (the Gen2 and Gen3 materials, which are also layered compounds, but with different metals substituted for some of the Co) all show steady improvement, but still substantial heat release. Newer materials, such as the Mn_2O_4 spinel material and the FePO_4 olivine material, are negligible on the scale of the figure, and yet still remain a risk for thermal abuse and runaway.

It is also worth noting that, despite the elevated safety risk provided by these chemistries, the layered compounds are still in wide use in the battery industry, due to their lower cost, greater lifetime, and superior charging rates. Many issues determine whether a particular battery chemistry will succeed in the marketplace, safety being only one of them.

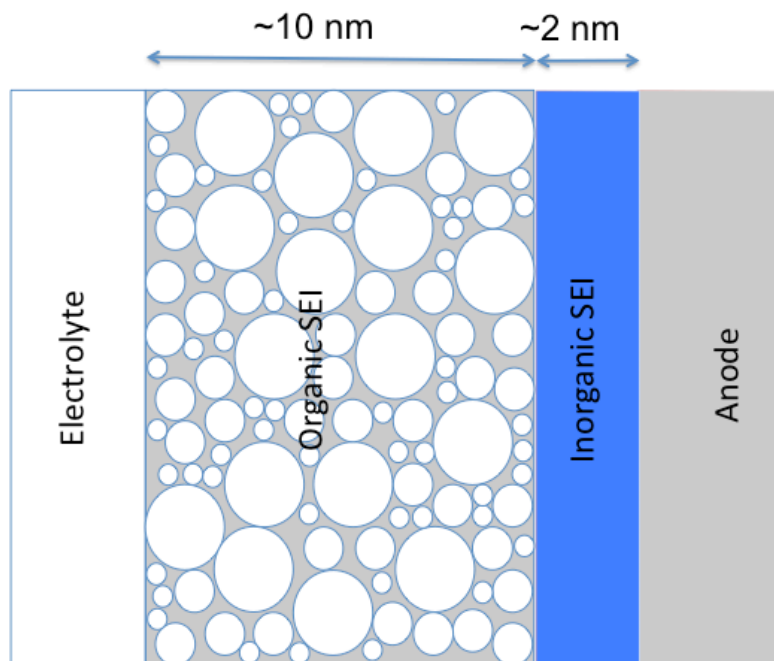


Figure 7: Hypothetical structure of the SEI layer.

Figure 7 shows a hypothetical structure of the SEI layer. The exact structure has been hard to characterize, since the interphase is amorphous, polycrystalline, and at least partially soluble in the EC solution. What is known is that the SEI is composed broadly of two different types of precipitates: a denser layer made up of inorganic precipitates such as Li_2CO_3 , LiF , and Li_2O , and a more porous layer made up of organic precipitates such as alkyl carbonates and dicarbonates. The composition of the inorganic layer is thought to be largely composed of Li_2CO_3 , and the

structure of the organic layer is thought to be largely composed of lithium ethylene dicarbonate ($\text{LiCO}_3\text{C}_2\text{H}_4\text{CO}_3\text{Li}$) (Zhuang, Xu et al. 2005).

The SEI forms when lithiated carbon in the anode reacts with the electrolyte. The accepted formation mechanism is due to Aurbach (Aurbach, Gofer et al. 1992; Aurbach, Einely et al. 1994), and consists of singly reduced species forming the organic/semicarboxylate SEI layer



and doubly reduced species forming the inorganic layer



The thicknesses of the different SEI layers remain something of a mystery. The inorganic layer is thought to be ~2 nm thick, and can be seen as an electron-transfer-limited passivation layer; because the inorganic materials will be insulating, electrons flow from the anode surface and form more inorganic layer until a sufficient insulating thickness is formed to prevent further electron flow. The organic layer is thought to range from 10-50 nm, and it is hard to understand the formation of such a thick insulating layer being formed by direct electron transfer from the surface.

The reactions (1.1.2)-(1.1.4) are exothermic and produce substantial heat as they occur. Normally a battery is made by putting layers of (delithiated) anode, separator, and (lithiated) cathode materials together, adding electrolyte, and then connecting the electrodes to a voltage supply to run through a preprogrammed “formation cycle”. In this process the battery is brought slowly through the charging process so that a stable SEI layer can be formed and so that the heat resulting from this formation can be properly dissipated. Once a stable insulating layer forms, however, the electrons are prevented from passing through the SEI layer, and must instead pass through the external circuit, where they can perform work. The Li^+ cations do diffuse through the SEI layer, where they join with the electrons in the cathode. Were the SEI layer of a fully charged battery to suddenly disappear, the exothermic reactions (1.1.2)-(1.1.4) would rapidly occur, producing substantial heat and thermal runaway.

A very promising approach to modeling thermal abuse in transportation batteries comes from Jeff Dahn and coworkers (Hatchard, MacNeil et al. 2001), who define a simple thermal model for the battery containing heat production terms for the anode

$$P = H_1 A_1 x_f^n \exp\left(\frac{-E_1}{k_B T}\right) + H_2 A_2 x_i \exp\left(\frac{-E_2}{k_B T}\right) \quad (1.1.5)$$

as well as for the cathode

$$P = HA \exp\left(\frac{-E}{k_B T}\right) \alpha^m (1 - \alpha)^n \quad (1.1.6)$$

where the H , A , and E terms are thermodynamic parameters for the various heat production reactions (e.g. eqs (1.1.2)-(1.1.4)) at the anode and cathode, and where the x parameters are related to the thickness of the SEI layer.

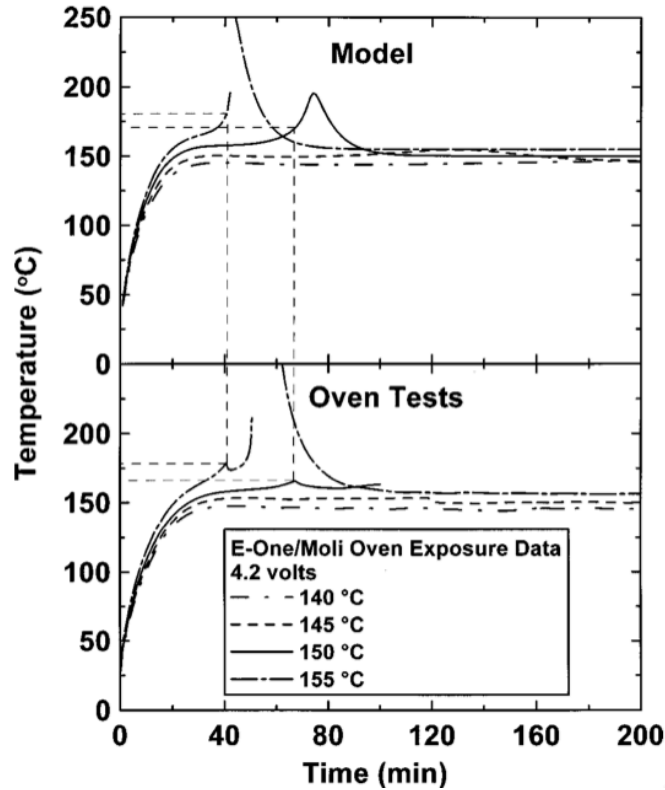


Figure 8: Computational model for thermal abuse of Li-ion batteries (top), compared to experimental results (bottom), from (Hatchard, MacNeil et al. 2001).

Figure 8 shows the excellent agreement these models give when fit to experiment. One of the aims of our project is to develop computational tools that would allow equations of the form (1.1.5) and (1.1.6) to be developed from first principles. The reason we suggest that different functional forms may be required, and not simply different parameters to existing functional forms, can be seen in Figure 9. Here we compare Dahn's functional form with several different activation barriers, and find poor agreement with experimental data (left). In contrast, using a reaction-diffusion form (right) gives much better agreement.

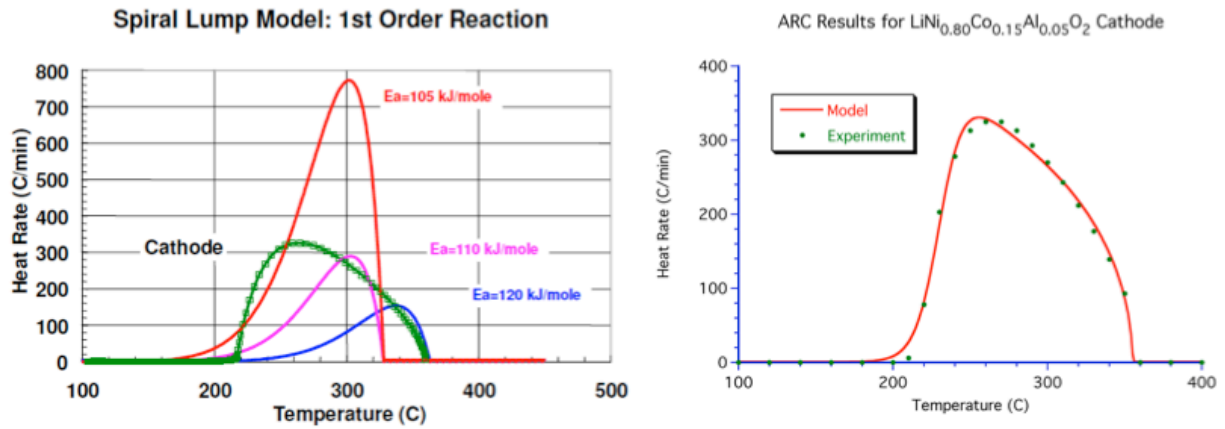


Figure 9: Comparison of fits (left, red, purple, blue lines) using Dahn autocatalytic functional form shows poor agreement with data (left, green points), regardless of activation barrier; in contrast, using a more sophisticated reaction-diffusion functional form (right, red lines) shows much better agreement to data (right, green points).

Our aim in the current work is to understand the chemical mechanisms leading to the formation and decomposition of the SEI layer, as this process has been inexorably linked to thermal abuse and runaway. Modeling such processes is a considerable challenge: accurate modeling of the reaction chemistry in equations (1.1.2)-(1.1.4) requires quantum methods such as density functional theory that can provide sufficient accuracy at high computational cost, a cost that precludes their applications to something even as large as the 50 nm thick SEI layer, much less application to an entire battery cell. We therefore use a multiscale approach to modeling as described below to provide the accuracy of techniques such as density functional theory (DFT) to predict the rates and the thermodynamics of the elementary reactions, yet still be capable of describing the evolution of the SEI microstructure as well as the overall battery cell performance.

2 MODELING RESEARCH AND DEVELOPMENT

2.1 Overview

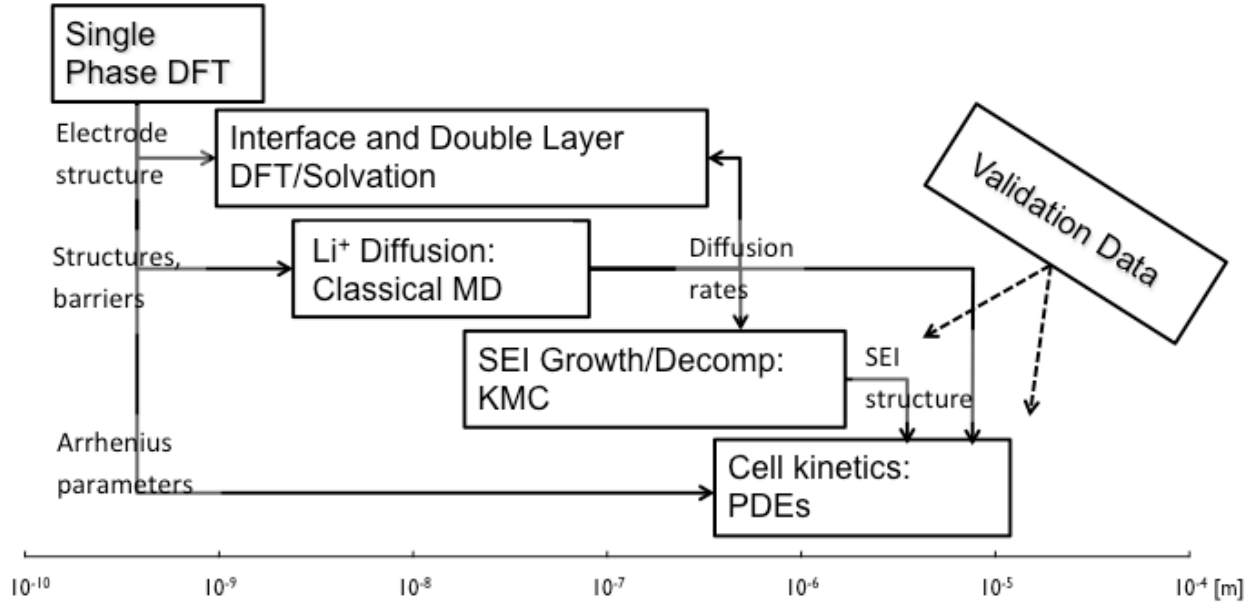


Figure 10: Hierarchy of multiscale modeling approaches used to understand and predict battery safety.

Figure 10 describes the multiscale modeling approach used in the current project. We use single-phase (i.e. gas phase or 3D periodic boundary conditions) DFT calculations to understand structures and bulk thermodynamics of different materials. This type of calculation is described in Section 2.2 below. These calculations provide input to an electrode interface capability that we have developed as part of this project and that is described below; this capability describes an electrode and the double-layer of the solvating electrolyte, to understand the impact of the electrode structure and the applied voltage, if any, on reactions that occur at the electrode-electrolyte interface. The electrode-electrolyte interfacial calculations are described in Section 2.3, below.

We use molecular dynamics (MD) techniques using classical force fields to predict Li⁺ diffusion through the various phases in the battery cell. These calculations may be validated against the barriers and the structures predicted by the quantum capabilities, above, and provide diffusion rate constants for the mesoscale and cell modeling components. This capability is described in Section 2.4.

We use the chemical mechanisms developed using the DFT capabilities in Section 2.2 and 2.3 for EC decomposition to predict the growth of the SEI passivating layers using mesoscale

modeling techniques, including kinetic Monte Carlo (KMC) and phase field methods. This technique is described in Section 2.5.

Finally, we take the rates from the DFT capabilities, the diffusion constants from the MD capabilities, the SEI microstructure and growth/decomposition rates from the mesoscale capabilities and input this into a macrohomogeneous cell model that describes battery operation under normal and abusive conditions. This capability is described in Section 2.6.

2.2 Single Phase Quantum DFT Mechanisms

We first consider the energetics of battery electrolyte decomposition leading to SEI formation, computing reaction energetics of simple molecules, in the gas phase, or in dielectric continuum regions representing the electrolyte solution. For this consideration, we use DFT calculations (Kohn and SHAM 1965) using a hybrid B3LYP functional (Becke 1993) and a double-zeta plus polarization basis set with diffuse functions included to treat anionic species. Because EC decomposition in batteries occurs in the battery electrolyte solvent (roughly a 50:50 mixture of EC and DMC), we also include the effect of the solvent on the energetics, using a Poisson-Boltzmann solvation (Marten, Kim et al. 1996) dielectric with a dielectric constant of 40 (chosen to match measurements (Sasaki, Hosoya et al. 1997) on a 50:50 EC/DMC mixture), and with a solvent radius chosen to match that of EC. All calculations were performed using the Jaguar quantum chemistry package (2009).

2.2.1 Bond Breaking Reactions

We first consider simple bond-breaking reactions. Given the components of a battery electrolyte, we determine which bonds are the easiest to break, as these are the most likely to break when exposed to the Li^+ and e^- coming from the anode when the SEI layer forms.

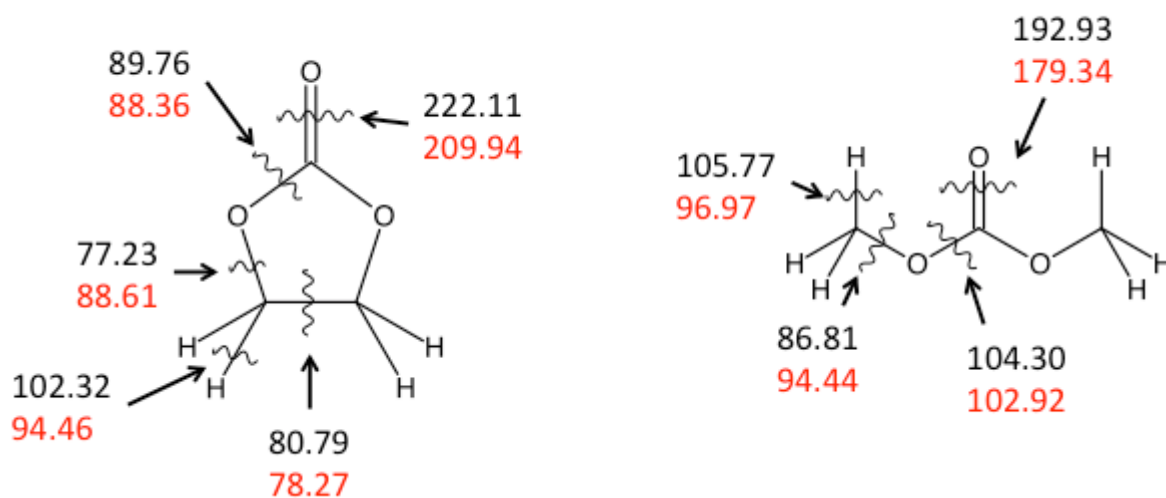


Figure 11: Energies (kcal/mol) for breaking the indicated bonds in EC (left) and DMC (right), computed using B3LYP/6-31G*** (black) and MP2/6-31G*** (red) levels in the gas phase.

Figure 11 shows the energy (in kcal/mol) required to break various bonds in EC and DMC. The numbers in black are for B3LYP/6-31G*** calculations, the primary method we will use throughout this section. As a validation of the method, we also present MP2/6-31G*** calculations here for the same reactions.

In EC at the B3LYP level, the CH₂-O bond is the easiest bond to break, which agrees with most other studies (Wang and Balbuena 2001; Wang and Balbuena 2002; Wang and Balbuena 2002; Wang and Balbuena 2005; Bedrov, Smith et al. 2012) of EC decomposition. What is interesting is that several other bond-breaking reactions are competitive with this reaction at the MP2 level, including the CH₂-CH₂ bond and the O-CO bond. In DMC, the CH₃-O bond is the easiest to break when computed using B3LYP; as with EC, when the MP2 method is used, other bonds become competitive, including C-H dissociation.

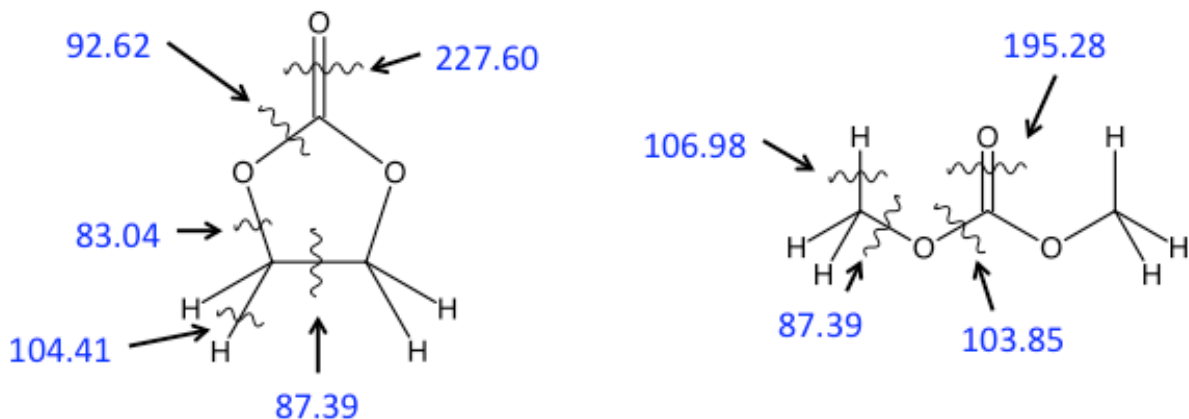


Figure 12: Energies (kcal/mol) for breaking the indicated bonds in EC (left) and DMC (right), computed using B3LYP/6-31G**++ in a solvation dielectric corresponding to a 50:50 EC/DMC mixture (blue).

Figure 12 reports bond breaking energies (kcal/mol) using the B3LYP/6-31G**++ method, in the reaction field given by a Poisson-Boltzmann continuum dielectric whose dielectric constant of 40 is chosen to correspond to a 50:50 mixture of EC/DMC (Sasaki, Hosoya et al. 1997), and whose solvent radius is chosen to correspond to that of EC. Here the overall trend is similar to that of the gas phase B3LYP calculations (as is generally expected for uncharged species): again, the CH₂-O bond breaks most readily in EC, and the CH₃-O bond breaks most readily in DMC.

Figure 13 reports bond breaking energies (kcal/mol), again using B3LYP/6-31G**++, in the gas phase (black) and solvated with the above reaction field that corresponds to EC/DMC (blue), but for an EC anion. Here we see substantial differences over the analogous reactions for the neutral molecule. In particular, the CH₂-O bond breaking is now exothermic in both the gas-phase and in solution, and the O-CO bond is close to energetically neutral in both gas-phase and in solution.

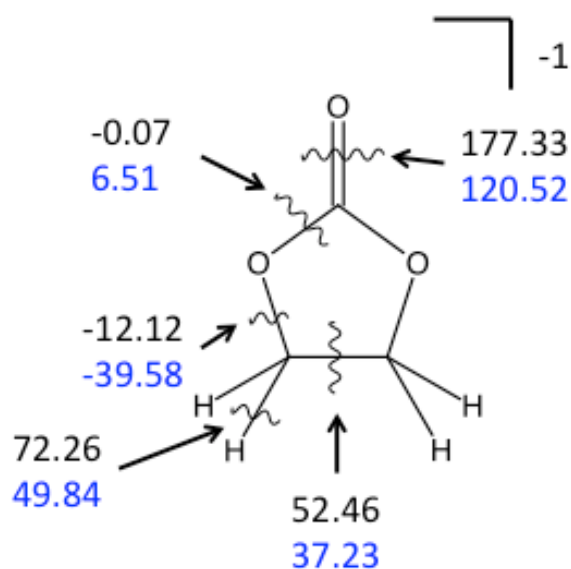


Figure 13: Energies (kcal/mol) for breaking the indicated bonds in EC⁻ computed using B3LYP/6-31G^{***} in the gas phase (black) and in a solvation dielectric corresponding to a 50:50 EC/DMC mixture (blue).

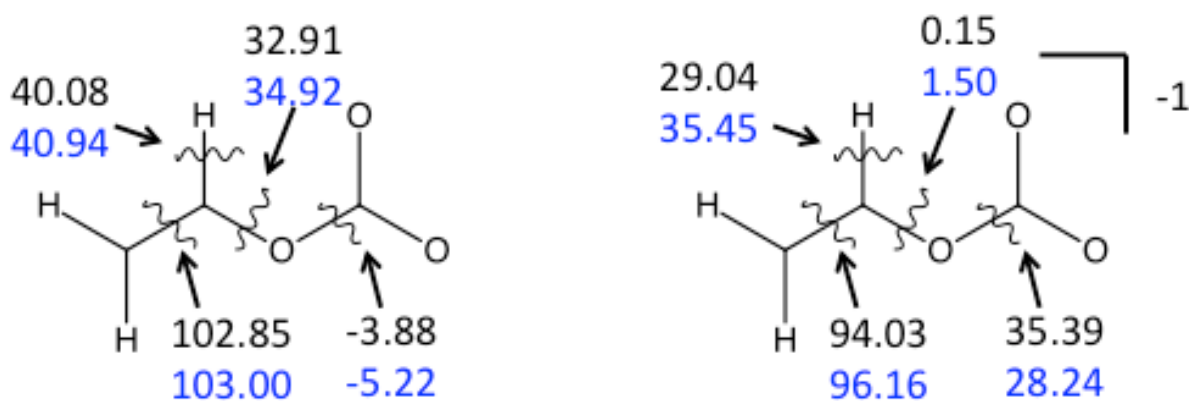


Figure 14: Energies (kcal/mol) for breaking the indicated bonds in ring-opened EC (left) and ring-opened EC⁻ (right) computed using B3LYP/6-31G^{***} in the gas phase (black) and in a solvation dielectric corresponding to a 50:50 EC/DMC mixture (blue).

Finally, Figure 14 reports B3LYP bond breaking energies for ring-opened EC (ROEC), an EC molecule with the CH₂-O bond broken, using both gas phase (black) and solvated (blue) methods, for the neutral (left) and anionic (right) species. Notable is the dominance of the O-CO₂ bond breaking reactions in the gas phase, and the HC-OCO₂ bond in solution.

If we consider only the most likely bond breaking reactions determined above we can already obtain a very simple (as well as oversimplified) picture of EC decomposition. The EC molecule will most likely break the CH₂-O bond, either before or after reduction, and will subsequently break the HC-OCO₂ bond or the O-CO₂ bond. Such a decomposition pathway would lead to C₂H₄, OC₂H₄, CO₂, and CO₃ fragments in various states of charge, all of which have been observed experimentally (Roth 2008).

2.2.2 Mechanisms for SEI Formation

We now consider mechanisms for SEI formation. The accepted mechanism due to Aurbach (Aurbach, Gofer et al. 1992; Aurbach, Einely et al. 1994) is listed as equations (E2)-(E4). To a large extent, the results in the previous section corroborate such a mechanism: certainly equation (E2) is the most likely first step, and something along the lines of (E4) is also a likely reaction for subsequent reductions. However, reaction (E3) is somewhat suspect, as it requires two free-radical species to collide and react with one another in solution, something that goes against simple chemical kinetics, which would typically assume that highly reactive species such as free radical are more likely to react with less reactive (and thus more stable and thus more likely to be present) species rather than more reactive species. But what is present to react with other than another ROEC molecule? The solution we propose is that the EC solvent itself is far more likely to react with a stable EC molecule than with another reactive ROEC molecule.

We now consider the steps that lead to formation of organic and inorganic SEI layers. As above, we compute energetics for isolated molecules in a dielectric that represents a mixture of EC/DMC. For the purposes of these reactions, we assume that electrons can be added at zero energetic cost. This overestimates the likelihood of reduction reactions somewhat.

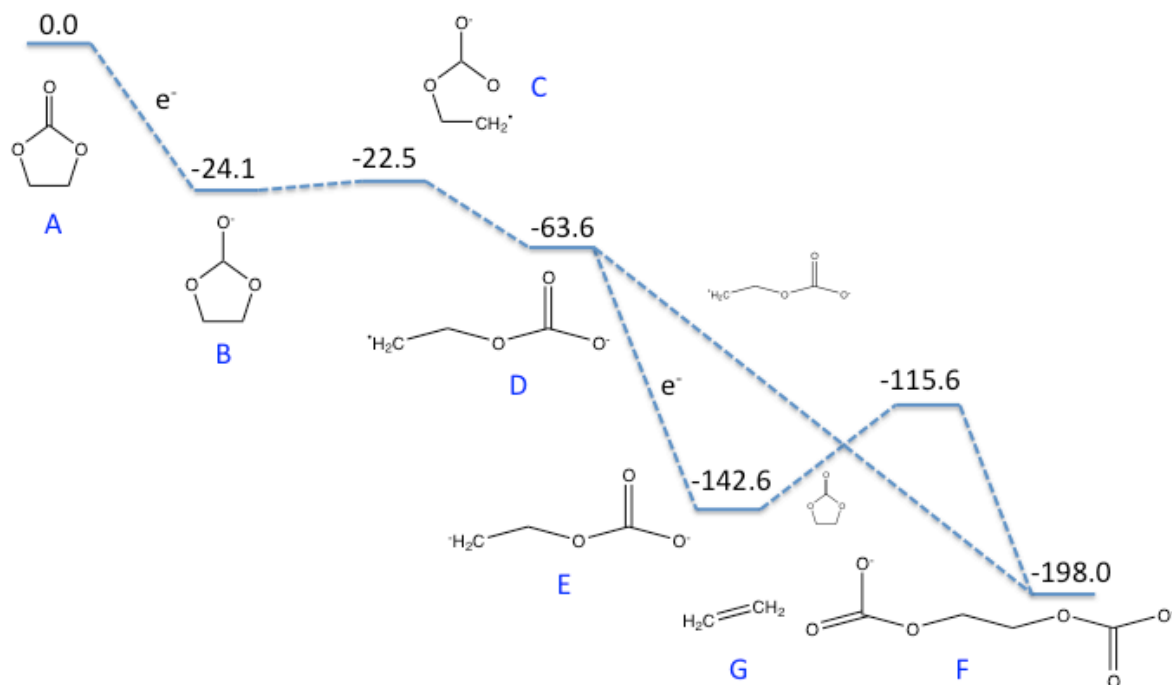


Figure 15: Reactions leading to the formation of organic SEI compounds, primarily EDC. B3LYP/6-31G**++ energies in kcal/mol computed using a dielectric representing a 50:50 EC/DMC mixture.

Figure 15 shows formation of EDC from EC. We find that the most energetically favorable reaction is adding a single electron to EC (structure A), forming the anionic EC⁻ species (structure B). With a very slight barrier (1.6 kcal/mol, to structure C), the EC⁻ molecule can ring open to form CH₂CH₂OCO₂⁻, a species that we shall hereafter refer to as ring-opened EC⁻ (ROEC⁻, structure D). We have investigated several reactions from this point in the reaction scheme; the most likely of these turns out to be a second reduction of the ROEC⁻ species, forming a dianionic species, structure E. This species, it is found, can add to the native EC solvent with a low (as of yet undetermined) barrier, to form EDC dianion, structure F, and ethylene gas, structure G. Because the Aurbach mechanism represents the reaction of two radical species, we believe this reaction should occur extremely rapidly, essentially without a barrier, to couple two of the D structures to the F+G species; however, for kinetic reasons referred to above, we do not believe this reaction is likely to happen to a great extent in solution.

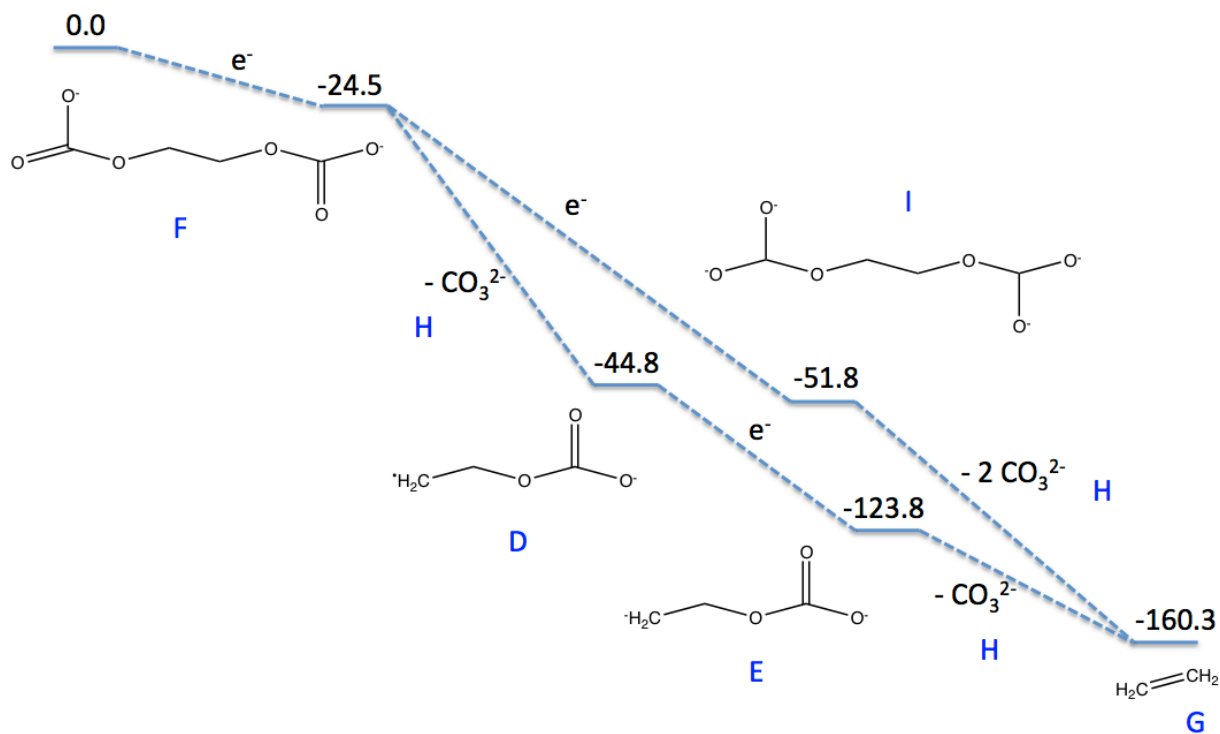
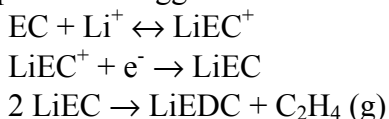


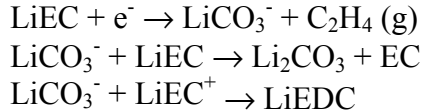
Figure 16: Reactions leading to the formation of inorganic SEI compounds, primarily Li_2CO_3 . B3LYP/6-31G**++ energies in kcal/mol computed using a dielectric representing a 50:50 EC/DMC mixture.

Figure 16 details several additional schemes that can occur to form the inorganic Li_2CO_3 compound. We can reduce the EDC compound, structure F, which can then either dissociate a carbonate (CO_3^- , structure H) group that will precipitate with Li^+ in the cell, forming ROEC $^-$, structure D. This species can either participate in the reactions to form the organic SEI species in Figure 15, or can again be reduced and dissociate a second carbonate group, structure H again, forming more ethylene. The sequence of these reactions can either occur reduction-dissociation-reduction-dissociation, or reduction-reduction-dissociation-dissociation, as shown in the figure.

Given the fact that the inorganic species are energetically downhill from the organic species, why do we see the organic species form at all? This discussion amounts to speculation on our part, but one explanation is that the organic species are kinetically favored, and form first and fastest. It is known experimentally that the organic layer is more porous and can allow electron transfer. In contrast, the inorganic layer should be a typical insulating oxide layer that will not allow electron transfer. When the subsequent reactions occur to form inorganic species from the organic species, this can only occur until a sufficiently thick layer forms to fully insulate the surface and shut off electron transfer. We assume that this should take 2-10 nm, in agreement with experimental observation.

These processes suggest the reaction scheme, this time including the Li^+ species,





We have used this reaction scheme in the subsequent sections to model SEI growth processes.

2.3 Electrode-Electrolyte Interfacial Modeling

2.3.1 Modeling an Electrochemical System

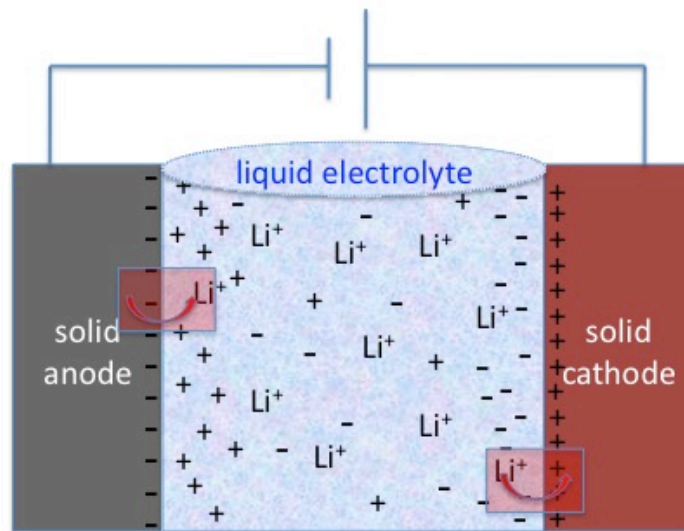


Figure 17: Conceptual model of a lithium-ion battery

Figure 17 depicts an idealization of a lithium-ion battery system, which serves as a conceptual model from which to design an approach to simulate the crucial chemistry of interest at the electrode-electrolyte interface.

A solid anode and solid cathode are separated by a liquid electrolyte. As a function of charging (or discharging), with an applied potential, a Li ion is removed from one electrode, migrates through the electrolyte, and inserts into the other electrode, while the electron, is forced to travel through the conductive circuit, the electrolyte not being conductive. It is the chemistry at the interface, and particularly the insertion of the Li ion from the electrolyte into the electrode (or vice versa), highlighted in the red squares in the figure, that needs to be quantified with modeling. Complicating this picture, with an applied potential, there is build up of charge at the electrode surface, and electrolyte responds to screen that surface charge with solvated ions, forming a double layer. The distribution of charges affects the local chemistry, and a predictive model must take this into account. Further complicating this simple picture is the formation of a solid-electrolyte-interphase at the interface. It is the detailed interplay of the state of charging of the overall systems, the consequent distribution of charge at and near the electrode-electrolyte

interface, and the energetics of the individual chemical processes—insertion or removal of Li ion, formation of SEI phases, decomposition of electrolyte at the interface, etc.—that govern the performance of a battery chemistry and the breakdown of that chemistry in thermal abuse. To model chemical reaction processes between the electrode and electrolyte with sufficient fidelity, a quantum chemical approach is needed, but quantum chemistry can only model systems with a few hundred atoms effectively, and not the full conceptual model. That model must faithfully represent the boundary conditions of the full system, and also include the statistical and dynamical properties of the electrolyte in an adequate thermodynamical treatment, formal challenges that have not been fully overcome. In this section we describe the development of an approach to develop an integrated method to compute interfacial chemistry.

To simplify the immediate task, we will focus on a particular cathode material, lithium manganese oxide, as the cathode is less prone to formation of SEI layers than the anode and this spinel is considered a good and interesting cathode material. This next section discusses the quantum calculations for the bulk crystal substrate. The correct treatment of the electrostatic boundary conditions in the supercell approximation, in systems with net charge and electric fields, is the subject of the following section. Next, within conventional DFT calculations, a slab model is used to simulate the surface, and also the interface, and we describe the limitations of that model and review approaches that been used to simulate the interface. A statistical approach to model the electrolyte describing the distribution of charge within the electrolyte, a fluids density functional theory, is then described. And finally, our approach, which coordinates the quantum DFT treatment of the solid and the interface with the fluids-DFT description of the electrolyte, communicating the correct electrostatic boundary conditions back and forth, is described.

2.3.2 Bulk DFT simulations of materials – lithium manganese oxides

Manganese oxides are of particular interest for use as cathode materials in lithium based battery chemistries. The spinel structures readily and reversibly take up and discharge lithium, starting with $\text{Li}_0(\text{Mn}_2\text{O}_4)$ “Li0” through $\text{Li}_1(\text{Mn}_2\text{O}_4)$ “Li1” to $\text{Li}_2(\text{Mn}_2\text{O}_4)$ “Li2” composition, without large changes in structure (one characteristic desired for a viable electrode material). The potential for high energy density and cyclability make the spinel a good candidate for a cathode material. The relatively simple structure, in addition to its relevance to current cathode development, make this a good choice for an example problem to illustrate methods for the treatment of electrolyte-electrode interfaces.

A necessary prerequisite for developing a surface model of the spinel for the interface DFT calculations, is characterization of the bulk properties of the material. To avoid computational artifacts, the treatment of the surface must be consistent with the treatment of the bulk substrate (Magyar, Mattsson et al. 2011). The Li0 compound is cubic, but as lithium atoms are intercalated, the compound lowers its symmetry, to orthorhombic for the Li2 compound. The structure of the lithiated manganese spinels has been the object of first-principles density functional theory calculations (Mishra and Ceder 1999; Grechnev, Ahuja et al. 2002; Fang and de Wijs 2006), and these studies have characterized some of the complexity in the structures

when transitioning from Li0 to Li2, and Mishra and Ceder (Mishra and Ceder 1999), in particular, demonstrate the importance of spin-polarization and magnetic effects in obtaining a good consistent picture of the different lithiated spinels, and further point out that a generalized gradient approximation (GGA), such as implemented in the Perdew/Burke/Ernzerhof (PBE) functional (Perdew, Burke et al. 1996) is needed to get a good description of the bulk properties; a local density approximation (LDA) functional (Ceperley and Alder 1980 ; Perdew and Zunger 1981) does not.

Examination of the nominal oxidation states of the atoms in the manganese oxides immediately illustrates the origin of the Jahn-Teller instability and the importance of magnetic effects. As shown in the following Figure 18.

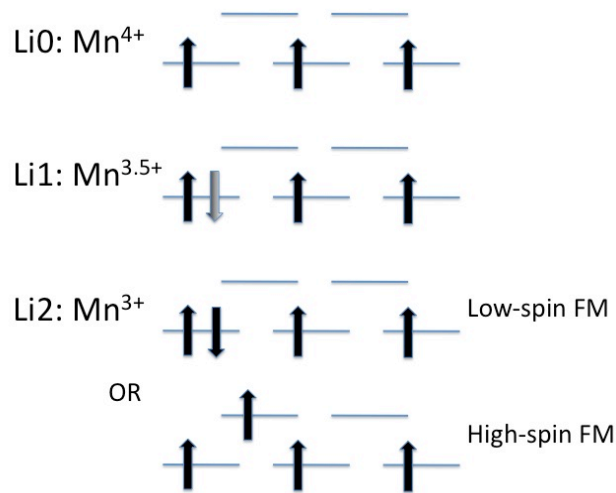


Figure 18: Illustration of the local level structure on the Mn atom in the $\text{Li}_{(0,1,2)}\text{Mn}_2\text{O}_4$ compound.

The crystal field in the cubic spinel splits the five d -states on Mn into two sets of states: a triply-degenerate t_{2g} and a pair of higher e_g states. In the Li0 compound, the three valence electrons on the Mn fill each of the lower states with one electron, and by Hund's rule, these will couple into a high-spin state. This state is non-degenerate, and keeps a cubic structure. Upon lithiation, the extra electron either falls into the lower states, reducing the net magnetism or, with large enough exchange coupling, can stabilize an electron in the state with an increased net spin. In either case, a degeneracy in the state occupations (ambiguity concerning which one of the degenerate state to put the extra electron into) leads to a structural instability and slight distortion to an orthorhombic state. Here, we restrict our attention to just the cubic structure; the distortions, being driven by non-bonding d -electrons, are modest, and, for the purpose of demonstrating the new methods for modeling boundary conditions at the surface, can be ignored.

Departing from earlier example (Fang and de Wijs 2006), we use the rhombohedral (fcc) primitive unit cell, $\text{Li}_x\text{Mn}_4\text{O}_8$, rather than the larger, conventional cubic units cells composed of eight formula units. The calculations are equivalent for crystal calculations, and the smaller

primitive cells leads to faster calculations. We use the SeqQuest code (Schultz 2012) to perform the DFT calculations to optimize the crystal structure. Carefully converged pseudopotentials (PP) and optimized contracted-Gaussian basis set were used for all atoms, taken from the SeqQuest library. Following earlier examples (Mishra and Ceder 1999; Grechnev, Ahuja et al. 2002; Fang and de Wijs 2006), we use the PBE flavor of GGA in the calculations. We performed optimization of the crystal structure, both atomic positions (the oxygen parameter u_o) and cell shape. With the location of Mn in the Periodic Table, the semicore $3p^6$ electrons on the Mn atom can affect the valence chemistry, and we tested the adequacy of the PP to determine whether their effects can be adequately embodied through a non-linear core correction to the PP (Louie, Froyen et al. 1982), designated “p0”, or if the shell of six semicore p -electrons must be included explicitly in (more expensive) calculations, denoted “p6”. The structural calculations were done for both non-magnetic (NM) and ferromagnetic (FM) spin states. The Li2 structural optimizations were done for the low-spin (2 electrons/Mn: FM(2)) and high-spin (4 electrons/Mn:FM(4)) ferromagnetic states. The results of these calculations are in the following table.

Table 1: Results of DFT structural calculations for lithium manganese spinels, a_o in Å (u_o).

Compound	Current DFT results		Other DFT results		
	p0	p6	Mishra’99	Grechnev’02	Fang’06
Li0	Experiment: 8.04 Å (0.389)				
NM	7.974 (.389)	8.031 (.389)	-	8.02	-
FM(3)	8.099 (.389)	8.164 (.389)	8.18 (.390)	8.16	8.148 (.389)
Li1	Experiment: 8.23 Å (0.3875)				
NM	8.038 (.380)	8.041 (.380)	-	7.99	-
FM(2.5)	8.130 (.387)	8.178 (.387)	8.12 (.386)	8.13	8.156 (.3879)
Li2	Experiment: n/a (orthorhombic)				
NM	8.003 (.379)	8.048 (.379)	-	-	-
FM(2)	8.083 (.381)	8.131 (.281)	-	-	-
FM(4)	8.388 (.382)	8.437 (.382)	8.38 (.381)	-	-

(a) The Grechnev results did not perform a relaxation of the internal coordinates, the oxygen position, determined by the positional parameter u_o , was set to the experimental value.

The current results seem to indicate that the explicit treatment of the semicore $6p$ electrons does not affect the structure strongly. The predicted lattice parameter is slightly larger, but the positional parameters do not change, and the difference between the results of the two PP is of the same size or smaller as the error in the use of DFT, i.e., between either of the PP calculations and experiment. This is convenient, as use of the more p0 PP is computationally cheaper, and will facilitate calculations for larger surface models.

The inclusion of magnetism has more prominent importance, confirming the observation made by Mishra and Ceder (Mishra and Ceder 1999). As expected, there are significant energy lowerings with magnetization, and the exchange-mediated repulsions increase the lattice parameter significantly, the greater the spin per Mn, the greater the increase in the lattice parameter. The relatively modest increases for the spin-3e(or 2.5e) forms of about ~ 0.1 Å jumps to almost 0.4 Å for the difference between the NM and high-spin 4-electron FM(4) state of Li2.

Moreover, the non-magnetic forms are all metallic, to obtain a gap consistent with an insulating material, it is necessary to include magnetism. Another consequence of this distinction is that calculations for the NM forms exhibited much greater difficulty in achieving electronic self-consistency and cell optimization. For expedience, to illustrate the implementation of the double-layer boundary conditions, the later surface calculations will use the simplest GGA approximation without spin. Ultimately, for predictive computational description of chemical properties at the surface, the affects of magnetism, and possible calculations beyond even the spin-polarized GGA might be desired.

The calculated structures are in general agreement with previous DFT results and experiment (Mishra and Ceder 1999; Grechnev, Ahuja et al. 2002; Fang and de Wijs 2006), particularly for Li0 and Li1. The calculation of Li2 merits greater attention. The high-spin FM(4) results match well the results of Mishra and Ceder (Mishra and Ceder 1999), but the low-spin FM(2) form, not considered in that earlier work, are very competitive in energy to the FM(4), and the “true” form preferred Mn^{+3} is quite likely beyond the accuracy of standard local DFT methods like those used here.

2.3.3 Electrostatic boundary conditions in periodic DFT calculations

Periodic boundary conditions are a mainstay of electronic structure methods for solid state (non-molecular systems). Crystalline materials are naturally treated with density functional theory codes, a unit cell, typically the primitive cell is treated explicitly within DFT, and the Bloch’s theorem is used to incorporate the infinite lattice through infinite periodic replicas of the unit cell through translation symmetry. To treat non-periodic systems, a supercell approximation is used, as illustrated in Figure 19, where the local, reduced dimension feature—be it a localized defect in a solid or a molecule, or a solid-vacuum interface—is treated as a large crystal.

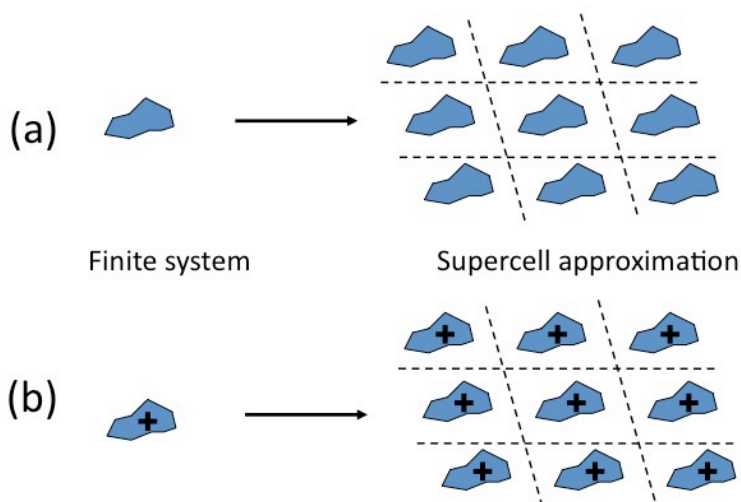


Figure 19: The supercell approximation.

For a molecule or a localized defect in a bulk crystal, as shown in Figure 19(a), the finite system is transformed into a periodically replication crystal. With sufficient buffering between the localized species, either vacuum for molecules or bulk crystal atoms for bulk defects, the direct interactions between the species decreases. In practice, this buffering is quite effective, giving the isolated limits to desired accuracies for relatively small supercells. However, this is only true for species that have no long-range interactions, and this condition is violated if considering a system with a net charge, as illustrated in Figure 19(b). The periodic array of positive charges leads to a divergent electrostatic potential, with infinite energies. The long-range $1/r$ potential of the Coulomb interaction is long-range, and the potential of the central cell of interest is corrupted by the long-range $1/r$ potentials from the infinite periodic replicas of the charge. Obtaining the correct local potential, without these corrupting tails, and recovering a usable and meaningful energy expression requires careful avoidance of these infinities.

In any reduced dimension system with long-range charge (or dipole) potentials, reconstructing the correct boundary conditions for electrostatic is necessary for predictive simulations. Ad hoc solutions, such as using a flat background charge or “jellium” to neutralize the charge in a supercell, allowed calculations to be performed, but while these eliminate the problematic infinity, they do not correct the shape of the corrupted electrostatic potential and quantitative calculations are confounded by the lack of a useful reference potential to relate energies of supercells containing different net charge.

The local moment countercharge (LMCC) method (Schultz 1999; Schultz 2000) created an approach to handle non-periodic systems with problematic charge (and dipole moments) within a supercell approximation, using a hybrid-dimensional solution to the Poisson equation to separate the solution of the problematic, non-periodic part of the electrostatics potential from the non-problematic periodic part. The Poisson equation to solve for the Coulomb potential is linear in the charge (electron) density—the potential from a sum of two densities is exactly equal to the sum of the potentials due to the charge densities taken separately. The LMCC approach takes advantage of this linearity of electrostatic potential by separating the total charge density $\rho_{\text{tot}}(\mathbf{r})$ in the unit cell into two components, a localized model charge density $\rho_{\text{lm}}(\mathbf{r})$ that has the entire charge and, in principle, other problematic local multipole moments (particularly a dipole) and a remainder density $\rho'(\mathbf{r})$:

$$\rho_{\text{tot}}(\mathbf{r}) = \rho'(\mathbf{r}) + \rho_{\text{lm}}(\mathbf{r}). \quad (2.3.1)$$

With judicious design of the local moment charge density and its location, the problematic moments that have potential tails that extend beyond the boundary of the cell are removed from the potential for the remainder periodic density $\rho'(\mathbf{r})$, and the potential for the local moment density $\rho_{\text{lm}}(\mathbf{r})$ is solved analytically with the non-periodic boundary conditions appropriate to the dimensionality of the physical system being simulated. For zero-dimensional systems (ionization potentials or electron affinities in molecules, or point defects in bulk systems), sums of simple Gaussian charge densities were particularly useful to construct $\rho_{\text{lm}}(\mathbf{r})$ —being highly localized, having fast and convenient analytical solutions for their Coulomb potentials, and

leaving a remainder density $\rho'(\mathbf{r})$ with favorable Fourier-transform properties for the periodic part of the Poisson solve. To handle a point dipole moment simply required the sum of two Gaussians, with opposite signs. A simple generalization of the LMCC approach, using a pair of one-dimensional planes to treat the slab surface dipole remove the inter-slab fields and enables resolution of the Poisson Equation with the correct boundary conditions appropriate to an isolated slab (Schultz 1999), within a the same framework as for an isolated molecule. Effectiveness of the LMCC method to isolate long-range Coulomb tails is demonstrated by insensitivity of the results to changes in the supercell size in non-periodic directions, and the LMCC solutions show no variation once the atomic densities attenuate into vacuum, as a practical matter, about 5 Å from any atom.

These LMCC-based solutions introduce discontinuities in the electrostatic potential at the edge of the supercell. For a molecule or slab in vacuum, these discontinuities occur in a vacuum region where there is no density and are inconsequential. For bulk materials, e.g., a defect in semiconductors or, as later, solid-liquid interfaces, additional care must be taken to avoid these discontinuities. For defects, a finite defect supercell model based on the LMCC (Schultz 2006; Schultz and von Lilienfeld 2009) enables quantitative calculations of systems with net charge, illustrating the flexibility of the LMCC approach to solving the Poisson Equation for non-periodic problems within a periodic supercell approximation. Calculations for defect charge transition energy levels in silicon (Schultz 2006), and GaAs (Schultz and von Lilienfeld 2009) indicate that an accuracy of 0.1-0.2 eV is achievable. For the purpose of modeling chemistry at an electrode-electrolyte interface, combining the artifice of a slab geometry and added complexity of a bulk (fluid) environment to model the interface, we generalize the LMCC approach yet further.

2.3.4 Modeling bulk surfaces and solid-liquid interfaces with charge with supercells

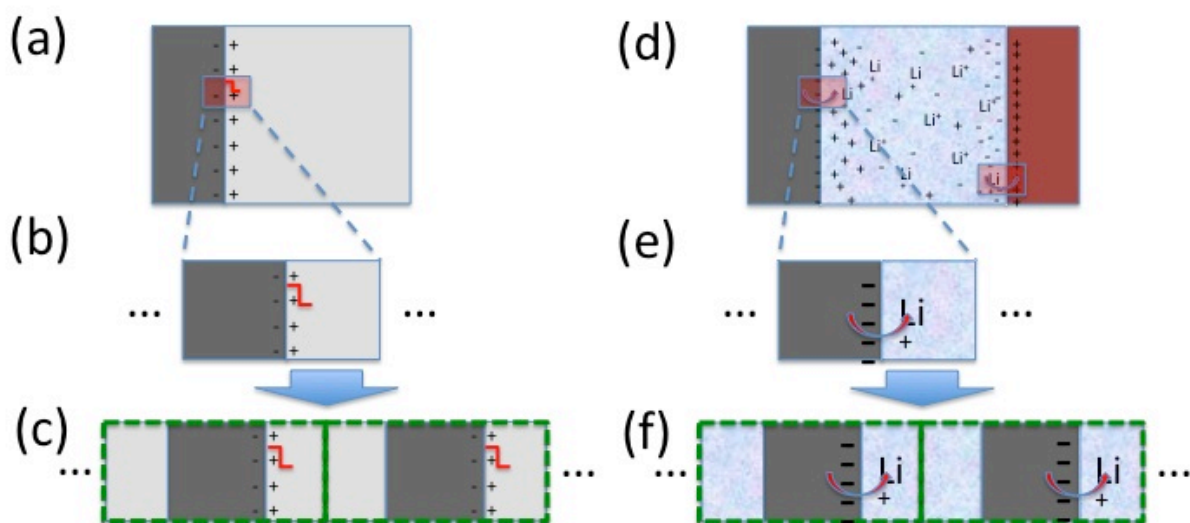


Figure 20: Slab supercell model for a vacuum surface, and electrode-electrolyte interface

Figure 20 depicts the process of the creating a computational model for a surface system, and the electrostatic issues that arise.

Figure 20 (a)-(c) illustrate the steps to construct a slab supercell computational model of a solid surface to vacuum, and (d)-(f) illustrate the more complex chemical challenges of an electrochemical system. To model a surface, a slab model, a periodically repeated thin film of bulk material and vacuum is typically used, and design of this supercell approximation is fraught with delicate construction issues (Magyar, Mattsson et al. 2011). A DFT model excises a small region around a chemical process (in red). The semi-infinite model of (b) is not cast in form usable by computational codes, and a finite slab is periodically replicated normal to the surface with intervening vacuum. If there is a surface dipole (normal to the surface), either for the clean surface or investigation of chemical adsorption), that dipole generates a long range electric field that communicates spurious electrostatic fields between the replicas of the slab.

The most common approach to fix the error introduced by the artificial dipole field is to place a counter-dipole in the middle of the vacuum region, at the cell (Neugenbauer and Scheffler 1993; Bengtsson 1999). A slab LMCC (Schultz 1999) also accomplishes the goal of eliminating the replica dipoles, but with an approach that proves more versatile for other applications (such as molecular multipole moments).

An applied external electric field, a very simplified abstraction of the Coulomb effects from a double layer at the surface of an electrochemical system, can be readily incorporated into a vacuum-slab model through the addition of a sawtooth potential (Neugenbauer and Scheffler

1993; Feibelman 2001). SeqQuest has applied external electric fields among its features, but for modeling electrochemical interfaces this approach is insufficient. First, this approach is only viable with a vacuum gap between slabs, due to the discontinuous potential at the boundary; second, it neglects the effects of the solvent on the charged species at the surface; and, finally, the bulk surface (and therefore the slab supercell model that expresses it) has a net charge in general. The counterbalancing charge is in the distribution of ions in the solvent that make up the other part of the double layer, and it is this Helmholtz gap that is responsible for the electric field at the interface. The overall physical system, incorporating the full double layer is neutral, but the volume contained within the DFT computational supercell will possess a net charge, from the surface. As with bulk defects, a periodic system with net charge leads to divergent (infinite) Coulomb potentials, with the attendant challenges those infinities involve.

A uniform background density—“jellium”—has been used to cancel the net charge placed onto the slab in the supercell and allow a DFT calculation to go forward (Lozovoi, Alavi et al. 2001; Filhol and Neurock 2006), but it suffers the same issues of jellium in bulk defect systems or molecules: the artificial flat density overlaps the slab density, corrupting the resulting electrostatic potential. An improved method for cancelling the slab charge adds a planar countercharge at the cell boundary between slab replicas, as a one-dimensional Gaussian (Fu and Ho 1989; Bohnen and Kolb 1998; Lozovoi and Alavi 2003). The problem, shared with the jellium approach, that the energy is sensitive to (artificial) periodic separation between the slab replicas was solved (Lozovoi and Alavi 2003), but these approaches continued to have inappropriate periodic boundary conditions—the countercharge acted from both sides of the slab.

An important innovation involved using a Green’s function approach to use a (implicitly solvated) charge layer outside one surface of the slab to balance the surface charge (Otani and Sugino 2006). This enables obtaining a self-consistent electrostatic potential of the slab supercell, with a non-periodic solution that incorporates the effects of a double layer on one side of the slab (i.e., a discontinuity in potential at the cell boundary, corresponding to the dipole potential shift). The method has the versatility to incorporate either vacuum or a solvent interface on the slab surface, and defined a mathematical model consistent with the electrochemical system and enabled practical DFT calculations of surface structure with fields.

The approach we develop, described in greater detail later, has virtue of similarly incorporating the electrostatic effects of the double layer on a surface, using a generalization of the same LMCC framework used routinely to model slab surface calculations with dipole moments, while carefully segregating a more accurate treatment of the fluid from the internal aspects of the DFT code. This modular treatment enables an accurate description of the DFT region with the correct electrostatics, naturally incorporating the electrostatic potentials from a more general charge distribution, and, in principle, more accurate description of the fluids, with the potential for greater accuracy and for greater versatility in representing the solid-solvent interface.

The solvent interface poses additional challenges. Explicit inclusion of counterions in the DFT supercell, e.g., including explicit protons in a layer or water molecules on a slab surface

(Skulason 2007), neglects the statistical (thermodynamic) behavior in the solvent, and is limited to very short double layer lengths. Instead, modeling the solvent as a structureless dielectric in a Poisson-Boltzmann approach caused “solvated” charge to accumulate right at the surface, this unphysical screening did not take into account the granularity of the solvent particles, a failing remedied using a modified Poisson-Boltzmann (MPB) approach that incorporated the finite size of the solvated ions into the charge distribution in the solvent at the interface (Borukhov, Andelman et al. 1997), and adopted in subsequent studies of solid-solvent interfaces, including the Green’s function approach of Otani and Sugino, and perhaps brought to its culmination in work that combined the DFT and MPB through a “smooth and flexible dielectric model function” (Jinnouchi and Anderson 2008). It had the additional advantage of being implemented in a local orbital code, that avoids problems stemming from Kohn-Sham electrons overlapping the numerically problematic discontinuities that arise at the supercell boundary, i.e., the non-periodic boundary condition appropriate to a non-periodic double layer potential.

A yet more sophisticated technique to couple the quantum DFT and fluids DFT in a “joint-DFT” approach has recently been presented (Letchworth-Weaver and Arias 2012) within which some of the more ad hoc assumptions of earlier, simple approaches are shown to be reasonable simplifications of a more rigorous underlying theory. Ultimately, a coupling of a quantum DFT calculation with appropriately imposed boundary conditions derived from an accurate description of the solvent and its ions in a fluids density functional in a couple approach is needed to achieve quantitative, defensible predictions of chemistry at surfaces. A high-fidelity description of the solvent that carefully incorporates solvent particle distribution in a fluids density functional (f-DFT) is the subject of the next section.

2.3.5 *Fluids-DFT Overview*

As has been described above, predictive models of chemical reactions at the electrode-electrolyte interface require a reasonable model of the charge distribution in the electrolyte. The most commonly used model of the electrical double layer is the Gouy-Chapman-Stern (GCS) model, also called the Poisson-Boltzmann (PB) model (or approximation) (Bard and Faulkner 2001; Henderson and Boda 2009). More modern theories that include additional physics typically result in significant improvements over the PB model. Here we describe one of these theories, classical or fluids density functional theory (f-DFT) (Wu 2006), and discuss why f-DFT is a superior approach to traditional PB models of the double layer.

The PB or GCS model is an extremely simple model that gives analytic results for an electrolyte near a smooth planar surface. In the PB model, the electrolyte consists of point charges in a continuum dielectric background with dielectric constant ϵ . The ions are assumed to be distributed according to their Boltzmann weight in the electrostatic potential ϕ :

$$\rho_i(x) = \exp(-\beta z_i e \phi(x)), \quad x > d_i/2 \quad (2.3.2)$$

where $\rho_i(x)$ is the density of ions of species i a distance x from the electrode, $\beta = 1/k_B T$ where T is the temperature and k_B is Boltzmann's constant, z_i is the valence of species i , and e is the electron charge. This distribution is assumed to hold for all distances further than $d_i/2$ from the electrode surface, where d_i is the diameter of ion i . The diffuse layer consists of this layer of ions. At distances less than half the ion diameter, $x < d_i/2$, the densities $\rho_i(x)=0$, which is termed the inner (or Stern) layer. The PB model consists of solving Eq. (2.3.2) along with Poisson's equation for the electrostatic potential,

$$\nabla^2 \phi = - \sum_i \frac{\rho_i}{\epsilon \epsilon_0} \quad (2.3.3)$$

We have written Poisson's equation in SI units, where ϵ_0 is the permittivity of free space.

The PB model gives relatively reasonable results for the ion distributions near an electrode with constant surface charge, for 1:1 electrolytes in aqueous solution at low concentrations and for not too high surface charges. When these various conditions are not met, the PB method gives results which deviate considerably from, for example, direct molecular simulations (either molecular dynamics (MD) or Monte Carlo (MC) simulations) (Henderson and Boda 2009). The method is inaccurate for nonaqueous solvents, low temperatures, high concentrations, asymmetric electrolytes or multivalent ions, etc. These shortcomings are due to the extremely simple nature of the model. The ions are treated as point charges as opposed to objects with excluded volume, and all correlations are ignored. As we will see below, correlations due to excluded volume and to the charges are important for capturing many phenomena associated with the double layer.

A number of methods can be used to improve upon the PB (GCS) theory. For a given model of an electrolyte, molecular simulations are the gold standard in terms of accuracy, but often a theoretical approach is needed. This is because simulations can be too slow for large or complicated systems, and also cannot handle small concentrations of a given species. Here we give a brief overview of our approach, f-DFT.

Classical density functional theories are based on minimization of a free energy functional of the fluid densities. They are related to quantum DFTs (q-DFT) in that both theories rely on the same variational principle. q-DFTs are based on an energy functional of the electron density, while f-DFTs are based on a free energy functional of the densities of the molecular species in a fluid that obeys classical statistical mechanics. f-DFTs are typically developed in the grand canonical ensemble, and the grand free energy is minimized.

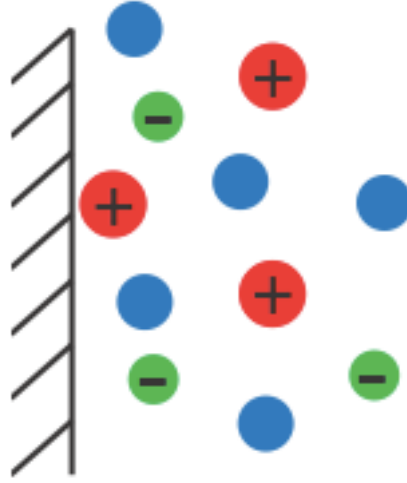


Figure 21: Sketch of the SPM model near a hard surface, showing cations (red), anions (green), and neutral solvent (blue).

To describe a given fluid system with f-DFT, one needs both a model of the fluid and an expression for the grand free energy functional. The fluid models are typically coarse-grained, i.e. they usually do not include full atomic detail, although this is possible for very simple systems. Here we describe a common model for electrolytes in f-DFT, namely the “semi-primitive” model (SPM), as sketched in Figure 21. In this model, the ions are treated as charged hard spheres. The solvent is a neutral hard sphere, with all species interacting in a background continuum dielectric constant ϵ . The hard spheres in general have different diameters. It is also possible to include attractive interactions among the different molecular species using a mean-field perturbation theory, but we do not discuss attractive interactions here.

The grand free energy of the system is

$$\beta\Omega[\rho_\alpha(\mathbf{r})] = \beta F[\rho_\alpha(\mathbf{r})] + \sum_\alpha \int d\mathbf{r} \rho_\alpha(\mathbf{r}) [V_\alpha^{ext}(\mathbf{r}) - \mu_\alpha] \quad (2.3.4)$$

where F is the Helmholtz free energy, $V_\alpha^{ext}(\mathbf{r})$ is an external potential due to, for example, surfaces bounding the fluid, and μ_α is the chemical potential of species α . The terms included in the Helmholtz free energy are based on the model system. In the SPM, we have

$$F[\rho_\alpha(\mathbf{r})] = F_{id}[\rho_\alpha(\mathbf{r})] + F_{hs}[\rho_\alpha(\mathbf{r})] + F_C[\rho_\alpha(\mathbf{r})] + F_{corr}[\rho_\alpha(\mathbf{r})], \quad (2.3.5)$$

where the terms on the right hand side are the intrinsic Helmholtz free energies for the ideal gas, hard sphere interactions, mean-field Coulombic interactions, and charge correlations. The ideal gas term is simply

$$\beta F_{id}[\rho(\mathbf{r})] = \sum_\alpha \int d\mathbf{r} \rho_\alpha(\mathbf{r}) (\ln \rho_\alpha(\mathbf{r}) - 1) \quad (2.3.6)$$

and accounts for translational entropy. DFTs for hard spheres are very accurate; in general we use the “White Bear” version of the fundamental measure theory for the hard sphere interactions, (Roth, Evans et al. 2002) which has the general form

$$\beta F_{hs}[\rho_\alpha(\mathbf{r})] = \int d\mathbf{r} \Phi[n_\alpha(\mathbf{r})] \quad (2.3.7)$$

where the free energy density Φ is a function of a set of weighted densities:

$$\eta_\alpha(\mathbf{r}) = \sum_\alpha \int d\mathbf{r}' \rho_\alpha(\mathbf{r}') w_i^\alpha(|\mathbf{r} - \mathbf{r}'|)$$

The explicit form of Φ used here is based on the Mansoori-Carnahan-Starling-Leland bulk equation of state for multi-component hard sphere mixtures, (Mansoori, Carnahan et al. 1971) and can be found in the original reference along with the weight functions w (Roth, Evans et al. 2002).

The free energy due to Coulomb interactions includes the mean-field part

$$F_C[\rho(\mathbf{r})] = \frac{1}{2} \int d\mathbf{r} \rho_c(\mathbf{r}) \phi(\mathbf{r}) \quad (2.3.8)$$

where ρ_c is the total charge density of fluid species in the system and ϕ is the electrostatic potential, which satisfies Poisson’s equation (Eq. 2.3.3) along with appropriate boundary conditions on ϕ . The contribution to F due to charge correlations is not known exactly. An approximate form is

$$\beta F_{corr}[\rho(\mathbf{r})] = -\frac{1}{2} \sum_{\alpha\beta} \int d\mathbf{r} \int d\mathbf{r}' \rho_\alpha(\mathbf{r}) \rho_\beta(\mathbf{r}') \Delta c_{\alpha\beta}(|\mathbf{r} - \mathbf{r}'|) \quad (2.3.9)$$

where Δc is related to the direct correlation function of the bulk fluid, and is found from integral equation theory using the MSA approximation. The f-DFT proceeds by minimizing the grand potential free energy with respect to the fluid densities:

$$\frac{\delta\Omega[\rho_\alpha(\mathbf{r})]}{\delta\rho_\alpha(\mathbf{r})} = 0$$

This leads to a set of nonlinear integral equations to solve for $\rho_\alpha(\mathbf{r})$.

These integral equations are implemented in our fluids DFT code, Tramonto (see <http://software.sandia.gov/Tramonto>), which has been developed at Sandia. The equations are solved in real space on a Cartesian grid, in three dimensions. The real-space implementation allows the surface geometry to be arbitrary. Poisson’s equation is solved using a finite-element approach. Boundary conditions can include either surfaces at constant charge or at constant electrostatic potential. Details of the numerical implementation of f-DFT have recently been published elsewhere (Heroux, Salinger et al. 2007; Frink, Frischknecht et al. 2012).

As part of this LDRD project, we made several additions to Tramonto. First we corrected the evaluation of the electrostatic free energy in Tramonto. The calculation was verified by comparison with the expected results in the PB limit. Additionally, we checked that the code satisfies the appropriate sum rules (Henderson 1992). These are exact relations derived from statistical mechanics, and provide a check on the accuracy of our numerical solution of the DFT calculations. The results of these verifications are summarized in Appendix A. The general form of Eq. (2.3.9), which is applicable to hard spheres of arbitrary sizes, was implemented in Tramonto as in the work of Oleksy and Hansen (Oleksy and Hansen 2006). Additionally, we implemented a slightly improved version of the hard sphere functional, Eq. (2.3.7), in order to compare results with those of Oleksy and Hansen.

In order to illustrate the differences between the f-DFT and PB predictions for the structure of the double layer, here we consider a simple 0.1M aqueous NaCl solution near a planar charged surface. The dimensionless surface charge is $\sigma^* = 0.043$ (see Appendix A), and since water is the solvent we take $T = 298$ K and $\epsilon = 78.5$. In the f-DFT calculations, the species diameters are 1.9 Å for Na⁺, 3.62 Å for Cl⁻, and 2.8 Å for water. We use the highest level of theory available in the f-DFT, namely we include the electrostatic correlations from Eq. (2.3.9) and use the improved hard sphere functional. Figure 22 shows the density profiles for the three species in the case of the SPM model from f-DFT, and the two charged species in the PB model. The densities have been normalized by their bulk values ρ_b . In both models, the negative Cl⁻ ions adsorb to the positively charged surface while the Na⁺ ions are depleted near the surface, thus giving the expected double layer. The ion profiles decay to their bulk values over a relatively long distance. This is a case where the PB model is reasonably accurate, especially at large distances from the surface, but we see significant differences near the surface due to the atomistic nature of the SPM model. In particular, the presence of the explicit solvent and the finite sizes of the ions leads to oscillations in the density profiles near the surface, out to a distance of about 12 Å. The realistic sizes of the ions in the f-DFT also give a more accurate model of the Stern layer (which we have left out in the PB calculations here). Finally, the contact densities and excess adsorptions of the ions on the surface are considerably different in the two theories; in the f-DFT the contact density for the Cl⁻ ions is 145.7 ρ_b , whereas it is only 24.4 ρ_b in the PB calculation. This is another reflection of the implicit solvent in the PB theory, which is inherently a theory for dilute solutions, as compared to the explicit solvent at a liquid-like density in the f-DFT. We note that the f-DFT calculations here reproduce those of Figure 22 in Oleksy and Hansen (Oleksy and Hansen 2006).

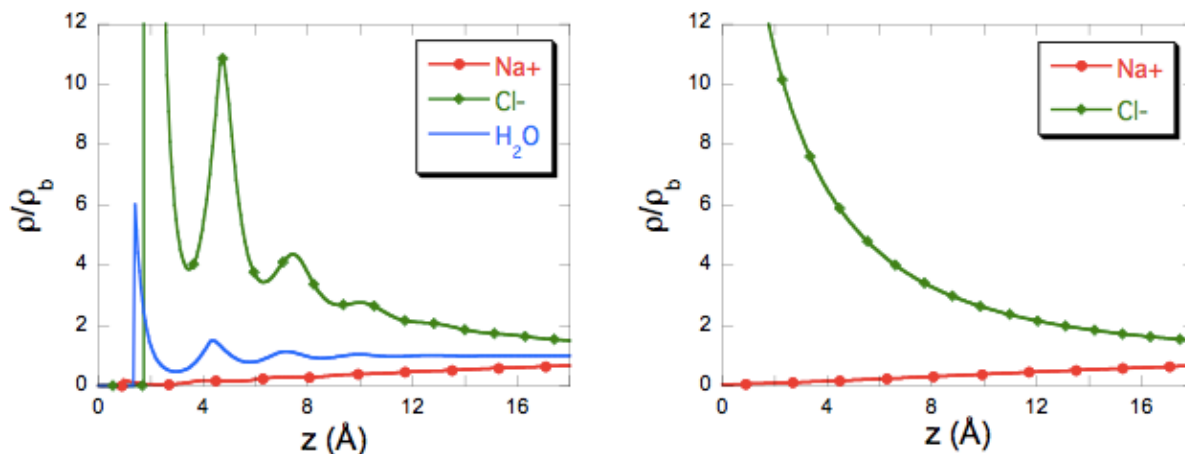


Figure 22 Density profiles as a function of distance from a positively charged surface calculated using the SPM model in c-DFT (left) and using the Poisson-Boltzmann model (right), for the same set of model parameters.

An excellent review of theory and simulation of the electrical double layer can be found in Henderson and Boda (Henderson and Boda 2009). They show computer simulation results as compared to PB theory and f-DFT for a “restricted primitive model” in which the ions are charged hard spheres in a background dielectric. They show that the PB theory fails to follow the simulation results in various limits, while the f-DFT is in nearly quantitative agreement with the simulations. Thus, f-DFT is an attractive route to determining the structure of the double layer at a nearly atomistic level.

Ultimately, determining reactions rates at the electrode surface will require calculating the density profiles and free energy for an electrolyte adjacent to a realistic, 3D electrode surface with atomic resolution. Here we show one simple 3D calculation as a proof of principle. We consider an SPM electrolyte between two flat surfaces in the yz -plane at constant potential. One of the surfaces also has an adsorbed, positively charged spherical atom emerging from the surface. We employed reflective boundary conditions in the y and z -directions. Figure 23 shows a 2D slice of the charge density of the negative ions in this system. The negative ions adsorb on the flat surfaces and on the spherical ion, but we see the density is once again nonmonotonic and shows interesting spatial heterogeneity around the adsorbed atom. These kinds of details will be important in determining accurate rates for surface reactions in electrolytes, and can be obtained from f-DFT.

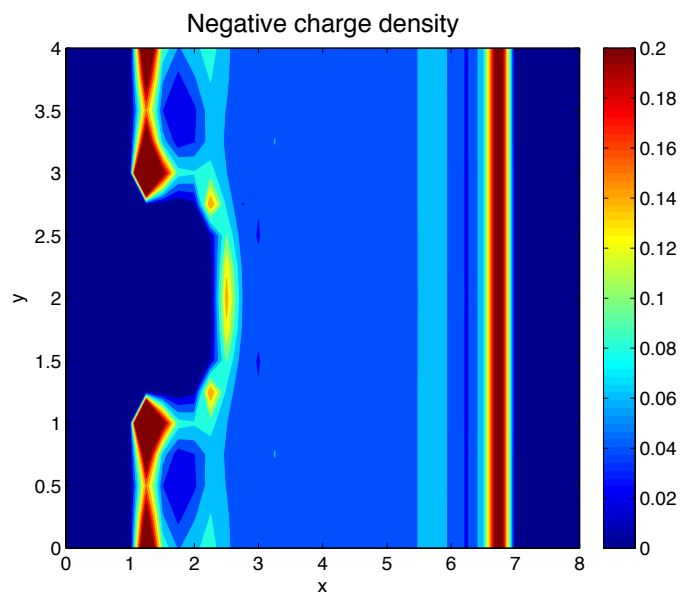


Figure 23: Two-dimensional projection of a f-DFT calculation of the charge density of negative ions between two flat surfaces at constant potential, with a positively charged spherical atom on the left.

2.3.6 A model for the electrode-electrolyte interface

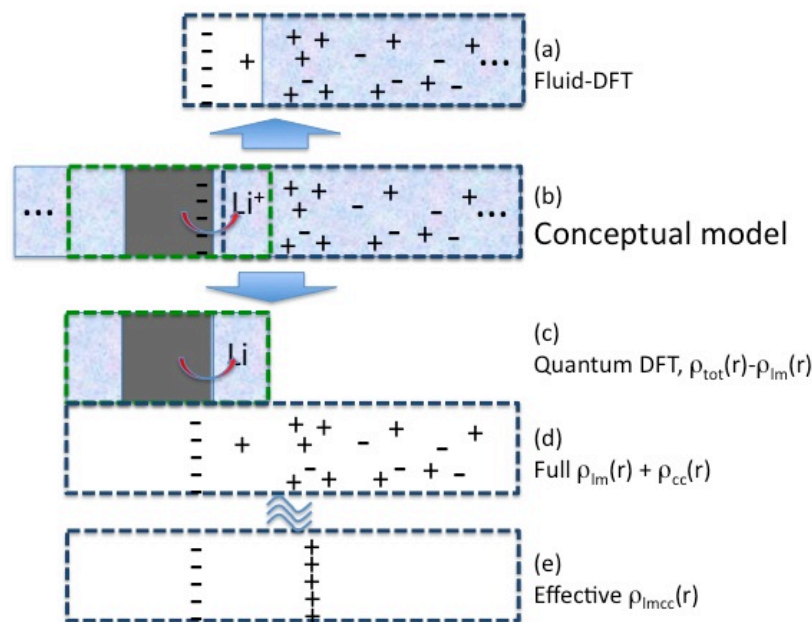


Figure 24: Conceptual model for a DFT description of the double layer

In this section we assemble the conceptual basis for the computational model we have developed for simulations of chemistry at solid-electrolyte interfaces in the presence of a double layer, and describe its implementation and verification. The process of decomposing a simulation of a semi-infinite solvated, charge surface with a double layer into a useful supercell DFT calculation informed by an implicit description of the solvent with a high-fidelity resolution of the particle distribution is presented in Figure 24.

The desired simulation is of a charge surface with a semi-infinite solvent layer that contains a distribution of charge ions that exactly cancels the charge on the surface, the double layer. This conceptual representation is illustrated in (b). The DFT slab supercell, in general cannot contain enough the solvent within its volume to cancel their charge, and also cannot generate the statistics necessary to reproduce the thermodynamics within the solvent. Moreover, depending on the ionic strength of the solvent, the extent of the double layer, the Helmholtz gap, can become much wider than is practical to include a DFT supercell. A fluids-DFT model is ideal for modeling the free energy of fluid with solvated ions, but cannot compute the reaction chemistry within the slab. The conceptual model couples a DFT supercell slab with a fluids-DFT model of the solvent in combined solution of the overall problem. The fluids-DFT takes a surface charge density in the slab, determined by the quantum DFT, and uses this surface charge as a boundary condition to predict the distribution of ions within the solvent and its free energy. In turn, the DFT supercell does a Kohn-Sham calculation on the electrons within the supercell, but that supercell has a net charge. The net charge must be excised for a periodic solve of the Poisson Equation to be viable, and the full double layer potential applied to the electrons within the volume of the supercell (including the net charge) in order to obtain a valid energy

expression. Following the LMCC strategy, a local moment analysis identifies the position of the surface plane, and specifies construction of the local moment charge $\rho_{lm}(\mathbf{r})$, such that the remainder electron density in the cell $\rho'(\mathbf{r})$ has no net charge, and no surface dipole, as depicted in (c). Conversely, a second local moment analysis performed on the ion charge density in the solvent determines the position of a second charge plane in the solvent, of equal and opposite charge to the surface charge, and with a long range electrostatic potential equivalent to the full distribution of charge within the solvent. Combining these two densities, the double-layer contribution to the surface electrostatic potential is reduced to the potential generated by $\rho_{lmcc}(\mathbf{r})$, as depicted in (e). A numerically convenient means to represent these charge planes is as one-dimensional Gaussians. Adding $\phi_{lmcc}(\mathbf{r})$, the potential generated by $\rho_{lmcc}(\mathbf{r})$, to the potential of the neutralized supercell $\phi'(\mathbf{r})$, compute using a periodic solution to the Poisson Equation for $\rho'(\mathbf{r})=\rho_{tot}(\mathbf{r})-\rho_{lm}(\mathbf{r})$, to obtain a total electrostatic potential $\phi_{tot}(\mathbf{r})=\phi'(\mathbf{r})-\phi_{lmcc}(\mathbf{r})$ results in a mathematically faithful representation of the double layer potential and energy.

The reduction of the double-layer contribution to the electrostatic potential to this simple LMCC form is particularly convenient. The form of this model density $\rho_{lmcc}(\mathbf{r})$ —two planar densities—is exactly the same form used in the LMCC solution of the potential for a *neutral* slab with a surface dipole (Schultz 1999). The solution of the Poisson Equation to obtain the corresponding potential, $\phi_{lmcc}(\mathbf{r})$, takes the same analytic form, and the necessary code to compute this potential existed and had been comprehensively verified. Adapting the code used to compute boundary conditions for a neutral slab dipole, for use in implementing the double layer boundary condition, required adaptations in two aspects. First, the local moment density $\rho_{lm}(\mathbf{r})$ in the double layer code removes only one pole (surface charge) of the dipole, to excise the net charge from the system, while the potential calculation needed to incorporate the other pole of the LMCC dipole, implicit in the solvent region. Second, that solvent countercharge, in principle, could be either inside the volume of the supercell, or outside, or sit astride the cell boundary, depending upon the nature of solvent (ionic strength) and the width of the supercell. Computation of the countercharge potential within the supercell might require consideration of countercharge density that lies outside the supercell, requiring assumptions (and associated error-checking) concerning the locality of densities within this Poisson solver code to be modified. However, the most complicated, and therefore risky, coding of the double layer potential could leverage not only the theoretical machinery, but also much of the pre-existing code, easing implementation and verification.

In this one-dimensional form, the electrostatic potential from a LMCC treatment of the double-layer boundary condition is functionally equivalent to the Green's function approach described above (Otani and Sugino 2006). The advantage of modularity in the current approach, separating the slab code (SeqQuest) and solvent code (Tramonto), is minor in the 1D example, as the information passed between the two scales can be reduced to the location of a 1D solvent countercharge potential, but will become much more prominent once the surface of interest develops corrugation and roughness where a 2D or 3D representation of atoms and charges become important.

The current slab-solvent coupling passes only 1D information, but the generalization for the potential and density exchange in 2D and 3D between SeqQuest and Tramonto is a straightforward extension of the 1D approach. Details of extending to use 2D and 3D data are

not trivial, but both codes, independently, can describe complex interface topologies, and manipulate potentials and densities on regular grids that are easily inter-communicated. In SeqQuest, the code implementing the (1D) double layer electrostatic boundary conditions is completed and tested, a facility to export internal slab densities and electrostatic potentials to an external code (e.g. to Tramonto) and import double layer structure (e.g. from Tramonto) implemented, and released in production version SeqQuest 2.63.

2.3.7 Method and code verification, and application to a double layer system

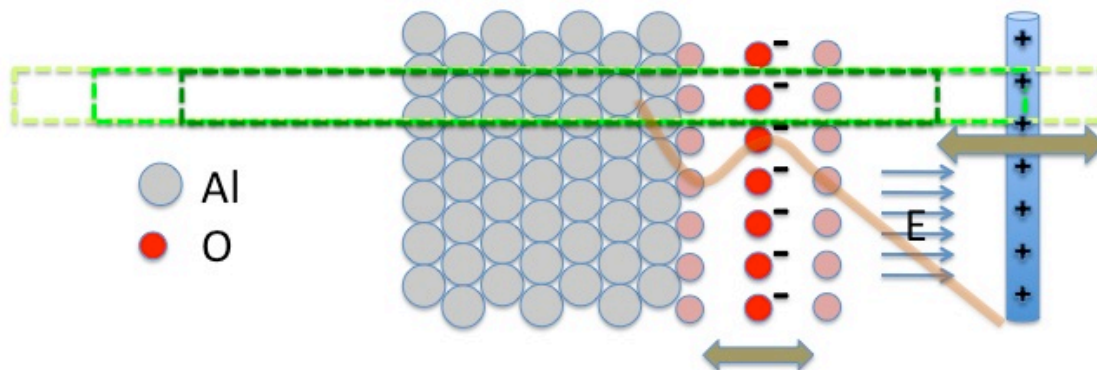


Figure 25: Test system for double layer boundary conditions in DFT supercell

Testing of the double layer implementation in SeqQuest was performed using an artificial system, oxygen adsorbed on the close-packed (111) surface of Al, both as a neutral system, and as negatively charged. This example is relatively simple, and versatile in its exploration of different aspects of the implementation. The model and its salient aspects are depicted in Figure 25.

The model we use is a 7-layer slab of fcc aluminum, with closed-packed (111) surfaces. The lattice constant is set to computed LDA lattice constant, 3.970 Å, and the Al atoms are held fixed to the bulk positions, i.e., are not allowed to relax at the surface. This is selected for expedience, the choice of functional is inconsequential to the assessment of the double layer code, as is the relaxation of the Al atoms in the surface. Pseudopotentials and basis set are taken from the SeqQuest atomic library. We use a 1x1 supercell, so that each supercell has one Al atom per layer, and one oxygen atom in the adsorbed case.

With adsorption of neutral oxygen, added in the fcc hollow site where the next layer of Al atoms would have been in the continued crystal, the slab develops a dipole, as the oxygen pulls electrons from the surface. Correct treatment as an isolated slab confirms the efficacy of the LMCC slab dipole code, before proceeding on to the generalization to a double layer boundary condition; this being demonstrated by an insensitivity in the results to variation of the width of the supercell in non-periodic directions.

To assess the double layer code, we now add an electron to the slab, nominally creating O^{-1} adsorbed at the surface. A solvent countercharge plane is placed 13 Å above the top layer of Al atoms. The surface charge is much larger than is reasonable for any real electrochemical system, and the solvent countercharge deeper into the solvent than would be typical for a Helmholtz layer in an electrolyte, but these choices allow crucial aspects of the implementation to be rigorously tested. With the very high fields in this model, the 48umeric are severely tested. The wide range between the surface and the countercharge plane allow a potential energy surface to be explored in different regimes, moving the (red) layer of oxygen atoms in and out to fully adsorbed to full desorbed (pink) positions. Just as for the neutral case, if the double layer implementation is correct, the results should be insensitive to whether the countercharge plane resides inside (the vacuum part) of the supercell, astride the boundary, or entirely outside the supercell. This is tested by varying the size of the supercell (demarcated in green in the figure), in our case from 15 to 25 to 35 layer spacings, that place the supercell boundary 10.3 Å, 21.8 Å, and 33.3 Å above the top Al atom layer. The position of the countercharge layer is imposed here to define the test, but in the coupled DFT codes, this position would be determined by the fluids DFT code and communicated to the slab DFT code.

With the high electronegativity of oxygen, it can stabilize a net negative charge at the surface (at least using a local basis set), enabling a test of the new double layer code in the same slab model. The charged oxygen adlayer has a bound state on the surface. This enables tests of the double layer potential both in a chemical regime, as a species bound to the surface, and in the unbound regime, dominated by the electric field inside the double layer that pulls the atom away from the surface, the potential energy surface for adsorption being schematically illustrated in the orange overlay in the figure. This constitutes an unphysically large surface charge density created by the dense layer of oxygen anions, but the large charge and strong fields allows testing of the double layer code in numerically severe circumstances, building confidence in the method and its implementation.

The neutral oxygen calculation finds an energy minimum 0.72 Å above the plane of the top Al atoms. Adding an electron to the system, the adsorbed O^{-1} shifts negligibly from this position, the bonding to the surface apparently not affected by the extra charge. This is a curious result; how is the geometry of the atom not affected with the change in charge state? As part of its workings, the double layer code computes the local moments of the net charge in the supercell, and thereby the effective position of the electron charge layer in the supercell. For the adsorbed species, the extra electron is centered in a layer 1.71 Å above the oxygen, in what seems to be a somewhat diffuse lone pair state pointed away from the surface and, unsurprisingly, along the strong double layer electric field toward the solvent countercharge layer. As the oxygen departs from the surface into the unbound (field-dominated) part of the potential surface, this electron shrinks back to a plane only 0.93 Å away from the oxygen atom, into a compact lone-pair-like state. The diffuse adsorbed state suggests only tenuous attachment of the electron to the oxygen in the slab, and almost certainly, in a plane wave basis method, this electron would be drawn into the depth of the electrostatic well at the solvent counter charge at the cell edge rather than in the plane (Feibelman 2001; Magyar, Mattsson et al. 2011). The use of the local orbital approach, with no variational accessibility for this edge state, can avoid this artificial entrapment, a useful advantage when attempting to manipulate external fields in a DFT supercell calculation.

Both a force-relaxed and energy-minimization calculation produce the same minimum, to within typical and small numerical errors, demonstrating the consistency of the force and energy expressions within the double layer code. The consistency of force and energy curves was further tested using finite differences farther out along the potential energy surface, with similar numerical agreement. The force and energy code, independent calculations separately implemented in the code, are consistent with each other, have the correct asymptotic behavior, providing verification that the implementation is correct.

A final series of tests confirmed that the boundary condition constructed in the slab normal direction correctly reproduce the aperiodic behavior of the double layer. Leaving all other part of the calculation unchanged, the supercell calculation was repeated with three different widths of the supercell, ranging from a width that left the solvent countercharge outside the supercell to one that fully contained the full countercharge plane within the volume of the supercell (a supercell 35 Al layer spacings—of which 7 layers ate aluminum—or 80.2 Å wide). The slab DFT double layer results are insensitive to this variation of the computational model, completing the last verification test of the double layer boundary condition code.

Having verified the implementation of the double layer boundary condition in the slab DFT code, we shift to a more realistic physical system of relevance to batteries, and demonstrate a (trivial) coupling of the slab DFT code with a fluid model in Tramonto. For this example, we will use a Mn_2O_4 cubic spinel surface and examine the behavior of a electron capture at an oxygen vacancy at the surface, a relatively simple yet physically interesting chemistry at a candidate cathode surface.

We use the fully de-lithiated spinel, which is unambiguously cubic both in nature and in the calculations, so as to avoid spurious surface interface reconstructions related to bulk phase stability. To construct our slab model, we take a $1 \times 1 \times 1$ conventional cubic unit cell with (001) surfaces containing 60 atoms, 20 Mn and 40 O. The non-polar surfaces avoid surface dipoles that complicate any analysis. Having the same stoichiometry as bulk avoids unintentional local charging, and preserves the bulk oxidation states for all atoms in the slab model. The calculations used the PBE functional and the Mn PP with the semicore p -electrons in the core. To expedite the calculations, a non-magnetic calculation was performed, and, furthermore, the k -sampling was restricted to just the Γ -point. The slab lattice parameter was set to the theoretical value in this computational context, $a_0=7.92$ Å. The slab surpercell is 1×1 surface cell, and one cell thick, and the supercell repeat vector places two layers of vacuum, i.e. 15.85 Å, between the slabs for a total width of 23.76 Å.

This ideal cell model is then allowed to fully relax. In the top layer of the slab, there are 4 Mn atoms and 8 O atoms, slightly rumpled, with 4 O atoms ~ 0.41 Å above the planar Mn atoms, and the other 4 O atoms only 0.24 Å above the Mn plane.

These oxygen atoms, protruding slightly above the other atoms at the surface, are prime candidates for vacancy sites, and, given that the spinel is strongly ionic, a vacant site is likely to bind electrons, much like an F -center in alkali halides. In this ideal slab model, two of the highest oxygen atoms were removed to leave two oxygen vacancies, and the this new defected surface relaxed while kept at neutral net charge. The oxygen vacancies caused slight relaxations

at the surface, the Mn atoms descending 0.09 Å, and the oxygen atoms rising, the two top ones by 0.07 Å and the four lower ones by 0.10 Å. This neutral surface structure was then used for all the subsequent surface calculations of charged vacancies at the surface.

Two different charge states were considered, the first where two electrons were added to the surface, one for each oxygen vacancy, the second where four electrons, two for each oxygen vacancy, saturate the nominal valence left vacant by the missing oxygen atoms. To jumpstart the slab DFT calculation, the countercharge plane was postulated to be 3 Å beyond the assumed solvent edge, i.e., a van der Waals radius above the top surface oxygen atoms. Taking the oxygen radius to be 1.5 Å, this plane was placed 4.5 Å above the top oxygen atoms. As it later emerges, the results are not strongly sensitive to modest variations in the solvent countercharge position, a convenient outcome that makes self-consistency between the quantum slab DFT and solvent fluid DFT easier to achieve—a small number of exchanges of potentials and densities is needed to achieve a converged result.

Minimal modifications to Tramonto were needed for our initial coupled calculations. These can be carried out in two ways. For the most general approach, Tramonto was modified to read in a file with the electron charge density $\rho_e(z)$ of the electrode obtained from SeqQuest. The charge density was then treated as a sum of point charges: $q_i = \rho_e(z)\Delta z$ where Δz is the mesh spacing in the SeqQuest profile. The entire SeqQuest simulation box was placed inside the “wall” in Tramonto, where the fluid densities are identically zero. A flat, neutral planar surface was placed where the electron density becomes zero. The Tramonto calculation proceeded by including both the electron density region from SeqQuest and the electrolyte region in the Poisson solve done by Tramonto. This approach gives the electrostatic potential throughout the entire electrode-electrolyte system. A simpler approach, which is all that is needed for structure determination and an initial coupling of the codes, is to place the entire excess surface charge density determined by the SeqQuest calculation on a smooth planar surface that bounds the electrolyte, and calculate only the electrolyte response in Tramonto. We describe these calculations here.

We used the SPM model for the electrolyte in Tramonto, which we took to be a typical Li-ion battery electrolyte of LiPF₆ in EC/DMC. We assumed the Li⁺ ions had a diameter of 2 Å and the PF₆⁻ ions had a diameter of 6.8 Å, based approximately on the minima in the appropriate radial distribution functions from our MD simulations of LiPF₆ in EC/DMC (see section 2.4). For simplicity, we take the diameter of the solvent molecules to be the same as that of the PF₆⁻ ions. The solvent is assumed to have a reduced density of $\rho d^3 = 0.722$ and a dielectric constant of 78.5. These parameters could of course be adjusted in future refinements of the model.

The structure of the current SeqQuest-Tramonto coupled calculation is very simplified for the 1D modeling. SeqQuest computes charged surface calculation with double layer boundary conditions, using an assumed value for the solvent countercharge plane (perhaps with an initial guess provided by a preliminary Tramonto calculation for a continuum-model surface with the indicated charge density). With the double layer boundary conditions, SeqQuest completes a self-consistent calculation that obtains a charge density due to the redistribution of electrons in the slab region. SeqQuest then outputs this density and potential into a file. Tramonto picks up this information, in particular computing the location of the effective charge plane for the slab density and its relation to the hard-wall surface plane used by Tramonto, to perform a fluids-DFT

calculation to compute the response of the solvent to the surface boundary condition determined by the slab DFT calculation, and in particular, computing the ion charge distribution in the solvent. Figure 26 illustrates this hand-off, where on one side, the SeqQuest electron redistribution is plotted as planar averages over the width of the slab supercell, and on the other side, the ion densities in the solvent are plotted as planar averages as a function of the distance from the surface, for a 1M LiPF_6 solution.

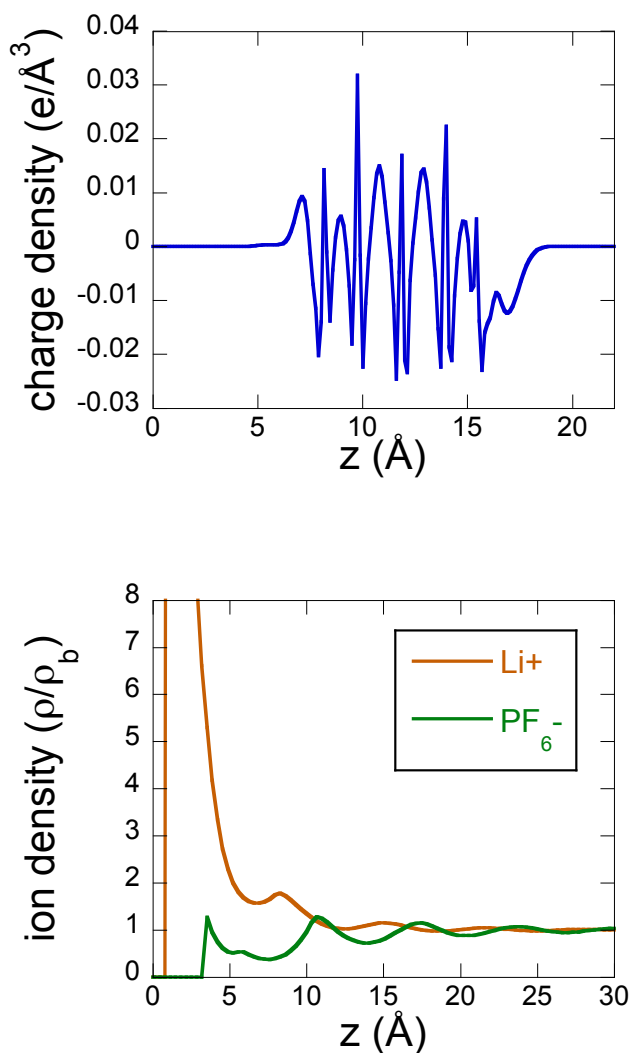


Figure 26: Coupled slab DFT and fluids DFT calculations. Top, electronic density from SeqQuest. Bottom, ion densities (relative to their bulk values) from Tramonto, for the electronic surface charge density of $0.03/\text{\AA}^2$ represented in the top figure. The moment of the ion charge density is located 2.16\AA from the surface. The contact density of Li^+ is $131\rho_b$.

The very fast wiggles in the SeqQuest plot simply indicate the positions of atoms in the slab, as electrons within Mn_2O_4 redistribute around atoms, and from Mn to O atoms to get to the ionic oxidation states. The interesting part is the relative long deep valley on the right side of that plot, which indicates the location of the surface charge. In the 2-electron negative charge, the centroid of the negative charge is computed to be 0.36 \AA above the oxygen site left vacant. This relatively modest shift, well within the van der Waals radius that separates the oxygen site from the solvent region hard-wall, increases to 0.82 \AA for the 4-electron (2 electron per vacancy) charged surface.

On the solvent side, this surface charge causes the ions within the solvent to redistribute, causing a buildup of positive ions and reduction of negative ions near the surface (with respect to the bulk solvent limit), with an oscillatory structure near the surface, dictated by the finite ion size, eventually dying off to the structureless bulk concentrations. The net charge in the solvent must exactly cancel the surface charge, since the electrolyte cannot sustain a net field at equilibrium. This ion charge distribution is communicated back to SeqQuest. In the 1D case, all that is actually needed is the moment of the charge, the centroid of a positive charge plane. The slab density does not extend sufficiently into the solvent region to make the detailed structure of the ion distribution important to the electronic energy, and the position of a countercharge layer position is sufficient to determine the electrostatic potential where there is appreciable electron density. With the coupled calculation, Tramonto computes the global electrostatic potential and free energy of the fluid, and SeqQuest computes the electronic energy of the explicit atoms in the slabs subject to the boundary conditions provided by Tramonto. The 1D implementation of the double layer code is complete, and awaits practical applications.

2.3.8 Future Development

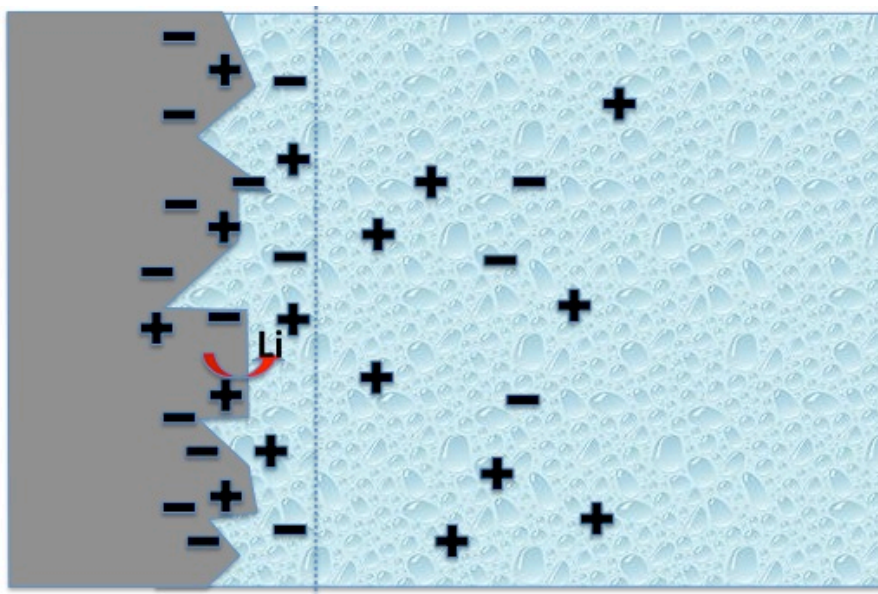


Figure 27: The challenge of a three-dimensional interface

For these, the detailed distribution of ions within the solvent will be crucial to describe the electrostatic effects on localized reactions at the surface, and the structure of the surface and the distribution of charge within the surface will have a profound effect on the response of the ions in the electrolyte. SeqQuest is able to handle large surface structures, with very flexible input of external boundary conditions, and Tramonto implements the best methods for describing the fluid response in complicated interface topologies, where the granularity of the solvent will be of particular importance. The ability of SeqQuest and Tramonto to accurately treat these regimes, and effectively communicate their respective boundary conditions in a unified calculation will be crucial to obtaining quantitative results for chemistry at realistic electrode-electrolyte interfaces.

Among the capabilities that would need to be completed to fully generalize this coupled tool from model 1D to realistic 3D problems is to fully communicate 3D structures, potentials, and densities. In the 1D simulations, the computational cost is almost entirely dominated by the slab DFT, the 1D Tramonto calculation being trivial in comparison, making interchange between the calculations trivial. A 3D Tramonto calculation becomes more expensive, comparable to the SeqQuest calculation, becoming a massive parallel computation rather than a desktop problem. The interchange between the codes will need to be handled dynamically, as both codes run in parallel. Rather than a custom coupling between the codes, this would best be handled by an integration framework. A modeling framework to couple sub-continuum codes lies outside the scope of this LDRD, but would be useful to facilitate other coordinated simulations (e.g., SeqQuest-LAMMPS, Tramonto). The construction of a full free energy expression, driven by Tramonto's treatment of the thermodynamics of the solvent and incorporating the internal energy of the explicit treatment of the slab electron in a full 3D exchange should also be implemented into separate tool, incorporated into a framework, in principle, enabling easy modular replacement of the model of the substrate (with a different DFT tool such as VASP) or with alternate treatments of the solvent (with a simplified Poisson-Boltzmann model, or explicit classical particles in a molecular dynamics simulation).

The approach developed here only describes the electrostatic interactions between the solid and the electrolyte, assuming the contact terms at the interface are negligible. While the electrostatic effects certainly dominate, incorporating improved models that treat the contact between the explicit atoms and electrons of the slab with the implicit particles in the solvent will be needed in the future. Recent developments in joint-DFT may provide a means to achieve this end (Letchworth-Weaver and Arias 2012). Another route, recently applied to biological systems, treats the substrate with conventional Kohn-Sham (KS) DFT, and its interactions with the solvent through an orbital-free DFT (OF-DFT) (Hodak, Lu et al. 2008). Ultimately, describing electrochemistry will require dynamical simulations of chemical processes, and methods will be needed to allow particles to be interchanged between the two environments as a dynamical simulation evolves. The explicit KS-DFT —implicit OF-DFT treatment at the interface offers intriguing avenues to explore.

2.4 Mechanisms for Chemical Diffusion in Materials

2.4.1 *Simulation of Bulk Diffusion of Li Ions*

In the multiscale modeling of abuse and failure of batteries, mass transport by chemical diffusion contributes to important processes in battery operation and potentially in failure of the battery. For lithium ion transport in secondary batteries, the efficiency and lifetime of the battery is dependent on diffusional transport of lithium cations through the organic-based electrolyte and separator. Perhaps less significant due to the presence of large chemical potentials and shorter distances (microns compared to millimeters of electrolyte material), diffusion within anode and cathode components can be a concern. However, for predictive models of battery performance diffusion of lithium ions through the organic and inorganic SEI phases at the anode needs to be accurately addressed. Decomposition of the electrolyte at the anode occurs over multiple charge and discharge cycles and creates lithium carbonate and a variety of alkyl carbonate phases.

Intracrystalline or volume diffusion is often a controlling mechanism for the transport of ions in oxide phases at relatively high temperatures (greater than 400 to 500°C). Diffusion can occur through several defect mechanisms depending on the chemical species that is being transported in response to a compositional gradient. Crystalline defects can occur as simple vacancies or as interstitials. Additionally, the coordinated motion of multiple atoms through various configurations can result in diffusion (exchange mechanism). Figure 28 provides conceptual models of various mechanisms for diffusion in crystalline materials. Vacancies can be generated intrinsically by thermal effects where high temperatures create vacancy sites while maintaining charge neutrality (cation and anion Schottky pair defects). Crystal surfaces or line defects provide a sink for the rejected ions. Similarly, interstitial defects can be thermally created when typically a small cation is displaced from a crystallographic site into an alternative lattice site (Frankel defect); charge neutrality is implicitly maintained.

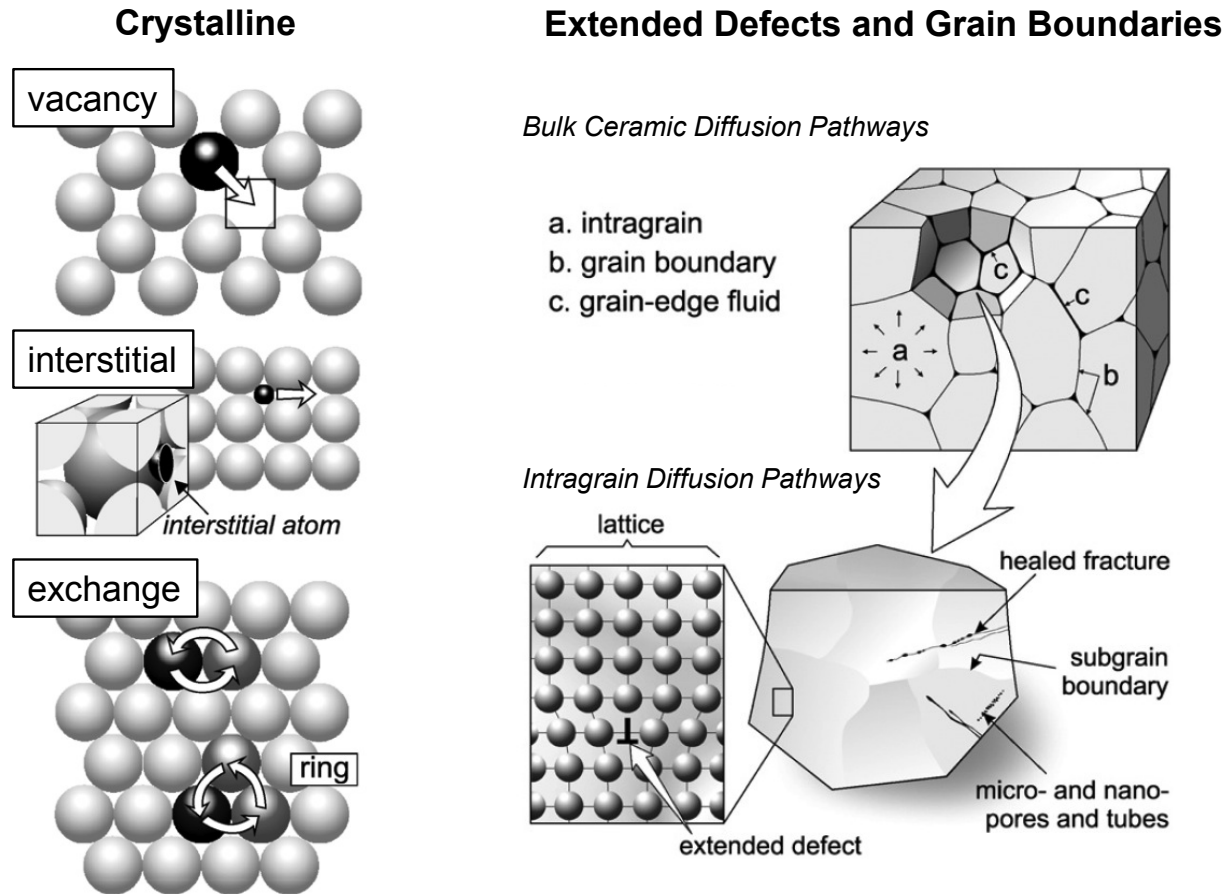


Figure 28: Schematic representation of crystalline diffusion and the role of extended defects and grain boundaries as they relate to diffusion mechanisms. Modified from (Watson and Dohmen 2010).

In contrast to these intrinsic defect structures and mechanisms, extrinsic diffusion mechanisms occur for materials that are impure or contain multivalent metal cations. The defect structure of such a material is controlled by the oxygen fugacity in equilibrium with the crystal and which also effects the relative concentration of the different valence states for a metal (for example, $\text{Fe}^{3+}/\text{Fe}^{2+}$) and ultimately affects the diffusion mechanism. In other words, the defects are considered chemical species that follow strict thermodynamic behavior where their existence and concentrations are controlled by extensive variables.

Alternative extrinsic pathways for chemical diffusion in bulk materials include extended defects and grain boundaries. Extended defects are crystal surfaces, line defects, subgrain boundaries (including crystal twinning), fractures, cracks, and other related physical boundaries of the bulk crystalline phase. Grain boundaries, which dominate ceramic materials and minerals, would be associated with the SEI phases in the operational battery. Figure 28 also includes graphical models of these additional diffusion pathways. These fast-diffusion pathways are typically considered to be extrinsic processes due to the preexistence of such large-scale defects in the material.

The Arrhenius relation for chemical diffusion processes is typically used to evaluate the variation in diffusion rate as a function of temperature; two versions of the Arrhenius expression are provided:

$$D = D_o \exp (-E_a / RT) \quad (2.4.1)$$

$$\log D = \log D_o - E_a / 2.3026 R (1/T) \quad (2.4.2)$$

where D is the diffusion coefficient, D_o is a pre-exponential factor, E_a is the activation energy, R is the gas constant, and T is absolute temperature. Figure 29 provides a representation of the Arrhenius relation as described by Equation (2.4.2) for two different diffusion mechanisms. The high-temperature (low $1/T$ values) example represents an intrinsic mechanism that includes two contributing processes. The activation energy includes an enthalpy for the thermal formation of defects (Δh_f); the k factor represents the stoichiometry associated with the defect formation reaction. The second term represents the migration enthalpy (Δh_m) for the diffusing species. Migration enthalpy is equivalent to the energy barrier for the transition state as the diffusing species moves from an occupied site to a vacant or interstitial site. The preexponential term D_o , or intercept for Equation (2.4.2) at infinite temperature ($\log D_o$), effectively incorporates the entropic part of the free energy for diffusion and the jump frequency (Barr and Lidiard 1971).

An extrinsic diffusion mechanism is represented in Figure 29 by the low-temperature (high $1/T$ values) example where the smaller slope of the Arrhenius line only incorporates the migration enthalpy (Δh_m), which may be equivalent to the migration enthalpy associated with the intrinsic diffusion mechanism. As noted earlier, extrinsic diffusion mechanisms involve defect structures that are controlled by multivalent metal species. Both intrinsic and extrinsic mechanisms are present at all temperatures (note dashed extensions of Arrhenius lines) but the controlling mechanism becomes evident when the diffusional flux is significant to dominate for a particular temperature range. Multiple diffusion mechanisms, and multiple Arrhenius relations, can exist for some materials. In these cases, one would expect smaller and smaller activation energies for the dominating mechanism as temperature decreases. Grain boundary diffusion mechanisms would be such a case where activation energies are always less than those observed for crystalline diffusion.

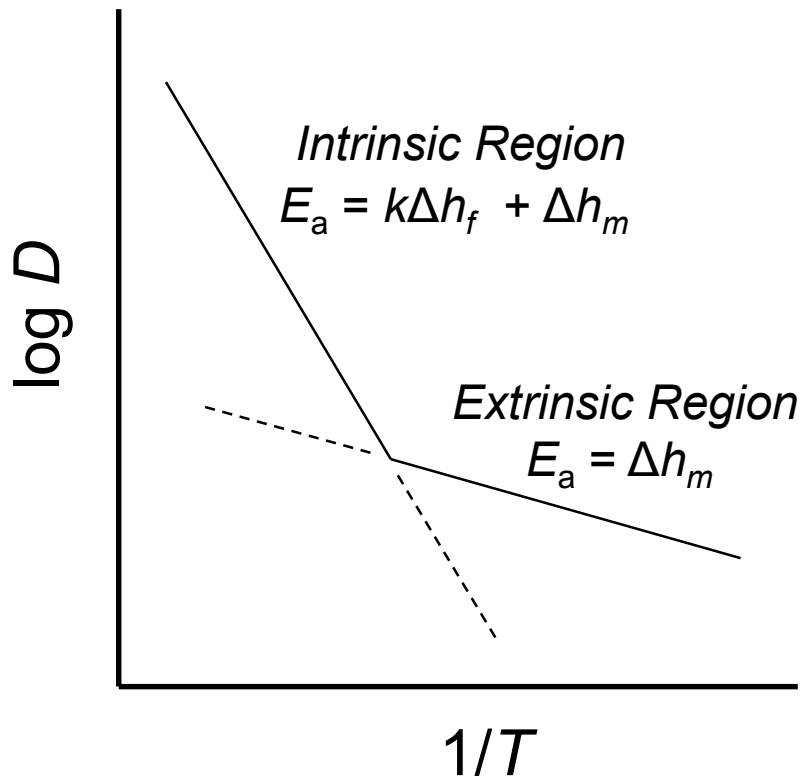


Figure 29: Schematic representation of an Arrhenius plot showing the transition between intrinsic diffusion processes at high temperature and the extrinsic region at lower temperature where the activation energy is lower and is equivalent to the migration enthalpy.

For the SEI phases at the anode of a battery, grain boundary diffusion can be an effective diffusion mechanism for the transport of lithium ions to and from the electrolyte at relatively low operating temperatures. However, experimental diffusion data is unavailable to make this determination. Certainly, crystalline diffusion (or diffusion through an amorphous-like SEI phase) may occur at operational temperatures and during high-temperature excursions during battery failure.

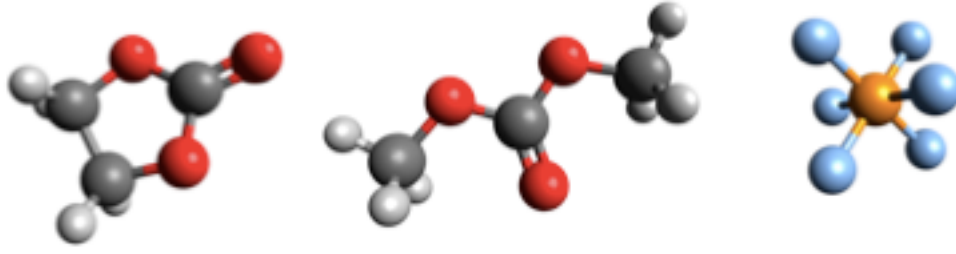


Figure 30: Ethylene carbonate (EC), dimethyl carbonate (DMC), and hexafluorophosphate (PF_6^-).

2.4.2 Analysis of molecular clusters in simulations of lithium ion battery electrolytes

Molecular dynamics (MD) was used to study the properties of lithium ion battery electrolytes composed of non-aqueous solvent (ethylene carbonate (EC) and/or dimethyl carbonate (DMC)) with LiPF_6 salt. Figure 30 shows the minimum energy (B3LYP/aug-cc-pvdz, vacuum) structures of EC, DMC, and PF_6^- . MD simulations were performed for all combinations of three temperatures (300, 350, and 400 K), three solvent compositions (pure EC, pure DMC, and 1:1 EC:DMC), and three LiPF_6 concentrations (approximately 0.1, 0.3, and 1.0 M) – i.e. a total of 27 temperature/solvent/concentration combinations. The pressure for each simulation was set to 1.0 atm. A total of 1000 solvent molecules was used in each simulation. The number of LiPF_6 pairs in each simulation was 8, 24, or 75.

A simple “Class I” forcefield model was used to describe bonded and non-bonded interactions between atoms

$$E_{total} = \sum_{bonds} K_r (r - r_0)^2 + \sum_{angles} K_\theta (\theta - \theta_0)^2 + \sum_{dihedrals} K_{\varphi,n} [1 + \cos(n\varphi - \gamma)] + \sum_{i < j} 4\epsilon_{ij} \left[\left(\frac{\sigma_{ij}}{r_{ij}} \right)^{12} - \left(\frac{\sigma_{ij}}{r_{ij}} \right)^6 \right] + \sum_{i < j} \frac{q_i q_j}{r_{ij}} \quad (2.4.3)$$

The bonded interaction parameters K_r , K_θ , and $K_{\varphi,n}$ are force constants; r_0 is equilibrium bond length; θ_0 is equilibrium bond angle; and n and γ are periodicity and phase angle, respectively, for dihedral interactions. Note that the summation over dihedral bonds includes both conventional and “improper” dihedrals. Accounting for nonbonded contributions to the potential energy, the Lennard-Jones parameters ϵ and σ describe repulsive and dispersive interactions, and the point charges q describe electrostatic interactions. For Lennard-Jones interactions between different atom types, the parameters ϵ_{ij} and σ_{ij} were calculated using Lorentz-Berthelot combining rules:

$$\epsilon_{ij} = \sqrt{\epsilon_{ii} \epsilon_{jj}} \quad \sigma_{ij} = \frac{\sigma_{ii} + \sigma_{jj}}{2} \quad (2.4.4)$$

Intramolecular nonbonded interactions between atoms separated by one or two bonds (“1-2” and “1-3” interactions) were set to zero; Lennard-Jones and electrostatic pairwise interactions between atoms separated by three bonds (“1-4” interactions) were scaled by 0.5 and 0.8333, respectively; and atoms separated by more than three bonds were unscaled. Note that the functional form of the forcefield used in this study does not explicitly model atomic polarizability. While a polarizable forcefield (Rappe and III 1991) has the potential to improve quantitative accuracy over a wider range of conditions, especially for electrolyte systems such as this, the greater resources required to use such a forcefield were not justified by the goals of this study.

Forcefield parameters for lithium ion were taken from the OPLS forcefield (Jensen and Jorgensen 2006). To develop forcefields for other molecules, an energy-minimized *ab initio* structure was first generated using Gaussian03 (Frisch, Trucks et al. 2004) at the B3LYP/aug-cc-pvdz level of theory. From the results of this calculation, the Antechamber (Wang, Wang et al. 2006) suite of forcefield tools was used to assign initial bonded and nonbonded forcefield parameters from the Generalized AMBER Force Field (GAFF) (Wang, Wolf et al. 2004). Also during this step, atomic point charges were calculated from the *ab initio* results via Antechamber using the restrained electrostatic potential (RESP) (Bayly, Cieplak et al. 1993; Cieplak, Cornell et al. 1995) method. After initial assignment of parameters via Antechamber, the resulting forcefield for a given molecule was refined, if necessary, by assigning different GAFF atom types in order to yield a pattern of bond types more consistent with *ab initio* results. Lennard-Jones, bond, angle, and dihedral parameters for the various atom types were not changed from their GAFF values. Using the forcefields described above, all MD simulations for this study were conducted using the open source LAMMPS (version: 19 Jul 2011) MD code (Plimpton 1995; Plimpton 2012).

For a given combination of solvent composition and salt concentration, an initial low-density system was constructed by randomly placing the required molecules into a cube using the open source simulation setup tool Packmol (Martinez, Andrade et al. 2009) and then compressing the system to a density close to experimental values over 0.1 ns at 300K. Subsequent isothermal-isobaric (NPT) simulations were started from these initial systems. Total NPT simulation time was 10 ns to 20 ns. The first 1 ns of data was discarded from each simulation to allow systems to relax. For the systems with the slowest dynamics (i.e. 300 K and pure EC), system volume and energies were oscillating around their long-term averages after 0.5 ns.

System trajectory snapshots were recorded every 1 ps. This data was post-processed to calculate mean-squared-displacements, diffusivities, conductivities, pair correlation functions, coordination numbers, pair autocorrelation functions, and cluster network topologies for each of the 27 systems described previously.

The mean-square displacement of the center of mass of a set of N molecules during time t is

$$MSD(t) = \frac{1}{N} \sum_i^N \langle [\mathbf{r}_i(t_0+t) - \mathbf{r}_i(t_0)]^2 \rangle \quad (2.4.5)$$

where $\mathbf{r}_i(\tau)$ is the position of molecule i at time τ and $\langle \rangle$ denotes an ensemble average over possible starting times t_0 . The self-diffusion coefficient D for a species i can be calculated from Equation (2.4.5) using the Einstein relation

$$D_i^{app}(t) = \frac{MSD_i(t)}{6t} \quad (2.4.6)$$

$$D_i = \lim_{t \rightarrow \infty} D_i^{app}(t) \quad (2.4.7)$$

where $D_i^{app}(t)$ is the apparent value of D calculated for a finite time t .

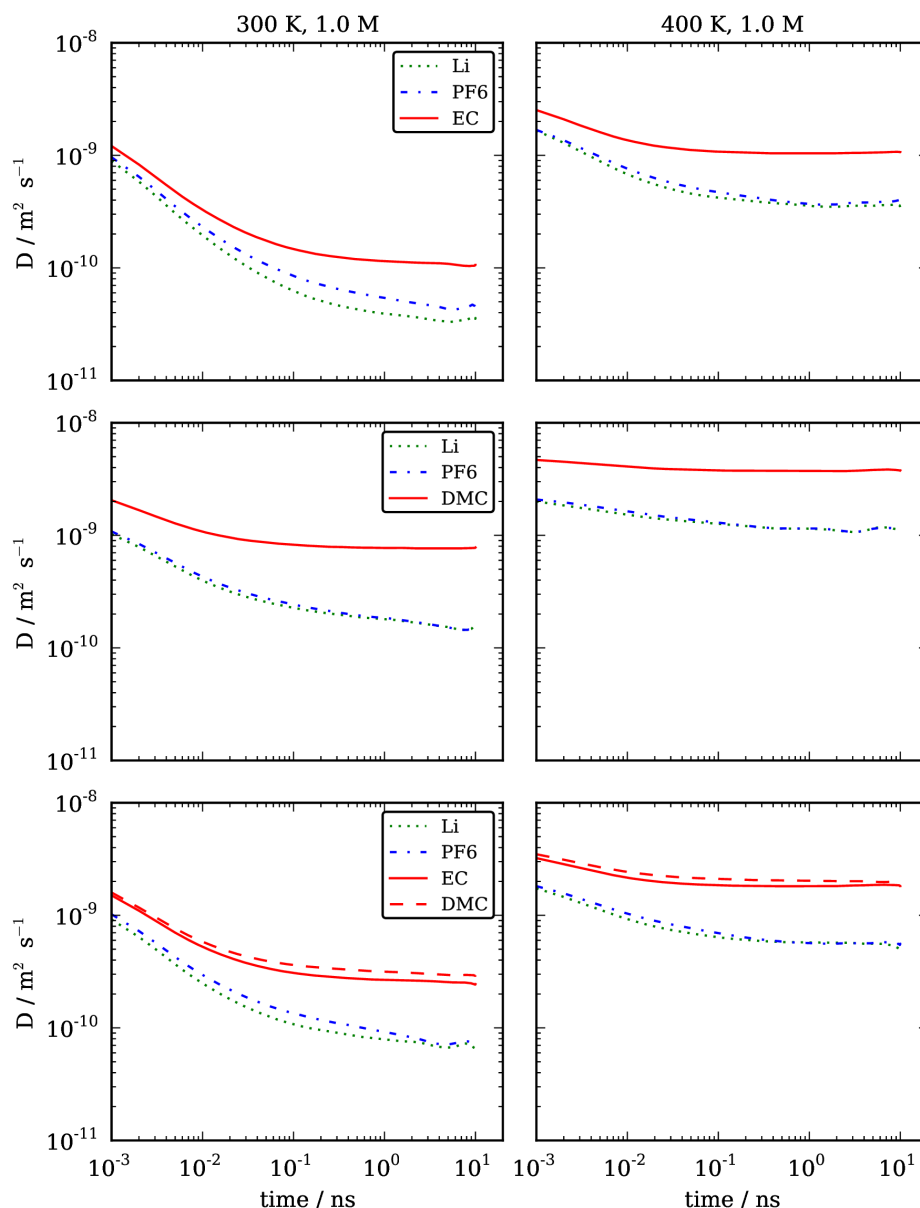


Figure 31: Self-diffusion coefficients versus time for 1.0 M LiPF_6 in EC (top), DMC (middle), and EC/DMC (bottom) solvents at 300 K and 400 K.

Figure 31 shows self-diffusion coefficients (Equation 2.4.6) versus time for 1.0 M LiPF_6 in EC, DMC, and EC/DMC solvents at 300 K and 400 K. Solvent diffusivities are significantly higher in pure DMC systems than in pure EC systems, particularly at 300 K. This is consistent with experimental measurements of diffusivity and viscosity and EC's relatively high melting point (310 K versus 268 K for DMC (Linstrom and Mallard)). In mixed EC/DMC systems, DMC and EC diffusivities are nearly identical and approximately equal to the average of the values observed in corresponding pure DMC and EC systems. Solvent diffusivities are 2-5x larger than ion diffusivities for any particular system, which would be consistent with the formation of bulky, slowly-diffusing molecular clusters around ions. Variations in ion diffusivity between different systems match the trends observed for variations in solvent diffusivity. At 300 K Li and

PF₆ diffusivities do not attain their long-time values within the available simulation time, indicating sub-diffusive behavior. For pure DMC systems, note that the Li⁺ and PF₆⁻ curves coincide perfectly, suggesting strong ion pairing. Li and PF₆ curves for EC and EC/DMC systems are close but do not coincide perfectly. Decreasing LiPF₆ concentration to 0.1 M (not shown) leads to increased diffusivities, which would be consistent with decreased cluster formation and a reduced system viscosity. This effect is slight for the pure DMC systems (1.2x) but significant for pure EC systems (3x at 300 K and 1.7x at 400 K), suggesting that EC and DMC may interact fundamentally differently with the Li⁺ and/or PF₆⁻ ions present in the system.

Ionic conductivity λ can be calculated using the Einstein relation

$$\lambda^{app}(t) = \frac{e^2}{6tVkBT} \sum_i^N \sum_j^N z_i z_j \langle [\mathbf{r}_i(t_0+t) - \mathbf{r}_i(t_0)] [\mathbf{r}_j(t_0+t) - \mathbf{r}_j(t_0)] \rangle \quad (2.4.8)$$

$$\lambda = \lim_{t \rightarrow \infty} \lambda^{app}(t) \quad (2.4.9)$$

where $\lambda^{app}(t)$ is the apparent value of λ calculated for a finite time t , $\langle \rangle$ denotes an ensemble average over possible starting times t_0 , e is the charge of an electron, V is the simulation box volume, kB is Boltzmann's constant, T is temperature, z_i is the charge on ion i in units of electrons, $\mathbf{r}_i(t)$ is the position of molecule i at time t , and summation is done over all N ions in the simulation box. The diagonal ($i=j$) terms in Equation (2.4.8) represent the Nernst-Einstein (uncorrelated) conductivity, i.e. the ideal conductivity arising only from ion self-diffusion. The off-diagonal terms in Equation (2.4.8) account for correlated ion motion, which generally reduces electrolyte conductivity relative to the Nernst-Einstein value.

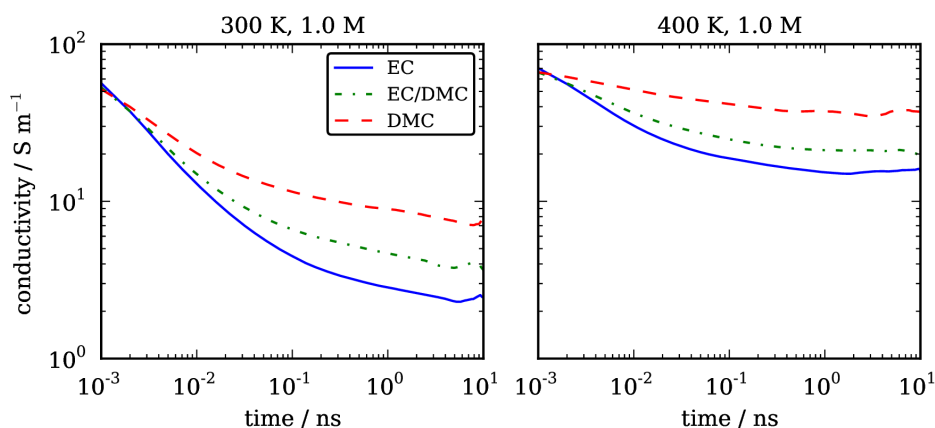


Figure 32: Ideal Nernst-Einstein (uncorrelated) ionic conductivity versus time for 1.0 M LiPF₆ in EC, DMC, and EC/DMC solvents at 300 K and 400 K.

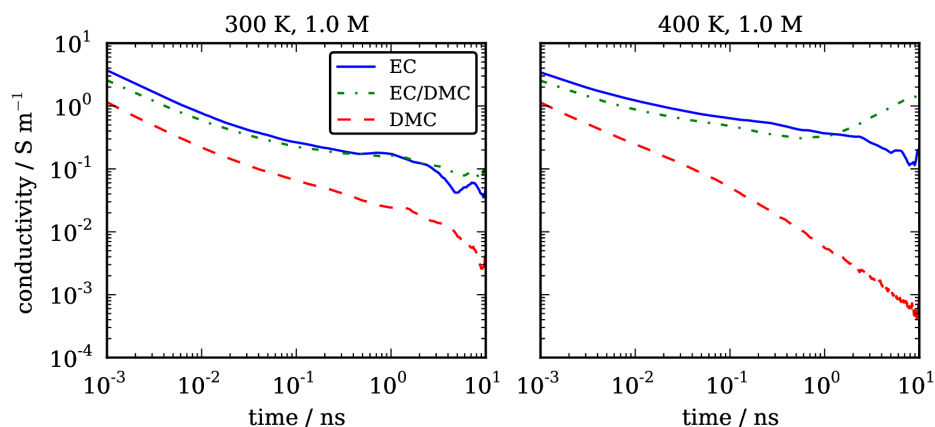


Figure 33: As in Figure 32, except true (correlated) ionic.

Figure 32 shows the ideal Nernst-Einstein ionic conductivity versus time for 1.0 M LiPF_6 in EC, DMC, and EC/DMC solvents at 300 K and 400 K. The Nernst-Einstein conductivities follow the same trends observed for ion diffusivity; i.e. conductivity for pure DMC systems is significantly higher than for pure EC systems, with intermediate values for mixed EC/DMC systems. The Nernst-Einstein conductivity increases significantly as salt concentration is increased from 0.1 M to 1.0 M (not shown). Figure 33 shows the true ionic conductivity for the same systems as in Figure 33. While the curves for true conductivity in Figure 33 do not attain steady values within the allotted simulation time, indicating that longer simulations are required to get precise values for conductivity, several trends are nonetheless apparent. First, as expected, true conductivities are significantly lower (by at least an order of magnitude) than the Nernst-Einstein values. More interestingly, conductivities for pure EC systems are significantly higher than for pure DMC systems, which is opposite the trend for Nernst-Einstein conductivities. More specifically, the steady and consistent downward trend for the DMC curves in Figure 33, particularly at higher temperatures, suggests conductivity in DMC systems is essentially negligible, in spite of significantly higher diffusivity. Also unlike the Nernst-Einstein case, conductivities for mixed EC/DMD systems more closely match conductivities for pure EC systems, as opposed to taking values approximately equal to the average of the pure EC and pure DMC conductivities. Further, conductivity does not appear to change significantly as salt concentration is varied between 0.1 M, 0.3 M, and 1.0 M (not shown), but this is difficult to judge due to the short simulation times. These observations all suggest conductivity is strongly influenced by correlated ion movement and this correlated movement can vary significantly between solvents. With regard to the ionic conductivities predicted for pure EC systems, the simulation values appear to be approximately 20% to 50% of experimental conductivity values. In addition to neglecting any electronic contribution present in experiment, this is not unexpected when using a non-polarizable forcefield with full integer charges on the ionic species, which tends to result in slowed dynamics.

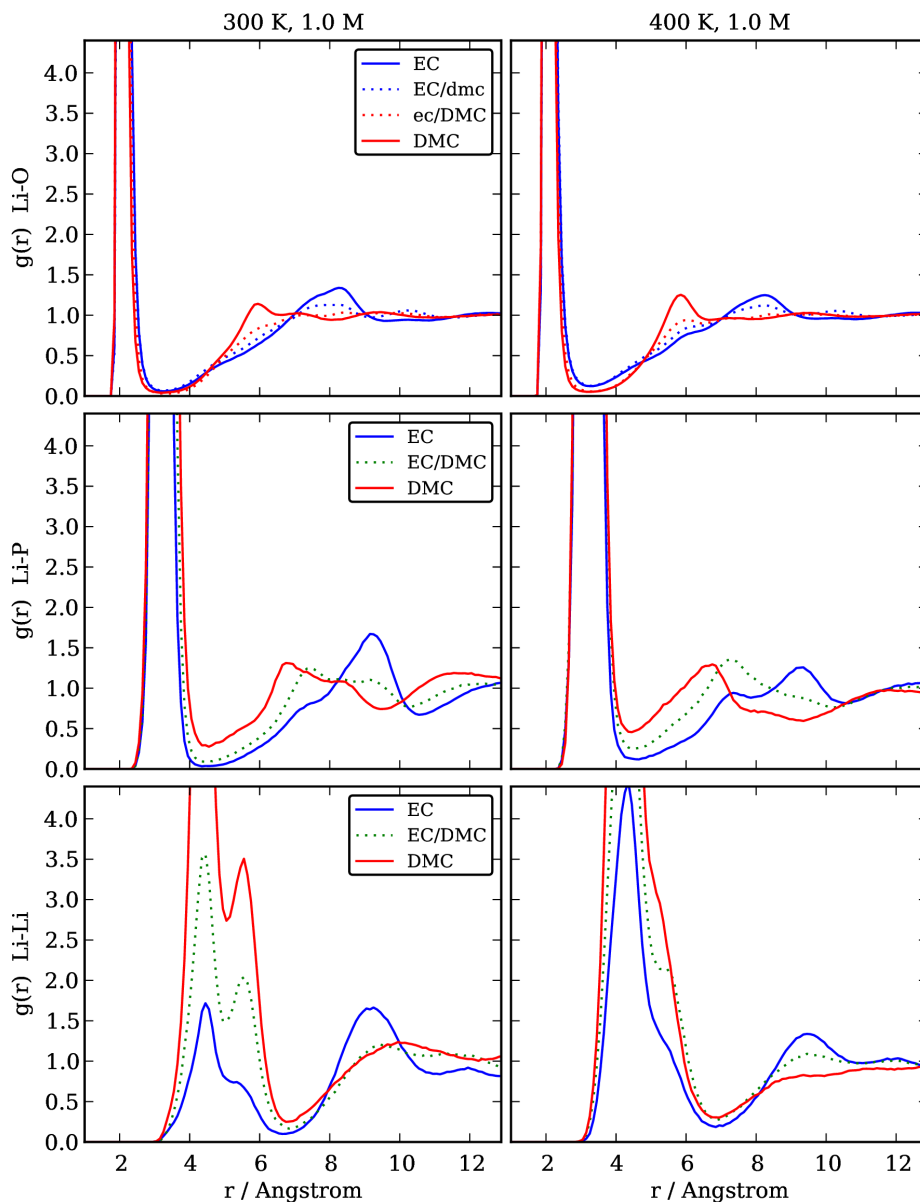


Figure 34: Pair correlation functions $g(r)$ versus separation r for Li^+ with solvent carbonyl oxygens (Li-O), PF_6^- (Li-P), and other Li^+ (Li-Li) for 1.0 M LiPF_6 in EC, DMC, and EC/DMC solvents at 300 K and 400 K. “EC/dmc” and “ec/DMC” denote coordination of Li with EC and DMC, respectively, in mixed EC/DMC solvent systems.

Figure 34 shows the pair correlation functions $g(r)$ versus separation r for Li^+ with solvent carbonyl oxygens (Li-O), PF_6^- (Li-P), and other Li^+ (Li-Li) for 1.0 M LiPF_6 in EC, DMC, and EC/DMC solvents at 300 K and 400 K. The primary Li-O peaks occur at approximately $r=2.1$ for both EC and DMC in all solvent systems. Very slight secondary Li-O peaks occur at approximately $r=8.1$ for EC and $r=5.9$ for DMC. As temperature is increased, the secondary peak for DMC becomes slightly more prominent, and the secondary peaks for both EC and DMC

shift to slightly lower values of r . Changes in LiPF_6 concentration (not shown) do not appear to significantly change the Li-O $g(r)$ for any solvent/temperature combination.

Similar to the Li-O case, primary Li-P peaks occur at the same point, approximately $r=3.2$, for all solvent systems; and very slight secondary peaks occur at approximately $r=9.1$ for EC and $r=6.6$ for DMC. As temperature is increased, the secondary Li-P peak for EC becomes less prominent and broadens to include a shoulder at approximately $r=7.1$, whereas the secondary Li-P peak for DMC becomes more prominent and less broad. Lower LiPF_6 concentration (not shown) may increase the prominence of the secondary Li-P peaks for all solvent/temperature combinations, but results are noisy due to poor statistics with the reduced number of Li and PF_6 species.

The primary Li-Li peaks $g(r)$ in Figure 34 have maxima at approximately $r=4.3$ and shoulders or sub-peaks at approximately $r=5.7$ for all solvent systems. The primary Li-Li peaks for EC are significantly less prominent than those for DMC, with EC/DMC values being intermediate. Secondary Li-Li peaks occur at approximately $r=9.2$ for EC systems but are minor to non-existent for DMC systems. Increasing temperature greatly increases the prominence of the primary Li-Li peak for EC, decreases prominence of any secondary peak, and reduces shoulders or sub-peaks in the primary peak for all solvent systems. Results from lower LiPF_6 concentrations (not shown) are inconclusive due to poor statistics with the reduced number of Li species.

Table 2: Average number of solvent carbonyl oxygen atoms within first coordination shell of Li^+ for all combinations of solvent, temperature, and LiPF_6 concentration used in this study. “EC/dmc” and “ec/DMC” denote coordination of Li with EC and DMC, respectively, in mixed EC/DMC solvent systems.

	0.1 M			0.3 M			1.0 M		
	300 K	350 K	400 K	300 K	350 K	400 K	300 K	350 K	400 K
EC	5.2	5.0	4.2	5.1	4.2	3.6	4.0	3.3	2.9
EC/dmc	3.0	2.4	2.0	2.5	1.8	1.6	1.6	1.5	1.3
ec/DMC	2.0	1.6	1.4	1.8	1.5	1.3	1.6	1.4	1.2
DMC	2.6	2.1	2.1	2.5	2.1	2.0	2.3	2.0	2.0

Table 3: As in Table 2, except for coordination of PF_6^- ions with Li^+ .

	0.1 M			0.3 M			1.0 M		
	300 K	350 K	400 K	300 K	350 K	400 K	300 K	350 K	400 K
EC	0.4	0.4	0.8	0.4	0.9	1.1	1.1	1.4	1.6
EC/DMC	0.5	0.9	1.2	0.8	1.4	1.6	1.5	1.7	1.9
DMC	1.7	2.0	2.0	1.9	2.1	2.2	2.1	2.2	2.2

Table 4: As in Table 2, except for coordination of Li^+ ions with Li^+ .

	0.1 M			0.3 M			1.0 M		
	300 K	350 K	400 K	300 K	350 K	400 K	300 K	350 K	400 K
EC	0.0	0.0	0.1	0.0	0.3	0.5	0.4	0.7	0.9
EC/DMC	0.0	0.2	0.3	0.1	0.6	0.7	0.9	1.1	1.3
DMC	0.9	1.0	1.0	1.4	1.4	1.6	1.6	1.6	1.7

Tables 2, 3, and 4 list the average number N of solvent carbonyl oxygen atoms (N_{LiO}), PF_6^- ions (N_{LiP}), and Li^+ ions (N_{LiLi}), respectively, within the first coordination shells of Li^+ ions for all combinations of solvent, temperature, and LiPF_6 concentration used in this study. These first shell coordination numbers are equal to the area under the first peaks of the corresponding pair correlation functions $g(r)$ (e.g. Figure 34). N_{LiO} for EC systems varies from 2.9 (1.0 M, 400 K) to 5.2 (0.1 M, 300 K) and for DMC systems from 2.0 (1.0 M, 400 K) to 2.6 (0.1 M, 300 K). N_{LiO} results for mixed EC/DMC systems take on intermediate values, with N_{LiO} for EC molecules always at least slightly greater than N_{LiO} for DMC molecules. N_{LiO} decreases for all solvent systems as either temperature or LiPF_6 concentration is increased, with EC coordination being the most sensitive. N_{LiP} trends are generally opposite those for N_{LiO} , suggesting that solvent carbonyl oxygen atoms and PF_6^- compete for coordination with Li^+ . N_{LiP} for EC systems varies from 0.4 (0.1 M, 300 K) to 1.6 (1.0 M, 400 K) and for DMC systems from 1.7 (0.1 M, 300 K) to 2.2 (1.0 M, 400 K). N_{LiP} results for mixed EC/DMC systems again take on intermediate values, generally staying closer to the pure EC results. Unlike N_{LiO} , N_{LiP} increases for all solvent systems as either temperature or LiPF_6 concentration is increased, with EC coordination still being the most sensitive. N_{LiLi} trends generally match those for N_{LiP} , suggesting that association of Li^+ with other Li^+ may depend upon PF_6^- as an intermediary. N_{LiLi} for EC systems varies from 0.0 (0.1 M, 300 K) to 0.9 (1.0 M, 400 K) and for DMC systems from 0.9 (0.1 M, 300 K) to 1.7 (1.0 M, 400 K).

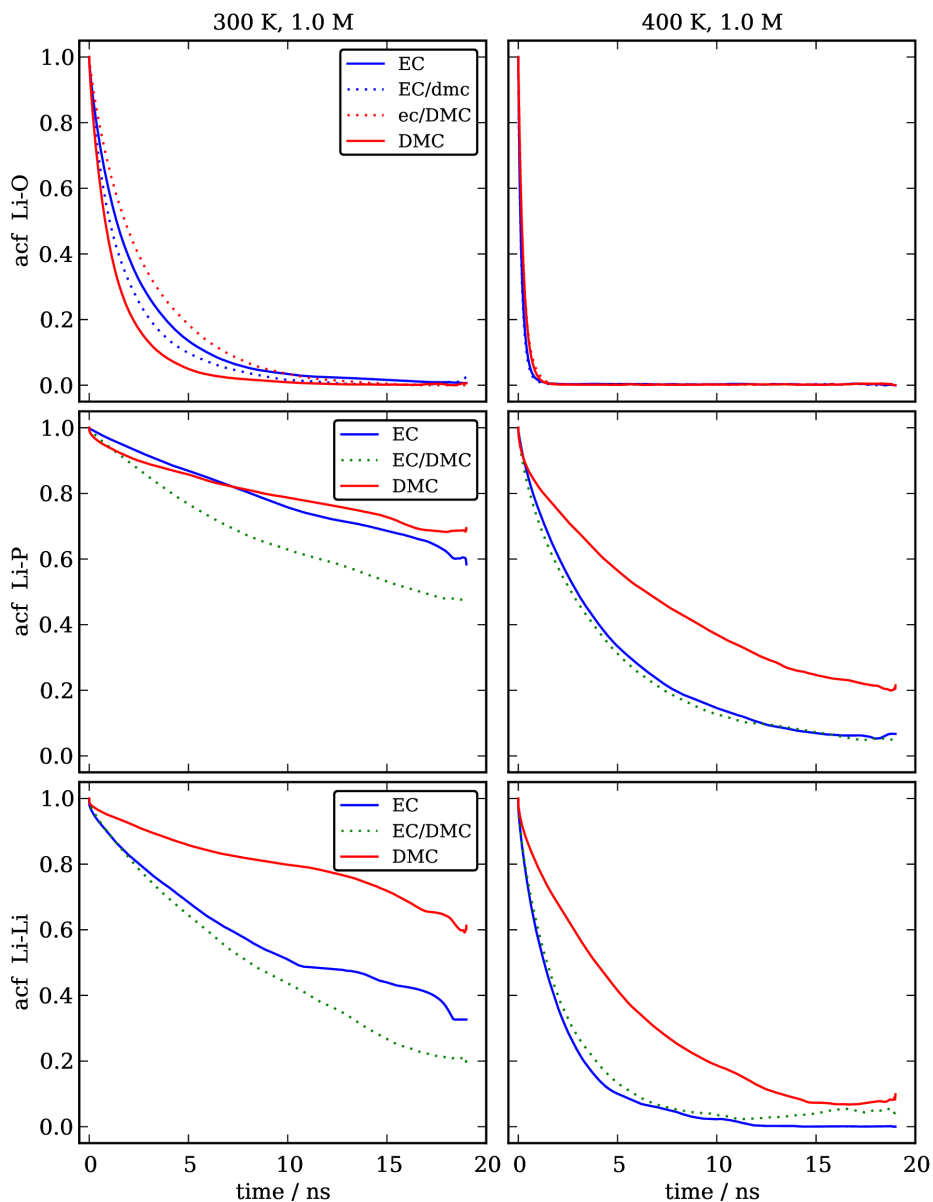


Figure 35: Neighbor autocorrelation function (acf) versus time for Li^+ with solvent carbonyl oxygens (Li-O), PF_6^- (Li-P), and other Li^+ (Li-Li) for 1.0 M LiPF_6 in EC, DMC, and EC/DMC solvents at 300 K and 400 K. A “neighbor” is defined as an atom closer than the minimum after the first peak of the corresponding $g(r)$ in Figure 34.

For any given timestep, if a particular PF_6^- or Li^+ ion is within the first coordination shell of a particular Li^+ ion, those ions are defined to be “neighbors”. Similarly, if a particular solvent carbonyl oxygen atom is within the first coordination shell of a particular Li^+ ion, that solvent molecule and that Li^+ are neighbors. (Other solvent oxygen atoms are ignored for the purpose of neighbor determination, because their association with Li^+ is negligible compared to the carbonyl oxygen.) An adjacency matrix $A(\tau)$ is formed wherein $A_{ij}(\tau)=1$ if object i (e.g. one of the Li^+

ions) and object j (e.g. one of the PF_6^- ions) are neighbors at time τ and 0 otherwise. The neighbor autocorrelation function $R(t)$ is the probability that a particular neighbor pair at time t_0 will also be neighbors at t_0+t . $R(t)$ is calculated according to

$$R(t) = \langle A_{ij}(t_0)A_{ij}(t_0+t) \rangle \quad (2.4.10)$$

where $\langle \rangle$ denotes an ensemble average over possible initial times t_0 and indices i and j .

Figure 35 shows $R(t)$ versus time for coordination of Li^+ with solvent carbonyl oxygens (Li-O), PF_6^- (Li-P), and other Li^+ (Li-Li) for 1.0 M LiPF_6 in EC, DMC, and EC/DMC solvents at 300 K and 400 K. The $R(t)$ curves for Li-O indicate that Li^+ ions tend to swap solvent neighbors within a few nanoseconds at 300 K and within a nanosecond at 400 K. Reducing LiPF_6 concentration does not appear to significantly influence characteristic times for Li-O pairing (not shown). The characteristic times for Li-P pairing are longer than the 20 ns simulation time at 300 K and are approximately 5 ns to 15 ns at 400 K. Characteristic times for Li-Li pairing are much longer than Li-O values and appear to be approximately half the Li-P values, which is consistent with Li-Li association occurring through PF_6^- intermediates. Characteristic times for Li-P and Li-Li pairing appear to be significantly reduced for systems containing EC solvent. Trends in Li-P and Li-Li pairing for lower LiPF_6 concentration are not discernable due to poor statistics.

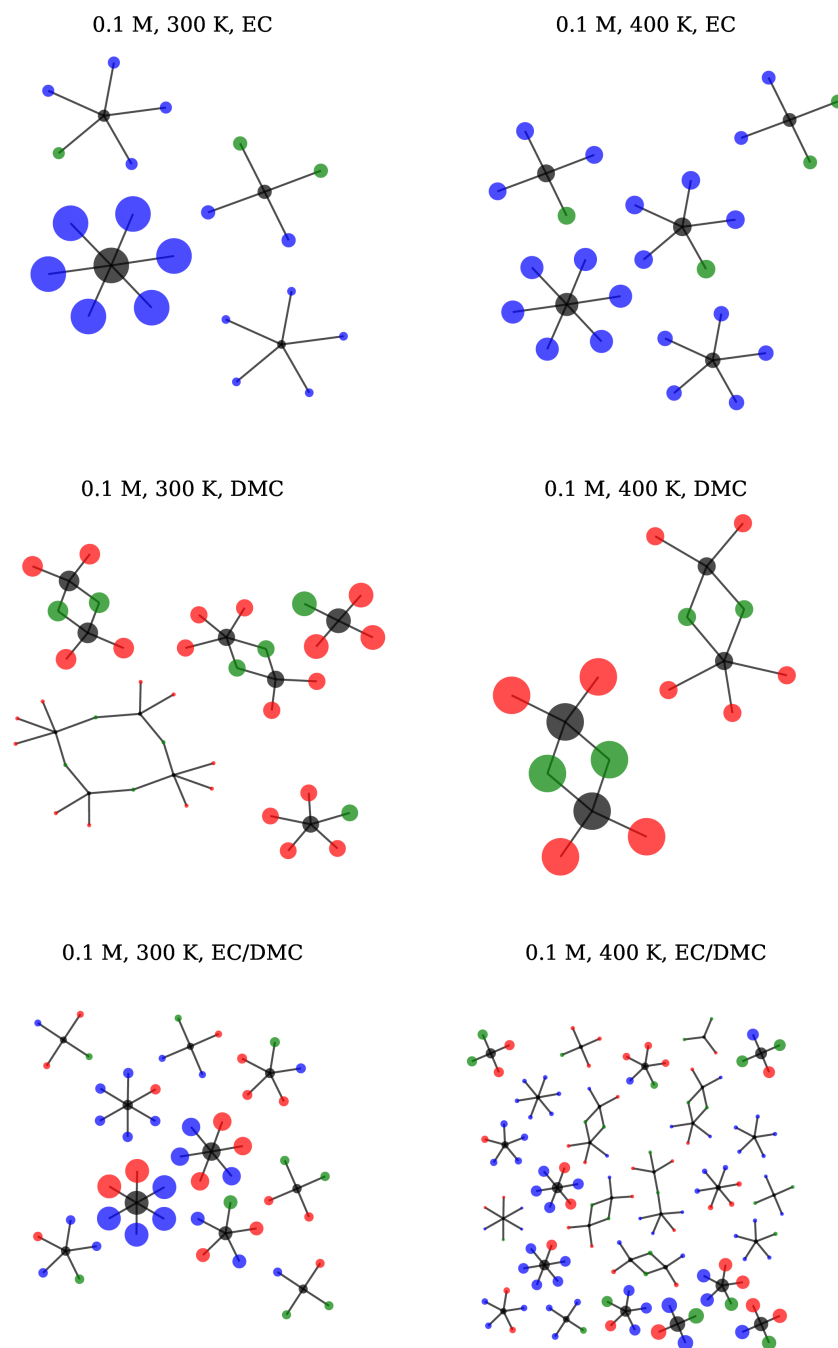
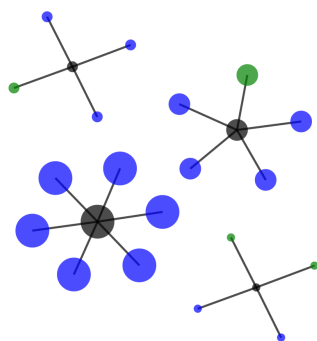
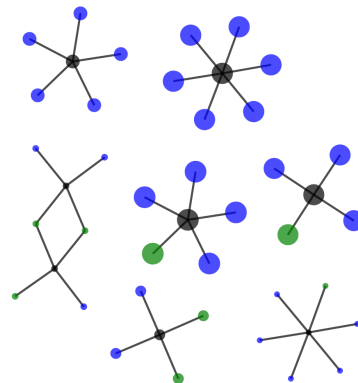


Figure 36: Common cluster topologies formed by Li^+ (black) neighboring with PF_6^- (green) or solvent carbonyl oxygen atoms (EC = blue, DMC = red). Lines represent neighbor pairing. Node size is proportional to the frequency with which a cluster topology was observed. The systems are composed of 0.1 M LiPF_6 in EC, DMC, or EC/DMC at 300 K and 400 K.

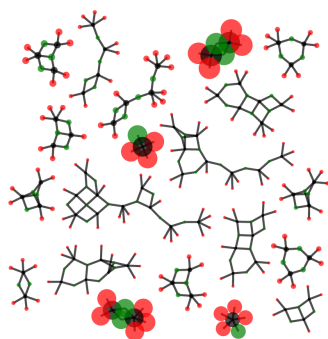
0.3 M, 300 K, EC



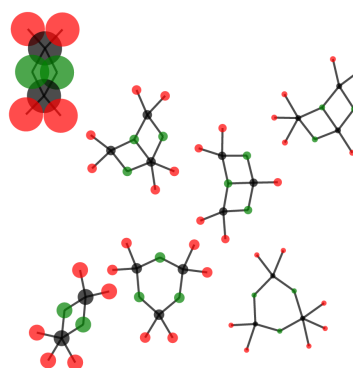
0.3 M, 400 K, EC



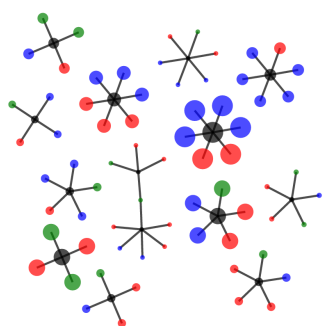
0.3 M, 300 K, DMC



0.3 M, 400 K, DMC



0.3 M, 300 K, EC/DMC



0.3 M, 400 K, EC/DMC

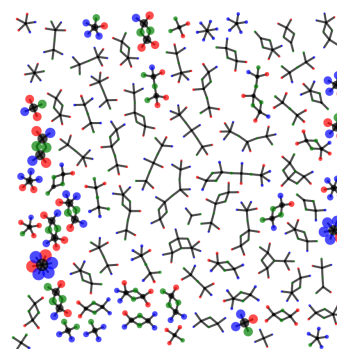


Figure 37: As in Figure 36, except 0.3 M LiPF_6 .

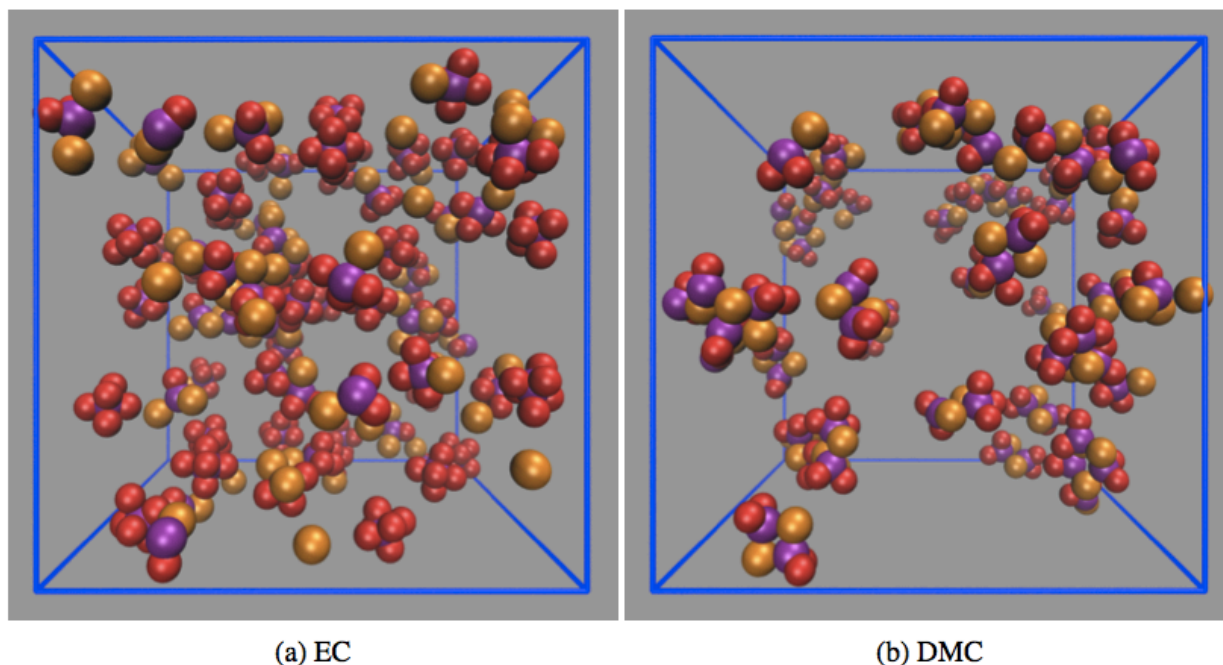


Figure 38: Snapshots showing all Li^+ ions (purple), all P atoms (orange) from PF_6^- , and only solvent carbonyl oxygen atoms (red) neighbored with a Li^+ . The systems are 1.0 M LiPF_6 in pure EC and DMC at 300 K. The blue box outlines the periodic simulation cell. Note that some clusters may span periodic boundaries.

For any given timestep τ , a theoretical graph or network can be constructed in which the nodes represent specific Li^+ ions, PF_6^- ions, or solvent carbonyl oxygen atoms and edges connect specific Li-O and Li-P neighbor pairs (as defined above). For this discussion we define a cluster as a connected component of that graph, i.e. a subgraph in which every node is connected to every other node in the subgraph by at least one path and is not connected to any node not in the subgraph. For every timestep there will then exist a set of clusters with a variety of network topologies or patterns of connectedness. Two clusters are isomorphic if they have the same topology. (Cluster analysis was aided by the open source Python package NetworkX v1.7 (Hagberg, Schult et al. 2008).) Figure 36 shows the most common cluster topologies formed by Li^+ neighboring with PF_6^- and solvent carbonyl oxygen atoms for systems composed of 0.1 M LiPF_6 in EC, DMC, or EC/DMC at 300 K and 400 K. For clarity the least commonly observed cluster topologies are omitted, but the clusters shown represent at least 90% of the topologies observed for a particular system. Figure 37 represents systems composed of 0.3 M LiPF_6 . (1.0 M systems are not shown, because the number of minor topologies becomes too numerous to display clearly.)

For EC systems the most common cluster topology is a single Li^+ ion surrounded by six EC molecules, resulting in a cluster with +1 charge (Figure 36 and Figure 37, top row). The next most common topologies have fewer EC molecules and zero, one, or two PF_6^- ions, resulting in clusters with +1, 0, or -1 charge. Averaging over all observed clusters, the number of EC molecules or PF_6^- ions around a Li^+ ion is equal to the coordination numbers listed in Table 2 and Table 3. Note that the most common cluster topology does not match the coordination implied by

the results these tables. Increasing temperature and LiPF₆ concentration generally results in a greater variety of cluster topologies for EC systems and a greater likelihood of forming clusters with zero charge. This increased formation of clusters with zero charge may offset the gains in conductivity expected with increased temperature and salt concentration. The extent of this effect will be influenced by the characteristic lifetime of individual clusters; but given the relatively long correlation time for neighboring between Li⁺ and PF₆⁻, this effect is expected to be non-negligible. Figure 38a is a simulation snapshot showing Li⁺ ions, PF₆⁻ ions, and solvent carbonyl oxygen atoms neighbored with Li⁺ for the system composed of 1.0 M LiPF₆ in pure EC at 300 K. The common topology of Li⁺ surrounded by six solvent molecules is readily apparent.

For DMC systems the most common cluster topology involves two Li⁺ ions neighbored with two or three distinct solvent molecules and connected to each other via two shared PF₆⁻ neighbors. At 300 K clusters composed of a single Li⁺, a single PF₆⁻, and three or four solvent molecules are also relatively common. Increasing LiPF₆ concentration leads to increased cluster variety, but unlike EC systems, the vast majority of clusters observed in DMC systems have zero charge. Given the relatively long correlation time for neighboring between Li⁺ and PF₆⁻, particularly for DMC systems, the formation of primarily neutral clusters is consistent with the negligible ionic conductivity observed for DMC systems. Also unlike EC systems, decreasing temperature generally results in a reduced variety of cluster topologies. Relative to EC systems, the formation of extended chains or rings is much more likely in DMC systems. In all clusters containing more than one Li⁺, the Li⁺ associate via one to three (typically two) intermediate PF₆⁻. Solvent carbonyl oxygens were not observed simultaneously neighboring with multiple Li⁺. Figure 38b is a simulation snapshot showing Li⁺ ions, PF₆⁻ ions, and solvent carbonyl oxygen atoms neighbored with Li⁺ for the system composed of 1.0 M LiPF₆ in pure DMC at 300 K. Relative to the EC system shown in Figure 38a, there are fewer and larger clusters for the DMC system.

Due to the presence of two solvent types, a wide variety of cluster topologies is observed for EC/DMC systems. The general pattern of topologies, however, is more similar to EC systems than DMC systems, with minimal formation of extended chains or rings and more clusters with nonzero charge. This observation is consistent with ionic conductivity for EC/DMC systems more closely matching EC systems than DMC systems. Given that the high melting point of EC prevents its use as a room-temperature electrolyte solvent, the dominance of cluster formation similar to that in EC systems rather than DMC systems is fortunate. In addition to the many other constraints and trade-offs necessary when choosing an electrolyte composition, it seems the ideal solvent must associate strongly enough with the cations and/or anions to minimize their pairing and the formation of neutral clusters, without being overly viscous. In the case of EC/DMC blends used in commercial lithium ion batteries, a compromise is apparently reached, wherein the highly dielectric EC inhibits cation and anion association and DMC allows sufficient fluidity and diffusion.

2.5 Modeling Passivation Layer Growth and Decomposition

In order to maintain stability and long life in a battery, the electrolyte should be inert with respect to the anode and cathode surfaces, so that direct reduction or oxidation of the electrolyte

molecules is prevented. Many material combinations used in Li-ion batteries do not possess this property; in particular, ethylene carbonate (EC) molecules can easily be reduced through electron transfer at a clean Li or graphene anode surface. The fact that EC and graphene can be successfully used in Li-ion batteries is due to the formation of a passivation layer, named the solid electrolyte interphase or interface (SEI) by Peled (Peled 1979), at the anode surface. The SEI layer forms during the early stages of charging, and allows diffusion of Li^+ ions while insulating the surface from electron transfer.

The morphological structure of the SEI layer is fairly complex. The prevailing picture, introduced by Peled et al (Peled, Golodnitsky et al. 1997), is a mosaic of microphases, a collection of grains of different materials. However, there is some organization to this mosaic, and experiments indicate a general two-layer structure: a thin layer of inorganic species (e.g. LiF , Li_2O , LiOH) close to the electrode material, and a thicker outer layer made up of organic compounds. Measurements of the thicknesses of these layers vary, but typical estimates are 1-2 nm for the inner layer, and tens of nanometers for the outer organic layer (Andersson, Henningson et al. 2003).

Although an electronically insulating SEI layer is necessary for stability, the characteristics of the SEI layer can have further effects on battery performance. Because lithium is consumed in the formation of the SEI layer, this layer contributes to the reduction of battery capacity, especially if it continues to grow throughout the lifetime of charge-discharge cycles; thickening of this layer slows lithium ion diffusion and increases the total impedance. SEI layer phenomena also appear to be closely tied to thermal abuse behavior. In typical thermal models of Li-ion cells (Hatchard, MacNeil et al. 2001; Kim, Pesaran et al. 2007), exothermic decomposition reactions within the SEI layer at moderate temperatures (100°C) can provide a temperature boost that accelerates reactions in the rest of the cell, leading to run-away. The mechanical response of the SEI layer to the volume expansion of the anode during lithiation may also be an important phenomenon in the performance and failure of batteries.

In this project, we have made progress on developing three separate capabilities to model SEI growth and behavior; each approach has distinct strengths. A continuum model, implemented in COMSOL, uses well-established governing principles and allows a rapid initial look at the phenomena presumed to be at work. A kinetic Monte Carlo (KMC) model allows more detailed treatment of the complex geometry of the SEI microstructure, and provides a bridging scale between atomic-scale processes (like individual molecular reactions and diffusion-hops) and meso- and macro-scale phenomena. A phase field model of the SEI growth complements both of these, using continuum-level transport equations while allowing a natural treatment of the changing layer geometry and structure.

2.5.1 Comsol Modeling of SEI Growth



Figure 39: Schematic of COMSOL model regions and their interfaces.

The COMSOL model of the SEI is a 1D model made up of four separate regions representing the carbon anode, the SEI layer, the inner Helmholtz plane (IHP), and the outer Helmholtz plane (OHP); these regions are linked at their interfaces, as shown schematically in Figure 39.

In the carbon anode, the transport of lithium is described by a simple diffusion equation:

$$\frac{\partial c_{Li}}{\partial t} = D \frac{\partial^2 c_{Li}}{\partial x^2} \quad (2.5.1)$$

where c_{Li} is the concentration of lithium and D is the diffusivity. In the SEI layer, the transport of lithium ions is modeled; in addition to diffusion, electromigration and the reaction source term S are also included:

$$\frac{\partial c_{Li^+}}{\partial t} + \frac{\partial uc_{Li^+}}{\partial t} = D \frac{\partial^2 c_{Li^+}}{\partial x^2} + S \quad (2.5.2)$$

The electromigration velocity u is proportional to the gradient of the electric field ϕ :

$$u = -\mu \frac{\partial \phi}{\partial x} \quad (2.5.3)$$

The electric field satisfies a Poisson equation within the SEI:

$$\epsilon \epsilon_0 \frac{\partial^2 \phi}{\partial x^2} = -ec_{Li^+} \quad (2.5.4)$$

The IHP and OHP are treated as single nodes, so that the rate of change of lithium ion concentration is determined by a flux difference plus a reaction source term:

$$\frac{\partial c_{Li^+}}{\partial t} = J_R - J_L + S \quad (2.5.5)$$

2.5.2 Kinetic Monte Carlo Modeling of SEI Growth

A kinetic Monte Carlo (KMC) model of SEI growth has been developed and implemented in the Sandia KMC code SPPARKS. There are several reasons for using KMC to approach this modeling problem. KMC provides a natural bridging scale between continuum and atomistic descriptions. The lattice-based description used in the KMC model allows straightforward modeling of the evolving SEI geometry and microstructure. Finally, a KMC model addresses some of the inaccuracies associated with mean-field continuum theory, particularly for configurations with small concentrations of individual species.

In order to have overlap with continuum models, our KMC model should capture the same phenomena, including lithium diffusion, chemical reactions, electron tunneling effects, and electric field-driven migration of charged species. The first two of these, diffusion and reactions, can be included in a KMC model in a very natural way. The latter two, electron tunneling and electro-migration, are included more approximately for now, although future work may improve the fidelity of the representation of these phenomena.

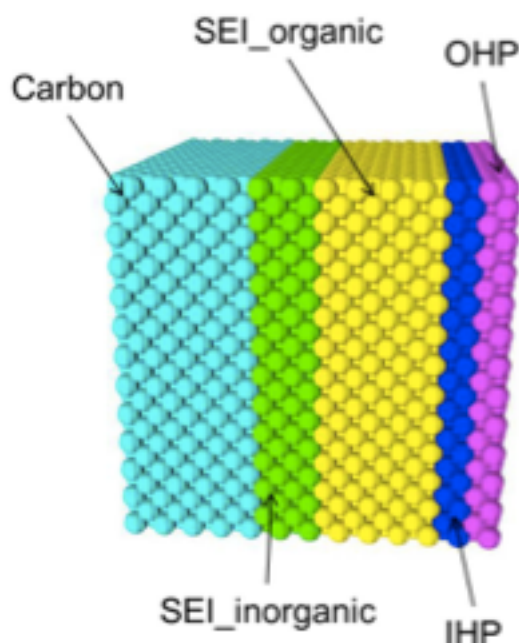


Figure 40: Example geometry lattice for KMC simulation. Each site is labeled with a material identifying its location in the anode/SEI/electrolyte structure.

The geometry of our KMC model is made up of a discrete lattice of sites (Figure 40). The lattice is a face-centered cubic (FCC) crystal with lattice constant a , so that each site has 12 nearest neighboring sites at a distance $a/\sqrt{2}$. Each site is labeled with a “material”, where the material identifies in which part of the anode/SEI/electrolyte structure the site is located. The material can

be carbon, SEI-inorganic, SEI-organic, IHP, OHP, or electrolyte. Note that some of these (like IHP and OHP) are not true material identifiers, but label the sites according to their location relative to the structure. Material labels can change throughout the simulation; for example as the SEI layer grows individual sites are changed to SEI material. Wherever the SEI (organic or inorganic) sites are located, the nearest neighbor that are not SEI or carbon are labeled as IHP sites; the nearest neighbors to the IHP sites that are not SEI, carbon, or IHP are labeled as OHP. The geometry and lattice are oriented so that the anode surface is a <111> crystal plane, the close-packed plane in the FCC lattice, and is normal to the z axis.

In addition to its material label, each site may contain a “species”, representing occupation of the site by a particular mobile atom or molecule. Types of species allowed in the current model are Li, Li⁺, EC, EC⁻, LiEC, LiEC⁺, LiOCO₂⁻, LiEDC, and Li₂CO₃. Each site may contain at most one species (although a site can be empty).

Finally, the KMC model is defined by a set of events that can take place. Possible events include movement of a species from one site to another, chemical reaction (which transforms the species of a set of sites), or creation or destruction of SEI material (which transforms the material of a set of sites). Details of possible events are given below.

The KMC simulation progresses in time by executing events one at a time. For a given configuration, the list of possible events is constructed, along with the corresponding rate for each event (k_i for event i). An event is chosen at random with weighted probability, with the probability of each event i given by:

$$P_i = \frac{k_i}{\sum_j k_j} \quad (2.5.6)$$

That event is executed, and the system clock is updated by a computed timestep:

$$\Delta t = \left(\sum_i k_i \right)^{-1} \ln \left(\frac{1}{r} \right) \quad (2.5.7)$$

where r is a random number between 0 and 1 with uniform distribution. After the event, a new event list and rates must be computed for the resulting new configuration.

Most of the computational time in the KMC simulation is spent computing possible events and their rates. Ideally, for efficiency, when an event is executed the list of possible events and rates for the new configuration needs to be updated only for events involving nearby sites. There are two requirements for this to be true. First, the possibility for an event, and the computation of its rate, should be a function only of the states (material and species) of nearby sites. Second, a given event should change the state (material and species) only of nearby sites. This is true for events like diffusion – the hopping of a species from one site to another – which is inherently local. More problematic are events that depend on an electric field, such as electro-migration, since the electric field depends on the charge distribution throughout the domain, and local changes to charged species therefore have long-range effects on the field. A successful KMC simulation requires efficient treatment of these types of events.

Our KMC model has been implemented as an application in the SPPARKS KMC solver developed at Sandia (Plimpton, Battaile et al. 2009). The battery model application defines lattice sites, events, and rates, as well as how the execution of an event changes the state of the model. The SPPARKS framework handles efficient storage and random event selection, along with common tasks like I/O. SPPARKS also allows spatial decomposition and parallelization through an approximation that assumes independent events taking place on each processor.

2.5.2.1 Event Descriptions

There are two main types of events in the model: diffusion/migration events, which involve the hopping of a species from one site to a neighboring site, and reaction events, which may involve species at multiple sites and lead to changes in the species or materials at one or more sites. The rates for each type of event must be specified, and in some cases we choose these rates based on corresponding parameters in the continuum model for SEI growth.

Diffusion We allow diffusion of lithium atoms within the carbon anode, so that the Li species can hop from a carbon site to a neighboring carbon site if it is unoccupied. Lithium is the only species that is present in the anode, and neutral lithium atoms are not present elsewhere outside the anode. Lithium ions, on the other hand, can diffuse through the bulk of the SEI material (organic or inorganic), along the surface between two IHP sites, or across the SEI/IHP interface. The rate k for species hopping events is related to the continuum diffusivity D through the relation(Doll and Voter 1987):

$$D = \frac{1}{2d} \sum_i k l_j^2 \quad (2.5.8)$$

where d is the dimensionality and l_j is the distance between the current site and site j . For an FCC lattice where hops are limited to one of 12 equivalent nearest neighbors ($l = a/\sqrt{2}$), this is simply:

$$D = k a^2 \quad (2.5.9)$$

Electromigration In order to account for electromigration, the electric potential φ must be computed. Our approach to this is a modification of that taken by Lau et al. (Lau, Turner et al. 2008) and Pornprasertsuk et al. (Pornprasertsuk, Holme et al. 2009). To approximate φ efficiently, we assume that it is only a function of the z direction (the direction normal to the anode surface), so that each z -plane of atoms i has a constant potential φ_i . The potential can be separated into two contributions:

$$\dots \quad (2.5.10)$$

Here, φ_s^i is the part of the potential corresponding to the arrangement of charged species in the domain; φ_b^i is due to the charged species accumulated at the boundaries. These two parts of the potential can be thought of, respectively, as the particular and homogeneous solutions to the Poisson equation $\nabla^2 \varphi = -\rho/\epsilon$.

To obtain the space charge potential ϕ_s^i , we can first compute the electric field E_s^i that corresponds to this potential at each z -plane. In the continuum limit:

$$E_s = -\frac{\partial \phi_s}{\partial z} \quad (2.5.11)$$

$$\epsilon \frac{\partial E_s}{\partial z} = \rho \quad (2.5.12)$$

The discrete value of E_s^i can be computed by summing the average charge densities over the planes:

$$E_s^i = \frac{h}{2\epsilon_i} \left(\sum_{k=0}^i \rho_k - \sum_{k=i+1}^N \rho_k \right) \quad (2.5.13)$$

where ρ_k is the average charge density in plane k , and h is the inter-plane spacing in the z direction ($h = a/\sqrt{3}$ for close-packed planes in an FCC lattice). The space charge potential ϕ_s^i can then be calculated by:

$$\phi_s^i = -h \sum_{j=0}^{i-1} E_j \quad (2.5.14)$$

To compute the potential due to surface charge, we denote the surface charge densities at the boundaries (e.g. anode and OHP) as ρ_{b1} and ρ_{b2} . Then the potential across the domain is

$$\phi_b^N = \frac{L}{2\epsilon} (\rho_{b2} - \rho_{b1}) \quad (2.5.15)$$

where L is the distance between boundaries. When the permittivity ϵ is variable, this must be solved from a numerically integrated Poisson equation:

$$\phi_b^i = \phi_b^N \left(\sum_{j=1}^N \frac{1}{\epsilon_j} \right)^{-1} \sum_{k=1}^i \frac{1}{\epsilon_k} \quad (2.5.16)$$

For a constant ϵ this simplifies to $\phi_b^i = \frac{i}{N} \phi_b^N$. The total potential at the z -plane i is therefore:

$$\phi^i = -h \sum_{j=0}^{i-1} E_j + \phi_b^N \left(\sum_{j=1}^N \frac{1}{\epsilon_j} \right)^{-1} \sum_{k=1}^i \frac{1}{\epsilon_k} \quad (2.5.17)$$

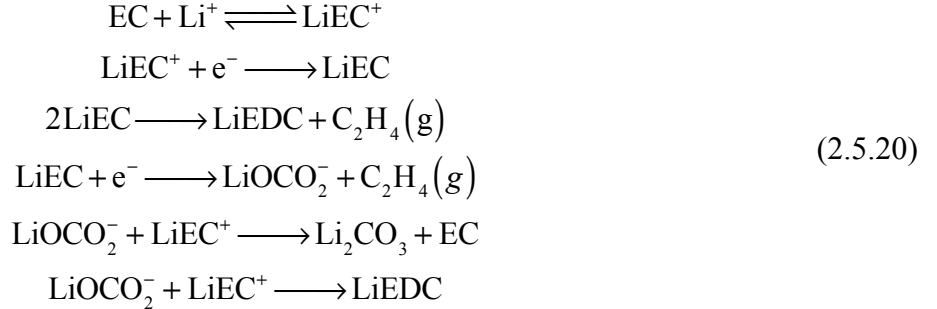
The effect of the potential on the motion of charged species, i.e. electromigration, is accounted for by computing the change in activation energy for a species hop from plane i to plane j . For a potential difference of $\Delta\phi^{ij} = \phi^j - \phi^i$, the activation energy is

$$\Delta E^{ij} = \Delta E_0^{ij} + \alpha q \Delta\phi^{ij} \quad (2.5.18)$$

where ΔE_0^{ij} is the diffusion energy barrier in the absence of an electric field, α is a symmetry factor taken as 1/2, and q is the charge of the diffusing species. Thus, the effect of the electric field on the event rate is modified by the electric field by a multiplicative factor on the electric field-free rate k_0 :

(2.5.19)

Chemical reactions The SEI reactions currently accounted for take place in the IHP, that is, at the sites neighboring the surface of the SEI:



In the model, reaction events involving two reactants are possible when reactants are present at neighboring sites in the IHP (reactions involving a single reactant and an electron are discussed below). If a reaction is possible, it may take place with a probability corresponding to a rate k , where in our simple initial model we take $k = 1.0$ for all reactions.

Reactions involving an electron transfer are assumed to be limited by electron tunneling across the SEI layer into the IHP. In our model, the rate of such a reaction decays exponentially with the distance from the carbon anode surface to the reaction site:

$$k_t = k_t^0 \exp^{-\ell/\ell_c} \tag{2.5.21}$$

Here, ℓ is the normal distance to the carbon anode surface and ℓ_c is a critical length scale that can be prescribed.

The LiEDC and Li_2CO_3 products in our model occupy both of the sites originally occupied by the reactants in the corresponding reaction. After the reaction takes place, these sites are converted to SEI material: SEI-organic for LiEDC, and SEI-inorganic for Li_2CO_3 . This results in growth of the SEI layer, after which neighboring sites may be newly identified as IHP or OHP.

2.5.2.2 KMC Simulation Results

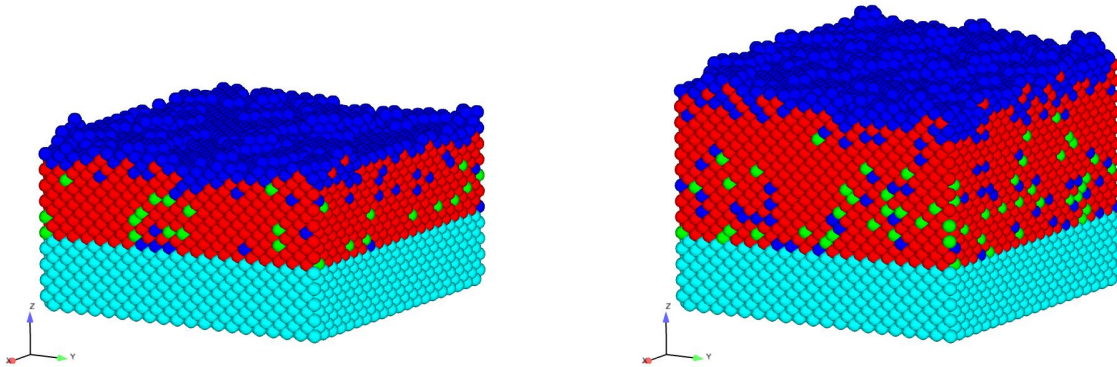


Figure 41: KMC simulation results at a nondimensional time of $t = 200$ for two different values of the tunneling length ℓ_c : (a) $\ell_c = a$, (b) $\ell_c = 2a$, where a is the unit cell size. In both figures, the light blue sites represent the carbon anode, red are the organic SEI, green are inorganic SEI, and blue are the IHP sites where surface reactions take place.

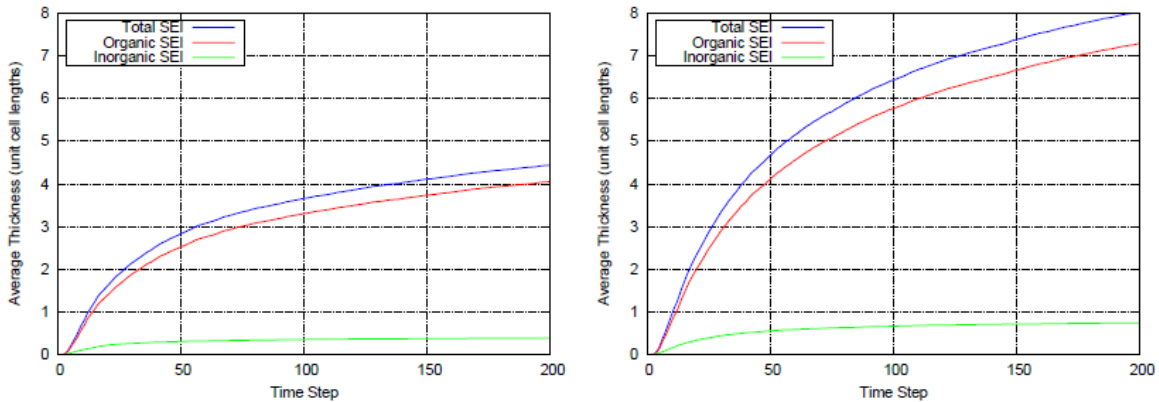


Figure 42: Average SEI layer thickness for two different values of the tunneling length ℓ_c : (a) $\ell_c = a$, (b) $\ell_c = 2a$

In the current version of the model implemented in SPPARKS, the electric field is not solved for a changing geometry, so that chemical reactions and electromigration are not included in the same simulation. In this section, we show typical results for a simulation of the growth of the SEI layer through chemical reaction.

Figure 41 shows the SEI layer at nondimensional time $t = 200$ for two different values of the electron tunneling length ℓ_c . A few observations are possible. First, the final layer thickness is obviously a function of the tunneling length, implying that transport of electrons through the layer to the growing SEI surface is the limiting step. Once the layer has become thick enough that electron tunneling is unlikely, layer growth slows (though it does not stop completely, as the

probability of electron transfer never goes completely to zero). Second, while inorganic SEI sites are sparse, they are more concentrated close to the anode surface. This is a consequence of the set of reactions in our model, in which two electron reductions are necessary to create inorganic SEI (Li_2CO_3), while only a single electron is needed to create organic SEI (LiEDC). Finally, we note that it is possible in this model for IHP sites to become “trapped” in the SEI. It is unclear whether this may be a possible mechanism for creating a porous SEI material structure.

Figure 42 shows the SEI growth curves vs. time for the same values of ℓ_c . The SEI thickness is computed by counting the total number of SEI sites in the simulation and computing the total volume of material. The red and green curves in the plots show the separate contributions from organic and inorganic SEI sites.

2.5.3 Phase Field Modeling of SEI Growth

Phase field models are mesoscale continuum models in which the interface is diffuse, such that material properties vary smoothly but rapidly across it. In contrast with sharp interface models, one or more phase field variables are added to phase field models to distinguish different phases. In the phase field model for SEI growth used in this study, we consider two bulk phases (SEI phase and electrolyte phase) in the domain, and use one phase field variable η to describe the material phase such that $\eta = 1$ in the SEI phase, $\eta = 0$ in the electrolyte phase, and $0 < \eta < 1$ in the SEI/electrolyte interfacial region. Five species are considered in the system: electrons e^- , lithium ions Li^+ , organic solvent M, SEI component N and an anion A^- , where Li^+ and A^- make up a lithium salt in the electrolyte. The mole fraction and mole concentration of these species are denoted by X_1, \dots, X_n and c_1, \dots, c_n , respectively, where $n = 5$ is the number of species. As in (Guyer, Boettinger et al. 2004), we treat electrons ($i = 1$) as interstitials with zero volume, and all other species (ions and neutral atoms) are substitutional species with identical molar volume Ω .

The molar volume at each spatial point is then given by $V_m = \Omega \sum_{i=2}^n X_i$. The molar concentration of each species is defined as $c_i = X_i / V_m$, and it follows that the concentrations of substitutional species are constrained by $\sum_{i=2}^n c_i = 1 / \Omega$.

In order to derive the evolution equations of species concentrations c_i and phase field η , we first construct the free energy functional of the system. Following the expression in (Guyer, Boettinger et al. 2004), the free energy functional of the system can be written as

$$f(\{c_i\}, \eta) = \int_V \left(f_b(\{c_i\}, \eta) + \frac{1}{2} \varepsilon |\nabla \eta|^2 + \frac{1}{2} \rho \phi \right) dV \quad (2.5.22)$$

which consists of the contributions from bulk energy, interfacial energy and electrostatic energy. In Eq. (2.5.22), ε is the gradient coefficient related to the thickness and energy of the diffuse interface, ϕ is the electric potential, and ρ is the charge density such that $\rho = F \sum_{i=1}^n z_i c_i$, where F is Faraday’s constant and z_i is the valence of species i . The bulk energy density is expressed as

$$f_b(\{c_i\}, \eta) = \sum c_i \left[\mu_i^{0\alpha} h(\eta) + \mu_i^{0\beta} (1 - h(\eta)) + RT \ln X_i + W_i g(\eta) \right], \quad (2.5.23)$$

where α and β denote SEI phase and electrolyte phase, respectively, and $\mu_i^{0\alpha}$ and $\mu_i^{0\beta}$ are the chemical potentials of pure component i in the respective phases. In Eq. (2.5.27), $h(\eta) = \eta^3(6\eta^2 - 15\eta + 10)$ is an interpolation function that satisfies $h(1) = 1$ and $h(0) = 0$. The entropy of mixing term is given by $RT \ln X_i$, where R is the gas constant and T is the temperature. A double-well function $g(\eta) = \eta^2(1 - \eta)^2$ keeps the interface from smoothing out, and W_i is the energy coefficient characterizing the energy barrier of species i moving across the interface.

Substituting Eq. (2.5.22) into Eq. (2.5.23) we get the full expression of the free energy functional of the system. Based on that, the evolution equations of the conserved variables c_i and non-conserved variable η can be written as

$$\begin{aligned}\frac{\partial c_1}{\partial t} &= \nabla \cdot (M_1 \nabla \bar{\mu}_1) + s_1 \\ \frac{\partial c_i}{\partial t} &= \nabla \cdot (M_i \nabla (\bar{\mu}_i - \bar{\mu}_1)) + s_i, \quad (i = 2, K, n) \\ \frac{\partial \eta}{\partial t} &= -L \frac{\delta f}{\delta \eta} = L \left(\epsilon \nabla^2 \eta - \frac{\partial f_b}{\partial \eta} \right)\end{aligned}\tag{2.5.24}$$

where $\bar{\mu}_i$ is the electrochemical potential of species i given by

$$\bar{\mu}_i = \frac{\delta f}{\delta c_i} = \frac{\partial f_b}{\partial c_i} + F\phi z_i, \quad (i = 1, K, n)\tag{2.5.25}$$

It is noted that substitutional species follow different governing equations compared with electrons since they are constrained by the volume conservation. Because of this conservation, we only need to solve for the concentrations of electrons and $n - 2$ substitutional species, and the concentration of the last substitutional species can then be obtained from $\sum_{i=2}^n c_i = 1/\Omega$. In Eqs. (2.5.24), L is the mobility coefficient of the interface, and M_i is the mobility coefficient of species i , which are related to the diffusivity of species i through

$$\begin{aligned}M_1 &= \frac{D_1(1 + \Omega c_1)c_1}{RT} \\ M_i &= \frac{D_i c_i c_n}{RT(c_i + c_n)}\end{aligned}\tag{2.5.26}$$

The electric potential ϕ is obtained from the Poisson equation:

$$\sigma \nabla^2 \phi + \rho = 0\tag{2.5.27}$$

where σ is the dielectric constant. The Poisson equation is used to solve for ϕ since the simulation domain in this work includes the entire interfacial region, and therefore electroneutrality cannot be assumed. Eq. (2.5.27) closes the governing equations of c_i and η .

The source term s_i in Eqs. (2.5.24) represents the generation or consumption of species i due to SEI formation reactions. The detailed SEI chemistry is not included here; instead, we use a simplified global reaction corresponding to SEI formation:



From the reaction (2.5.28) we can write the source term as

$$s_i = \nu_i R g(\eta) \quad (2.5.29)$$

where ν_i is the stoichiometric coefficient of species i in the reaction (2.5.28) such that $\nu_{\text{Li}^+} = \nu_{\text{e}^-} = \nu_{\text{M}} = -1$ and $\nu_{\text{N}} = 2$. The double-well function $g(\eta)$ constraints the reaction to occur only within the SEI/electrolyte interfacial region. R is the net rate of the SEI formation reaction, and its value can be obtained from the Butler-Volmer kinetics (Bockris 2001) such that

$$R = k_f c_{\text{Li}^+} c_{\text{e}^-} c_{\text{M}} \exp\left(-\frac{\alpha z F \Delta\phi}{RT}\right) - k_b c_{\text{N}}^2 \exp\left(\frac{(1-\alpha) z F \Delta\phi}{RT}\right) \quad (2.5.30)$$

where k_f and k_b are the rates of forward and backward reaction in (2.5.28), respectively, α is the symmetry factor, z is the number of charge transferred in the reaction, and $\Delta\phi$ is the electric potential difference in two phases. Since $z = 1$, by assuming $\alpha = 0.5$ we can rewrite Eq. (2.5.30) as

$$R = k \sqrt{c_{\text{Li}^+} c_{\text{e}^-} c_{\text{M}} c_{\text{N}}^2} \left[\exp\left(-\frac{F\eta_g}{2RT}\right) - \exp\left(\frac{F\eta_g}{2RT}\right) \right] \quad (2.5.31)$$

Where $k = \sqrt{k_f k_b}$ and $\eta_g = \Delta\phi - \Delta\phi_e$ is the overpotential. Note that, in contrast with sharp interface models, the concentrations of species vary across the diffuse interface in the phase field model. As such, the SEI formation reaction (2.5.31) is not strictly heterogeneous, and moreover, the overpotential η_g is not a constant and depends on the concentrations of species. The dependence of the overpotential on concentration is investigated by Bazant *et al.* (Bai, Cogswell et al. 2011; Cogswell and Bazant 2012), where the generalized Butler-Volmer kinetics is derived such that the overpotential is determined by the change in total electrochemical potential of the charge transfer reaction per charge transferred. In this case, the driving force for the charge transfer reaction is not the pure electric potential difference, but the difference in the total electrochemical potential. Following the derivation in (Bai, Cogswell et al. 2011; Cogswell and Bazant 2012), we may write the overpotential for the SEI formation reaction (2.5.33) as

$$\eta_g = \frac{2\bar{\mu}_{\text{N}} - (\bar{\mu}_{\text{Li}^+} + \bar{\mu}_{\text{e}^-} + \bar{\mu}_{\text{M}})}{zF} = \frac{2\bar{\mu}_{\text{N}} - (\bar{\mu}_{\text{Li}^+} + \bar{\mu}_{\text{e}^-} + \bar{\mu}_{\text{M}})}{F} \quad (2.5.32)$$

From Eqs. (2.5.31) and (2.5.32) we can see that $R > 0$ (i.e., SEI forms) when $2\bar{\mu}_{\text{N}} < \bar{\mu}_{\text{Li}^+} + \bar{\mu}_{\text{e}^-} + \bar{\mu}_{\text{M}}$, and *vice versa*. It is noted that in reality, the SEI formation is a complex process that involves multiple elementary reactions, and some of them may be irreversible, so the relation between the reaction rate and the concentration and electric potential goes beyond the single step Butler-Volmer kinetics. The incorporation of the detailed SEI chemistry is left for the future work.

Eqs. (2.5.24)-(2.5.27), (2.5.29), (2.5.31)-(2.5.32) comprise the phase field model of SEI growth. The boundary conditions for c_i and η are fixed c_i and $\nabla\phi = 0$ at boundaries. For the electric potential ϕ , we set $\phi = 0$ at the electrolyte boundary. At the electrode boundary, ϕ is determined by the applied current density i_a such that the fluxes of charged species, J_i , satisfies

$$i_a = F \sum_{i=1}^n z_i J_i.$$

Before closing this section, it is worthwhile to compare the phase field model of SEI growth with the Poisson- Nernst-Planck (PNP) equations (sharp interface model) that are widely applied in analysis of electrochemical systems. Both models capture the diffusion and electromigration of species, and solve Poisson's equation to get the electric potential. The main difference lies in the transport of species across the interface. In the sharp interface model, the PNP equations are solved at each bulk phase (i.e., SEI phase and electrolyte phase) separately, and species move across the SEI/electrolyte interface through the SEI formation reactions or other charge transfer reactions. These reactions are heterogeneous and occur only at the interface. The rates of these reactions determine the fluxes of species across the interface, which give the boundary conditions for the PNP equations. In the phase field model, the SEI/electrolyte interface is diffuse, and the model is solved in the whole domain including two bulk phases and the interfacial region. No boundary condition is needed at the diffuse interface since the species move across the interface naturally according to the nonequilibrium thermodynamics. Because of the diffuse interface, the SEI formation reactions are not strictly heterogeneous, and the fluxes of species through the interface are not only due to SEI formation reactions, but also driven by diffusion and electromigration. The full comparison of the performance of the phase field model and PNP equations is beyond the scope of this work. It will be shown later that the effect of diffuse interface on the kinetics of species across the interface is minor since SEI growth (i.e., interface motion) is dominated by SEI formation reactions rather than diffusion or electromigration of species.

2.5.3.1 Numerical Simulation

The phase field model developed in the previous section is solved to capture SEI growth using the finite difference method implicitly. At each time step, we first solve Eq. (2.5.27) to get the electric potential ϕ , and then update concentrations c_i and phase field η according to Eqs (2.5.24). In the simulation, we assume that the SEI phase mainly consists of Li^+ , e^- and N, and the electrolyte phase mainly contains Li^+ , M and A^- . The equilibrium fractions of each species in each phase are given in Table 5. Note that the fraction of electro-inactive species is set to be 10^{-6} rather than 0 for the sake of computational convenience.

Table 5: Initial concentrations X_i in bulk phases

	α (SEI)	β (Electrolyte)
e^-	$0.1 \cdot 10^{-6}$	10^{-6}
Li^+	0.1	0.05
N	$0.8 \cdot 10^{-6}$	10^{-6}
M	10^{-6}	$0.9 \cdot 10^{-6}$
A^-	10^{-6}	$0.05 \cdot 10^{-6}$

The equilibrium fraction of each species is its initial fraction in the simulations and these satisfy the electroneutrality condition in both phases. The equilibrium condition is achieved when the electrochemical potential of each species is the same in two phases, i.e., $\bar{\mu}_i^\alpha = \bar{\mu}_i^\beta$, so the equilibrium fraction of each species is related to its standard chemical potential through

$$\Delta\mu_i^0 = \mu_i^{0\alpha} - \mu_i^{0\beta} = RT \ln\left(\frac{X_i^{0\beta}}{X_i^{0\alpha}}\right) - Fz_i\Delta\phi^0 \quad (2.5.33)$$

where $\Delta\phi^0 = \phi_0^\alpha - \phi_0^\beta$ is the electric potential difference between the two phases when they are in equilibrium. $\Delta\phi^0$ is a material property depending on the choice of electrode and electrolyte.

The default values of parameters are: $T = 298$ K, $\Omega = 10^{-5}$ m²/s, $W_l = 0$, $W_i = 3.6 \times 10^5$ J/mol ($i = 2, \dots, n$), $\varepsilon = 3.6 \times 10^{-11}$ J/m, $D_l = 10^{-14}$ m²/s, $D_i = 10^{-9}$ m²/s ($i = 2, \dots, n$), $L = 10^{-2}$ m³/(J·s), $\sigma = 7.083 \times 10^{-11}$ F/m, $k = 2.5$ m^{4.5}/(mol^{1.5} · s), $\Delta\phi_0 = -0.1$ V, $i_a = 0$. Unless specified explicitly, default values of the parameters are used in all simulations. The initial SEI thickness is set to be 0.25 nm, and we assume the SEI layer is compact during its growth. In each simulation, we first let the system approach equilibrium without activating SEI formation reactions, after which we activate SEI formation reactions to capture the SEI growth.

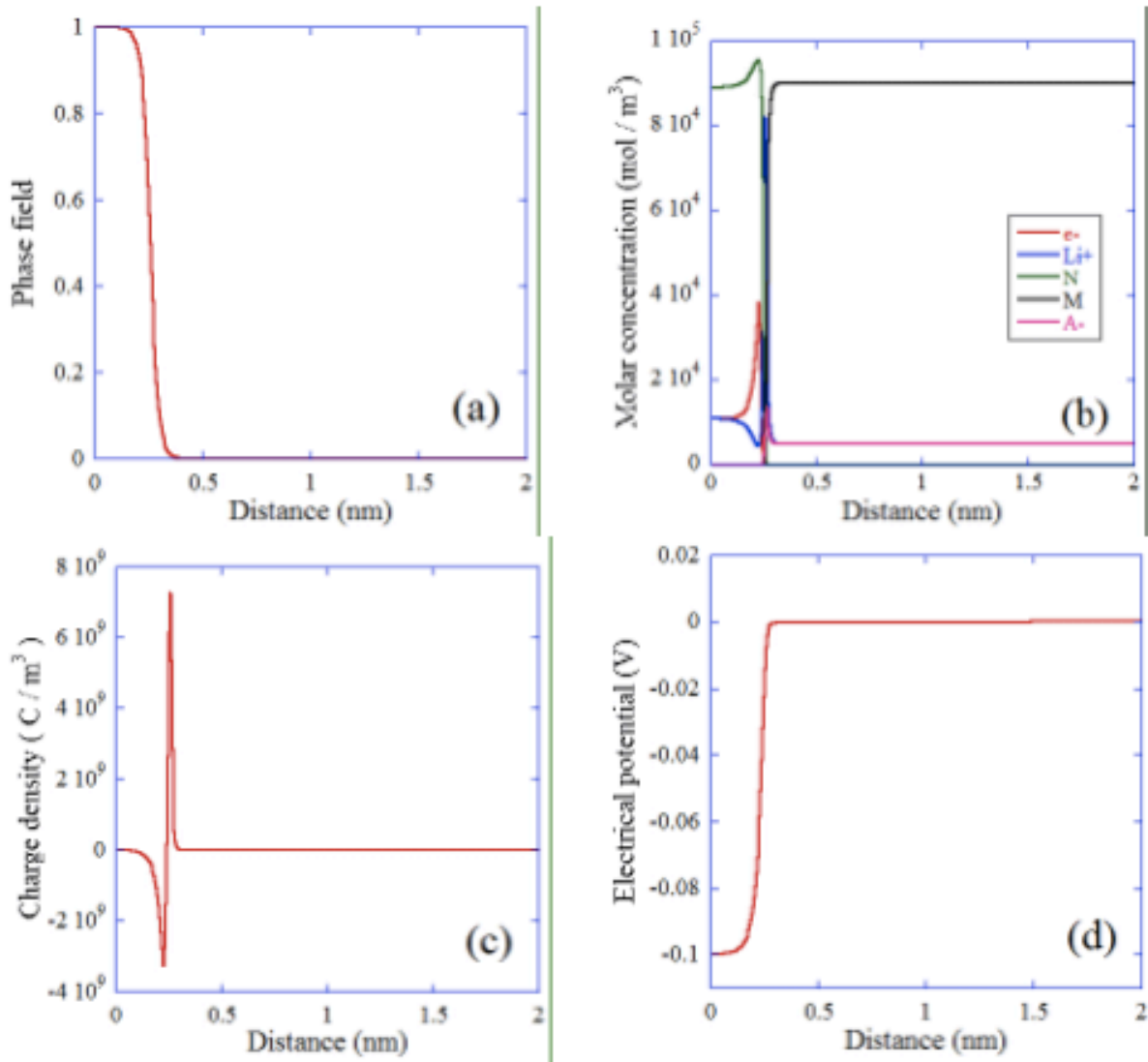


Figure 43: Distribution of (a) phase field, (b) concentrations of species, (c) charge density and (d) electric potential at equilibrium state.

Figure 43 shows the distribution of phase field, concentrations of species, charge density and electric potential at the equilibrium state. Figure 43a shows the phase field η , with $\eta = 1$ and 0 in the SEI and electrolyte phases, respectively. In the SEI/electrolyte interfacial region, η changes smoothly from 1 to 0. The concentration distribution of each species is given in Figure 43b, which shows that the concentrations in the bulk phases are constant, and they change rapidly but smoothly in the interfacial region. In particular, it is found that electrons are driven toward the SEI surface and therefore have a peak concentration at the left side of the interface. Because of the Coulomb force, the lithium ion concentration has a corresponding peak at the right side of the interface. Because of this distribution of charged species, the charge density across the interfacial

region is first negative and then positive before approaching zero in the bulk region, see Figure 43c. This demonstrates that the charge separation and the double-layer structure at the interface are well captured by the current model. Figure 43d gives the distribution of the electric potential. It clearly shows that the electric potential difference in two phases at equilibrium equals $\Delta\phi_0$, which is consistent with the Nernst equation since the initial fraction of each species is its equilibrium fraction.

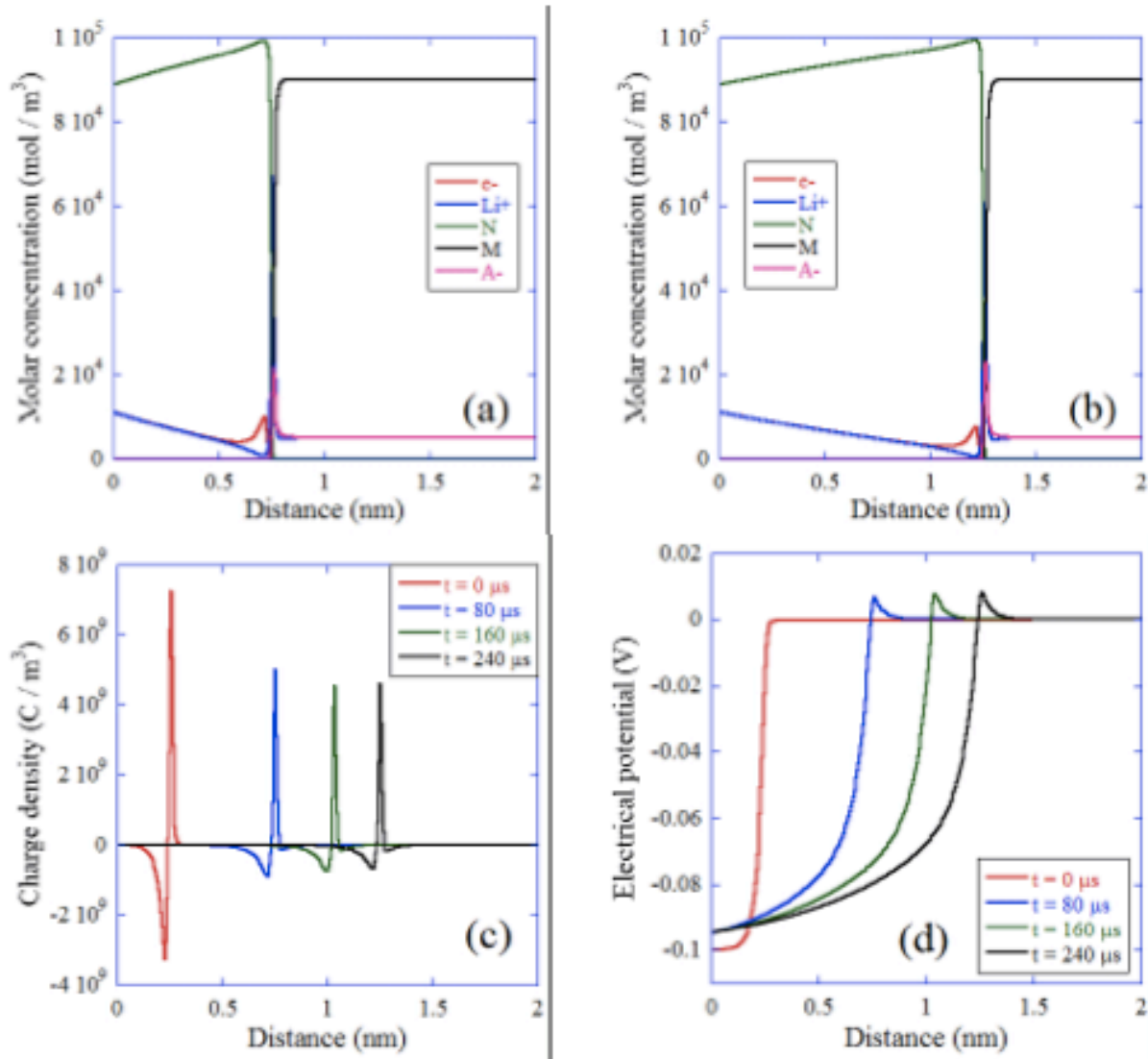


Figure 44: Concentrations of species at (a) 80 μs and (b) 240 μs; Distribution of (c) charge density and (d) electric potential at different time.

After the equilibrium state shown in Figure 43 is reached, the SEI formation reaction is activated to capture the SEI growth. Figure 44 a and b give the distribution of concentrations of all species at different time during SEI growth. The SEI/electrolyte interface moves towards the electrolyte phase after the SEI formation reaction is activated, which indicates that the SEI layer starts to

grow. Moreover, it is found that during SEI growth, the concentrations of Li^+ and e^- in the SEI bulk region are no longer constants, but a linearly decreasing function of distance from the SEI boundary. This concentration distribution reveals that the interface motion (i.e., SEI growth) is controlled by the diffusion of species. It is also found that as time increases, the concentrations of Li^+ and e^- at the interfacial region decrease. This trend is better captured by the evolution of charge density distribution shown in Figure 44c. It can be seen that as SEI grows, the charge separation remains, but with a decreasing charge density at the interface. The decrease of interfacial charge density reduces the SEI growth rate, as will be shown later. Figure 44d illustrates the evolution of electric potential distribution, which shows that in addition to a concentration gradient, an electric potential gradient is also built inside of SEI during its growth. In particular, since the electron diffusivity is very low, in order to keep electroneutrality in the SEI bulk region, the electric potential gradient in SEI is positive to assist the transport of electrons. The variation of electric potential and concentration of charged species in SEI observed in the current model agrees with the results obtained from the sharp interface model (Christensen and Newman 2004; Colclasure, Smith et al. 2011).

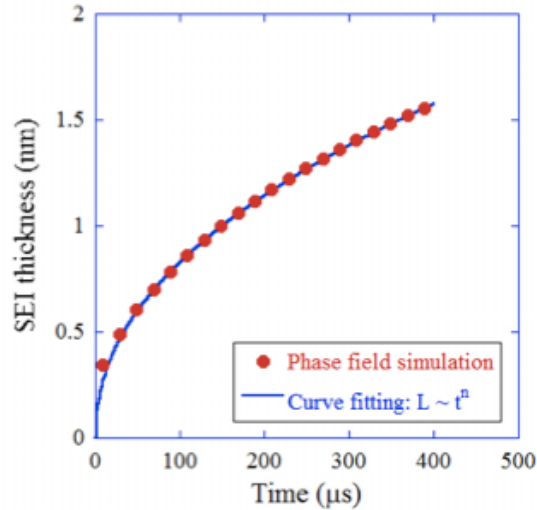


Figure 45: SEI thickness as a function of time.

The time evolution of SEI thickness is shown in Figure 45, from which we can see that at the beginning, SEI grows quickly since the concentration of charged species at the interface is high. As time increases, SEI growth rate decreases due to the decreased availability of electrons at the interface. The SEI thickness exhibits a power-law scaling with respect to time, where the exponent is close to 0.5. This growth law demonstrates that SEI growth is a diffusion-limited process. In order to see the dependence of SEI growth on the diffusion of charged species, the effect of electron diffusivity D_{e^-} on SEI growth and electric potential distribution is shown in Figure 46 a-b. It can be seen that SEI growth is very sensitive to D_{e^-} such that increasing D_{e^-} increases SEI growth rate considerably. Moreover, higher D_{e^-} corresponds to lower electric potential gradient in SEI since electrons with high diffusivity do not need a high electric potential gradient to assist their transport through SEI. In contrast, varying SEI formation reaction rate has only a minor effect on SEI growth and electric potential distribution, as shown

in Figure 46c-d. Therefore, high sensitivity of the SEI growth rate on D_{e^-} confirms that electron diffusion is the rate determining step for SEI growth.

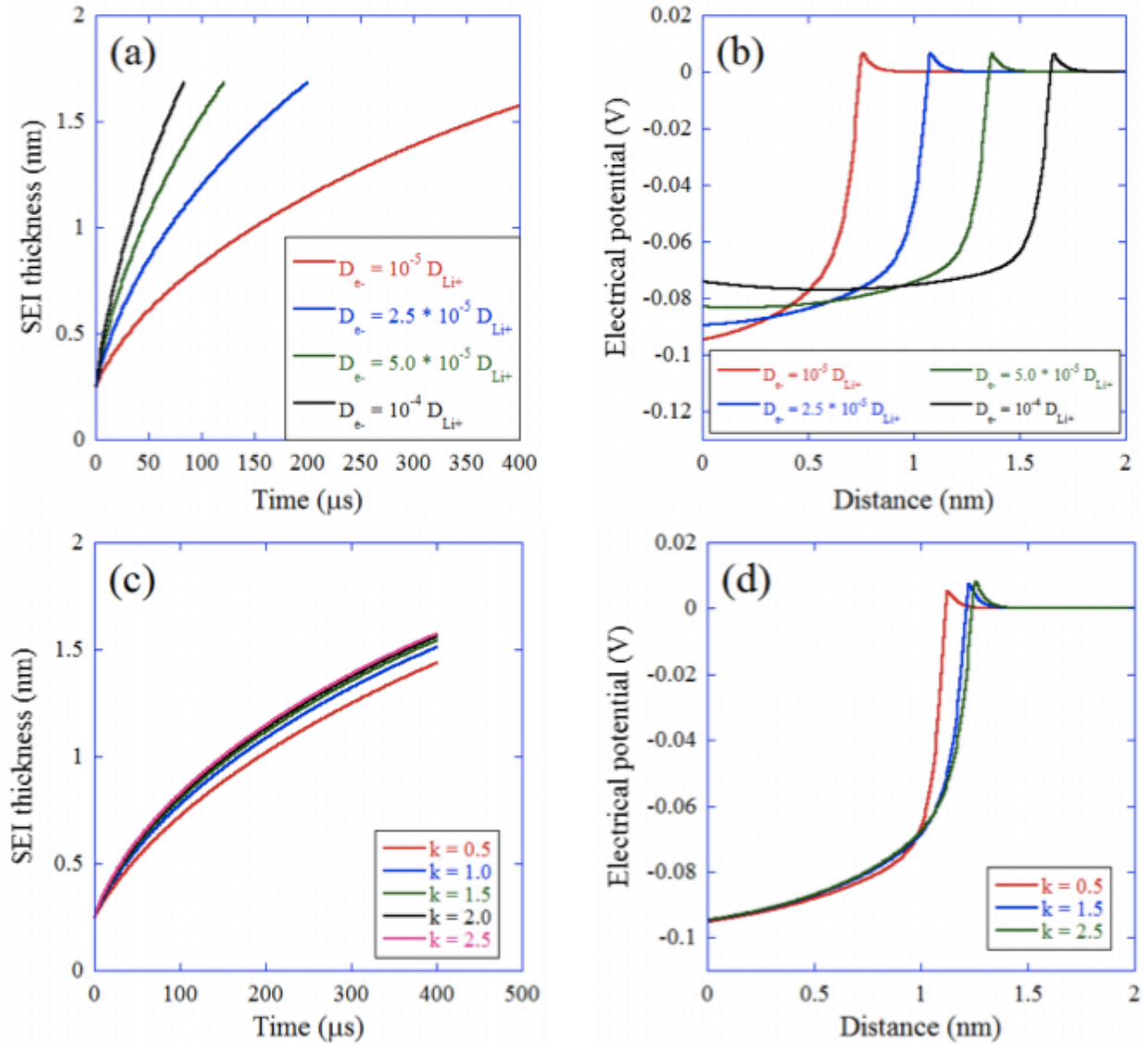


Figure 46: (a) SEI growth and (b) distribution of electric potential at time 80 μ s under different electron diffusivity; (c) SEI growth and (d) distribution of electric potential at time 240 μ s with different SEI formation reaction rate.

In addition to electron diffusivity and SEI formation reaction rate, the effects of other relevant material properties and conditions such as initial Li^+ fraction, equilibrium electric potential difference, applied current density and temperature on SEI growth are also investigated. The initial Li^+ fraction in SEI, $X_{Li^+}^{\alpha}$, can be related to the initial state of charge in the anode since the SEI is very thin at the beginning. Figure 47a-d illustrate the SEI growth, the distribution of electric potential and concentration of Li^+ and e^- under different $X_{Li^+}^{\alpha}$. In these simulations, the

initial electron fraction in SEI changes as $X_{\text{Li}^+}^\alpha$ varies in order to keep electroneutrality in SEI bulk phase. From Figure 47c-d we can see that the concentration gradient of Li^+ and e^- in SEI increases as $X_{\text{Li}^+}^\alpha$ increases. This is because c_{Li^+} and c_{e^-} at the SEI boundary (SEI/anode interface) remain the same as their initial values, and at the SEI/electrolyte interface, the fast SEI formation reaction drives c_{Li^+} and c_{e^-} to approach zero. A higher concentration gradient induces more flux of charged species moving through the SEI phase, which increases the SEI growth rate as shown in Figure 47a. Moreover, since electrons are driven more by diffusion under higher concentration gradient, the electric potential gradient in SEI decreases as $X_{\text{Li}^+}^\alpha$ increases, see Figure 47b. It is noted that the electric potential at the SEI boundary is nearly independent of $X_{\text{Li}^+}^\alpha$, and the effect of the initial state of charge on the electric potential at the SEI/anode interface is neglected in the current model. This effect will be considered in the future when the Li^+ concentration and electric potential in the anode are taken into account.

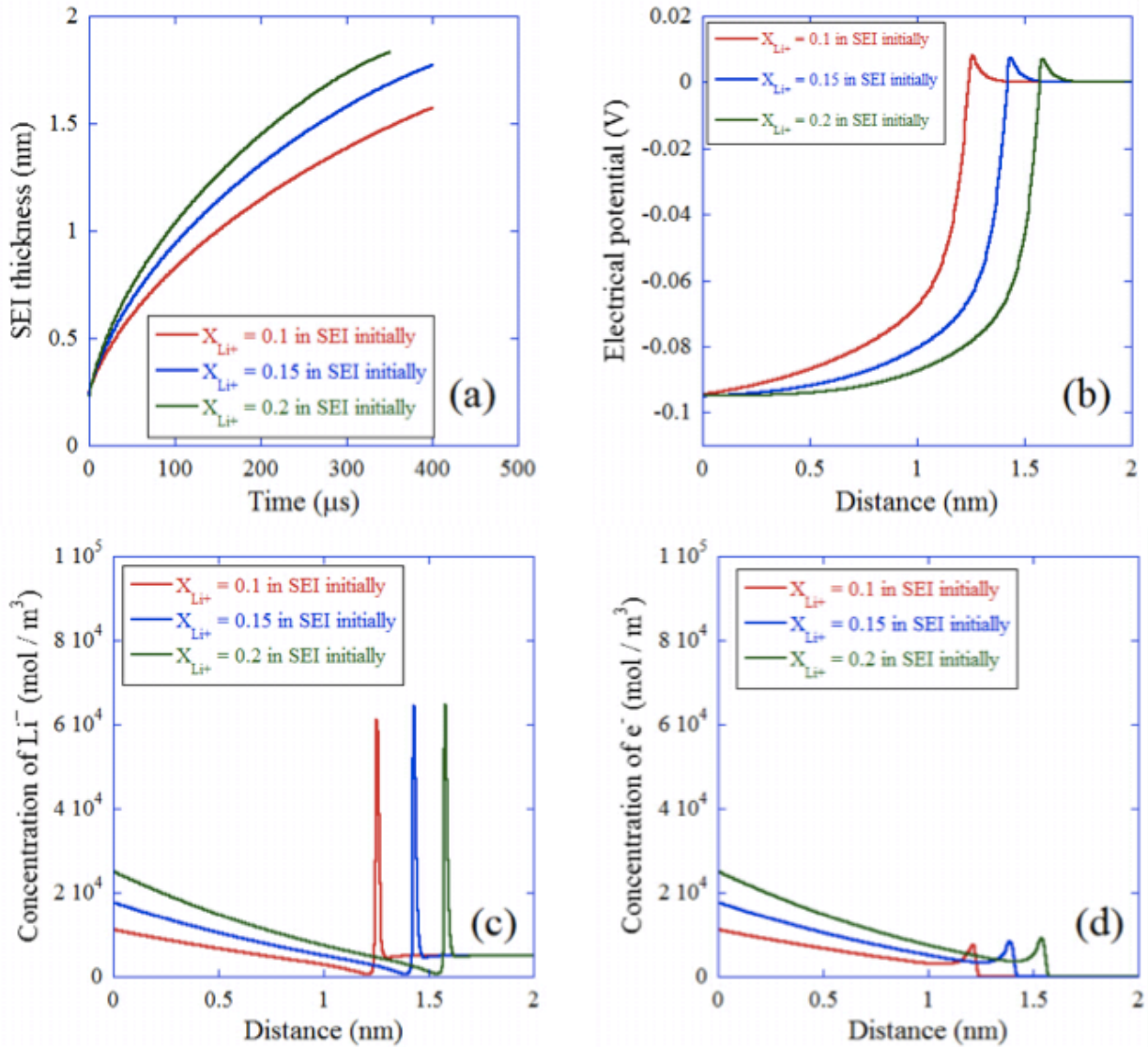


Figure 47: (a) SEI growth and distribution of (b) electric potential, (c) Li⁺ concentration and (d) e⁻ concentration at time 240 μs with different initial Li⁺ and e⁻ concentration in SEI.

The equilibrium electric potential difference between the two phases, $\Delta\phi_0$, is another important material property that depends on the selection of electrode and electrolyte. It is the potential-dependent portion of the chemical potential difference between two phases. Figure 48a gives the distribution of electric potential at equilibrium with different $\Delta\phi_0$. It can be seen that the electric potential difference between two phases equals $\Delta\phi_0$ at equilibrium, which is consistent with the Nernst equation. $\Delta\phi_0$ affects the charge density distribution as well. As shown in Figure 48b, when $\Delta\phi_0$ increases, the charge density at the left (right) side of interface becomes more negative (positive). This is because higher $\Delta\phi_0$ drives more e⁻ moving to and more Li⁺ moving away from the SEI/electrolyte interface, and then the concentration of e⁻ and Li⁺ at the left side of interface

increases and decreases, respectively, resulting more negative charge density. Moreover, higher e^- concentration attracts more Li^+ to the SEI surface and repels A^- from the SEI surface so that the charge density at the right side of interface increases. The effect of $\Delta\phi_0$ on the distribution of electric potential and charge density remains during SEI growth, see Figure 49a-c. It is found that the electric potential difference between the two phases during SEI growth increases as $\Delta\phi_0$ increases, while the electric potential gradient within the SEI is nearly the same when $\Delta\phi_0$ varies. The charge density distribution during SEI growth exhibits the same dependence of $\Delta\phi_0$ as at equilibrium. It is also found that the SEI growth rate increases slightly as $\Delta\phi_0$ increases due to higher e^- concentration at the interfacial region.

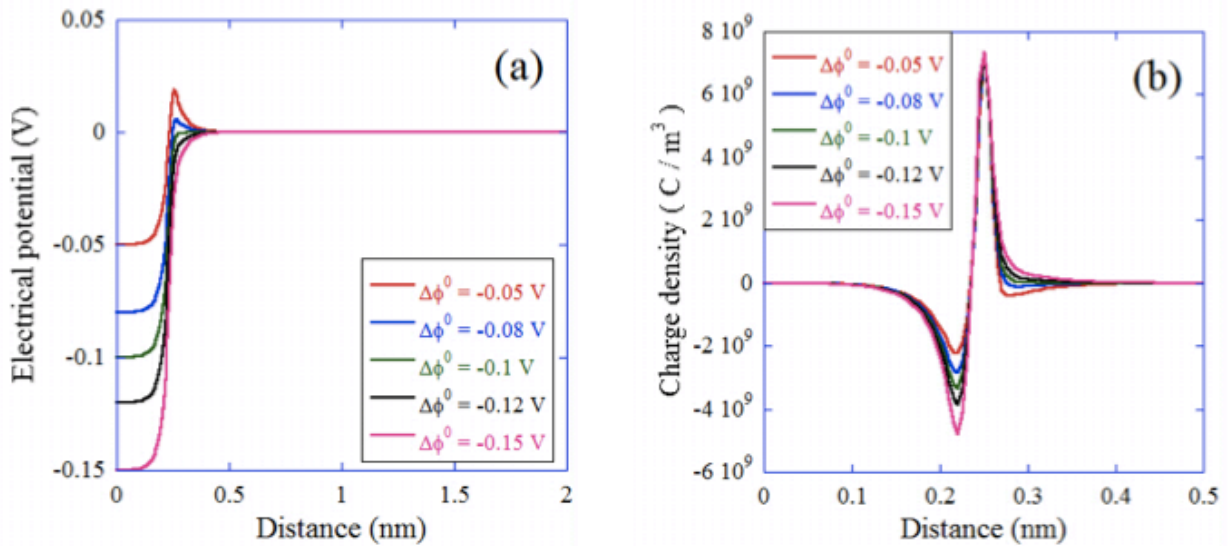


Figure 48: Distribution of (a) electric potential and (b) charge density at equilibrium state with different $\Delta\phi_0$.

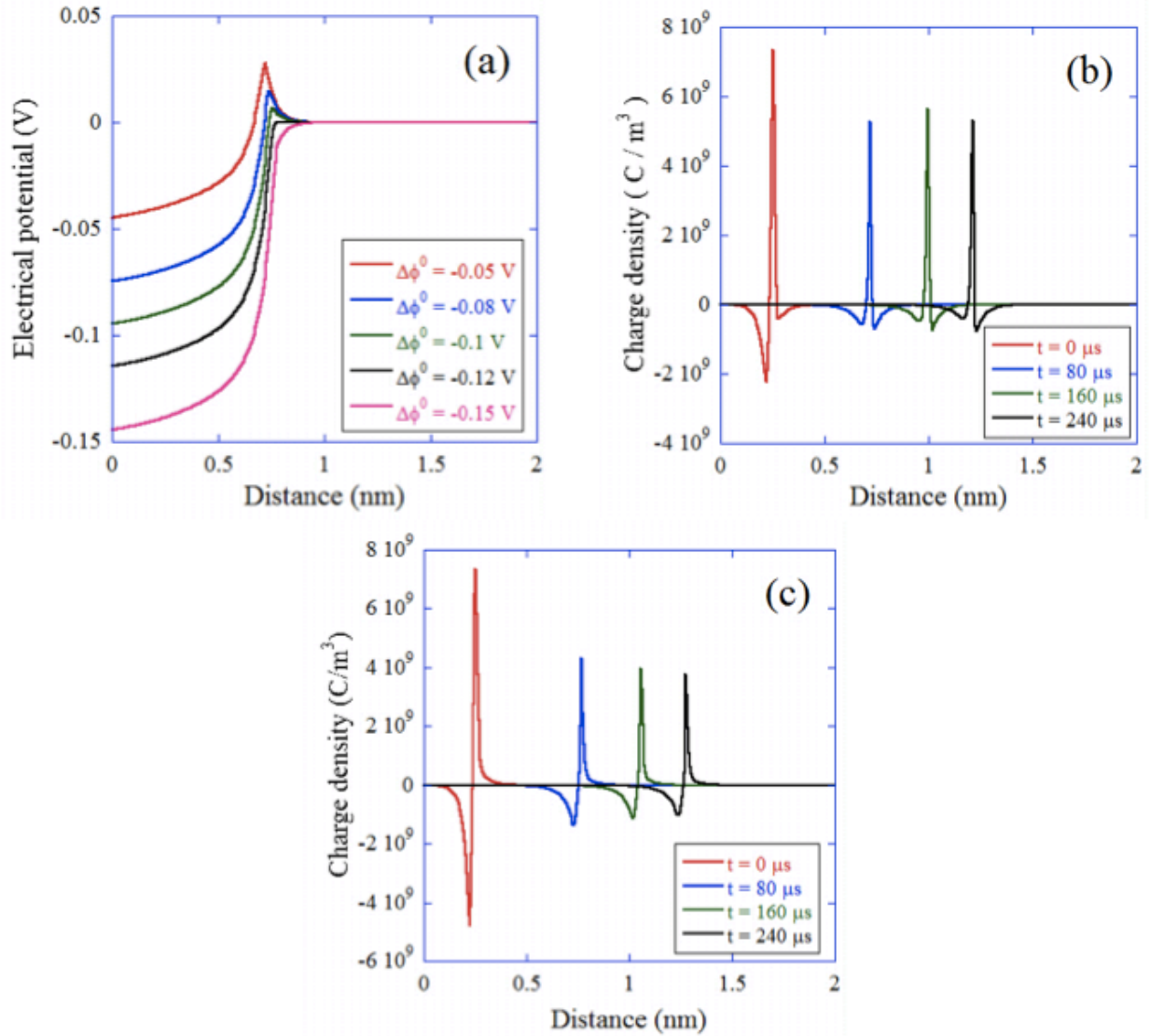


Figure 49: (a) Distribution of electric potential at time $80 \mu\text{s}$ with different $\Delta\phi_0$; (b) Charge density distribution at different time when $\Delta\phi_0$ is -0.05 V and (c) -0.15 V .

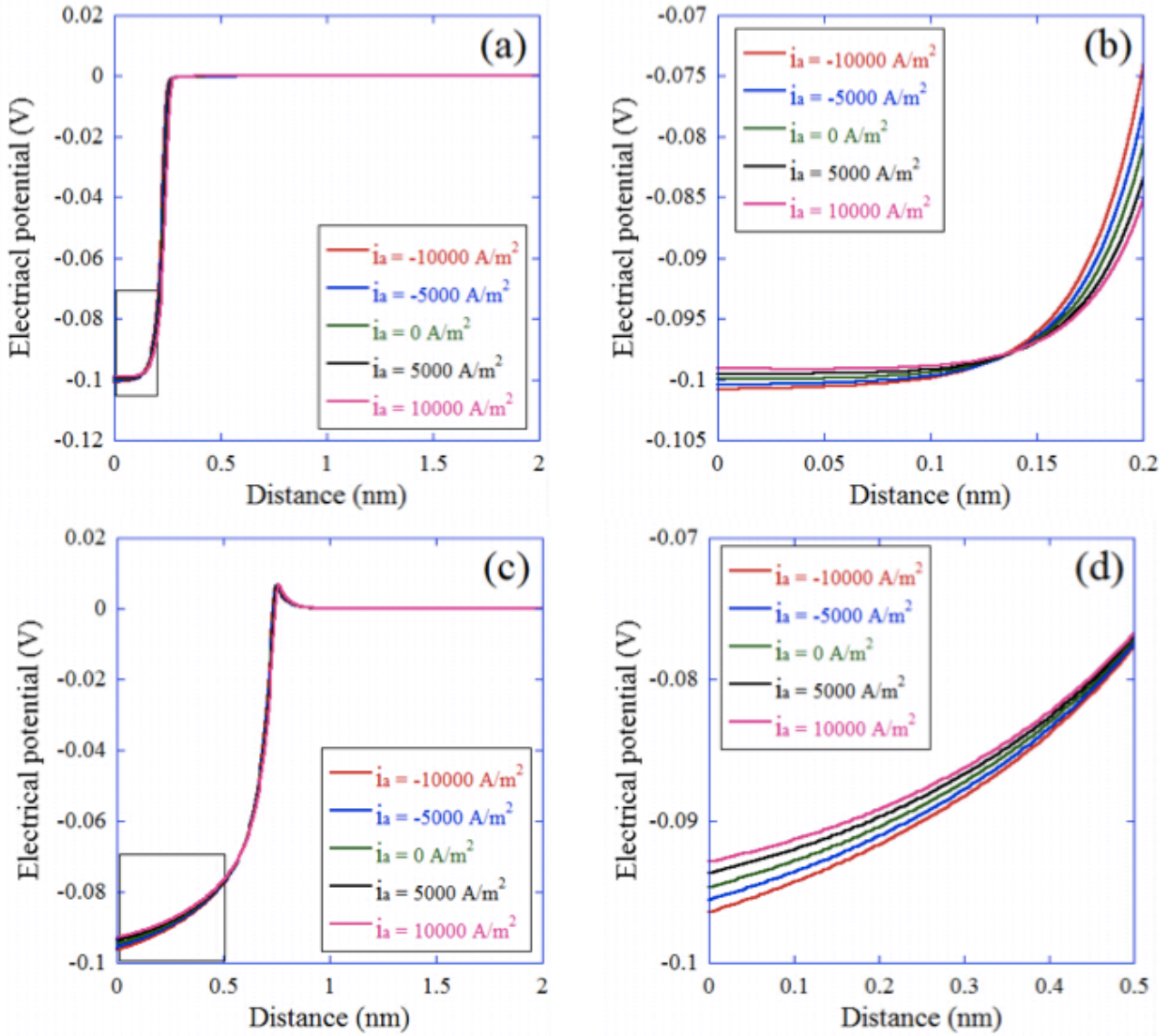


Figure 50: Distribution of electric potential at (a, b) time 0 and (c, d) time 80 μs under different applied current density. (b) and (d) illustrate the electric potential distribution in the region enclosed by the rectangular box shown in (a) and (c), respectively.

The above simulations correspond to the open-circuit case with zero current density i_a . In order to examine the behavior of SEI growth during a charge or discharge process, SEI growth under nonzero i_a is investigated. Figure 50a-d show the electric potential distribution at different time during SEI growth with different i_a . Although the SEI growth rate is nearly independent of i_a , it is found that the electric potential gradient in SEI changes as i_a varies. In particular, during the charging process ($i_a < 0$), the electric potential gradient in the SEI is higher than in the open-circuit case, and the transport of Li^+ due to electrical potential gradient is larger than the transport of Li^+ because of the concentration gradient. As a consequence, the net flux of Li^+

moves from the SEI/electrolyte interface to the SEI/anode interface. During the discharge process ($i_a > 0$), the net flux of Li^+ moves in an opposite direction since the transport of Li^+ is dominated by the concentration gradient. This dependence of the electric potential gradient on the charge/discharge process agrees with the observations in (Colclasure, Smith et al. 2011). It is also found that the overpotential, $\eta_0 = \Delta\phi - \Delta\phi_e$, depends on i_a , where $\Delta\phi$ is the difference between the electric potential at the electrolyte and at SEI/anode interface; $\Delta\phi_e = \Delta\phi$ when $i_a = 0$. The relation between η_0 and i_a at different times is shown in Figure 51a. It can be seen that i_a is linearly dependent on η_0 during SEI growth. This is consistent with the Tafel equation under small η_0 , $i_a = i_0 n F \eta_0 / RT$, where i_0 is the exchange current density. Moreover, the ratio $i_a / \eta_0 = i_0 n F / RT$ is found to decrease as time increases. This trend is clearly seen in Figure 51b, which shows that the exchange current density decreases as time increases; this indicates that the charge transfer rate decreases as the SEI becomes thicker, which is consistent with previous results that the charge density at the interface decreases as SEI grows.

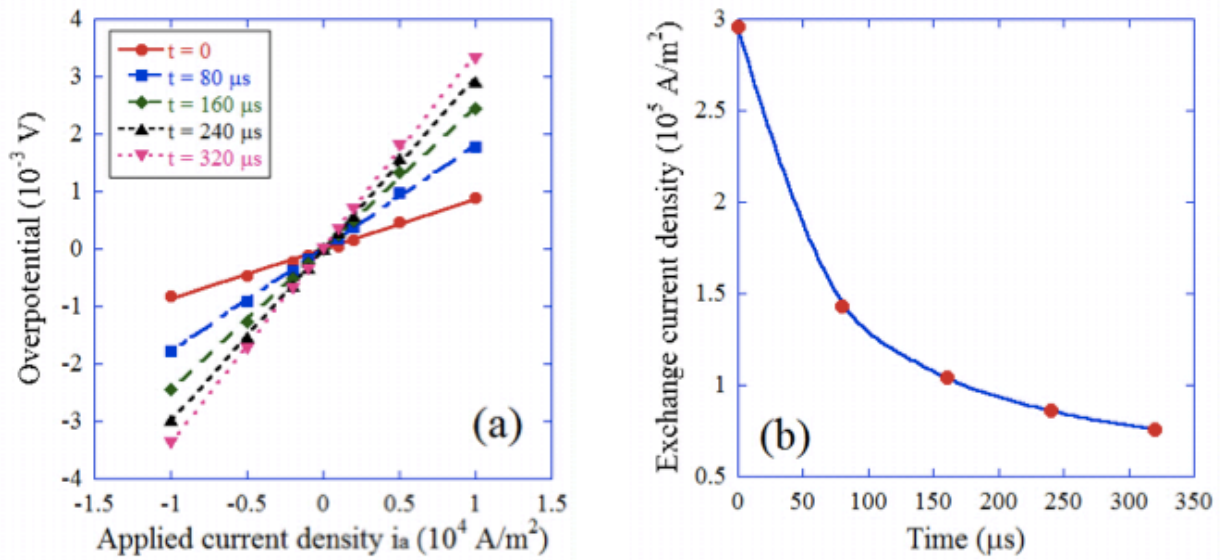


Figure 51: (a) Overpotential as a function of applied current density at different time; (b) Evolution of exchange current density during SEI growth.

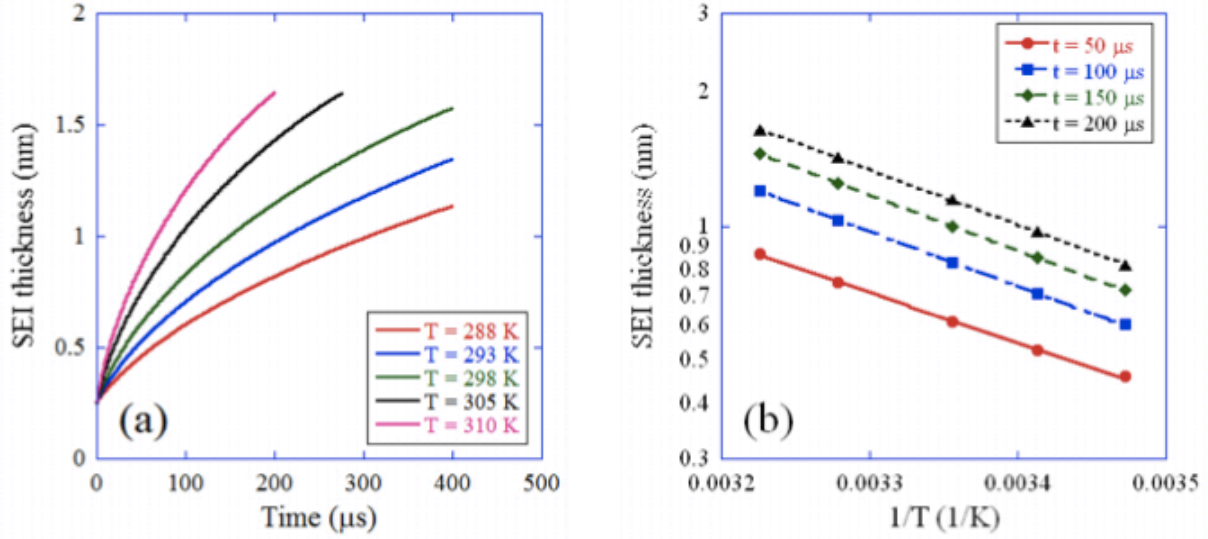


Figure 52: (a) SEI growth under different temperature; (b) SEI thickness as a function of temperature at different time.

As diffusion, electromigration and electrochemical reactions are all thermally-activated processes, temperature is an important factor that affects the SEI growth rate. Similar to the assumption in (Broussely, Herreyre et al. 2001), here we assume the diffusivity of species has the Arrhenius relation with respect to temperature, $D_i \propto \exp(E_a / RT)$, where E_a is the activation energy. The activation energy of Li^+ depends on the composition of SEI and electrolyte, which is found to be around 50 kJ/mol (Abe, Sagane et al. 2005; Yamada, Iriyama et al. 2009). In the current model, we set $E_a = 51$ kJ/mol for all species. The effect of temperature on SEI growth and SEI thickness is shown in Figure 52a-b. It can be seen that SEI growth rate increases as temperature increases due to faster diffusion. Moreover, the SEI thickness exhibits the Arrhenius relation with temperature since the SEI growth is controlled by the diffusion of electrons.

2.5.3.2 Discussion and Conclusion

A phase field model is developed to investigate the formation and growth of the SEI layer on the surface of an anode in a lithium ion battery. In this model, the electric potential is solved from Poisson's equation, and the governing equations of the concentrations of species are derived from the nonequilibrium thermodynamics such that they move in the direction of reducing the total free energy of the system. Ions and electrons are transported through diffusion and electromigration in the whole domain with concentration-dependent mobilities. At the SEI/electrolyte interface, the SEI formation reaction occurs to drive SEI growth, where the reaction rate is determined by the generalized Butler-Volmer equation.

Several important features of SEI growth have been captured. It is found that SEI growth is a diffusion-limited process. It exhibits a power law scaling with respect to time with the exponent close to 0.5, and it is mainly controlled by the diffusion of electrons rather than interface

reactions. During the SEI growth, the gradients of concentrations and electric potential both build inside of the SEI layer due to fast interface reactions and small electron diffusivity. These gradients decrease as the SEI thickness increases. It is also found that increasing the initial state of charge in the anode increases the SEI growth rate and concentration gradient in the SEI, but decreases the electric potential gradient in the SEI. On the other hand, variation of the equilibrium electric potential difference between the two phases, and variation of the current density, mainly affect the distribution of the electric potential and charge density, while their influence on SEI growth rate is minor. In addition, the SEI thickness at a given time is found to have an Arrhenius relation with temperature, and the SEI growth rate increases rapidly with increasing temperature.

An important advantage of the present model compared with previous models is that it captures the charge separation and the double-layer structure at the SEI/electrolyte interface, and reveals the profile of charge density and electric potential in the interfacial region. Although the SEI growth law found in this model is similar to previous results in the literature, we show the evolution of charge density and electric potential in the whole domain including the SEI/electrolyte interface during the SEI growth, which to our knowledge is novel. Since the distribution of interfacial charge density and electric potential determines SEI formation and growth, this information is very useful for the quantitative modeling of SEI growth.

The present model is flexible enough to include more species and more mechanisms (such as SEI chemistry) that are relevant to SEI growth. It can also be extended to higher dimensional space straightforwardly. Moreover, it can handle complex morphological evolution of interface. It is known that the SEI layer contains multiple phases such as organic/inorganic layers and grains with different compositions. The microstructure of these phases may be complex and their evolution or breakdown will affect the life of batteries. It is expected that extending the current model by considering more species and phases in higher dimensional space will allow simulation of microstructural evolution in the SEI, which will help to further reveal the role of the SEI in battery performance.

2.6 Cell Modeling

Cell modeling is defined as understanding and modeling a battery at the single cell level. This is usually carried out by using continuum equations, whose formulation was pioneered by the Newman group. This formulation is usually also restricted to one-dimensional or pseudo one-dimensional representations, because the geometry is essentially adequately handled by a one-dimensional representation. Cell modeling is enhanced by micro-scale or nano-scale models, some of which are described above.

At the most basic level, the battery consists of a cathode and anode having an electrochemical potential difference. These are connected by a conductor (likely through a load) and by an

electrolyte. The electrochemical potential between the two electrodes drives a flow of electrons through the conductor and a flow of ions through the electrolyte. The losses associated with the flow of ions and electrons cause a reduction in the electrochemical potential available for the load that the battery is driving. We will be concerned with the losses that can occur within the battery, those occurring between the current collector plates that are attached to each electrode. Within each electrode region, ohmic losses can occur through electron conduction in the electrode material and through ion transport through the electrolyte phase. Between these two phases within each electrode there is also a loss of potential associated with the interphase transport referred to as the overpotential. There is also a separator region between each electrode that prevents short circuits. Ionic flow through the separator region also results in an ohmic loss. With porous electrodes, the potential losses across the electrode thickness can vary, bringing additional challenges to the computation of the potential losses.

The problem will be formulated with respect to the potential at the cathodic and anodic collector plates. Since the absolute potential is arbitrary, we will define the potential of the anode to be zero while that of the cathode is defined to be V , which is a positive quantity. Then, the potential drop associated with the battery is the difference between the theoretical open circuit potential, U^0 , and this predicted/measured cell potential, V . A given potential drop is associated with a specific current density, I , given in ampere per unit area of the cell. The potential across the cell is expressed using Φ , with separate spatially-varying potentials associated with each conducting material, the anode, Φ_a , the electrolyte, Φ_e , and the cathode, Φ_c .

In analyzing the electrochemical evolution of a battery with porous materials, it is necessary to differentiate between quantities averaged over the porosity, referred to as superficial quantities, and quantities that are local to a phase or interface. For example, current is expressed as the superficial current, i , in amperes per unit area of the cell. However, the current transfer between the electrode and electrolyte is expressed in terms of the unit area of the porous material. The variable, a , will be used to denote the specific surface area, or the surface area per unit volume. In addition to flow variables, the concentration-like variables can be expressed either in terms of superficial quantities (averaged over the phase volume fractions) or in terms of phase-specific quantities. It will be convenient to express the separate phase compositions in terms of the phase-specific mole fraction, X_k , i.e., the mole fraction of species k in its own phase. If the volume fraction of the phase is denoted ϕ , then the superficial mole fraction (volume-averaged over all phases present) would be ϕX_k . Without a subscript, ϕ will denote the volume fraction of the electrolyte; subscripts on ϕ will be used to denote the anodic and cathodic phases and sub-phases within those materials.

2.6.1 *Transport models for electrolytes*

In this project we seek to provide mechanisms for the degradation of batteries due to various aging and insult phenomena by trying to understand the tools that are necessary to describe the phenomena. This necessarily requires us to look beyond the normal mechanisms of battery simulation to side phenomena that control the breakdown of normal battery operation.

For the electrolyte, this necessarily goes beyond the normal single electrolyte in a solvent treatment of transport towards understanding chemical effects of caused by contaminants. First we will review the original models for battery performance based on the Newman group work. Then, we will review other formulations that enhance these models to include more chemistry and mechanics phenomena.

We'll briefly review the gold standard for multicomponent transport modeling, the Stefan-Maxwell formulation as well as the lowest common dominator model, the Nernst-Planck formulation. Then, we'll derive a new formulation that lies in between the two and coincides quite nicely with available theories for developing correlations for transport parameters for concentrated electrolytes, a necessary corollary to the transport formulation.

This formulation, which I haven't observed in the literature yet, uses the single ion correlations for the ionic conductivities along with the simulation of the concentrated-solution electrical conductivities to create an N parameter correlation of multicomponent electrolytes instead of the prohibitively complex $\frac{1}{2} N(N-1)$ parameter correlation employed by the Stefan-Maxwell relations. Most importantly, the formulation is exact in the single salt – single solvent limit (i.e., when N is three). In other words, the correlation exactly reproduces the Stefan-Maxwell relations in this case, while being extensible to larger systems.

2.6.1.1 Definitions of Reference Velocities and Electrochemical Potentials

Within the electrolyte, the current and ohmic losses are associated with ionic transport in the electrolyte. Therefore, a coupled treatment of ionic flow and potential gradients is provided in the following. Within the electrolyte phase, ionic composition will be expressed in terms of the phase-averaged mole fraction, X_i (so that the superficial mole fraction is ϕX_i), and velocities will be expressed either on a solvent velocity basis, \mathbf{v}_o , a mole-averaged basis, \mathbf{v}^* , or a mass-averaged basis, \mathbf{v} . The species velocities can be split into the reference velocity plus a diffusion velocity, \mathbf{V}_i^d that satisfies

$$\sum_i X_i \mathbf{V}_i^d = 0 \quad (2.6.1)$$

The average velocity is defined as either the solvent velocity (a), the mass averaged velocity (b), or the mole averaged velocity (c).

$$\begin{aligned} \text{a)} \quad & \mathbf{v}_o = \mathbf{V}_0; \quad \mathbf{V}_0^d = 0 \\ \text{b)} \quad & \rho \mathbf{v} = \sum \rho_i \mathbf{v}_i \quad 0 = \sum \rho_i \mathbf{V}_i^d \\ \text{c)} \quad & c \mathbf{v}^* = \sum c_i \mathbf{v}_i^* \quad 0 = \sum c_i \mathbf{V}_i^d \end{aligned} \quad (2.6.2)$$

All velocities are superficial quantities. Thus, any influence of the porosity has already been worked into the flux relationships. This is necessary as gradients in the state quantities are necessarily superficial quantities.

The individual species diffusion velocities, \mathbf{V}_i^d , are driven by the combined effects of electrostatic potential and chemical potential gradients. The combined electrochemical potential will be used here.

$$\xi_i = \mu_i^0 + RT \ln(\gamma_i X_i) + z_i F \Phi_e = \mu_i(T, P, \mathbf{X}) + z_i F \Phi_e \quad (2.6.3)$$

Φ_e is the electrostatic potential in the electrolyte, F is Faraday's constant, z_i is the charge on species i , X_i is the mole fraction, γ_i is the activity coefficient, R is the ideal gas constant, T is the temperature and μ_i^0 is the chemical potential of species i at its standard state conditions at the temperature and pressure of the solution. It should be noted that in a concentrated electrolyte with variable concentrations, the concept of an electric potential is an ill-defined concept. The potential cannot be separated from the concept of chemical potential for non-ideal fluids.

Newman approaches this subject by either defining potentials in terms of a reference electrode that can be moved around within the fluid arbitrarily or by defining what he calls an electrostatic potential. An electrostatic potential is defined in terms of a single electrochemical potential of an ion, m . Eqn. (2.6.4) is the definition of the electrostatic potential.

$$\xi_m = \mu_m^0 + RT \ln(X_m) + z_m F \Phi_e \quad (2.6.4)$$

It turns out the definition in Eqn. (2.6.4) is exactly what Cantera has been defining in term of the specification of the ionic chemical potentials, with the slight twist that for fluids which are on the molality basis, the mole fraction in Eqn. (2.6.4) is replaced with the molality of ion m (Moffat and Colon 2009).

The next sections will describe the transport laws within electrolyte fluids. We start with the Stefan-Maxwell relations and then go on to special cases

2.6.1.2 Derivation of the “Normal Newman Battery” Equations for Single Electrolytes

In their paper (Fuller, M. Doyle et al. 1994), Fuller and Newman gives his expressions for the fluxes in the electrolyte. They start out with the Stefan-Maxwell relations. Then, they set the solvent velocity to zero to invert the Stefan-Maxwell equations. This solvent velocity reference frame is the standard way the Stefan-Maxwell equations are handled when being employed in battery calculations.

$$\mathbf{N}_+ = -v_+ D^c \nabla c + \frac{t_+^o \mathbf{i}}{z_+ F} + c_+ \mathbf{v}_o \quad (2.6.5)$$

$$N_- = -v_- D^c \nabla c + \frac{t_-^o \mathbf{i}}{z_- F} + c_- \mathbf{v}_o$$

In this expression c is the concentration of the binary electrolyte, $c = c_i / \nu_i$. And, the Stefan-Maxwell diffusion coefficients can be related directly to the measurable transport parameters, D^c , t_+^o , and κ . The material balance on the electrolyte yields a conservation equation for c , Eqn. (2.6.6).

$$\varepsilon \frac{dc}{dt} = \nabla \cdot (\varepsilon D^c \nabla c) - \frac{\mathbf{i}_2 \cdot \nabla t_+^o}{z_+ \nu_+ F} + \frac{S_+ (1 - t_+^o)}{\nu_+} + c \mathbf{v}_o \quad (2.6.6)$$

How do you derive Eqn. (2.6.6) from Eqn. (2.6.5)? Eqn. (2.6.6) appears ubiquitously throughout the battery literature. The end result for the expression for the current is given by the following equation, Eqn. (2.6.7).

$$\mathbf{i} = -\kappa \left(\nabla \Phi + \frac{2RT}{F} \left[(1 - t_-) + \frac{c}{2c_o} \right] \frac{d}{dx} \ln c \gamma_{\pm} \right) \quad (2.6.7)$$

The derivations of Eqns. (2.6.6) and (2.6.7) are now presented. Let's take the case of a binary electrolyte within a solvent. Let's write down the conservation equation for the three species in the system.

$$\begin{aligned} \frac{\partial (c_+ \phi)}{\partial t} &= -\nabla \cdot [N_+] + S_+ \\ \frac{\partial (c_- \phi)}{\partial t} &= -\nabla \cdot [N_-] + S_- \\ \frac{\partial (c_o \phi)}{\partial t} &= -\nabla \cdot [N_o] + S_o \end{aligned} \quad (2.6.8)$$

Let's write down a few relations.

$$\begin{aligned} c_+ &= c \nu_+ & c_- &= c \nu_- \\ N_+ &= c_+ \mathbf{v}_+ = c_+ \mathbf{v}_o + \frac{t_+^o \mathbf{i}}{z_+ F} - \frac{\mathcal{D}_e \nu_+ c_T}{\nu RT c_o} c \nabla \mu_e \\ N_- &= c_- \mathbf{v}_- = c_- \mathbf{v}_o + \frac{t_-^o \mathbf{i}}{z_- F} - \frac{\mathcal{D}_e \nu_- c_T}{\nu RT c_o} c \nabla \mu_e \\ N_o &= c_o \mathbf{v}_o \end{aligned}$$

where

$$\mathcal{D}_e = \frac{z_+ - z_-}{\frac{z_+}{D_{o+}} - \frac{z_-}{D_{o-}}} \quad (2.6.9)$$

The D_{o+} and D_{o-} expressions are Stefan-Maxwell diffusion coefficients. We will later show that they can be estimated from equivalent conductances and modified for ionic concentration dependencies. Therefore, the transport expressions will be well grounded in experimental data. Note, we are explicitly using the relationship that the reference velocity is the velocity of species 0, the solvent. Therefore, there is no diffusional velocity for species 0, nor is there a velocity due to the electric field for species 0.

Let's take z_+ times the first and z_- times the second in Eqn. (2.6.8).

$$\frac{\partial(z_+ c_+ \phi)}{\partial t} = -\nabla \cdot \left[z_+ c_+ \mathbf{v}_o + \frac{t_+^o \mathbf{i}}{F} - \frac{\mathcal{D}_e z_+ v_+ c_T}{v R T c_o} c \nabla \mu_e \right] + z_+ S_+ \quad (2.6.10)$$

$$\frac{\partial(z_- c_- \phi)}{\partial t} = -\nabla \cdot \left[z_- c_- \mathbf{v}_o + \frac{t_-^o \mathbf{i}}{F} - \frac{\mathcal{D}_e z_- v_- c_T}{v R T c_o} c \nabla \mu_e \right] + z_- S_-$$

Adding these up,

$$0 = -\nabla \cdot \left[\frac{\mathbf{i}}{F} \right] + z_+ S_+ + z_- S_-, \quad (2.6.11)$$

yields the Poisson equation for the electrolyte where $\mathbf{i} = z_+ N_+ F + z_- N_- F$. This is the expected result. What this says is that one of the continuity equations for the ions, Poisson's equation for the current, and the charge neutrality condition for the solution are all functionally the same condition.

We can take the top result of Eqn. (2.6.10) and divide by z_+ and v_+ to yield Eqn. (2.6.12).

$$\frac{\partial(c\phi)}{\partial t} = -\nabla \cdot \left[c \mathbf{v}_o + \frac{t_+^o \mathbf{i}}{z_+ v_+ F} - \frac{\mathcal{D}_e c_T}{v R T c_o} c \nabla \mu_e \right] + \frac{S_+}{v_+} \quad (2.6.12)$$

We can then add back in a multiple of Eqn. (2.6.11) to get the following expression, Eqn.(2.6.13)

$$\frac{\partial(c\phi)}{\partial t} = -\nabla \cdot [c \mathbf{v}_o] - \frac{\mathbf{i} \cdot \nabla t_+^o}{z_+ v_+ F} + \nabla \cdot \left[\frac{\mathcal{D}_e c_T}{v R T c_o} c \nabla \mu_e \right] + \frac{S_+}{v_+} (1 - t_+^o) \quad (2.6.13)$$

Eqn. (2.6.13) is the expression that is used as a starting point for the conservation equation set for battery modeling of the electrolyte (Fuller, M. Doyle et al. 1994) ((Doyle, Fuller et al. 1993) Eqn. 10) ((Mao, Vidts et al. 1994), Eqn. 3) . It appears in multiple papers with some variation depending on the implementation details. One big detail is the formulation of the diffusion operator. The one expressed by Eqn. (2.6.13) is the more general one that takes into account of the possibility of a non-ideal solution.

What's missing in the discussion above is an expression for the electric potential of the solution. This actually gets into a discussion of what actually is the potential in the solution, a very tricky subject as the definition of the potential cannot be separated from the definition of the chemical potentials of the species in the solution. The potential also brings in the third Stefan-Maxwell coefficient, \mathcal{D}_{+-} , which has hitherto been absent from the equation set. The end result to this discussion is an expression of the form, Eqn. (2.6.14).

$$\frac{F}{\kappa} \mathbf{i} = - \sum_k \frac{i_k^o}{z_k} \nabla \xi_k \quad (2.6.14)$$

In other words, the gradient of the sum of the electrochemical potentials multiplied by the ratio of the transference number to the species charge is identified with the current. From this expression the potential is defined and solved for by substituting in the definition of the electrochemical potential. Eqn. (2.6.14) is used for both the concentrated and dilute cases. Note, it's also the first time we have invoked the quantity κ the electrical conductivity of the solution within this equation description. Within κ is a dependence on the third Stefan-Maxwell relation, \mathcal{D}_{+-} .

Eqn. (2.6.14) can be expressed in other forms by substituting in the equation for the electrochemical potential. In that form, it clearly is seen that the current in a solution with concentration gradients is no longer directly related to the gradient of the electric potential. In fact Eqn. (2.6.14) is used extensively in the theory of liquid junctions where the current is assumed to be zero, and the electric potential difference is calculated for solutions with differing concentrations.

Eqn. (2.6.14) provides input for the equation formulation to determine the potential within the solution. Essentially, a conservation equation for the current, Eqn.(2.6.15), is written in the electrolyte, and the expression in Eqn. (2.6.14) is used within this expression (Fuller, M. Doyle et al. 1994; Mao, Vidts et al. 1994).

$$-(\nabla \cdot \mathbf{i}) = FS_e a \quad (2.6.15)$$

Note, one could also write down a Poisson equation for the electric field within the solution, which has on its rhs the mismatch in charge. Here the electric permittivity of the medium would be used to relate the electric field with the gradient in the electric potential. This formulation has to be directly the same as the formulation invoked by Eqn. (2.6.15); there can be no differences

as they should represent the same conservation law. Inevitably, when new the double layer or at distances representative of the Debye length in the fluid this alternative approach is used (Christensen and Newman 2004). Therefore, the source term for the charge differentials may be defined via this method and not the other way round.

What doesn't generalize about the formulation in this section is the extension to multicomponent electrolyte systems. Essentially Eqn. (2.6.13) is tailor made for binary electrolytes. One can in general form neutral molecule representations of the multicomponent electrolyte to get around this limitation, but in practice this appears to have never been done.

2.6.1.3 Conservation Equations for the Individual Ions

We have seen how the binary electrolyte can be worked out from the Stefan-Maxwell relations. However, for multiple charged species in the electrolyte the neutral molecular representation behind Eqn. (2.6.10) is insufficient because it refers only to binary electrolytes. Can we generate a representation that is more general than the dilute representation? In general we would like the representation to reduce to the binary electrolyte case whenever the case is appropriate. And, we would like it to reproduce key requirements of the multicomponent representation but be parameterized only by binary electrolyte data. At the end of this section we will demonstrate that this is possible.

However, in order to generalize the electrolyte conservation equation to multiple species, we must first start with a general expression for conservation of a single species. Conservation for species k can be expressed as Eqn. (2.6.16).

$$\frac{\partial(C_T \phi X_k)}{\partial t} + \nabla \cdot [C_T X_k (\mathbf{v}^* + \mathbf{V}_k^{d,*})] = w_k, \quad (2.6.16)$$

w_k is the molar production rate in per unit volume of the system and C_T is the total concentration of the solution. \mathbf{v}^* is the mole-averaged bulk velocity of the solution. Equation (2.6.16) will be used to obtain X_k once an expression for w_k is provided. Boundary conditions for species transport are obtained from no-flux Neumann conditions for the species at the collector plates. Thus at both the anodic collector plate at $x = 0$ and the cathodic collector plate at $x = L_a + L_s + L_c$ the boundary conditions for Eqn. (2.6.16) are

$$X_k \mathbf{v}_k = 0$$

for all species, $k = 1, \dots, N$. The flux of species is thus associated with the source terms on the right-hand side of Eqn. (2.6.16) in the anode and cathode regions. In the separator region, there are no source terms on the right-hand side of Eqn. (2.6.16), and the equation is simplified.

Additionally, the mole fractions of the electrolyte species must sum to one.

$$\sum_{k=1}^N X_k = 1 \quad (2.6.17)$$

And, electroneutrality is assumed everywhere in the electrolyte, Eqn. (2.6.18)

$$\sum_{k=1}^N z_k X_k = 1 \quad (2.6.18)$$

Eqn. (2.6.17) and Eqn. (2.6.18) take the place of the last two species conservation equations, Eqn. (2.6.16), in the equation formulation. Alternatively, Eqn. (2.6.17) may be implicitly included if Eqn. (2.6.16) is used instead of Eqn. (2.6.17) in the formulation, because the full set of equations (with Eqn.(2.6.17)) can only be satisfied if Eqn. (2.6.17) holds. However, for now, we will explicitly include Eqn. (2.6.17) in the equation system.

The summation of Eqn. (2.6.16) over all electrolyte species gives an equation for the bulk mole-averaged velocity, Eqn.(2.6.19).

$$\frac{\partial(C_T \phi)}{\partial t} + \nabla \cdot (C_T \mathbf{v}^*) = \sum_k w_k \quad (2.6.19)$$

Eqn. (2.6.19) is the total continuity equation for the electrolyte phase. Therefore, we are using the total continuity equation to obtain the bulk fluid velocity, which is the common occurrence in 1D systems. Note, however, that we can make a more sophisticated treatment by making the pressure correspond to the total continuity equation by introducing an axial momentum equation at the same time. The momentum equation will be an implementation of Darcy's law under typical battery conditions. This is what we are doing in the thermal battery program. Boundary conditions for Eqn. (2.6.19) at the collector interfaces is the no flux condition, so that at $x = 0$ and at $x = L_a + L_s + L_c$,

$$\mathbf{v}^* = 0. \quad (2.6.20)$$

The superficial flux is conserved at the transition between the electrode and separator regions. At those transitions, there is potentially a discontinuity in ϕ . The superficial velocities are continuous across the region boundaries. This relationship is expressed in Eqn.(2.6.21).

$$(C_T \mathbf{v}_{La}^-) \Big|_{\lim x \rightarrow L_a}^- = (C_T \mathbf{v}_{La}^+) \Big|_{\lim x \rightarrow L_a}^+ \quad (2.6.21)$$

However, the gradients of the mole fractions may be discontinuous at these boundaries. The mole fractions of species will be continuous across these boundaries. The total flux of an ion, k , N_k , may be represented by the sum of the convective and diffusive components, Eqn.(2.6.22).

$$N_k = C_T X_k (\mathbf{v}^* + \mathbf{V}_k^{d,*}) \quad (2.6.22)$$

The sum over all N_k 's may be used to obtain the net current density, \mathbf{i}_e , in the ionic salt, Eqn.(2.6.23). Note, the molar velocity \mathbf{v} drops out of the expression, because the salt is everywhere electroneutral.

$$\mathbf{i}_e = F \sum_k z_k \mathbf{N}_k = C_T F \sum_k z_k X_k \mathbf{V}_k^{d,*} \quad (2.6.23)$$

Electroneutrality (outside the double layer) implies that the net divergence of the current density is zero. This is obtained by summation of the product of Eqn. (2.6.16) with z_k over all species. Extending this summation over all phases leads to a relation between the electrode and electrolyte currents, Eqn.(2.6.24),

$$\nabla \cdot \mathbf{i}_e = -\nabla \cdot \mathbf{i}_{a/c}, \quad (2.6.24)$$

that provides the overall charge conservation. In Eqn. (2.6.24), we have ignored the buildup of charge at the interface, i.e., the surface capacitance or double layer charging, a factor that will have to be included in later for transient analysis of the system.

Comparison of Eqn. (2.6.23) with Eqn. (2.6.19) shows the relation between the current density, electrode reaction rate, and the accumulation of charged species, Eqn.(2.6.25).

$$\nabla \cdot \mathbf{i}_e = \nabla \cdot \left(\phi C_T F \sum_i z_i X_i \mathbf{V}_i^{d,*} \right) = \left[F \sum_i z_i w_i \right] \quad (2.6.25)$$

If only a single reaction, l , (see Eqn. (2.6.89) below) involving the transfer of one ion, k , leads to the surface current flux, the divergence of the current is directly related to the surface flux allowing Eqn. (2.6.19) to be written as

$$\frac{\partial(C_T \phi X_k)}{\partial t} + \nabla \cdot \left[C_T X_k (\mathbf{v}^* + \mathbf{V}_k^{d,*}) \right] = \frac{1}{z_k F} \nabla \cdot \mathbf{i}_e. \quad (2.6.26)$$

Within the separator Eqn. (2.6.24) simplifies to the following equation

$$\nabla \cdot \mathbf{i}_e = 0 \quad (2.6.27)$$

Both Eqn. (2.6.24) and Eqn. (2.6.27) are needed within the equation formulation. The independent variable associated with them is the potential of the electrolyte phase, Φ_e . The potential of the electrolyte phase will adjust itself so as to maintain current conservation. Because we have specified the electric potential datum at the anode-collector interface, we do not have need to specify any electric potential datum for Φ_e .

2.6.1.4 Stefan-Maxwell Equation Development

The driving force for transport is then proportional to the diffusional driving force which is obtained from the development of an entropy production equation using non-equilibrium statistical thermodynamics, Eqn. (2.6.28) (Bird, Stewart et al.), (Curtiss and Bird 1999; Curtiss and Bird 2001).

$$\begin{aligned}
 cRT\mathbf{d}_k &= c_k T \nabla \left(\frac{\mu_k}{T} \right) + c_k \bar{H}_k \nabla \ln T - Y_k \nabla p - \rho_k \mathbf{g}_k + Y_k \sum_j \rho_j \mathbf{g}_j \\
 &= c_k RT \nabla \ln a_k + c_k (\bar{H}_k - H_k^o) \nabla \ln T - Y_k \nabla p - \rho_k \mathbf{g}_k + Y_k \sum_j \rho_j \mathbf{g}_j \quad (2.6.28) \\
 &= c_k RT \left(\sum_{j=1}^{n-1} \frac{d \ln a_k}{dx_l} \Big|_{T,P,x_i} \nabla x_l \right) + (c_k \bar{V}_k - Y_k) \nabla p - \rho_k \mathbf{g}_k + Y_k \sum_j \rho_j \mathbf{g}_j
 \end{aligned}$$

In Eqn. (2.6.28), we will generally be concerned with several body forces: gravity, other accelerations, and the electric potential. The electrical body force for an ion with charge z_k provides a force equal to Eqn. (2.6.29)

$$\rho_k \mathbf{g}_k = -Fz_k \nabla \Phi_e \quad (2.6.29)$$

It can be shown that the last term in Eqn. (2.6.28) disappears from the analysis due to the charge balance constraint. Note, analogously the body force due to the electric field will also drop out due to the charge balance constraint. Eqn. (2.6.28) is rather specific in what it includes and what it doesn't, and it is almost always misinterpreted or simplified. For one, it is not equal to the gradient of the electrochemical potential, as that would involve including arbitrary temperature and pressure derivatives of the electrochemical potential, which it does not include. Also, Eqn. (2.6.28) is not actually equal to the gradient of the electrochemical potentials assuming isothermal and isobaric derivatives. The temperature and pressure derivatives of the activity are included in the Eqn. (2.6.28). However, the last line in Eqn. (2.6.28) refers to a condition where the temperature and pressure derivatives in the activity can be ignored under most conditions.

In general, the electrochemical potential is expected to be the dominant driving force for transport in ionic liquids of concern, but the pressure, gravitational/acceleration, and temperature terms also provide driving forces for diffusion. The driving force due to pressure, gravitational, and acceleration gradients are included in Eqn. (2.6.28). Diffusion in a temperature gradient make be included within Eqn. (2.6.28) as well, leading to an additional term given in Eqn. (2.6.30).

$$\sum_j \frac{X_k X_j}{\mathbf{D}_{kj}} \left(\frac{D_k^T}{\rho_k} - \frac{D_j^T}{\rho_j} \right) (\nabla \ln T) \quad (2.6.30)$$

Where D_k^T is defined as the multicomponent thermal diffusion coefficient, which satisfy the constraint that $\sum D_j^T = 0$. In the remainder of this discussion, the pressure and temperature terms are neglected except for an order of magnitude estimate.

Because thermal batteries can experience strong accelerations leading to pressure gradients, it is interesting to estimate the magnitude of this term. With acceleration induced pressure gradients, the first term in Eqn. (2.6.28) is the product of the acceleration times the species molar mass. For acceleration on the order of $1e5 g$ ($1e6 m/s^2$) this pressure potential term is on the order of $1e3 N/mol$. For $z_i=1$ comparing this with the last term in Eqn. (2.6.28) we see that this is responsible for a potential gradient comparable to $1e-2 V/m$. (This analysis has taken an appropriate value for M_i of $10 g/mol$ as intermediate between the various molar masses and has not carried out a more detailed analysis.) Future analysis will consider the range of potentials that might be associated with temperature gradients, though these are expected to be small.

In terms of the remaining driving forces, the relative velocities of the individual species are obtained from the following multi-component diffusion equation

$$X_k RT \nabla \ln a_k + X_k F z_k \nabla \Phi_e = X_k \mathbf{d}_k = \tau^2 RT \sum_j \frac{X_k X_j}{\mathbf{D}_{kj}} (\mathbf{V}_j - \mathbf{V}_k) \quad (2.6.31)$$

where D_{ij} the Maxwell-Stefan diffusion coefficients describing the interactions of species i and j . When other contributions to the diffusion potential appearing in Eqn. (2.6.31) are relevant (e.g. pressure gradients, thermal diffusion or body forces), these would be added to the left-hand side of Eqn. (2.6.31) by adding their contributions into the value of \mathbf{d}_k . Onsager's reciprocal relations requires that $\mathbf{D}_{kj} = \mathbf{D}_{jk}$. \mathbf{D}_{ij} is not relevant because $\mathbf{V}_k - \mathbf{V}_k = 0$, so there are $n(n-1)/2$ diffusion coefficients required for n species. For the LiCl - KCl system, the required diffusion coefficients are $\mathbf{D}_{Li^+Cl^-}$, $\mathbf{D}_{K^+Li^+}$ and $\mathbf{D}_{K^+Cl^-}$.

Also indicated in Eqn. (2.6.31) is the tortuosity factor, τ , that is employed to account for the influence of porosity on the reduction in the rate of transport including diffusion. The tortuosity is most simply modeled as being related to the volume fraction of the electrolyte phase, ϕ , by $\tau^2 = 1/\sqrt{\phi}$. It would have been cleaner to separate out the porous flow effects from the transport theory implementation. However, that is not possible. The gradients of the temperature and mole fraction that go into calculating the value of \mathbf{d}_k are superficial quantities, i.e., they are macroscale quantities independent of the porosity. The \mathbf{V}_k 's are actually liquid scale quantities and must be multiplied by ϕ to generate the macroscale fluxes. Therefore, dependence of the macroscale fluxes on the porosity represented by Eqn. (2.6.31) is proportional to $\phi^{3/2}$. This dependence is the commonly employed. With the substitution of one of the equations in Eqn. (2.6.2) for one of the equations in the rank-deficient system, Eqn. (2.6.31) can be inverted as

indicated in the Appendix. The resulting expression for the species velocity k is Eqn.(2.6.32), where L_{kj} represents the inverse of the matrix in Eqn. (2.6.31).

$$\mathbf{v}_k = \sum_j L_{kj} X_j \mathbf{d}_j \quad (2.6.32)$$

Again, if other driving potentials indicated in Eqn. (2.6.31) are significant, these are added to \mathbf{d}_k in Eqn. (2.6.31).

2.6.1.5 Dilute limit for the Electrolyte Phase

The flux of ionic species i in the dilute limit is equal to

$$N_i = -\frac{\mathcal{D}_i c_i}{RT} \nabla \xi_i + c_i \mathbf{v}_o = -\frac{\mathcal{D}_i c_i}{RT} (\nabla \mu_i + z_i F \nabla \Phi) + c_i \mathbf{v}_o \quad (2.6.33)$$

μ_i is the chemical potential of the i^{th} species. Φ is the electric potential in the solution. One can plug this equation into the balance equation for species i to yield.

$$\frac{dc_i}{dt} + \nabla \cdot [c_i \mathbf{v}_i] = \nabla \cdot [u_i c_i \nabla \xi_i] + R_i \quad (2.6.34)$$

Newman states you can't define the electric potential within a fluid with varying concentrations uniquely. The definition of the inner Galvani potential is intertwined with the definition of the chemical potentials of the species. He gets around this in two ways. One way is by defining the electric potential (which he now calls the quasi-static electric potential) in terms of the chemical potential of a single special ion n ,

$$\xi_n = RT \ln X_n + z_n F \Phi \quad (2.6.35)$$

Note in Eqn. (2.6.35) the definition of the electrochemical potential doesn't include any activity coefficient wrt the species n . We may then plug the equation back into the conservation equation Eqn. to generate a rigorous expression that includes the potential Φ . The other way Newman gets around this is by defining the electric potential in the solution solely by measurement of the electric potential from two reference electrodes inserted into the solution. In the limit of the activity coefficient of n going to one, the dilute equations are retained.

$$N_i = -\frac{z_i D_i c_i}{RT} \nabla \Phi - D_i c_i \nabla X_i - D_i c_i \nabla \left(\ln \gamma_i - \frac{z_i}{z_n} \ln \gamma_n \right) + c_i \mathbf{v} \quad (2.6.36)$$

2.6.1.6 Solution of Multicomponent diffusion equation for a single binary electrolyte in a solvent

Consider a single electrolyte consisting of a cation with a charge z_+ and an anion with a charge z_- . We will make the following definitions and then solve the system. Stefan-Maxwell relations can be used to describe the dependence of the diffusion velocities on the gradients in the electrochemical potentials.

$$\begin{aligned} c_+ \nabla \xi_+ &= K_{o+} (\mathbf{v}_o - \mathbf{v}_+) + K_{+-} (\mathbf{v}_- - \mathbf{v}_+) \\ c_- \nabla \xi_- &= K_{o-} (\mathbf{v}_o - \mathbf{v}_-) + K_{-+} (\mathbf{v}_+ - \mathbf{v}_-) \end{aligned} \quad (2.6.37)$$

The ξ_{\pm} are the electrochemical potentials. Well actually as the previous section indicated, they are gradients of the mole fraction parts of these potentials.

The last expression for the Stefan-Maxwell relations for the solvent is not linearly independent of the first two. It is replaced with the definition of the bulk velocity to be used. Newman usually chooses to set the solvent velocity as the reference velocity in contrast to the more natural treatment of using the mass average velocity. This should be noted in the presentation below. It should be noted that only parts of the treatment depend on the reference velocities. Specifically the generalized multicomponent diffusion coefficients and the transference numbers depend on the reference velocity, not the electrical conductivity or the current. The K values are given in terms of the Stefan-Maxwell diffusion coefficients \mathbf{D}_{ij} .

$$K_{ij} = \frac{RT c_i c_j}{c_T \mathbf{D}_{ij}} \quad (2.6.38)$$

Several other definitions, where ν_+ and ν_- are the stoichiometric coefficients for the salt.

$$c_T = c_o + c_+ + c_- \quad c = \frac{c_+}{\nu_+} = \frac{c_-}{\nu_-} \quad (2.6.39)$$

$$z_+ \nu_+ = -z_- \nu_-$$

The current is given by the following equation.

$$\mathbf{i} = \sum_k F z_k \mathbf{N}_k = F z_+ \mathbf{N}_+ + F z_- \mathbf{N}_- \quad (2.6.40)$$

Now we will solve the system to show that the system is equivalent to Eqn. (2.6.13). One of the keys is to define a chemical potential for the mixed ion, μ_e . This is the only chemical potential that has relevance.

$$\begin{aligned}\xi_e &= v_+ \xi_+ + v_- \xi_- = v_+ \mu_+^o + v_- \mu_-^o + RT \ln X_+^{v_+} \gamma_+^{v_+} + RT \ln X_-^{v_-} \gamma_-^{v_-} \\ &+ Fv_+ z_+ \Phi_e + Fv_- z_- \Phi_e = \mu_e\end{aligned}\quad (2.6.41)$$

We see that the electric potential drops out of this expression so we can call the chemical potential μ_e with no loss in accuracy. We may further define the mixed ion activity as

$$a_{+-}^{v_+ + v_-} = X_+^{v_+} \gamma_+^{v_+} X_-^{v_-} \gamma_-^{v_-} \quad (2.6.42)$$

The flux of cation and anion in the solvent velocity reference frame is given by Eqn. (2.6.43)

$$N_+ = c_+ \mathbf{v}_+ = c_+ (\mathbf{v}_o + \mathbf{V}_+^{d,o}) \quad N_- = c_- \mathbf{v}_- = c_- (\mathbf{V}_-^{d,o} + \mathbf{v}_o) \quad (2.6.43)$$

We may redefine the current based on these relations realizing that the bulk flow will drop out when the fluid is defined as being electro-neutral.

$$\mathbf{i} = \sum_k Fz_k N_k = Fz_+ N_+ + Fz_- N_- = Fz_+ c_+ \mathbf{V}_+^d + Fz_- c_- \mathbf{V}_-^d \quad (2.6.44)$$

We would like to find expressions for the fluxes in terms of the driving forces. The way to tackle this is to first calculate an expression for the gradient of μ_e . From the addition of the two Stefan-Maxwell relations.

$$c \nabla \mu_e = K_{o+} (\mathbf{v}_o - \mathbf{v}_+) + K_{o-} (\mathbf{v}_o - \mathbf{v}_-) \quad (2.6.45)$$

Then, we may use Eqn. (2.6.37) to eliminate one of the diffusional velocities.

$$c \nabla \mu_e = K_{o+} (\mathbf{v}_o - \mathbf{v}_+) + K_{o-} \left(\mathbf{v}_o - \left[\frac{\mathbf{i} - Fz_+ c_+ \mathbf{v}_+}{Fz_- c_-} \right] \right) \quad (2.6.46)$$

$$c \nabla \mu_e = (K_{o+} + K_{o-}) \mathbf{v}_o - K_{o+} \mathbf{v}_+ - \frac{K_{o-} \mathbf{i}}{Fz_- c_-} + K_{o-} \frac{z_+ c_+ \mathbf{v}_+}{z_- c_-}$$

$$c \nabla \mu_e = (K_{o+} + K_{o-}) \mathbf{v}_o - (K_{o+} + K_{o-}) \mathbf{v}_+ - \frac{K_{o-} \mathbf{i}}{Fz_- c_-}$$

$$\frac{c_+ c \nabla \mu_e}{(K_{o+} + K_{o-})} = c_+ \mathbf{v}_o - c_+ \mathbf{v}_+ - \frac{c_+ K_{o-} \mathbf{i}}{(K_{o+} + K_{o-}) Fz_- c_-}$$

$$N_+ = c_+ \mathbf{v}_+ = c_+ \mathbf{v}_o + \frac{K_{o-} \mathbf{i}}{z_+ (K_{o+} + K_{o-}) F} - \frac{c_+ c \nabla \mu_e}{(K_{o+} + K_{o-})}$$

Now we will identify individual terms

$$\begin{aligned}
\frac{c_+ c}{(K_{o+} + K_{o-})} &= \frac{c_+ c}{\left(\frac{RTc_o c_+}{c_T \mathcal{D}_{0+}} + \frac{RTc_o c_-}{c_T \mathcal{D}_{0-}} \right)} \\
&= \frac{c c_T}{RTc_o} \frac{c_+}{\left(\frac{c_+}{\mathcal{D}_{0+}} + \frac{c_-}{\mathcal{D}_{0-}} \right)} \\
&= \frac{c c_T}{RTc_o} \frac{v_+}{\left(\frac{v_+}{\mathcal{D}_{0+}} + \frac{v_-}{\mathcal{D}_{0-}} \right)} \\
&= \frac{c c_T}{RTc_o} \frac{1}{\left(\frac{1}{\mathbf{D}_{0+}} - \frac{z_+ / z_-}{\mathbf{D}_{0-}} \right)} \\
&= \frac{c c_T}{vRTc_o} \frac{v_+ + v_-}{\left(\frac{1}{\mathbf{D}_{0+}} - \frac{z_+ / z_-}{\mathbf{D}_{0-}} \right)} \\
&= \frac{c c_T}{vRTc_o} \frac{v_+ z_- + v_- z_+}{\left(\frac{z_-}{\mathbf{D}_{0+}} - \frac{z_+}{\mathbf{D}_{0-}} \right)} \\
&= \frac{v_+ c c_T}{vRTc_o} \frac{z_- - z_+}{\left(\frac{z_-}{\mathbf{D}_{0+}} - \frac{z_+}{\mathbf{D}_{0-}} \right)} = \frac{v_+ c c_T}{vRTc_o} \frac{z_+ - z_-}{\left(\frac{z_+}{\mathbf{D}_{0-}} - \frac{z_-}{\mathbf{D}_{0+}} \right)} = \frac{v_+ c c_T D_e}{vRTc_o}
\end{aligned} \tag{2.6.47}$$

Where \mathcal{D}_e is the effective binary thermodynamic diffusion coefficient for the electrolyte, i.e., one based on the gradient of the chemical potential.

$$\mathcal{D}_e = \frac{z_+ - z_-}{\left(\frac{z_+}{\mathbf{D}_{0-}} - \frac{z_-}{\mathbf{D}_{0+}} \right)} \tag{2.6.48}$$

The other term turns out to be the transference number with respect to the solvent velocity (note transference numbers depend on the reference velocities).

$$\frac{K_{o-}}{(K_{o+} + K_{o-})} = \frac{\frac{RT c_o c_-}{c_T \mathbf{D}_{o-}}}{\frac{RT c_o c_+}{c_T \mathbf{D}_{o+}} + \frac{RT c_o c_-}{c_T \mathbf{D}_{o-}}} = \frac{\mathbf{D}_{o+} c_-}{\mathbf{D}_{o-} c_+ + \mathbf{D}_{o+} c_-} = \frac{\mathbf{D}_{o+} z_+}{\mathbf{D}_{o+} z_+ - z_- \mathbf{D}_{o-}} = t_+^o \quad (2.6.49)$$

$$\mathbf{N}_+ = c_+ \mathbf{v}_+ = c_+ \mathbf{v}_o + \frac{t_+^o \mathbf{i}}{z_+ F} - \frac{\mathcal{D}_e \mathbf{v}_+ c_T}{\nu RT c_o} c \nabla \mu_e \quad (2.6.50)$$

Analogously it can be shown that

$$\mathbf{N}_- = c_- \mathbf{v}_- = c_- \mathbf{v}_o + \frac{t_-^o \mathbf{i}}{z_- F} - \frac{\mathcal{D}_e \mathbf{v}_- c_T}{\nu RT c_o} c \nabla \mu_e, \quad \text{where} \quad (2.6.51)$$

$$\begin{aligned} t_-^o &= \frac{K_{o+}}{(K_{o+} + K_{o-})} = \frac{\frac{RT c_o c_+}{c_T \mathbf{D}_{o+}}}{\frac{RT c_o c_+}{c_T \mathbf{D}_{o+}} + \frac{RT c_o c_-}{c_T \mathbf{D}_{o-}}} = \frac{\mathbf{D}_{o-} c_+}{\mathbf{D}_{o-} c_+ + \mathbf{D}_{o+} c_-} = \frac{-\mathbf{D}_{o-} z_-}{\mathbf{D}_{o+} z_+ - z_- \mathbf{D}_{o-}} \\ &= \frac{\mathbf{D}_{o-} z_-^2 c_-}{\mathbf{D}_{o+} z_+^2 c_+ + \mathbf{D}_{o-} z_-^2 c_-} \end{aligned} \quad (2.6.52)$$

The last line of Eqn. (2.6.52) demonstrates that the transference numbers from concentrated solution theory are the same as from the Nernst-Planck theory. Analogously, we next derive the expression for the current. Note if we add Eqn. (2.6.50) and Eqn. (2.6.51), we get a tautology. Therefore, we need to start again from Eqn.(2.6.37). First we solve for $V_+^{d,o}$ and $V_-^{d,o}$ by solving for the linear equation assuming $V_0^{d,o} = 0$.

$$V_+^{d,o} = \frac{-c_+ \nabla \xi_+ [K_{o-} + K_{o+}] - c_- \nabla \xi_- [K_{o+}]}{K_{o+} K_{o-} + K_{o+} K_{o-} + K_{o+} K_{o+}} \quad (2.6.53)$$

$$V_-^{d,o} = \frac{-c_+ \nabla \xi_+ [K_{o-}] - c_- \nabla \xi_- [K_{o+} + K_{o+}]}{K_{o+} K_{o-} + K_{o+} K_{o-} + K_{o+} K_{o+}}$$

Next we plug in the direct expression for the current

$$\begin{aligned} \frac{\mathbf{i}}{F} &= \frac{-c_+ \nabla \xi_+ [z_+ c_+ K_{o-}] - c_- \nabla \xi_- [K_{o+} z_- c_-]}{K_{o+} K_{o-} + K_{o+} K_{o-} + K_{o+} K_{o+}} \\ &= \frac{z_+ c_+}{K_{o+} K_{o-} + K_{o+} K_{o-} + K_{o+} K_{o+}} \left(-c_+ \nabla \xi_+ [K_{o-}] + c_- \nabla \xi_- [K_{o+}] \right) \end{aligned}$$

Now using $v_- = -z_+v_+/z_-$

$$\begin{aligned}
\frac{i}{F} &= \frac{-c_+ \nabla \xi_+ [z_+ c_+ K_{o-}] - c_- \nabla \xi_- [K_{o+} z_- c_-]}{K_{o+} K_{o-} + K_{+-} K_{o-} + K_{+-} K_{o+}} \\
&= \frac{z_+ c_+ c v_+ z_+}{K_{o+} K_{o-} + K_{+-} K_{o-} + K_{+-} K_{o+}} \left(-\nabla \xi_+ \left[\frac{K_{o-}}{z_+} \right] - \nabla \xi_- \left[\frac{K_{o+}}{z_-} \right] \right) \\
&= \frac{z_+ c_+ c v_+ z_+ (K_{o+} + K_{o-})}{K_{o+} K_{o-} + K_{+-} K_{o-} + K_{+-} K_{o+}} \left(-\nabla \xi_+ \left[\frac{K_{o-}}{z_+ (K_{o+} + K_{o-})} \right] - \nabla \xi_- \left[\frac{K_{o+}}{z_- (K_{o+} + K_{o-})} \right] \right) \\
&= \frac{z_+ c_+ c v_+ z_+ (K_{o+} + K_{o-})}{K_{o+} K_{o-} + K_{+-} K_{o-} + K_{+-} K_{o+}} \left(-\nabla \xi_+ \left[\frac{t_+^o}{z_+} \right] - \nabla \xi_- \left[\frac{t_-^o}{z_-} \right] \right)
\end{aligned} \tag{2.6.54}$$

Then

$$\frac{Fi}{\kappa} = -\nabla \xi_+ \left[\frac{t_+^o}{z_+} \right] - \nabla \xi_- \left[\frac{t_-^o}{z_-} \right] \quad \text{with} \quad \kappa = \frac{-F^2 z_+ c_+ c_- z_- (K_{o+} + K_{o-})}{(K_{o+} K_{o-} + K_{+-} K_{o-} + K_{+-} K_{o+})} \tag{2.6.55}$$

As a further note, we can show that the expression for κ in Eqn. (2.6.55) is equivalent to the Newman expression, Eqn.(2.6.56), for the conductivity of a concentrated binary electrolyte on p. 306 (Newman and Thomas-Alyea 2004) (not shown).

$$\frac{1}{\kappa} = \frac{-RT}{c_T z_+ z_- F^2} \left(\frac{1}{D_{+-}} + \frac{c_o t_-^o}{c_+ D_{o-}} \right) \tag{2.6.56}$$

We have previously shown that the equations can be simplified into Eqn. (2.6.13) repeated here.

$$\frac{\partial(c\phi)}{\partial t} = -\nabla \cdot [c v_o] - \frac{i \cdot \nabla t_+^o}{z_+ v_+ F} + \nabla \cdot \left[\frac{\mathcal{D}_e c_T}{v R T c_o} c \nabla \mu_e \right] + \frac{S_+}{v_+} (1 - t_+^o) \tag{2.6.57}$$

The diffusion term, which is expressed in terms of the gradient of the salt chemical potential may be replaced by a gradient of the salt concentration. First

$$\begin{aligned}
\mu_e &= v_+ \mu_+ + v_- \mu_- \\
&= v_+ (\mu_+^o + RT \ln m_+ \gamma_+) + v_- (\mu_-^o + RT \ln m_- \gamma_-) \\
&= v_+ \left(\mu_+^o + RT \ln \frac{m \gamma_+}{v_+} \right) + v_- \left(\mu_-^o + RT \ln \frac{m \gamma_-}{v_-} \right) \\
&= v RT (\ln m + \ln (\gamma_{+-})) + v_+ \mu_+^o + v_- \mu_-^o - RT \ln v_+^{v_+} v_-^{v_-}
\end{aligned} \tag{2.6.58}$$

Taking the derivative of the chemical potential with respect to molality at constant temperature and pressure

$$\frac{\nabla \mu_e}{RT} = \frac{\nu}{m} \left(1 + \frac{d \ln(\gamma_{+-})}{d \ln m} \right) \nabla m \quad (2.6.59)$$

Now using the definition of molality,

$$m = \frac{c}{c_o M_o} \quad m_+ = \frac{c_+}{c_o M_o} \quad (2.6.60)$$

And noting that the solvent concentration is a function of the solute concentration, we may find the derivative of the molality in terms of the derivative of the solute concentration

$$c \nabla m = m \nabla c - m \frac{d \ln c_o}{d \ln c} \nabla c = m \left(1 - \frac{d \ln c_o}{d \ln c} \right) \nabla c \quad (2.6.61)$$

Therefore,

$$\frac{\nabla \mu_e}{RT} = \frac{\nu}{m} \left(1 + \frac{d \ln(\gamma_{+-})}{d \ln m} \right) \nabla m = \frac{\nu}{c} \left(1 + \frac{d \ln(\gamma_{+-})}{d \ln m} \right) \left(1 - \frac{d \ln c_o}{d \ln c} \right) \nabla c \quad (2.6.62)$$

Then, we may define (yes it is a definition) the concentration diffusion coefficient in terms of the thermodynamic diffusion coefficient

$$D^c = \mathcal{D}_e \frac{c_T}{c_o} \left(1 + \frac{d \ln(\gamma_{+-})}{d \ln m} \right) \quad (2.6.63)$$

To yield

$$\frac{\mathcal{D}_e c_T}{\nu R T c_o} c \nabla \mu_e = D^c \left(1 - \frac{d \ln c_o}{d \ln c} \right) \nabla c \quad (2.6.64)$$

This may be plugged back into Eqn. (2.6.13) to yield

$$\frac{\partial(c\phi)}{\partial t} = -\nabla \cdot [c \mathbf{v}_o] - \frac{\mathbf{i} \cdot \nabla t_+^o}{z_+ \nu_+ F} + \nabla \cdot \left[D^c \left(1 - \frac{d \ln c_o}{d \ln c} \right) \nabla c \right] + \frac{S_+}{\nu_+} (1 - t_+^o) \quad (2.6.65)$$

Therefore, we have written the equation in terms of the gradient of the salt concentration, c , at the expense of adding some obfuscating terms. Note, what happens to the derivation of Eqn.

(2.6.65) when there are temperature and pressure gradients? The answer really lies in the formulation of the Stefan-Maxwell relations. The driving forces for diffusion are specifically defined for constant temperature and pressure. Therefore, these gradients aren't included in the derivation, and this principle filters down all the way to Eqn.(2.6.65). This means btw that gradients in the standard state chemical potentials of the cation and anion aren't included in Eqn.(2.6.65). For original work on this subject see (Newman and Chapman 1973).

2.6.1.7 Derivation of the Battery Equations assuming Nernst-Planck Formulation

For sufficiently dilute conditions, the diffusive flux of ions in a solution can be described by the Nernst-Planck conditions, Eqn. (2.6.66). This is the lowest common denominator for multicomponent transport formulations.

$$\mathbf{j}_k^o = -D_k^C \frac{c_T}{c_o} \left(\nabla c_k + z_k c_k \frac{F}{RT} \nabla \Phi \right) \quad (2.6.66)$$

Here, we have used the term D_k^C to describe the ion diffusion coefficient formulation that does not use the gradient of the chemical potential. We have also identified the diffusion flux as being relative to the solvent velocity by using the superscript o designation. In the dilute limit, this is arbitrary, but has repercussions down the road as we shall see. The two formulations can be compared to one another, however, not without some work. A particularly good reference for this is (Engelhardt and Strehblow 1995), which comes out of the corrosion literature. One goal is to define how they are related to the Stefan-Maxwell coefficients. The ratio of c_T/c_o is added to Eqn. (2.6.66) is unity in the dilute limit. However, in later sections we will see that it is necessary for the comparison of the Nernst-Planck equation to the Stefan-Maxwell equations.

We can translate the flux relation in Eqn. (2.6.66) to the current-flux species transport formulation via the following method. First, we define the transference number for species k in the solvent velocity reference frame, t_k^o

$$t_k^o = \frac{z_k^2 D_k^C c_k}{\sum_l z_l^2 D_l^C c_l} \quad (2.6.67)$$

Then, we can turn the equation into the following just by adding, subtracting, and rearranging terms.

$$\mathbf{j}_k^o = -\sum_l D_{kl}^o \nabla c_l + \left(\frac{\alpha_k^o \mathbf{i}}{F} \right) \quad \text{where } \alpha_k^o = \frac{t_k^o}{z_k} \quad (2.6.68)$$

$$D_{kl}^o = D_k^C \delta_{kl} - \frac{t_k^o D_l^C}{z_k} \quad (2.6.69)$$

Therefore, we see that if we use the current-flux formulation, Eqn. (2.6.68), as is typically used in the battery literature, the gradients of the species are already fundamentally coupled even using the Nernst-Planck formulation. Both formulations, Eqns. (2.6.66) and (2.6.68), plug into the normal conservation equation for species k .

$$\frac{dc_k}{dt} = -\nabla \cdot (\mathbf{j}_k^o + c_k \mathbf{v}_o) + s_k \quad (2.6.70)$$

Note, both the multicomponent diffusion coefficients and the transference numbers are dependent on the reference velocity used. This is best explained in de Groot's book (Groot and Mazur 1962), but it is also explained in (Engelhardt and Strehblow 1995) and in Newman's book. The current is invariant with respect to the reference velocity, but most other quantities depend on this definition. Following through on the formulation, we see that the electrical conductivity of the fluid, which is defined as the proportionality constant between the gradient of the potential and the current under constant composition conditions, is also specified by using the formula,

$$\mathbf{i} = F \sum z_k \mathbf{j}_k^o.$$

We see that the following value is found for the electrical conductivity (coul/(m²s) (m/volt))

$$\kappa^{NP} = \frac{F^2}{RT} \frac{c_T}{c_o} \sum_l z_l^2 D_l^C c_l \quad (2.6.71)$$

We have identified the diffusional flux to be based on the solvent velocity reference frame. To convert to the mass averaged velocity reference frame, the following transformation is effected.

$$\mathbf{j}_k = \mathbf{j}_k^o - \sum_{l=1} \frac{c_k M_l}{\rho} \mathbf{j}_l^o \quad (2.6.72)$$

This transformation affects the multicomponent diffusion coefficients, D_{kl}^o , and α_k^o as well (Engelhardt and Strehblow 1995).

$$D_{kl} = D_{kl}^o - \sum_{m=1} \frac{c_k M_m}{\rho} D_{km}^o$$

$$\alpha_k = \alpha_k^o - \sum_{l=1} \frac{c_k M_l}{\rho} \alpha_l^o$$

The last expression makes clear the dependence of the transference number on the reference velocity definition.

2.6.1.8 A New Multicomponent Transport Representation

After looking at the literature there doesn't seem to be a formal description of multicomponent transport in electrolyte systems that straddles the Nernst-Planck equations and the Stefan-Maxwell Formulations. However, there is a real need for this formulation, just as there is for gas-phase multicomponent transport systems. We will always assume that the Stefan-Maxwell relations hold. However, each of the coefficients in the S-M equations is temperature, pressure, and mole fraction dependent. Much of the important dependence refers to the mole fraction dependence as well. The S-M formulation has too much data to fit, so it is seldom used.

In gas-phase systems the analysis of multicomponent formulations of Coffee and Heimerl (Coffee and Heimerl 1981) is an example of a break-through formulation that is now used widely to describe multi-component transport. Here we seek to supply a formulation that only involves binary salt data except for the electrical conductivity data, which we will allow for a multicomponent formulation (see (Anderko, Wang et al. 2002)). We seek to provide a formulation that will be formally exact in the limit of a single salt in a single solvent. Therefore, we seek guidance from the binary salt representation. In that representation both the mutual diffusion coefficient and the transference number can be accurately represented by the Nernst-Planck equations, modified for the non-ideality of the solution. However, the electrical conductivity of the solution cannot be described by these equations solely. Instead the cross-term \mathcal{D}_{+-} fundamentally comes into play for κ only. This term cannot be reconciled with a Nernst-Planck formalism, and it is this term that breaks the Einstein relation. Thus, we seek a modification to the Nernst-Planck equation that takes this into account, Eqn. (2.6.73). χ_k is a fix-up term that will be added into the formulation.

$$\mathbf{j}_k^o = -\frac{\mathbf{D}_{ok}}{RT} c_k \frac{c_T}{c_o} (\nabla \xi_k) + \chi_k \quad (2.6.73)$$

First we note that the approximations will be carried out in the solvent velocity reference frame. We do this because we know that we can transform the system to the mass-averaged reference frame later using the transform introduced in Section 2.6.1.7. Also, the transference numbers calculated using the Nernst-Planck equations are only adequate in the dilute limit for the solvent-velocity reference frame where $V_o^{d,o}$ is equal to zero.

Moreover, we will seek a formulation of the diffusion operator such that we add linear combinations of gradients of the electrochemical driving force to the Nernst-Planck equation, Eqn. (2.6.74).

$$\mathbf{j}_k^o = c_k \mathbf{V}_k^{d,o} = -\frac{\mathbf{D}_{ok}}{RT} c_k \frac{c_T}{c_o} (\nabla \xi_k) + \sum_l \chi_{kl} \nabla \xi_l \quad (2.6.74)$$

This formulation is motivated by Eqns. (2.6.37) for the binary solution. One such formulation that fits the objectives is the following expression Eqn. (2.6.75).

$$\mathbf{j}_k^o = c_k \mathbf{V}_k^{d,0} = -\frac{\mathbf{D}_{ok}}{RT} c_k \frac{c_T}{c_o} (\nabla \xi_k) + \frac{\mathbf{i}^{NP}}{F} \frac{t_k^{o,NP}}{z_k} \left(\frac{\kappa - \kappa^{NP}}{\kappa^{NP}} \right) \quad \text{if } z_k \neq 0 \quad (2.6.75)$$

$$\mathbf{j}_k^o = c_k \mathbf{V}_k^{d,0} = -\frac{\mathbf{D}_{ok}}{RT} c_k \frac{c_T}{c_o} (\nabla \xi_k) \quad \text{if } z_k = 0$$

The $t_k^{o,NP}$ expression could be replaced with anything that sums to one over k . However, in the next section we will show that this term is exactly the needed expression to exactly capture the binary salt limiting case. $t_k^{o,NP}$ is obtained from Eqn. (2.6.67). From this expression we see that $t_k^{o,NP}/z_k$ is still zero for neutral molecules. Note for the mole averaged and mass averaged velocity reference frames $t_k^{o,NP}/z_k$ is no longer zero for neutral molecules. The expression κ^{NP} is the electrical conductivity that is calculated when assuming the Nernst-Planck equations are valid, Eqn. (2.6.71).

$$\kappa^{NP} = \frac{F^2}{RT} \frac{c_T}{c_o} \sum_l z_l^2 \mathbf{D}_{ol} c_l \quad (2.6.76)$$

The sum over the charged species is equal to one. \mathbf{i}^{NP} is the current obtained from the Nernst-Planck assumption.

$$F \mathbf{i}^{NP} = -\kappa^{NP} \sum_l \frac{t_l^{o,NP}}{z_l} \nabla \xi_l \quad (2.6.77)$$

We can plug these expressions into Eqn. (2.6.75) to find the expression for the current.

$$\begin{aligned} \mathbf{i} &= F \sum_k z_k \mathbf{j}_k^o = F \sum_k z_k c_k \mathbf{V}_k^{d,0} = F \sum_k \left(-\frac{\mathbf{D}_{ok}}{RT} z_k c_k \frac{c_T}{c_o} (\nabla \xi_k) + \frac{\mathbf{i}^{NP}}{F} t_k^{o,NP} \left(\frac{\kappa - \kappa^{NP}}{\kappa^{NP}} \right) \right) \quad (2.6.78) \\ &= \sum_k \frac{\kappa^{NP}}{F} \left(-\frac{t_k^{o,NP}}{z_k} (\nabla \xi_k) \right) + \sum_k \mathbf{i}^{NP} t_k^{o,NP} \left(\frac{\kappa - \kappa^{NP}}{\kappa^{NP}} \right) \\ &= \sum_k \frac{\kappa^{NP}}{F} \left(-\frac{t_k^{o,NP}}{z_k} (\nabla \xi_k) \right) + \mathbf{i}^{NP} \left(\frac{\kappa - \kappa^{NP}}{\kappa^{NP}} \right) \\ &= \sum_k \frac{\kappa^{NP}}{F} \left(-\frac{t_k^{o,NP}}{z_k} (\nabla \xi_k) \right) + \sum_k \frac{(\kappa - \kappa^{NP})}{F} \left(-\frac{t_k^{o,NP}}{z_k} (\nabla \xi_k) \right) \end{aligned}$$

Thus

$$Fi == -\sum_k \kappa \left(-\frac{t_k^{o,NP}}{z_k} (\nabla \xi_k) \right) \quad (2.6.79)$$

Therefore, the extra terms in Eqn. (2.6.75) has the effect of modifying the solution's electrical conductivity to establish the current results, consistent with the multicomponent Stefan-Maxwell results (see Eqn. (2.6.55)). Additionally, we have shown that Eqn. (2.6.53) is correctly reproduced by the method (Moffat 2011) verifying that the binary results of the S-M equation are fully reproduced.

To summarize we have shown that we have derived an N parameter transport theory, \mathcal{D}_{ok} and κ , that can completely reproduce the binary electrolyte S-M equations and that can be generalized to arbitrary numbers of species. The extra parameter is associated with the deviation from the electrical conductivities Einstein relation result. The next step, one we have not had time to pursue, is to model multicomponent electrolyte systems with good data from S-M equations and show that this transport theory can have predictive value even though it doesn't have a full complement of degrees of freedom that the S-M equations have. Additionally, parameterization of \mathcal{D}_{ok} and κ needs to be carried out in terms of parameters such as T , P , ionic strength and binary coupling parameters that may lead to ion association terms that would influence the value of κ . Systems that look promising involve the molten salt system, the aqueous brine system where there's the most data, and the organic solvent systems.

2.6.2 Electrode transport

The potential evolves in each phase according to ohmic losses. In the anode and cathode, the superficial resistivities are denoted σ_a and σ_c , and the potentials evolve according to

$$\mathbf{i}_a = -\sigma_a \nabla \Phi_a \text{ and } \mathbf{i}_c = -\sigma_c \nabla \Phi_c. \quad (2.6.80)$$

Here, the resistivities and currents are those associated with the cross sectional area of the cell. Models for the resistivities of the matrix phase must be constructed based on the percolation properties of the matrix phase. They must be cognizant of the original powder technologies for forming the porous anodes and cathodes, and must incorporate models for the morphological evolution of the electrode materials as a function of the battery utilization. Electrode materials that form as a function of the electrode utilization will have varying electrical conductivities. Interfaces between electrode materials will have interfacial electrical resistivities that may depend on the mechanical load imposed on the cell. Interfacial electrical resistivities are usually modeled assuming that there is a constriction resistance between two particles, an analysis of which starts with an estimate of the Hertzian contact area, which is dependent on the applied pressure of the contact and the elastic modulus of the two contacting materials. It's expected (and hoped) that the matrix materials in the anode and cathode are significantly above their percolation thresholds so that exponentials of the effective conductivities in these materials don't show significantly greater values than 1.0. Here we will use Eqn. (2.6.81) for an electrode

consisting of two materials M1 and M2 with mole fractions X_{M1} and X_{M2} and conductivities σ_{M1} and σ_{M2} , and having a volume fraction ε_M until otherwise driven to something else. This corresponds to a series-resistance type morphology model

$$\sigma_a = \varepsilon_M (X_{M1}\sigma_{M1} + X_{M2}\sigma_{M2}) \quad (2.6.81)$$

The chemical evolution of the electrode leads to changes in the phase and thereby in the volume fraction of various phases. These changes are further discussed in the section on Phase Evolution.

Equation (2.6.80) is supplemented by the equation for charge conservation given below, expressing the fact that current transfers from the matrix phase into the electrolyte via surface reactions.

$$\nabla \cdot \mathbf{i}_a = -\nabla \cdot \mathbf{i}_e \quad (2.6.82)$$

The boundary conditions for the potential and current are given at the collector plates. These boundary conditions are the problem input and output. Between the two electrodes, the current is carried by the electrolyte as described in the following section so that at the end of the electrode near the separator, the electrode current must be zero, providing another boundary condition. For the anode-collector boundary, at $x = 0$, the voltage datum is applied, Eqn.(2.6.83).

$$\Phi_a = 0 \quad (2.6.83)$$

At the anode separator interface, $x = L_a$, the anode material ends. Therefore, a no current condition is applied, Eqn.(2.6.84).

$$\mathbf{i}_a = 0 \quad (2.6.84)$$

The insulator at $x = L_a + L_s$ requires

$$\mathbf{i}_c = 0 \quad (2.6.85)$$

For the cathode, the boundary conditions at the cathodic collector plate at $x = L_a + L_s + L_c$, either the net voltage drop across the battery or the net current is specified.

$$\Phi_c = V \text{ or } \mathbf{i}_c = I \quad (2.6.86)$$

Usually, we will favor the current condition, because it is better behaved numerically for electrodes which exhibit plateau regions in their open circuit voltages as a function of electrical discharge.

2.6.3 Electrode reactions

Interphase Reactions

The molar production rate is largely associated with the surface reactions, the reduction and oxidation occurring at the cathode and anode interfaces. Rates of species production reactions at interfaces are obtained from Eqn. (2.6.87) [Goodwin et al, 2009].

$$s_k = \sum_{i=1}^{N_s} \nu_{ki} q_i \quad (2.6.87)$$

ν_{ki} are stoichiometric coefficients for the species k participating in reaction i . q_i are rates of progress for the i^{th} reaction. In this treatment electrons are defined just like any other species. However, they may be singled out with the subscript e so that the net rate of production of electrons at an interface, s_e , can be written as

$$s_e = \sum_{i=1}^{N_s} \nu_{ei} q_i \quad (2.6.88)$$

Where $\nu_{ei} = +1$ for reaction, i , which are in the anodic direction, and where $\nu_{ei} = -1$ for reactions in the cathodic direction. Note reactions which transfer more than one electron should be considered as global reactions, not elementary reactions. All elementary reactions transfer only one electron. The net current flux across the interface is given by

$$i = F s_e \quad (2.6.89)$$

s_e has units of $\text{kmol m}^{-2} \text{s}^{-1}$. In order to create per volume production terms for inclusion into the species conservation reactions from the s_e , one needs to multiply by values for the interfacial area of the electrode per unit volume, $a_{p-\alpha}$, for the particular interface that involves the reaction i , whose solid side involves the phase $p-\alpha$.

Consider a generic charge-transfer reaction written in the anodic direction (i.e., producing electrons) producing one electron.



The net rate of production may be written as the difference between the anodic and cathodic rates.

$$q = q_a - q_e \quad (2.6.91)$$

The anodic and cathodic rates of progress depend upon both the temperature and the electric-potential difference across the double layer, $E_a = \Phi_m - \Phi_s$, where Φ_m is the electric potential in

the metal, and Φ_s is the electric potential in the solution outside of the diffuse-charge region, according to Eqn. .

$$q_a = k_a(T) \tilde{a}_a \tilde{a}_b \exp\left[\frac{\beta_a FE_a}{RT}\right] \quad (2.6.92)$$

$$q_c = k_c(T) \tilde{a}_c \exp\left[\frac{-\beta_c FE_a}{RT}\right] \quad (2.6.93)$$

The thermal contributions $k_a(T)$ and $k_c(T)$ are usually written in Arrhenius form. For elementary reactions, the symmetry parameters β satisfy $0 < \beta < 1$. Further the anodic and cathodic symmetry parameters are constrained to satisfy $\beta_a + \beta_c = 1$. \tilde{a}_a are concentration activities, which are usually defined just as activities for liquid and solid phases. In global reactions, symmetry parameters are also relevant but usually called α not β and there are no specific constraints on the values of α .

Forward and reverse rate constants must still satisfy microscopic reversibility. That is

$$\frac{k_a}{k_c} = K_{eq} = \exp\left[\frac{-\Delta G^0}{RT}\right] \quad (2.6.94)$$

The electron does contribute to the value of ΔG^0 , because its value is set so as to provide a reference value for the potential drop across a reference interface. For aqueous systems, this reference interface is the well-known standard hydrogen electrode (SHE) interface. For molten salt systems, we are using the following reaction as a reference interface electrode reaction:



where Li(l) is a pure liquid lithium electrode and the electrolyte solution is defined as pure LiCl. For the generic charge transfer reaction, Eqn. (2.6.92), (2.6.93) and (2.6.94) result in the Nernst equation expressing the equilibrium electric potential difference at the anode as

$$E_a^{eq} = \frac{1}{F} \left[\Delta G^0 + RT \ln \left(\frac{\tilde{a}_c}{\tilde{a}_a \tilde{a}_b} \right) \right] \quad (2.6.96)$$

If there are multiple charge-transfer reactions, at equilibrium every charge-transfer reaction must be equilibrated simultaneously with the same value of E_a^{eq} ; in this case, the set of Nernst equations define constraints that the equilibrium species activities must satisfy. However, if for any reason the species activities are not in equilibrium, then it is not possible to unambiguously define a Nernst potential, especially with parallel charge-transfer pathways. For open circuit systems, mixed potential theory then comes into play where the voltage of the metal will float to a value where the net production rate of electrons is equal to zero.

If multiple charge-transfer pathways are active then away from equilibrium the value of E_a^{eq} as computed from Eqn. (2.6.96) has different values for each reaction, resulting in significant complications in using the Butler-Volmer formulation. By contrast the physical anode potential E_a has a single unambiguous value (after specification of the reference interface), independent of how many charge-transfer pathways are active. For models such as the present one, in which the anode potential, species activities and current density are all computed self-consistently, the Butler-Volmer form offers no substantial advantages compared to the elementary mass-action form. More importantly, representing reactions in the mass-action form does not suffer from restrictions that are inherent in the Butler-Volmer form. For a single reaction, the Butler-Volmer form may also be represented in terms of the mass action form (Moffat, Hewson et al. 2009).

In summary, using Eqn. (2.6.88) gives the current flux per interphase surface area. This current flux is linked through Eqn. (2.6.87) to species conservation in Eqns. (2.6.19) and (2.6.19). The phase potentials in Eqn. (2.6.92) and (2.6.93) are determined from the transport in the electrode and electrolyte phases described in the previous sections. The next section describes how these phenomena are brought together.

2.6.3.1 Comparison to the Specification of Electrode Reactions via the Open Circuit Voltage

Newman models make the implicit assumption that the thermodynamics are assigned to the reactions. For detailed kinetics one needs a consistent set of thermodynamic relations that may only be achieved by assigning the thermodynamics to the species, those providing a consistent set of parameters. At the same time electrochemical reactions are best presented in terms of an exchange coefficient formulation. I'll describe how to do this using Cantera in the following sections.

Cantera has been demonstrated to have all of the tools necessary to successfully implement what's known about the elementary steps of the reaction and to produce a global reaction rate in the Butler-Volmer format (where it's the appropriate form). With its emphasis/reliance on elementary steps, Cantera is a good vehicle for providing robust and reproducible links between experimental data and models attempting to reproduce experiment (see (Bessler, Warnatz et al. 2007) for a good example of this).

Assuming that we have established the thermodynamics for the electrode reactions (Moffat and Hewson 2009; Moffat and Hewson 2010), the next step is to establish the kinetics. In order to fully understand the intricacies of implementing electrode reactions within Cantera, there's no substitute for actually exhaustively carrying the process out on a sample reaction.

How electrode kinetics for thermal batteries is implemented within the Cantera framework (Goodwin and Aivazis 1999) is the emphasis of this note. Nothing necessarily new has been developed within Cantera to handle electrode reactions. This capability to model Butler-Volmer electrode reactions has previously been used extensively within Cantera to model solid oxide

fuel cells (H. Zhu, Kee et al. 2005; Bessler, Warnatz et al. 2007; Hao and Goodwin 2007; Goodwin, Zhu et al. 2009). I do, however, explain how this functionality is used within liquid electrolyte systems. Conventions are established for how we define the overpotential, the exchange current density, and the current. In particular, sign conventions are established for these quantities, which are internally consistent, and allow electrode reactions to be expressed in both the anodic and cathodic directions.

This memo describes the implementation of electrode reactions in the literature and in Cantera. We contrast the derivation of the equation set within the bulk Butler-Volmer formulation used in the battery literature with Cantera's derivation which is based on establishing specifications for the values of chemical potentials for all species in the equation set including electrons in the metal.

2.6.4 Cantera's Setup of Electrochemistry

2.6.4.1 Specifying the electron chemical potential and ion chemical potentials

Let's say we have an electrode reaction, i , that produces or consumes electrons within a solid phase. We will write this in the cathodic direction via the following reaction.



In Eqn. (2.6.97), $\nu_{k,i}^r$ is the reactant stoichiometric coefficient for species k in this i^{th} reaction. $\nu_{k,i}^p$ is the product stoichiometric coefficient for species k in this i^{th} reaction. Note that $\nu_{e^-,i}^r = n_{e,i}^r$. $n_{e,i}^r$ is the number of electrons consumed by the reaction. The summation is over all species, N_s , in all phases that may occur at the interface. These phases may consist of multiple bulk phases or surface phases. Within Cantera, we will insist that there be at least one surface phase at each interface even if the phase is empty of content, i.e., consists of just one species that has zero elements assigned to it.

The condition for chemical equilibrium is Eqn. (2.6.98).

$$\sum_k^{N_s} \nu_{k,i}^r \zeta_k + n_{e,i}^r \zeta_{e^-} \rightleftharpoons \sum_k^{N_s} \nu_{k,i}^p \zeta_k \quad (2.6.98)$$

$n_{e,i}^r$ is defined as the number of reactant electrons. The chemical potential of an electron in a metal is defined to be equal to Eqn. (2.6.99).

$$\zeta_{e^-} = \mu_{e^-}^o + z_{e^-} F \Phi \quad (2.6.99)$$

In this equation, $\mu_{e^-}^o$ is nonzero. Within Cantera we have used $\mu_{e^-}^o$ to assign a convention for the potential drop across an interface that is used throughout a particular calculation. In aqueous systems we have used the Standard Hydrogen Electrode (SHE) convention to assign $\mu_{e^-}^o$ (Moffat and Colon 2009). For molten salt system, we use the convention of $E_{\text{Li(l)}-\text{LiCl}}^o = 0$ at standard state conditions, for the lithium melt reaction, (R4).



The chemical potential for the electron must then be equal to the expression provided in Eqn.(2.6.100). Note this expression is not consistent with the SHE expression, but is entirely analogous to the SHE formulation (Moffat and Hewson 2009).

$$\mu_{e^-}(T, P) = (\mu_{\text{Li(l)}}^o(T) - \mu_{\text{LiCl(l)}}^o(T) + RT \ln(2)) + z_{e^-} F \Phi_M \quad (2.6.100)$$

Also, the electron chemical potential $\mu_{e^-}^o(T, P)$ for electrons in all metals associated with electroactive interfaces within a particular problem will be given by Eqn.(2.6.100), thereby providing a relative standard. In addition to the use of Eqn.(2.6.100), the standard state chemical potential of the chlorine ion in liquid LiCl is defined by convention to be equal to zero at all temperatures and pressures, (Moffat and Hewson 2009)

$$\mu_{\text{Cl}^-}^o(T, P) = 0, \quad (2.6.101)$$

due the charge neutrality constraint creating an essentially immeasurable degree of freedom. This degree of freedom is satisfied by arbitrarily assigning the chlorine ion to have a zero standard state chemical potential, where the standard state is defined to be the pure LiCl molten salt state. Therefore, writing down the standard state Gibbs free energy change of reaction for (R4),



results in Eqn. (2.6.102).

$$\Delta G_{R4} = \mu_{\text{Li(l)}}^o - \mu_{\text{Li}^+}^o - \mu_{e^-}^o = 0 \quad (2.6.102)$$

Applying the relationship between the standard electrode potential and the Gibbs free energy of reaction,

$$\Delta \zeta_{R4}^o = \Delta G_{R4}^o + nFE^o = 0 \quad \rightarrow \quad nFE_{\text{Li(l)}-\text{LiCl}}^o = -\Delta G_{R4}^o = 0,$$

Eqn. (2.6.100) is derived. The electron is assumed to be in its own “electron electrode phase” within Cantera, because of the form of Eqn.(2.6.100).

```

<phase dim="3" id="metal_Li_LiCl_electrons">
  <elementArray datasrc="elements.xml"> E </elementArray>
  <speciesArray datasrc="#species_electrode"> electron_Li_LiCl </speciesArray>
  <thermo model="StoichSubstance">
    <referenceInterface> Li(l)-LiCl </referenceInterface>
    <density units="g/cm3">100.</density>
  </thermo>
  <transport model="None" />
  <kinetics model="none" />
</phase>

<!-- species definitions -->
<speciesData id="species_electrode">
  <species name="electron_Li_LiCl">
    <atomArray>E:1.0</atomArray>
    <charge>-1</charge>
    <thermo>
      <Shomate Pref="1 bar" Tmax="700.0" Tmin="400.0">
        <floatArray size="7"> -40.71053 , 6.411257 , -6.010738 , 4.150772 , -0.007908 ,
          410.01408 , -77.614337
        </floatArray>
      </Shomate>
      <Shomate Pref="1 bar" Tmax="2700.0" Tmin="700.0">
        <floatArray size="7"> -47.17129 , 14.679607 , -3.696837 , 0.794099 , 0.330556 ,
          412.93171 , -85.545107
        </floatArray>
      </Shomate>
    </thermo>
    <density units="g/cm3">100.</density>
  </species>
</speciesData>

```

Figure 53 XML format for the electron phase within Cantera for molten salt systems

Figure 53 provides the Cantera implementation of this electron phase within a metal relative to the Li(l)-LiCl interface. The phase itself is named `metal_Li_LiCl_electrons`, and is defined as a stoichiometric phase, meaning that it consists of one species. It contains one species named `electron_Li_LiCl`, with the nontrivial Shomate polynomial form necessary to satisfy Eqn.(2.6.100). The nontrivial nature of the representation is due to the fact that the chemical potential of the Lithium liquid, $\mu_{\text{Li}(l)}^o$, and the chemical potential of the liquid molten salt, $\mu_{\text{LiCl}(l)}^o$, are taken from the NASA and JANAF databases, and are nontrivial functions of temperature. In those databases the conventions are to assign the heats of formation of elements in their standard states at one bar and 298.15 K to be equal to zero. This is the convention that has been adopted throughout in Cantera's aqueous chemistry and electrochemistry work.

We have adopted the same type of formulation for the chemical potential when using organic solvents common to lithium-ion batteries. In these types of systems it's common to assign the zero potential to the following reaction which takes place on a solid lithium anode, which takes the place of the SHE electrode within aqueous systems.



R(8) takes more explaining. We define the standard state chemical potential of the Rxn. (2.6.103) as being equal to zero, and then define the chemical potential of the electron in order to make it

so. Li(s) refers to the solid lithium metal. Li⁺ refers to the lithium ion in the common organic solvent used in batteries; this is a mixture of ethylene carbonate, propylene carbonate, and dimethyl carbonate. The cation is matched by an equivalent part of the anion, PF₆⁻, and the concentration of the ions in the solvent are defined as 1.0E-3 molar, which is equivalent to the 1 molality convention for the H⁺ aqueous ion convention. Just as in the aqueous system, we also must specify the convention that we will assume for the chemical potential of the ion pair. Here we will assume that the standard state of the chemical potential of the Li⁺ is equal to zero. Also, we will assume that the activity coefficient of the Li⁺ is zero as a function of the ionic strength, an analog assumption to the pH convention used in aqueous systems that is specified on the Cl⁻ ion. With this assumption, then, the entire heat of solution of LiPF₆ from the dry salt into the organic liquid solution would then be assigned to the enthalpy of the PF₆⁻ ion. Note also that assigning the chemical potential of Li⁺ to zero requires that the standard state volume of Li⁺ is also equal to zero.

The chemical potential of species *i* in phase *a*, where *a* may be the electrode, the solution, or the interface between the two, is equal to Eqn. (2.6.104).

$$\zeta_k = \mu_k(T, P, x_i) + z_k F \Phi_{a,k} \quad (2.6.104)$$

$\mu_k(T, P, x_i)$ may have multiple formats. For example it may be a stoichiometric phase, such as an oxide, it may be an ideal solution on the mole fraction basis, or it may be an electrolyte solution, whose activities are defined on the molar or molality scale.

Let's expand the electrochemical potentials in Eqn. (2.6.98) using Eqn. (2.6.104) to develop an expression for equilibrium of an electrode reaction.

$$\sum_{i=1}^{N_s} \nu_i^r \mu_i + \sum_{i=1}^{N_s} \nu_i^r z_i F \Phi_i + n_{e,i}^r \mu_{e^-}^o - n F \Phi_{\text{electrode}} = \sum_{i=1}^{N_s} \nu_i^p \mu_i + \sum_{i=1}^{N_s} \nu_i^p z_i F \Phi_i \quad (2.6.105)$$

ν_i^r is the stoichiometric coefficient for reactants in the reaction. ν_i^p is the stoichiometric coefficient for products in the reaction. Collecting terms results in Eqn. (2.6.106).

$$\sum_{i=1}^{N_s} \nu_i^r z_i F \Phi_i - \sum_{i=1}^{N_s} \nu_i^p z_i F \Phi_i - n_{e,i}^r F \Phi_{\text{electrode}} = \sum_{i=1}^{N_s} \nu_i^p \mu_i - \sum_{i=1}^{N_s} \nu_i^r \mu_i - n \mu_{e^-}^o \quad (2.6.106)$$

The rhs of Eqn. (2.6.106) is ΔG , the Gibbs free energy of reaction. Φ_i is the potential of the phase in which species *i* belongs. However, to simplify the lhs of Eqn. (2.6.106), we will make the assumption that all charged species that are reactants are located in the electrolyte solution phase. Therefore, $\sum_{i=1}^{N_s} \nu_i^r z_i = n_{e,i}^r$. And, we may define the potential difference between the electrode and solution phase as *E*:

$$E = \Phi_{\text{electrode}} - \Phi_{\text{soln}} \quad (2.6.107)$$

Then, Eqn. (11) simplifies to

$$-n_{e,i}^r FE = \sum_{i=1}^{N_s} \nu_i^p \mu_i - \sum_{i=1}^{N_s} \nu_i^r \mu_i - n_{e,i}^r \mu_{e^-}^o = \Delta G_i \quad (2.6.108)$$

We may also generalize Eqn. (2.6.108) so that it may be written in both the cathodic and the anodic directions if we define the net production of electrons in a reaction, n , by Eqn.(2.6.109).

$$n = n_{e,i}^p - n_{e,i}^r \quad (2.6.109)$$

So that

$$nFE = \sum_{i=1}^{N_s} \nu_i^p \mu_i - \sum_{i=1}^{N_s} \nu_i^r \mu_i - n_{e,i}^r \mu_{e^-}^o = \Delta G_i \quad (2.6.110)$$

We may separate the Gibbs free energy of reaction out into its standard state contribution, ΔG^o , defining an equivalent standard potential, E^o , based on ΔG^o ,

$$nFE^o = \sum_{i=1}^{N_s} \nu_i^p \mu_i^o - \sum_{i=1}^{N_s} \nu_i^r \mu_i^o - n_{e,i}^r \mu_{e^-}^o = \Delta G^o, \quad (2.6.111)$$

and the deviation from the standard state contribution,:

$$nF(E - E^o) = \Delta G - \Delta G^o \quad (2.6.112)$$

The later may be rewritten as Eqn.(2.6.113).

$$E = E^o + \frac{\Delta G - \Delta G^o}{nF}, \quad (2.6.113)$$

Eqn. (2.6.113) is recognized as the Nernst equation for the reaction, after $\Delta G - \Delta G^o$ is written out in terms of the logs of the activity coefficients.

To summarize, we've formulated chemical potentials for all ions and the electron specific to a particular electrode for which we have specified the voltage. We have seen that the latter condition is equivalent to specifying the standard chemical potential of the electron. We've also shown in several cases how to get around the degeneracy of specifying ion chemical potentials, caused by not being able to measure the thermo of phases with net charge, by setting one ion chemical potential by convention. Then, the thermodynamics all other ions in solution may be calculated without degeneracy.

2.6.5 Formulation of the Kinetics in Terms of Elementary Steps

2.6.5.1 Equivalence of Butler-Volmer Formulation with Reversible Elementary Reaction Formulation

Cantera's implementation of kinetics involving charge transfer is based on the extension of mass action kinetics to the interfacial charge transfer case where electrons are treated as any other species. Mass action kinetics for the forward reaction is described by Eqn. (2.6.114).

$$ROP_{f,i} = k_{f,i} \left(\prod_k^{N_s} (c_k^a)^{\nu_{k,i}^r} \right) \quad (2.6.114)$$

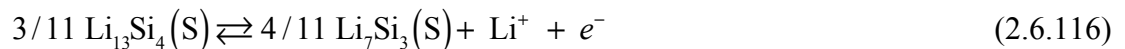
The formulation for the forward and reverse reaction rate coefficients for the Rxn. (2.6.97) is given by Eqn. (2.6.115).

$$k_{f,i} = A_{f,i} T^{b_{f,i}} \exp \left[\frac{-E_{f,i}}{RT} \right] \exp \left[\frac{-\beta_i^f F \left(\sum_k \nu_{k,i} z_k \Phi_k \right)}{RT} \right] = k_{f,i}^c \exp \left[\frac{-\beta_i^f F \left(\sum_k \nu_{k,i} z_k \Phi_k \right)}{RT} \right] \quad (2.6.115)$$

where $\nu_{k,i} = \nu_{k,i}^p - \nu_{k,i}^r$ is the net stoichiometric coefficient for species k in reaction i . Eqn. (2.6.115) is the same form as Eqn. (16) in (Goodwin, Zhu et al. 2009) with the same sign conventions as above.

$k_{f,i}^c$ is the "chemical part of the rate coefficient including a chemical activation energy, $E_{f,i}$ $\beta_i^f F \left(\sum_k \nu_{k,i} z_k \Phi_k \right)$, which includes a contribution from an electron reactant or product, may be thought of as the change in the activation energy barrier (or the relative transition state energy level) due to the potential energy difference between the products and reactants in the reaction. The motivation for the form is based on transition state theory applied to electron transfer reactions and is supplied in several standard electrochemistry books (see (Bockris and Khan 1993)). β_i^f is the symmetry factor for the transition state, and is an additional input parameter (actually the only additional input parameter) for electron transfer reactions.

Let's take a look at this term for the case of first LiSi Reaction,



One electron is transferred when the reaction is written in the anodic direction.

$$\sum \nu_k z_k \Phi_k = -n(\Phi_{\text{metal}} - \Phi_{\text{soln}}) = -nE \quad \text{where} \quad n = \nu_e \quad (2.6.117)$$

In Eqn. (2.6.117), n is defined as the stoichiometric coefficient for the electron in the reaction; n may be negative if the reaction is expressed as a cathodic reaction. The forward reaction, which is the anodic direction, is enhanced for positive values of E , and reduced for negative values of E . This makes sense, because high values of Φ_{metal} stabilize the presence of electrons in the metal by reducing the chemical potential of electrons.

The reverse rate of progress for reaction i may be expressed in the following analogous form

$$ROP_{r,i} = k_{r,i} \left(\prod_k^{N_s} (c_k^a)^{v_{k,i}^p} \right) \quad (2.6.118)$$

where

$$k_{r,i} = A_{r,i} T^{b_{r,i}} \exp \left[\frac{-E_{r,i}}{RT} \right] \exp \left[\frac{\beta_i^r F \left(\sum_k v_{k,i} z_k \Phi_k \right)}{RT} \right] = k_{r,i}^c \exp \left[\frac{\beta_i^r F \left(\sum_k v_{k,i} z_k \Phi_k \right)}{RT} \right] \quad (2.6.119)$$

$k_{r,i}^c$ is the chemical part of the reverse rate constant. The symmetry coefficients are restricted being related by $\beta_i^f + \beta_i^r = 1$. Eqn. (2.6.119) is the same form as Eqn. (17) in (Goodwin, Zhu et al. 2009). c_k^a is the activity concentrations of the product species k , ($c_k^a = c_k^s a_k$), where c_k^s is the standard concentration and a_k is the activity of species k).

However, the reverse reaction rate may also be calculated from the electrochemical equilibrium constant, which includes the electrical potential energy term in Eqn. (2.6.117):

$$\sum v_k \zeta_k = 0. \quad (2.6.120)$$

$$\Delta G_R^o + RT \ln \left[\frac{\prod_k^p a_k^{v_k^p}}{\prod_k^r a_k^{v_k^r}} \right] + F \sum_k v_k z_k \Phi_k^{eq} = 0, \quad \Delta G_R^o = \sum_k v_k \mu_k^o \quad (2.6.121)$$

ΔG_R^o is the standard Gibbs free energy of the reaction, the last term on the rhs may be solved for E , the equilibrium value of the potential drop across the interface that would induce an equilibrium condition for the elementary reaction. Eqn. (2.6.121) can be rewritten as

$$\frac{\prod_k^p a_k^{v_k^p}}{\prod_k^r a_k^{v_k^r}} = \exp \left[\frac{-\Delta G_R^o - F \sum_k v_k z_k \Phi_k^{eq}}{RT} \right] = \exp \left[\frac{-\Delta G_R^o + nFE^{eq}}{RT} \right] \quad (2.6.122)$$

$$\text{where } E^{eq} = \Phi_{\text{metal}}^{eq} - \Phi_{\text{soln}}^{eq}$$

Next, we will switch back to the reaction. The reaction must be consistent with the thermodynamic limit, Eqn. (2.6.122). The numerator in the lhs of Eqn. (2.6.122) is a multiplication over the products of the reaction, while the denominator is a multiplication over the reactants of the reaction. Therefore, we may formulate the reverse rate constant of the reaction by equating the two rates of progress under equilibrium conditions.

$$ROP_f^{eq} = ROP_r^{eq} \quad (2.6.123)$$

Then, we may multiply a form of Eqn. (2.6.122) into Eqn.(2.6.118) and Eqn. (2.6.119).

$$ROP_{r,i}^{eq} = k_{r,i}^c \left(\frac{\prod_k^r (a_k)^{v_k^r}}{\prod_k^p (a_k)^{v_k^p}} \right) \exp \left[\frac{-\Delta G_r^o - (1 - \beta_i^r) F \sum_k v_{k,i} z_k \Phi_k^{eq}}{RT} \right] \prod_k^p (c_k^a)^{v_{k,i}^p} \quad (2.6.124)$$

to generate an expression for $k_{r,i}$ that is consistent with electrochemical equilibrium, Eqn. (2.6.122). Here we plug Eqn. (2.6.124) into Eqn. (2.6.123) to yield Eqn. (2.6.125).

$$\begin{aligned} k_r^c \left(\frac{\prod_k^r (a_k)^{v_k^r}}{\prod_k^p (a_k)^{v_k^p}} \right) \exp \left[\frac{-\Delta G_r^o - (1 - \beta_i^r) F \sum_k v_k z_k \Phi_k^{eq}}{RT} \right] \prod_k^p (c_k^a)^{v_k^p} \\ = k_{f,i}^c \exp \left[\frac{-\beta_i^f F \sum_k v_k z_k \Phi_k^{eq}}{RT} \right] \prod_k^r (c_k^a)^{v_k^r} \end{aligned} \quad (2.6.125)$$

Eqn. (2.6.125) may be simplified.

$$k_{r,i}^c = k_{f,i}^c \frac{\prod_k^r (c_k^s)^{v_k^r}}{\prod_k^p (c_k^s)^{v_k^p}} \exp \left[\frac{+\Delta G_r^o + (1 - \beta_i^f - \beta_i^r) F \sum_k v_k z_k \Phi_k^{eq}}{RT} \right] \quad (2.6.126)$$

In Eqn. (2.6.126), c_k^s is the standard concentration of species k , which in many liquid and solid systems is equal to one. Eqn. (2.6.126) can be solved for several forms. In terms of just the chemical reaction rate, the original form of the reverse chemical potential can be generated, Eqn. (2.6.127). This is the original form of the reverse rate constant used within Cantera.

$$k_{r,i}^c = k_{f,i}^c \frac{\prod_k^r (c_k^s)^{\nu_k^r}}{\prod_k^p (c_k^s)^{\nu_k^p}} \exp \left[\frac{\Delta G_r^o}{RT} \right] \quad (2.6.127)$$

In terms of the total rate forward rate constant, the reverse total rate constant obtained by plugging Eqn. (2.6.127) into Eqn. (2.6.119) to give Eqn. (2.6.128).

$$k_{r,i} = k_{f,i}^c \frac{\prod_k^r (c_k^s)^{\nu_k^r}}{\prod_k^p (c_k^s)^{\nu_k^p}} \exp \left[\frac{\Delta G_r^o + (\beta_i^r) F \sum_k \nu_k z_k \Phi_k}{RT} \right] \quad (2.6.128)$$

This may be further manipulated to yield Eqn. (2.6.129)

$$\begin{aligned} k_{r,i} &= k_{f,i}^c \frac{\prod_k^r (c_k^s)^{\nu_k^r}}{\prod_k^p (c_k^s)^{\nu_k^p}} \exp \left[\frac{\Delta G_r^o + (\beta_i^r + \beta_i^f) F \sum_k \nu_k z_k \Phi_k}{RT} \right] \\ &= k_{f,i}^c \frac{\prod_k^r (c_k^s)^{\nu_k^r}}{\prod_k^p (c_k^s)^{\nu_k^p}} \exp \left[\frac{\Delta G_r^o + F \sum_k \nu_k z_k \Phi_k}{RT} \right] \end{aligned} \quad (2.6.129)$$

When the electric potential drop across the interface is at the equilibrium value, $-nE^{eq} = \sum_k \nu_k z_k \Phi_k^{eq}$, the forward rate of progress and reverse rate of progress are equal. However, the potential drop across the interface may not be at equilibrium and will not be for finite currents crossing the interface electrode. Define this difference as the surface overpotential, η_s .

$$-n(\Phi_{\text{metal}} - \Phi_{\text{soln}}) = -nE = -n(E^{eq} + \eta_s) = \sum_k \nu_k z_k \Phi_k \quad \text{or} \quad E = E^{eq} + \eta_s \quad (2.6.130)$$

The surface overpotential η_s represents the departure from the equilibrium potential at the specific conditions of the electrode (including the calculation of the activities), and it is also given by the expression:

$$-Fn\eta_s = n\zeta_{e^-} + \sum_i^p \nu_i^p \zeta_i - \sum_i^r \nu_i^r \zeta_i \quad (2.6.131).$$

Note, we have defined η_s away from the standard state conditions where all unity activities are assumed, and even irrespective of equilibrium conditions. Therefore it's valid under any circumstance, especially one in which there is a net current flowing across the interface. The forward and reverse rates of progress may be reorganized so that the Butler-Volmer form of the equation is generated. Following the derivation in (Bessler, Warnatz et al. 2007) the forward rate of progress is expressed as:

$$\begin{aligned} ROP_f &= k_f^c \exp \left[\frac{\beta_i^f F n (E^{eq} + \eta_s)}{RT} \right] \prod_k^r (c_k^a)^{v_k^r} \\ &= k_f^c \exp \left[\frac{\beta_i^f F n E^{eq}}{RT} \right] \prod_k^r (c_k^a)^{v_k^r} \exp \left[\frac{\beta_i^f F n \eta_s}{RT} \right] \end{aligned} \quad (2.6.132)$$

Then, we may also write the reverse rate of progress in terms of η_s . We start with Eqn. (2.6.118), Eqn. (2.6.119), and Eqn. (2.6.127).

$$ROP_r = k_f^c \left(\frac{\prod_k^r (c_k^s)^{v_k^r}}{\prod_k^p (c_k^s)^{v_k^p}} \right) \exp \left[\frac{\Delta G_r^o + \beta_i^r F \sum_k v_k z_k \Phi_k}{RT} \right] \prod_k^p (c_k^a)^{v_k^p} \quad (2.6.133)$$

Then, we apply the relation derived from Eqn. (2.6.122).

$$\exp \left[\frac{\Delta G_r^o}{RT} \right] = \left(\frac{\prod_k^r a_k^{v_k^r}}{\prod_k^p a_k^{v_k^p}} \right) \exp \left[\frac{-F \sum_k v_k z_k \Phi_k^{eq}}{RT} \right] \quad (2.6.134)$$

To reduce the expression to

$$\begin{aligned} ROP_r &= k_f^c \left(\frac{\prod_k^r (c_k^s)^{v_k^r}}{\prod_k^p (c_k^s)^{v_k^p}} \right) \left(\frac{\prod_k^r a_k^{v_k^r}}{\prod_k^p a_k^{v_k^p}} \right) \exp \left[\frac{-F \sum_k v_k z_k \Phi_k^{eq} + \beta_i^r F \sum_k v_k z_k \Phi_k}{RT} \right] \prod_k^p (c_k^a)^{v_k^p} \\ &= k_f^c \left(\prod_k^r (c_k^a)^{v_k^r} \right) \exp \left[\frac{F n E^{eq} - \beta_i^r F n (E^{eq} + \eta_s)}{RT} \right] \\ &= k_f^c \exp \left[\frac{\beta_i^f F n E^{eq}}{RT} \right] \prod_k^r (c_k^a)^{v_k^r} \exp \left[\frac{-(1 - \beta_i^f) F n \eta_s}{RT} \right] \end{aligned} \quad (2.6.135)$$

Then, the net rate of progress for the reaction may be written as

$$ROP_{net} = k_f^c \exp\left[\frac{\beta_i^f FnE^{eq}}{RT}\right] \left(\prod_k^r (c_k^a)^{v_k^r}\right) \left(\exp\left[\frac{\beta_i^f Fn\eta_s}{RT}\right] - \exp\left[\frac{-(1-\beta_i^f)Fn\eta_s}{RT}\right]\right) \quad (2.6.136)$$

Eqn. (2.6.137), derived from Eqn. (2.6.122), may be used to eliminate E^{eq} from the Eqn.(2.6.136).

$$\exp\left[\frac{\beta^f FnE^{eq}}{RT}\right] = \left(\frac{\prod_k^p (c_k^a)^{v_k^p \beta^f}}{\prod_k^r (c_k^a)^{v_k^r \beta^f}}\right) \left(\frac{\prod_k^r (c_k^s)^{v_k^r \beta^f}}{\prod_k^p (c_k^s)^{v_k^p \beta^f}}\right) \exp\left[\frac{\beta^f \Delta G_R^o}{RT}\right] \quad (2.6.137)$$

to yield

$$\begin{aligned} ROP_{net} &= k_f^c \left(\frac{\prod_k^p (c_k^a)^{v_k^p \beta^f}}{\prod_k^r (c_k^a)^{v_k^r \beta^f}}\right) \left(\frac{\prod_k^r (c_k^s)^{v_k^r \beta^f}}{\prod_k^p (c_k^s)^{v_k^p \beta^f}}\right) \exp\left[\frac{\beta^f \Delta G_R^o}{RT}\right] \left(\prod_k^r (c_k^a)^{v_k^r}\right) \\ &\quad \left(\exp\left[\frac{\beta^f Fn\eta_s}{RT}\right] - \exp\left[\frac{-(1-\beta^f)Fn\eta_s}{RT}\right]\right) \\ &= k_f^c \left(\prod_k^p (c_k^a)^{v_k^p \beta^f}\right) \left(\frac{\prod_k^r (c_k^s)^{v_k^r \beta^f}}{\prod_k^p (c_k^s)^{v_k^p \beta^f}}\right) \exp\left[\frac{\beta^f \Delta G_R^o}{RT}\right] \left(\prod_k^r (c_k^a)^{v_k^r(1-\beta^f)}\right) \\ &\quad \left(\exp\left[\frac{\beta^f Fn\eta_s}{RT}\right] - \exp\left[\frac{-(1-\beta^f)Fn\eta_s}{RT}\right]\right) \end{aligned} \quad (2.6.138)$$

Now the net rate of electron generation may be calculated from ROP_{net} :

$$\frac{d[e^-]}{dt} = (n) ROP_{net} \quad , \quad (2.6.139)$$

and the current through the electrode and into the solution may be defined in terms of the electron generation rate as

$$I = -z_{e^-} F \frac{d[e^-]}{dt} = -z_{e^-} nF (ROP_{net}^i) = nF (ROP_{net}^i) \quad (2.6.140)$$

Then, the rate of progress for elementary electrode reactions may be defined in terms of the current density, i , in the traditional Butler-Volmer form as

$$i = i_o \left(\exp \left[\frac{\beta^f F n \eta_s}{RT} \right] - \exp \left[\frac{-(1-\beta^f) F n \eta_s}{RT} \right] \right) \quad (2.6.141)$$

where i_o , the exchange current density, is given by:

$$i_o = n F k_f^c \left(\prod_k^r (c_k^a)^{v_k^r (1-\beta^f)} \right) \left(\prod_k^p (c_k^a)^{v_k^p \beta^f} \right) \left(\frac{\prod_k^r (c_k^s)^{v_k^r \beta^f}}{\prod_k^p (c_k^s)^{v_k^p \beta^f}} \right) \exp \left[\frac{\beta^f \Delta G_R^o}{RT} \right]. \quad (2.6.142)$$

Or, an alternative form is:

$$i_o = n F k_f^c \exp \left[\frac{\beta^f F n E^{eq}}{RT} \right] \left(\prod_k^r (c_k^a)^{v_k^r} \right) \quad (2.6.143)$$

Therefore, for elementary kinetics steps, Cantera's implementation leads to the Butler-Volmer format given by Eqn. (2.6.141) and (2.6.142), a point that has already been made in (Bessler, Warnatz et al. 2007). The Eqn. (2.6.142) agrees with Eqn. (11) in (Bessler, Warnatz et al. 2007).

Let's go through the signs. In Eqn. (2.6.141), i is the current from the metal into the solution. i is positive when the overpotential of the reaction is positive. When i is positive, electrons in the metal are created. When the overpotential is positive the potential of the metal is higher than the solution (see Eqn. (2.6.130)). Making the metal potential positive means that electrons have a lower chemical potential (see Eqn. (2.6.99)), thus favoring their formation. The overpotential must be negative for reactions to lead to the destruction of electrons.

Let's explore the signs involved with reactions written in the cathodic direction. For reactions in the cathodic direction, $n = -1$. This means that the exchange current density from Eqn. (2.6.143) is negative. This is ok, and is a direct result of the formulation of the current convention, expressed in Eqn. (2.6.140). It's also true that for reactions written in the cathodic direction to proceed in the cathodic direction then the overpotential, defined as $\eta_s = E - E^{eq}$, must be a negative quantity. This is again ok, and reflects the fact that the potential E must be reduced from its equilibrium potential E^{eq} in order to drive the destruction of electrons. Therefore, we must expect that the exchange current density for cathodically written reactions will be negative. We must also expect that the overpotential for reactions which destroy electrons should be negative. For sets of interfacial electrode reactions, especially when they are intermixed with non-electrode reactions, the resulting global current density may or may not be reducible to Butler-Volmer form. A more general approach is needed.

2.6.5.2 Activation Energies for Charge Transfer Reactions

Activation energies for charge transfer reactions can be approached from two methods. The first method we will pursue is to assume that the overpotential is fixed. Then, we may use the Butler-Volmer form of the reaction repeated here as a starting point.

$$i = i_o \left(\exp \left[\frac{\beta^f F n \eta_s}{RT} \right] - \exp \left[\frac{-(1-\beta^f) F n \eta_s}{RT} \right] \right) \quad (2.6.144)$$

where i_o , the exchange current density, is given by:

$$i_o = n F k_f^c \left(\prod_k^r (c_k^a)^{v_k^r (1-\beta^f)} \right) \left(\prod_k^p (c_k^a)^{v_k^p \beta^f} \right) \left(\frac{\prod_k^r (c_k^s)^{v_k^r \beta^f}}{\prod_k^p (c_k^s)^{v_k^p \beta^f}} \right) \exp \left[\frac{\beta^f \Delta G_R^o}{RT} \right]. \quad (2.6.145)$$

In the first treatment we will take the overpotential, η_s as constant as we change the temperature. Let's calculate the activation energy for the charge transfer, $E_{\eta_s}^i$, Eqn. (2.6.146), at constant overpotential.

$$E_{\eta_s}^i = -RT^2 \left. \frac{d(\ln i)}{dT} \right|_{\eta_s, X_i, P} \quad (2.6.146)$$

First we will define the activation energy of the exchange current reaction.

$$E^{i_o} = -RT^2 \left. \frac{d(\ln i_o)}{dT} \right|_{X_i, P}$$

Then,

$$\begin{aligned} E_{\eta_s}^i &= -RT^2 \left. \frac{d(\ln i)}{dT} \right|_{\eta_s, X_i, P} \\ &= E^{i_o} + F n \eta_s \left[\frac{\beta^f \exp \left[\frac{\beta^f F n \eta_s}{RT} \right] + (1-\beta^f) \exp \left[\frac{-(1-\beta^f) F n \eta_s}{RT} \right]}{\exp \left[\frac{\beta^f F n \eta_s}{RT} \right] - \exp \left[\frac{-(1-\beta^f) F n \eta_s}{RT} \right]} \right] \end{aligned} \quad (2.6.147)$$

The expression in brackets is well behaved as $\eta_s \rightarrow 0$ adding a constant RT to the activation energy, independent of the value of β^f . The expression for the activation energy of the exchange current density is Eqn. (2.6.148).

$$E^{i_0} = E_{f,i} - \beta^f \Delta G_R^o - RT^2 \left((1 - \beta^f) \sum_k \nu_{k,i}^r \frac{d \ln \gamma_k}{dT} + (\beta^f) \sum_k \nu_{k,i}^p \frac{d \ln \gamma_k}{dT} \right) \quad (2.6.148)$$

E^{i_0} is an observable quantity. Note, the quantity ΔG_R^o is set by convention via setting the value at any one interface via the chemical potential of the electron. ΔG_R^o is not an observed quantity. We note that we can obtain any effective observed value of E^{i_0} even if ΔG_R^o is set by convention to an arbitrary constant by adjusting the value of $E_{f,i}$ commensurately. $E_{f,i}$ and $E_{r,i}$ should therefore be considered to be a function of the electron chemical potential convention for reactions involving electron transport across interfaces. For this reason, it is probably best to switch to a formulation of surface kinetics that sets the value of E^{i_0} directly. This is carried out within Cantera by specifying the Exchange Current Rate coefficient formulation for specifying surface reaction rate coefficients.

2.6.5.3 Formulation of existing charge-transfer reactions

In order to contrast Cantera's implementation we will explore a more traditional formulation based on Newman's lithium ion battery work. Lithium insertion into an electrode is represented by Eqn. (2.6.149).



This reaction is usually represented in terms of a Butler-Volmer representation, Eqn. (2.6.150).

$$j_n = k^a (c_t - c_s)^\alpha (c_s)^\alpha \left(\exp\left(\frac{\alpha F}{RT}(E-U)\right) - \exp\left(\frac{-\alpha F}{RT}(E-U)\right) \right) \quad (2.6.150)$$

This is represented in terms of the exchange current density, Eqn. (2.6.151).

$$i = i_o \left(\exp\left(\frac{\alpha_a F}{RT}(E-U)\right) - \exp\left(\frac{-\alpha_c F}{RT}(E-U)\right) \right) \quad (2.6.151)$$

η , the overpotential, is defined as Eqn. (2.6.152).

$$\eta = \Phi_1 - \Phi_2 = E - U \quad (2.6.152)$$

Φ_1 is the voltage within the electrode, while Φ_2 is the voltage in the solution adjacent to the electrode. When $E = U$ there will be no current crossing the interface according to Eqn. (2.6.150). The definition of the overpotential in this section is the same as was used in the preceding

section. The value of U we defined in Eqn. (2.6.150) is equal to E^{eq} , which we have defined in the last section.

The open-circuit potential of insertion materials varies with the amount of lithium inserted and is expressed by a general function of composition of the electrode.

$$U = U^\theta - U_{ref}^\theta + F(c_s) \quad (2.6.153)$$

This is a point that is mentioned in the Newman work. However, it needs to be emphasized how important these parameters are to the numerical model's success at fitting experimental discharge curves. The calculation of U^θ involves the same amount of complexity as the solution of Eqn. (2.6.122); it's just buried within the Newman formalism and then typically parameterized from experiment.

The determination of U_{ref}^θ is of particular note. U_{ref}^θ is set such that the potential drop across a particular electrode within the "current" calculation is zero. This is exactly what we did when we set the electron chemical potential in Eqn. (2.6.100) and Rxn. (R4). However, Cantera's implementation is more formal, and therefore the results end up less error prone.

In summary, Cantera's representation in terms of mass-action kinetics formulations is consistent with Newman's formulations, but an argument can be made that it is more generalizable and formal.

2.6.6 Enthalpy Formulation of the Heat Equation

The enthalpy formulation of the energy equation has been widely used in systems involving phase changes due to its inherent simplicity and coherency. We use it here to describe the thermal behavior of batteries. In the past thermal management of batteries have usually started off with the temperature equation, see (Gu and Wang 2000). We start with formulations developed for deformable porous media. The enthalpy formulation of the energy equation has been widely used in systems involving phase changes due to its inherent simplicity and coherency. We use it here to describe the thermal behavior of batteries. In the past thermal management of batteries have usually started off with the temperature equation, see (Gu and Wang 2000). We start with formulations developed for deformable porous media (Martinez and Stone 2008; Martinez, Stone et al. 2011) We add convection of enthalpy and the add the electrochemical energy of charged species in a voltage field to arrive at Eqn. (2.6.154) The enthalpy formulation of the energy equation has been widely used in systems involving phase changes due to its inherent simplicity and coherency. We use it here to describe the thermal behavior of batteries. In the past thermal management of batteries have usually started off with the temperature equation, see (Gu and Wang 2000). We start with formulations developed for deformable porous media.

$$\frac{d\left(\sum_p \rho_p \hat{\mathcal{U}}_p\right)}{dt} + \nabla \cdot \left(\sum_p \rho_p \hat{\mathcal{H}}_p \mathbf{v}_p\right) + \nabla \cdot \left(\sum_p \hat{\mathbf{q}}_{e,p}\right) = Q \quad (2.6.154)$$

is the specific internal energy of the phase p in the mixture, also including terms associated with charged species in a potential field. Ignored in the present treatment, this term could also include changes in the electric capacity via charging of the double layer. However, all phases in the current treatment are considered to be charge neutral up to this point. $\hat{\mathcal{H}}_p$ is the specific mixture enthalpy of the phase p with additions for charges in electric fields. Again, because phases, especially the electrolyte, are electro-neutral, these extra terms are zero. \mathbf{v}_p represents the superficial velocity of phase p .

$\hat{\mathbf{q}}_{e,p}$ represents the diffusive flux of energy in phase p . We sum over phases here, because there may be separate conduction processes in connected phases of a multiphase material if they are above the percolation threshold. $\hat{\mathbf{q}}_{e,p}$ includes the flux of enthalpy due to diffusion with additions for charged species.

$$\hat{\mathbf{q}}_{e,p} = -\lambda_p \nabla T + \sum_k \mathbf{j}_k \cdot \nabla H_k \quad (2.6.155)$$

Within Eqn. (2.6.155) we may separate out the terms due to charge transfer to yield

$$\begin{aligned} \hat{\mathbf{q}}_{e,p} &= -\lambda_p \nabla T + \sum_k \mathbf{j}_k \cdot \nabla H_k - \mathbf{i}_p \cdot \nabla \phi_p \\ &= -\lambda_p \nabla T + \sum_k \mathbf{j}_k \cdot \nabla H_k - \nabla \cdot (\mathbf{i}_p \phi_p) + \phi_p (\nabla \cdot \mathbf{i}_p) \end{aligned} \quad (2.6.156)$$

The latter form in Eqn. (2.6.156) is the form that's implemented in the 1D battery code. It's recognized that the second to last term in Eqn. (2.6.156) is eventually the reversible power output of the battery.

2.6.7 Darcy's flow Equation for flow and Changes in Electrode Porosity

Bulk flow of the electrolyte is necessary when the electrodes change their volumes. The axial momentum equation is replaced by Darcy's flow in porous media, written for a two phase flow implementation where S_e is the relative saturation of the electrolyte in the pore space of the electrode, and S_g is the relative saturation of a gas phase, if present.

$$\frac{d}{dt}(\phi(S_e \rho_e)) + \nabla \cdot (\rho_e \mathbf{v}_e^d) = Q_e \quad (2.6.157)$$

$$\frac{d}{dt}(\phi(S_g \rho_g)) + \nabla \cdot (\rho_g \mathbf{v}_g^d) = Q_g \quad \text{where} \quad S_e + S_g = 1$$

ϕ is the porosity of the electrode, and ρ_e is the density of the electrolyte phase. Q_e is the mass source term for the electrolyte phase, which will be nonzero due to Li^+ production and destruction in the electrodes. \mathbf{v}_e^d is the Darcy velocity for the electrolyte phase

$$\mathbf{v}_e^d = -\frac{k_{re} k}{\mu_e} \nabla P_e \quad \mathbf{v}_g^d = -\frac{k_{rg} k}{\mu_g} \nabla P_g \quad (2.6.158)$$

Where P_e is the pressure of the electrolyte phase., μ_e is the viscosity of the phase, k is the permeability of the porous phase, k_{re} is the relative permeability of the electrolyte phase. A key quantity is the capillary pressure, p_c , relating the pressures in the two phases

$$p_c = P_g - P_e \quad (2.6.159)$$

Both the relative permeabilities of the phases and the capillary pressure are parameterized as functions of the surface tension, and relative saturation of the phases with common parameterization functions (not included here) being Udell and Fitch (Udell and Fitch 1985) and van Genuchten (Genuchten 1978) (see (Martinez, Stone et al. 2011) for a detailed explanation).

The porosity of the media may be determined by an effective stress principle for porous media in principle and by tracking the solid mechanics of the porous medium (Martinez, Stone et al. 2011). This is a complicated process employing many empirical relations. However, here we employ a simple correlation based on how much a swelling of the electrode leads to an increase in the superficial volume of the electrode compared to how much it shrinks the electrolyte porosity. In some cases this is a readily observable experimental quantity. Each cell in the electrode is an extensive solid volume. Let's the cell's extensive volume, V_j^{sub} and lets call the actual solid volume of the object V_j^s . Then, the porosity of the cell may be calculated from Eqn. (2.6.160).

$$V_j^{sup} = \frac{V_j^s}{1-\phi} \quad (2.6.160)$$

Let's define the following empirical swelling function for the superficial velocity gain due to a solid velocity gain, Eqn. (2.6.161).

$$\frac{dV_j^{sup}}{dV_j^s} = \frac{\alpha}{1-\phi} \quad \text{where} \quad \alpha \rightarrow 1 \quad \text{as} \quad \phi \rightarrow 0 \quad (2.6.161)$$

α may be a function of the porosity that varies between 0 and 1. But, for stability and physical considerations, it must be the case that it goes to 1 as the porosity disappears. Then, the

Lagrangian solid mesh motion may be determined from Eqn. (2.6.161), and the porosity of the electrode may be calculated from Eqn. (2.6.160). Of course what's missing from Eqn. (2.6.161) is a feedback on α of the applied effective stress on the electrode. In other words the more the electrode is squeezed the tighter the pore space is reduced compared to its expansion. While this is beyond the current implementation, linear elastic implementations have been carried out in Goma and Aria, but without the swelling component of the electrode that changes the materials reference state configuration via Eqn. (2.6.161). A program is being started within Aria to combine all of these features.

2.6.8 Modular Architecture for 1D Electrode Model

The 1D electrode code has a modular approach to domain construction, depicted in Figure 54. There are two different types of domains: surfaces and volumes. Volume domains contain a control volume cell formulation for a single set of equations. Volume domains are then sandwiched between surface domains. Surface domains serve several purposes. First, boundary conditions for volume domain equations may be applied on surfaces. Secondly, tie conditions may be applied on surfaces. Tie conditions combine the conservation equations for neighboring cells into a single conservation equation. For example, the conservation equation for the Li^+ electrolyte species in the Volume anode domain and the Volume Separator domain are tied together so that the species is conserved across the domain boundary and so that there is only a single unknown specified at the interface between the domains for the Li^+ species concentration.

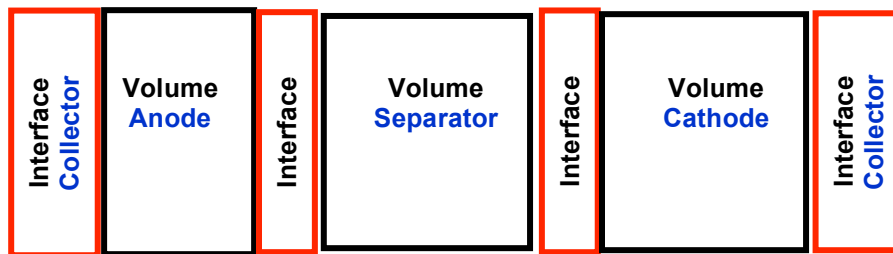


Figure 54 Modular Approach to construction of the Domain: Volume Domains are sandwiched between Surface Domains, on which boundary conditions and tie conditions are applied.

The third reason for surface domains is that actual unknowns may be associated with the domain. We have used this capability to model plate electrodes for example, where the electrode becomes a surface boundary condition instead of a volumetric source term.

Within each volume domain, a traditional node-centered control volume implementation is carried out. Most of the unknowns are located at the nodes. The axial velocities are formally located at the cell faces, which are positioned half-way between the nodes. Strict first order

upwinding is used for all convection operators; therefore, formally a strict maximum principle applies to the conservation equations. Diffusive fluxes are calculated at the cell faces, using independent state properties that are interpolated between the node points. Cells that are located at the ends of the domain are half-sized, since the corresponding node is located at the domain boundary. No attempt has been made to implement second order boundary conditions for fluxes at the ends of the domain. A mesh refinement algorithm has been targeted for this application, but has not been implemented.

The resulting set of equations is solved using Trilinos. Vectors and matrices are implemented with `Epetra` vectors and the `Epetra_VBR` matrix objects respectively. The algorithm can formally be solved in a multiprocessor context, using a ghost node formulation, where nodes are owned by processors, and rows are stored on a processor. Ghost rows in the vectors and Ghost columns within matrices are then implemented where needed. However, we have not kept up with the MP implementation due to time constraints. Solution vectors are primarily written out using an XML protocol, while the input file is controlled by an ASCII nested-block interpreter that reads a block keyline format.

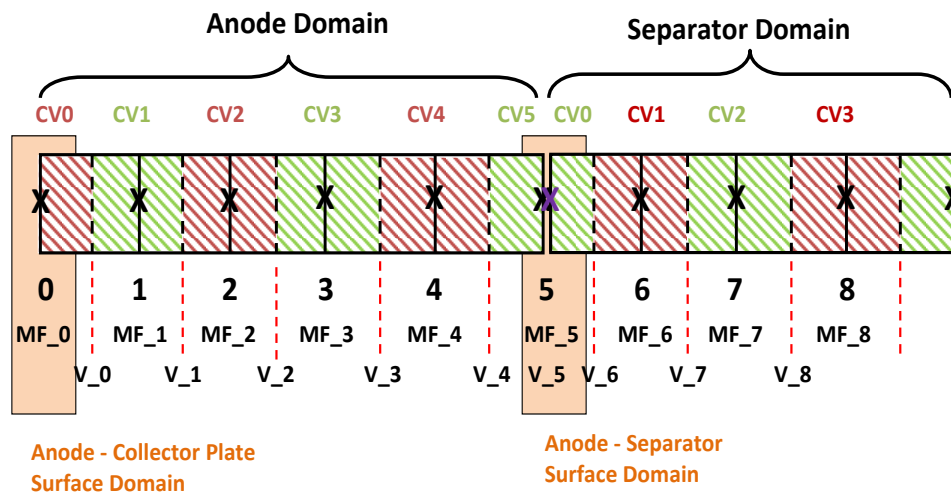


Figure 55 Node-centered Control volume implementation within each domain. Most variables are located at the nodes. Control volume faces are located at the midpoint between nodes. Axial velocities are located at the control volume faces.

2.6.9 Summary of the Equations System Solved by the 1D Electrode Model

The following equations are associated with the following independent variables. We separate the system into three cases, depending upon whether there is a pressure unknown introduced into the system and whether there is a gas phase. Currently, only system 1 has been completed. System 2 and 3 are under construction.

Equation	Unknown
System 1: (Reservoir assumption)	
Total continuity equation Eqn.	Reference Electrolyte Velocity \mathbf{v}^*
Conservation for species $1, \dots, N-2$ (Li^+) Eqn. (2.6.16)	----- Mole Fraction X_{Li^+}
Sum of mole fractions Eqn. (2.6.17) (solvent species)	----- Mole Fraction X_0
Electroneutrality Eqn. (2.6.18) (major anion)	----- Mole Fraction X_{N-1}
Current conservation Eqn. (2.6.24) and Eqn. (2.6.79).	----- Voltage Φ_e
Current conservation for Solid Eqn. (2.6.24)	----- Voltage Φ_s
Volume Conservation	----- Porosity ϕ
System 2: (Compressible, saturated Media approximation)	
Darcy's law electrolyte Eqn. (2.6.158)	---- Reference Electrolyte Velocity \mathbf{v}^*
Total Electrolyte continuity equation Eqn. (2.6.157)	---- Pressure P_e
Conservation for species $1, \dots, N-2$ (Li^+) Eqn. (2.6.16)	----- Mole Fraction X_{Li^+}
Sum of mole fractions Eqn. (2.6.17) (solvent species)	----- Mole Fraction X_0
Electroneutrality Eqn. (2.6.18) (major anion)	----- Mole Fraction X_{N-1}
Current conservation Eqn. (2.6.24) and Eqn. (2.6.79).	----- Voltage Φ_e
Current conservation for Solid Eqn. (2.6.24)	----- Voltage Φ_s
Enthalpy Conservation Equation Eqn. (2.6.154)	----- Temperature
Swelling Equation	----- Mesh Movement X_j^{node}
System 3: (Compressible, unsaturated dual phase approximation)	
Darcy's law electrolyte Eqn. (2.6.158)	Reference Electrolyte Velocity \mathbf{v}^*
Darcy's law gas Eqn. (2.6.158)	----- Reference gas Velocity \mathbf{v}^*
Total Electrolyte continuity equation Eqn. (2.6.157)	---- Pressure P_e
Total gas continuity equation Eqn. (2.6.157)	----- Pressure P_g
Conservation for species $1, \dots, N-2$ (Li^+) Eqn. (2.6.16)	----- Mole Fraction X_{Li^+}
Sum of mole fractions Eqn. (2.6.17) (solvent species)	----- Mole Fraction X_0
Electroneutrality Eqn. (2.6.18) (major anion)	----- Mole Fraction X_{N-1}
Conservation for gas species $1, \dots, N-2$ Eqn. (2.6.16)	----- Mole Fraction X_{H_2}

Sum of gas mole fractions Eqn. (2.6.17)	-----	Mole Fraction X_{N_2}
Current conservation Eqn. (2.6.24) and Eqn. (2.6.79).	-----	Voltage Φ_e
Current conservation for Solid Eqn. (2.6.24)	-----	Voltage Φ_s
Enthalpy Conservation Equation Eqn. (2.6.154)	-----	Temperature
Swelling Equation	-----	Mesh Movement X_j^{node}

A key to the implementation of System 2 and 3 has initially been found to be an implementation of artificial compressibility for the electrolyte phase. Unlike System 1 which has a reservoir, a phase within the System 2 system must compensate for changes in the volume of other phases facily. We've chosen the electrolyte system, where we are adding a compressibility term to the electrolyte equation of state.

2.6.10 Calculation of Source terms – Need for integrated source terms

The electrode may have an internal state represented by internal morphology, and therefore the electrode may have internal state variables that are not posted to the exterior of the object. Therefore, all source term evaluations done on the electrode must formally be couched in terms of integrated changes in time. Let A_i^E be the set of variables that are external to the electrode. All of the A_i^E will be part of the solution vector. Therefore, their time step truncation errors will be controlled as part of the predictor-corrector integration procedure. The following independent variables are part of A_i^E , the external variables for electrode i .

- X_k Electrolyte species mole fractions,.
- v Mass or mole averaged velocity of the electrolyte.
- V_a Anode voltage
- V_e Electrolyte voltage
- ϕ Electrolyte volume fraction, from volume conservation equation

However, there are variables that are not part of the global solution vector that are part of the intrinsic solution vector of each Electrode object. The set of these variables will be denoted by the Greek symbol, α . Within α , the following variables will be solved for, depending on the sophistication of the implicit model for the electrode.

- N_k^s Number of moles of each solid component of the electrode
- A_{e-pi}^s Surface area of each solid phase wrt the electrolyte phase e

A_{pi-pj}^s Surface area of each solid phase i wrt another solid phase j

How does this fit into the integration scheme? Let's take the example of the solution electrolyte phase.

To formulate the equation system we apply a control volume scheme around cell i , and employ a control volume discretization scheme in the time domain as well, to formulate a conservative scheme. Eqn. (2.6.162) results. $V_{i,n+1}$ is the volume of cell i at time $n+1$. $A_{iL,n+1}$ is the surface area of the left boundary of cell i at time $n+1$.

$$\frac{(V_i C_T \phi X_k)_{n+1} - (V_i C_T \phi X_k)_n}{t_{n+1} - t_n} + n_{iL} \bullet [A_{iL} C_T \phi X_k (\mathbf{v} + \mathbf{V}_k)] + n_{iR} \bullet [A_{iR} C_T \phi X_k (\mathbf{v} + \mathbf{V}_k)] = (V_i w_k)_{n+1} \quad (2.6.162)$$

In Eqn. (2.6.162), $(w_k)_{n+1}$ is the source term for species k evaluated at the conditions pertinent to $t = t_{n+1}$. The source term is evaluated at the conditions of the external variables, i.e., at $t = t_{n+1}$. But, also represents an integration from conditions at $t = t_n$ to $t = t_{n+1}$ within the internal state of the electrode object. This may involve abrupt transitions in the electrode structure, or it may involve non-uniform source terms wrt time within the $t = t_n$ to $t = t_{n+1}$ period due to changes in the internal morphology or internal state of the electrode. Keeping track of these changes requires us to use a formulation where we integrate the internal state of the electrode from $t = t_n$ to $t = t_{n+1}$ and use that within Eqn. (2.6.162). This concept is expressed by Eqn. (2.6.163).

$$V_i w_{k,n+1} (A_{n+1}^E, z_{n+1}, t) \rightarrow \frac{\int_{t_n}^{t_{n+1}} S_k^E (A_{i,n+1}^E, z, t) dt}{t_{n+1} - t_n}, Z_{n+1} - Z_n = \int_{t_n}^{t_{n+1}} f (A_{n+1}^E, Z, t) dt \quad (2.6.163)$$

S_k^E is the source term for the Electrode object written as an explicit process. \mathbf{Z} is a vector of explicit quantities that represent the internal state of the electrode. Note, we do not achieve any extra level of time-step accuracy from this treatment, because we still use a constant value of A_{n+1} throughout the t_n to t_{n+1} integration. There are several advantages nonetheless. First, we achieve a level of separation between the models for the electrode and the 1D models for the cell. \mathbf{Z} doesn't have to be included in the source term vector for the 1D model. The number of unknowns within \mathbf{z} may vary as well from treatment to treatment. We can handle abrupt changes in the electrode structure such as the disappearance of a phase easily within the integration step. Eqn. (2.6.163) leads us to understand how embedded implicit coupling schemes should be handled in a general way, especially considering when the subgrid model gets to be very expensive.

In order to handle the implicit coupling within the 1D code, a jacobian must be formulated consisting of the variation of $V_i w_{k,n+1} (A_{n+1}^E, z, t)$ with respect to variables with the set, A_{n+1}^E . This

is easily achieved by integrating Eqn. (2.6.163) repeatedly with respect to deltas of each of the A_{n+1}^E variables.

In order to understand the time step truncation errors, predicted vs. corrected values of the A_{n+1}^E variables are calculated. This means that the time step error in these variables are controlled. The time step errors in the z variables are not under global time step error control. This issue may have to be addressed in the future by establishing a subcycling strategy that seeks to control the time step error within the Eqn. (2.6.163) integration step.

2.6.11 Models for the Electrode Object

The electrode object consists of a set of solid phases, a set of surface phase that bound the solid phases, an electrolyte phase, and constitutive relations relating the transport and reactions in these phases. We seek to describe an electrode using a general description that may be used in multiple contexts. In order to motivate the description, we will first describe the Newman problem from which originates the Electrode object in order to discover what properties the electrode object must have in order to function within the Newman equations

There are several view of the object. The external view is described by the following. The solid phases are described by independent variables consisting of temperature pressure and solid phase mole fractions of all of the solid phase species in the solid phases. A solid phase electrode at any particular point in space consist of a set of individual solid phases, α, β, χ, K . There may be more than one solid phase in an electrode at any time. Frequently, there will be two or more solids phases that exist at any time, since this represents the case of a plateau in the open cell voltage for the system. Mole numbers of phases are represented by the symbol n_{α}^p . The number of moles of species k (local phase index in the phase is given by the symbol $n_{\alpha,k}^p$. This same number may be represented by the symbol n_{ke}^e , where ke represents the index of the species in a group that represents all species in all phases within the object. In general, we treat the electrode as an extrinsic system, meaning that it has a given a set amount of moles to start. The number of moles of electrode and the resulting volume may vary as reactions occur. The vector, n_{ke}^e , partly represents the internal state of the electrode.

Separating each solid phase from each other, there is a surface phase representing the interface between each of the solid phases. Each surface phase has a surface area associated with it. On each surface there are optionally a set of surface species and a surface reaction object which has a set of reactions involving the surface species and the two neighboring bulk phases. Surface may be subdivided further. Some surfaces will represent interfaces with the electrolyte; these are put in a separate category. The surface concentrations of species are added to the total list of species in the electrode, n_{ke}^e . The concentration of a surface phase depends on the concentration of the two bulk phases which the surface phase separates. Obviously, if one of the adjacent bulk phases has a zero concentration, the surface phases which adjoin it also have zero concentrations. The bulk electrolyte phase is assumed to always be present.

Within each bulk phase there may be a diffusion object representing the diffusional transport of ions, and electrons/holes within the object. Diffusional transport occurs between surfaces surrounding the bulk phase. Electron and hole transport is also assumed to occur between adjacent cells, each of which has an electrode object. The effective conductivity of the electron and hole transport is a constitutive property of the electrode that depends upon the morphology of the electrode.

Each bulk phase within the Electrode object may have its own voltage. However, for inclusion into the Newman equations, the identification of a voltage of the electrode is needed. This is carried out by assuming that there is a phase which constitutes the contiguous bulk phase within the Electrode object, i.e., the matrix phase. The voltage of this matrix phase will be associated with the voltage of the bulk of the electrode.

The way we will start up the system in the simplest cases is to assume that the electrode is a collection of N_p interconnected sphere, where N_p is picked to represent the exact amount of material represented by the extrinsic Electrode object given an input particle size.

Initially we have assumed that the electrode exhibits pseudo steady state diffusion. However, recently we have started to relax that assumption so that we may get all of the time scales inherent in solid state diffusion and reaction so that we may model impedance spectroscopy results. Below we describe a few of the electrode models. This is not an exhaustive list of models; we have left some models out of the description. From a computer science perspective each of these models are subclasses of a general Electrode class that can be used in multiple codes and contexts.

2.6.11.1 Continuously Stirred Tank Reactor (CSTR) Model

The CSTR model assumes that the Electrode object is a well-mixed solid solution consisting of N_{part} identical particles. Each particle has a mixture of solid phase species in the particle given by the total mole number, n_{ks} of species of type ks within the electrode object. The total surface area of a single particle is given by $a_{sa,part}$; this may vary throughout the calculation as the volume of the particle changes due to reactions, but a spherical geometry is currently assumed. The rate of change of the mole numbers of species calculated from a single interfacial kinetics object with the possibility of multiple reactions occurring on the exterior surface, Eqn. (2.6.164).

$$\frac{dn_{ks}}{dt} = a_{sa,part} N_{part} \sum_{j=1}^{N_r} (ROP_j) \alpha_{ks,j} \quad (2.6.164)$$

ROP_j is the rate of progress of the j^{th} surface reaction. $\alpha_{ks,j}$ is the stoichiometric coefficient for the ks solid-phase species in the j^{th} reaction. For this object the state variables, z , mentioned in the previous section refer to the n_{ks} solid phase species. The formulation of ROP_j has been mentioned in previous sections, see Section 2.6.5 for example. The rate of progress to reemphasis, depends on temperature, pressure, the voltage across the interface and the mole

fractions of the species in the solid solution, the availability of phases in the solid solution, and the mole fractions of species in the electrolyte phase.

The expression for the source term is given by Eqn. (2.6.163). The source term fits into continuity equations at the 1D electrode level like Eqn. (2.6.162). There are source term expressions for Li^+ in the solution and electrons in the solid phase. To be precise the source term for Li^+ for the CSTR Electrode object can then be written as Eqn. (2.6.165), which is written as an explicit representation with units of kmol s^{-1} .

$$\left(V_i w_{\text{Li}^+} \right)_{n+1} \left(A_{n+1}^E, z_{n+1}, t \right) = \frac{\int_{t_n}^{t_{n+1}} S_{\text{Li}^+}^E \left(A_{i,n+1}^E, z, t \right) dt}{t_{n+1} - t_n} = \frac{N_{part} \int_{t_n}^{t_{n+1}} a_{sa,part} \sum_{j=1}^{N_r} \left(ROP_j \right) \alpha_{\text{Li}^+,j} dt}{t_{n+1} - t_n} \quad (2.6.165)$$

It should be mentioned that there are hard digital limits imposed on the mole fractions of solid phase species in some cases. The CSTR object will act as if it has run out of a particle species just as if the phase has disappeared. This is due to the fact that activity coefficient representations of solid solutions are sometimes fit over a limited set of conditions. Usage outside of that domain is not warranted and may lead to misleading results. In order to implement the hard limit, solution for the exact time at which the hard limit is reached has been implemented. The technique for this is explained later.

To approximate the effect of resistance due to the presence of an SEI layer, the CSTR Electrode object was extended to permit specification of a resistance across Anode-Separator (or Cathode-Separator) Surface Domains, i.e. the interface between the anode (or cathode) and the electrolyte. Given the current state of the Electrode object and a specified resistance, this extension to the CSTR model uses bisection to self-consistently find the resulting current and voltage drop across the electrode/electrolyte interface. This voltage drop results in a reduced overpotential in the Butler-Volmer kinetics for the surface interface reactions and thereby a reduced current across the interface, relative to the zero-resistance case. Figure 56 shows cell voltage as a function of charge during fixed-current charge/discharge cycles for two values of current (1 amp/m^2 and 5 amp/m^2) and two values of resistance at the anode/electrolyte interface (0.0 ohm m^2 and 0.5 ohm m^2). The cathode/electrolyte interface has zero additional resistance. As expected, the model predicts that higher current and/or higher resistance decreases cell voltage during discharge and increases required voltage when charging, resulting in overall less efficient cycling.

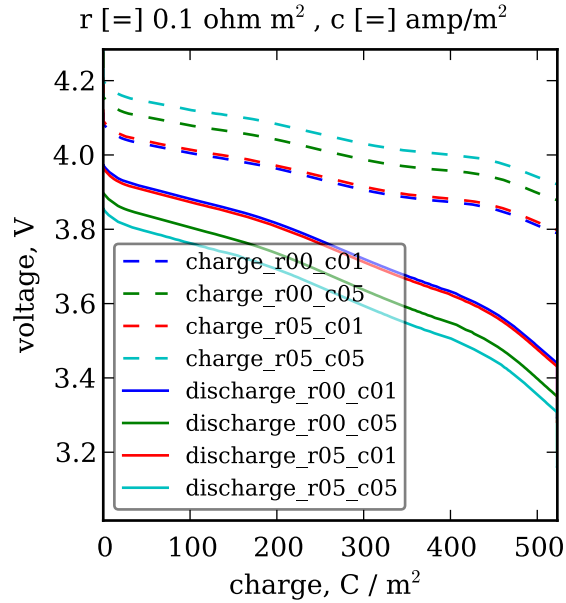


Figure 56: Cell voltage versus charge during fixed-current charge/discharge cycles for two values of current 'c' (1 amp/m² and 5 amp/m²) and two values of resistance 'r' at the anode/electrolyte interface (0.0 ohm m² and 0.5 ohm m²). The cathode/electrolyte interface has zero additional resistance.

2.6.11.2 Pseudo-Steady State Diffusion Model with Phase Change

Typically, within simple reaction mechanisms for anodes and cathodes involving the insertion or depletion of a single ion creating a new solid phase in the process, we can formulate the reaction rate via the following equation, Rxn. (AB)



But, now assume that we want to incorporate the effects of a solid diffusion process into the formulation. Then, we can expand the problem into the following form.

Assume we are solving a spherical diffusion problem from an inner sphere at radius r_i and concentration C_i to an outer sphere at radius r_o and concentration C_o . Assume the diffusion mechanism is pure Fickian with a diffusion constant of D . The model is roughly depicted in Figure 57.

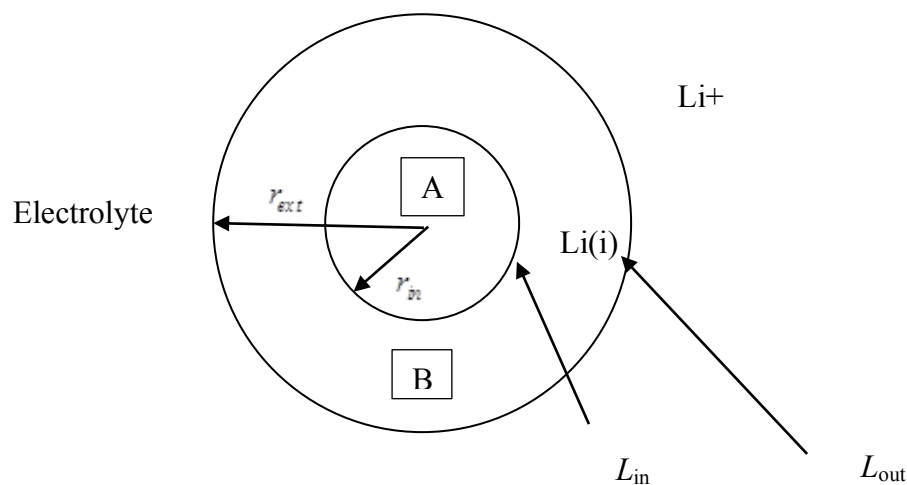


Figure 57 Schematic of the electrode model for Pseudo-State state diffusion involving phase transformation.

There is a general reaction at the exterior interface and a general reaction mechanism at the interior interface in. Between the two interfaces, solid phase diffusion of lithium is assumed to occur. In general, the actual problem involves time dependent diffusion within a sphere

$$\frac{dC}{dt} = \frac{D}{r^2} \frac{d}{dr} \left(r^2 \frac{dC}{dr} \right) \quad (2.6.166)$$

Boundary conditions of the third kind are implemented on the interior and external surfaces. We seek to find approximations to the solution of this problem. The first approach described in this section is to linearize all reactions and diffusion processes and assume that they are in steady state. Thus we will simplify, but in the process lose the performance of the model for short time scales.

At the inner surface depicted in Figure 57 we have an inner reaction.



At the exterior surface we have an exterior reaction. It is assumed that charge transfer occurs at the exterior reaction.



Li(i) are interstitial lithium atoms within the B phase. Rxn. (ext) represents the charge transfer reaction within the electrode. The electron is assumed to diffuse within the electrode via a separate mechanism involving the conduction band.

In the solution to this system, we first assume that either the outer or inner reactions are fast compared to diffusion and the other reaction. Then, we nondimensionalize the equations using a Damkoeler number. The details of the derivations are in (Moffat 2012). In the derivation of the equations care must be taken to formulate a complete model for all four rate constants involved with Rxn. (inner) and Rxn. (ext) such that the system is completely specified. The final equations are stated here.

For the situation where the inner reaction is rate limiting, the equations are

$$\frac{dn_A}{dt} = -(4\pi r_{in}^2 N_p) ROP_{inner} \quad \text{where} \quad ROP_{inner} = k_{r,inner} - k_{f,inner} [\text{Li(i)}_{inner}] \quad (2.6.167)$$

It has a ROP formulation that is equal to Eqn.(2.6.167). The diffusive flux at the inner surface is equated with the net ROP from the inner reaction to yield Eqn. (2.6.168).

$$ROP_{inner} = \frac{1}{1 + Da_{in}} \left[k_{r,inner} - k_{f,inner} \left(\frac{k_{r,outer}}{k_{f,outer}} \right) (ca_{Li^+}) (ca_{e^-}) \right] \quad (2.6.168)$$

$$Da_{in} = \frac{(r_{out} - r_{in}) k_{f,inner} r_{in}}{D c_o r_{out}}$$

For exterior reaction limited situations,

$$\frac{dn}{dt} = -4\pi r_{out}^2 ROP_{ext} \quad (2.6.169)$$

Where

$$ROP_{ext} = \frac{k_{f,ext}}{1 + Da_{out}} \left[L_{in} - \frac{(ca_{Li^+})(ca_{e^-})}{K_{ext}} \right] \quad Da_{out} = \frac{k_{f,ext} (r_{out} - r_{in}) r_{out}}{D c_o r_{in}} \quad (2.6.170)$$

Figure 58 and Figure 59 contain representative results from the electrode object for understanding the evolution of an FeS₂ cathode in a thermal battery. One of the goals of the analysis was to determine whether a solid phase diffusion mechanism could be distinguished from a mechanism based on fitting the exchange current density.

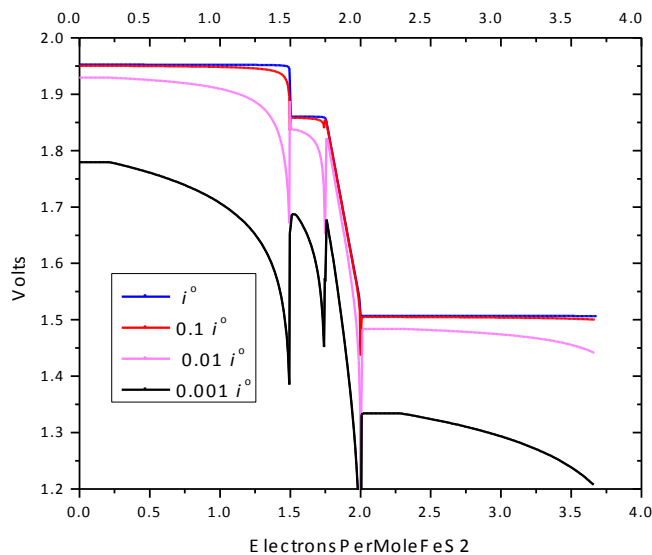


Figure 58 Variations of the constant current curves as the exchange current density is varied. 50 amp current at various exchange current densities assuming infinitely fast diffusion. In this version the reaction's rate of progress is proportional to the inner surface area.

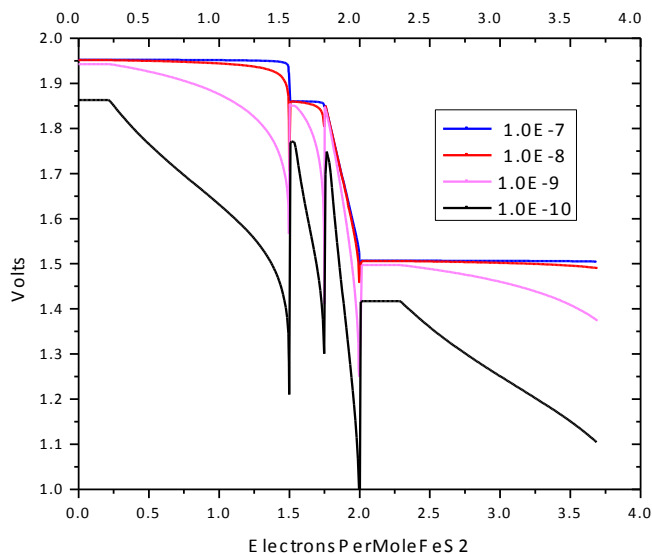


Figure 59 Variations of the constant current curves as the exchange current density is varied. 50 amp current at various exchange current densities for a fixed value of the diffusion coefficient of 1.0E-8

The FeS₂ electrode goes through multiple plateaus as it is discharged, a concept that will be addressed further on. However, it is clear that the gross DC behavior of the two limiting behaviors are roughly equivalent to one another. Therefore, from the DC behavior the rate limiting step can't be distinguished between exchange current density limited and solid phase diffusion limited. Note, however that the AC behavior between the two models is very different. This motivates the need to go to AC impedance modeling matched with experimental impedance spectroscopy to differential mechanisms.

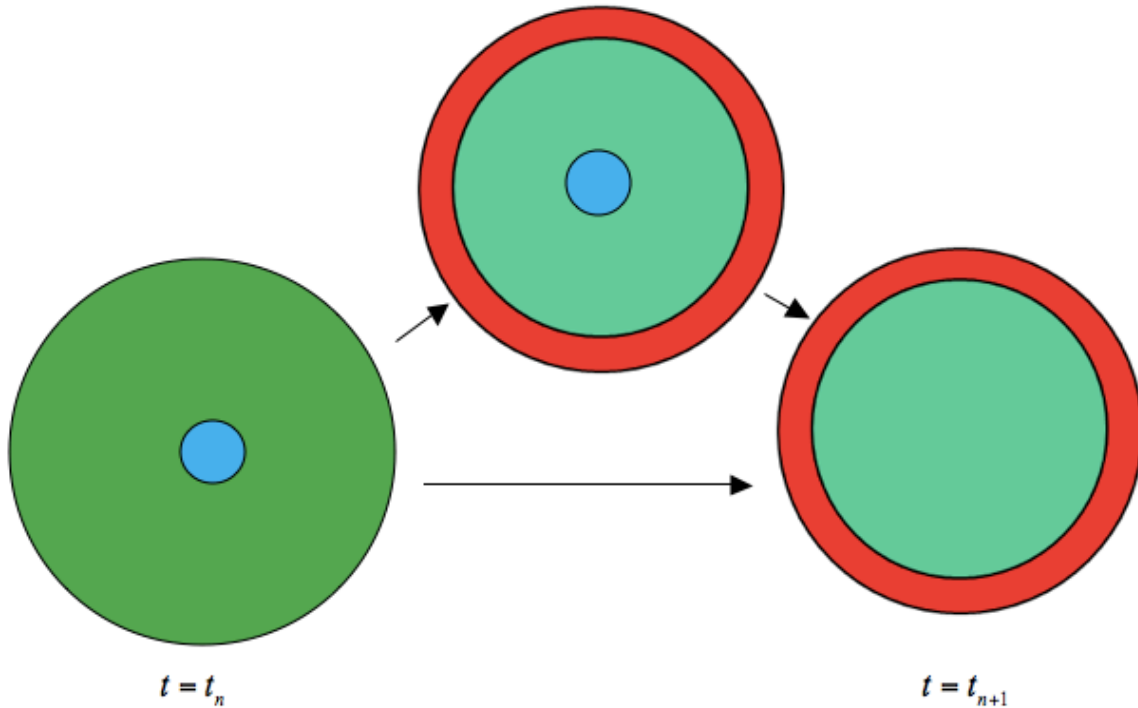


Figure 60: Phase blue disappears on going from $t = t_n$ to $t = t_{n+1}$, while phase red appears on the outside. Two cases may occur depending on whether red nucleates before blue disappears. In the text, the inner blue region will be called S1 (solid#1). The green region will be called S2, and the red region will be called S3. After blue disappears, green will be S1, and red will be S2.

2.6.12 Multiple Plateau Regions

It may be the case that there are two active surfaces at once where reactions are taking place. This would mean that there would be three different regions inside each particle with reactions on the two inner surfaces and on the exterior surface, all at once. Therefore, the depiction of morphology described in Figure 57 must be expanded to include the depiction in Figure 60. The reason for this is clearly shown in Figure 58 and Figure 59. Essentially there may be a solid phase diffusional resistance or a loss in surface area that reduces the production rate from the

inner surface as a plateau materials ends. This means that the voltage may have to drop so much from the open circuit voltage for the inner plateau in order to produce additional electrons that other reactions may start to be thermodynamically possible.

We start a treatment of this case here. We have developed the equations for the evolution of the radii starting with the inner region and then working our way out to the exterior radius. S1, S2, and S3 will denote the regions. We report the results here and refer the reader to original references for the details (Moffat 2012). The subscript *i* will denote the inner surface, *os* will denote the second surface, and *es* will denote the exterior surface.

The basic equations for evolution of the electrode depicted in Figure 60 do not change, but it gets generalized. Now there are multiple surfaces denoted by the symbol *b*, and the expression for the time dependent change of solid phase species *ks* becomes Eqn. (2.6.171).

$$\frac{dn_{ks}}{dt} = \sum_b^{N_s} a_{sa,part}^b N_{part} \sum_{j=1}^{N_r^b} (ROP_j^b) \alpha_{ks,j}^b \quad (2.6.171)$$

Now, there is an overall summation over active surfaces, which represent annular regions of the particle (see Figure 60). We currently limit the number of reacting surfaces to two plus the exterior surface. Each surface has its own `InterfaceKinetics` Cantera object, on which a variable number of reactions, N_r^b , can be defined.

From the basic species production equation, we may then define production rates for phases. Each phase is defined to exist on a particular region in the electrode. A region is defined as one of the colors in Figure 60. The electrode will usually exhibit a plateau in its open circuit voltage when two regions separated by a single boundary exists within the electrode. When a particular region is consumed then the open circuit voltage undergoes a noncontinuous change in value. If the region contains multispecies phases, then the open circuit voltage can vary continuously with the state of charge as the composition of the phase changes with state of charge.

As the phase numbers change in Eqn. (2.6.171), the relative volumes of the regions change, and therefore, the effective surface areas, $a_{sa,part}^b$, between the volumes change as a function of the state of charge. One notable difference in behavior between heterogeneous kinetics as described in Eqn. (2.6.171) and homogeneous kinetics systems that the reader may be more familiar with is their limiting time behavior. It can be shown that there is a finite time dependence to the destruction of phases in heterogeneous systems (for spheres it is proportional to $t^{1/3}$, whereas in homogeneous systems exponential decaying solutions of species profiles are the norm.

Essentially for the subgrid integrations of Eqn. (2.6.171), we employ a backwards Euler predictor corrector method. However, a strict backwards Euler implementation of Eqn. (2.6.171) leads to a direct failure of the method during geometry changes. This is because the equation depends on the surface area of the interface, $a_{sa,part}^b$, which actually approaches zero as the phase disappears, and much of the complications in dealing with the equation system has to do with this term. The exact formula for the time discretization is given below.

$$\frac{n_{ks}^{n+1} - n_{ks}^n}{\Delta t^n} = \sum_b^{N_s} a_{sa,part}^{b,eff} N_{part} \sum_{j=1}^{N_p^b} (ROP_j^{b,n+1}) \alpha_{ks,j}^b \quad (2.6.172)$$

Where

$$a_{sa,part}^{b,eff} = 0.5(a_{sa,part}^{b,n+1} + a_{sa,part}^{b,n})$$

We have experimented with additional formulas for $a_{sa,part}^{b,eff}$, including more logically consistent approximations. However, that is the formula currently being used and it has no numerical drawbacks. $a_{sa,part}^{b,n+1}$ is the surface area of the interface calculated at the end of the BE step, using the region volumes calculated from n_{ks}^{n+1} . For further information our thermal battery modeling references should be queried.

Within the approximation, we have logically assigned the global reaction rate to the inner surface and not the exterior surface. However, an alternative formulation would be to assume that an expanded model formulation involving a charge transfer process at the exterior of the particle with and/or diffusion of neutral interstitial lithium into the solid particle where it then undergoes a further reaction leading to phase change. This has led to the combination of the algorithm in Section 2.6.11.2 with the current algorithm. We have implemented initial versions of that algorithm but have not productionalized it.

2.6.13 Algorithms for Handling Births and Deaths of Phases

Algorithms for the birth and death of phases have not been substantially published to date. We have found that this is an extremely tricky topic, especially when the phases to be birthed involve multispecies, nonideal phases. Here, we publish an algorithm that is robust in handling this important issue. Extensions to other fields such as geochemistry, and crystallization phenomena are evident.

What we presented in the previous section where we wrote down the equations for the time dependent evolution of phases using the mole number of species as the basic independent unknown was actually not used, though it is algorithmically identical to the actual equation set when phases aren't changing status. We have determined that the equation set to be solved must differentiate between the mole numbers of phases and the mole fractions of phases.

$$\frac{dn_p}{dt} = \frac{n_p^{n+1} - n_p^n}{t^{n+1} - t^n} = a_{outer}^* S_{p,outer}^{n+1} + a_{inner}^* S_{p,inner}^{n+1} \quad (2.6.173)$$

$S_{p,outer}^{n+1}$ is the source term for the creation of moles of phase p at the outer reaction surface. It is strictly evaluated at a the final time in the time step, $t = t^{n+1}$, in a backwards Euler manner.

$S_{p,outer}^{n+1}$ is evaluated as a sum over the

$$S_{p,outer}^{n+1} = \sum_{i \in p} S_{i,outer}^{n+1} \quad (2.6.174)$$

$S_{i,outer}^{n+1}$ is the source term for species i , which belongs to phase p , at the outer surface. a_{outer}^* is the surface area of the outer surface, evaluated at an intermediate time between t_n and t_{n+1} . In previous sections we have calculated the optimal time to evaluate the area. However, in our initial implementation we used a trapezoidal rule. It's turning out that this is ok. What's essential, however, is that the area not be evaluated at the final time. This avoids a singularity in the equation system that occurs when a phase disappears.

In these equations, we have separated out the inner and outer surface for reaction.

For multispecies phases, additional equations for the mole fractions of all species are introduced. The equation formulation is given below.

$$\frac{dn_i}{dt} = \frac{n_p^{n+1} X_i^{n+1} - n_i^n}{t^{n+1} - t^n} = a_{outer}^* S_{i,outer}^{n+1} + a_{inner}^* S_{i,inner}^{n+1} \quad (2.6.175)$$

One of the key issues in these calculations is the birth and death of phases. The death of phases occurs when the plateaus react out. Either the inner radius disappears or the outer annulus region reaches a zero thickness condition. Under these conditions it can be shown that the mole number of phase p goes to zero at a finite rate, and at a particular time, t_p^{death} . At this time, the source terms for all species and phases undergo an unavoidable and physically-realistic discontinuity. We handle the discontinuity by adding another equation to the system.

$$n_p^{n+1} = 0 = n_i^n + (a_{outer}^* S_{i,outer}^{n+1} + a_{inner}^* S_{i,inner}^{n+1}) (t^{n+1} - t^n) \quad (2.6.176)$$

And we use the independent variable t^{n+1} as the extra variable. We actually choose the phase p , that Eqn. (2.6.176) refers to by calculating the possible times of deaths of all phases that can die and we choose the minimum of the death times, or the original step time, whichever is shorter, Eqn. (2.6.177).

$$t^{n+1} = MIN(t_p^{death} \forall p, t_{n+1}^o) \quad (2.6.177)$$

Note, we make sure to only change the choice of phase p in Eqn. (2.6.176) when we are evaluating the base residual and not during numerical jacobian calculations. Also, we make sure to not change the formulation of the problem, i.e., that a phase p will die, during the nonlinear solution procedure. If during the nonlinear solution procedure the phase doesn't die, then the step is considered a failure, the local time step is reduced, and the nonlinear problem is retried.

When the phase p disappears the equations for n_p^{n+1} and X_i^{n+1} for i in phase p may actually stay unaltered. It may be shown however, that the equation for the mole fraction at the final time, X_i^{n+1} , becomes equivalent to Eqn. (2.6.178).

$$X_i^n = \frac{-\left(a_{outer}^* S_{i,outer}^{n+1} + a_{inner}^* S_{i,inner}^{n+1}\right)}{-\left(a_{outer}^* S_{p,outer}^{n+1} + a_{inner}^* S_{p,inner}^{n+1}\right)} \quad (2.6.178)$$

Eqn. (2.6.178) is well posed if the source terms for the production/loss of species i is dependent on the mole fraction of species i . If that is not the case (which would be unusual) we have employed the following equation.

$$X_i^{n+1} = \frac{-\left(a_{outer}^* S_{i,outer}^{n+1} + a_{inner}^* S_{i,inner}^{n+1}\right)}{-\left(a_{outer}^* S_{p,outer}^{n+1} + a_{inner}^* S_{p,inner}^{n+1}\right)} \quad (2.6.179)$$

This is always well posed.

For the case of the birth of a phase, we have found that the equations are extraordinarily dependent on the initial guess of the mole fractions of the phases which are being born. In general, there is only a narrow range of mole fractions over which the phase will first be stable and thus exhibit a positive value of $S_{p,outer}^{n+1}$. Also on the first step it must be the case that for species $i \in p$ then

$$S_{i,outer}^{n+1} > 0 \quad (2.6.180)$$

This must be the case for there to be a solution to the equations such that $X_i^{n+1} \geq 0$ for all species $i \in p$. This is also a desirable condition for a predicted solution of the equation system for phases which are being born, and a necessary condition if bounds on the mole fractions are to be imposed within the nonlinear solver when relaxing the equation system, a practical necessity.

It turns out that this condition exactly dovetails with the solution of the phase pop problem used in the equilibrium solver. The condition for the existence of a phase pop is qualitatively equivalent to the existence of mole fractions such that Eqn. (2.6.180) holds for a particular set of mole fractions. The mole fractions found by the phase pop calculation minimize a functional describing the Gibbs free energy change from the formation of the phase given a certain composition of the phase from the component basis species of the mixture. While the equilibrium phase pop problem doesn't take the reaction rate constants into consideration, it can be shown that the condition Eqn. (2.6.180) is satisfied in practice, as long as modes of the reaction mechanism aren't kinetically frozen.

Therefore, we may obtain a good initial guess if we seed the calculation with predicted mole fractions from the equilibrium solver. This involves adding a predictor step to the solution of the equation set.

A key issue for the successful solution of the equation set is the use of numerical damping. We always bound the values of the mole fractions such that the solution never lets them get outside the 0 and 1. Additionally, for phases that are predicted to be birthed during a particular time step, we bound their values to a value greater than zero. We have found this helps the initial solution. Mole numbers corresponding to other phases which are not popping, n_p^{n+1} , are not bounded; their values may go to less than zero. They are allowed to die according to the algorithm described by Eqns. (2.6.176) and (2.6.177), which requires that n_p^{n+1} go less than zero in order for the equation set to converge. Note, however, that the mole fractions for dying phases are still bounded even during the backwards Euler step during which they die.

For interfacial reactions involving phase transformations, the kinetics solver must be informed of phases which don't exist, in addition to their mole fractions. This is a key requirement for the correct handling of heterogeneous reactions involving moving fronts. In other words, if a species in a phase is a reactant to a heterogeneous reaction, and the phase moles for that reactant is zero, then the heterogeneous reaction cannot proceed in a forward direction.

However, we have found that it's essential that these flags associated with the existence of phases within the kinetics solver are not changed during the nonlinear solution method. Thus, the flags aren't turned off for phases which are popping into existence nor are flags turned off for phases which are dying according to the Eqns. (2.6.176) and (2.6.177) algorithm during the nonlinear solver. The general principle is that the scenario for phase births and deaths are set up during the predictor stage. Then, during the corrector stage the scenario is not changed as the nonlinear solver relaxes the equation set. If a converged solution to the scenario is not found, the time step is halved and the procedure redone.

2.6.14 Diffusion Models based on Point Defect Thermodynamics models for solid phases: Lattice Phases

We have used the following procedure to expand the mechanism for each plateau.

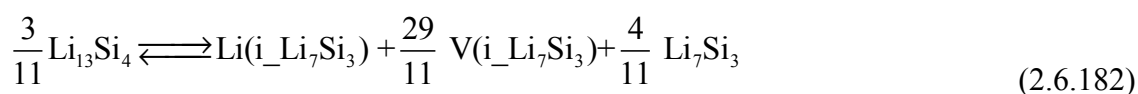
The diffusion mechanism presented in Section 2.6.11.2 lacks a physical basis that may be related to quantities calculated from first principles. In this section, we solve this problem for at least one example, linking it to Cantera's ability to model point defect thermodynamics models of solid phases. The example that we will use is the first plateau on a LiSi anode for a thermal battery. The overall reaction for this plateau is given as Eqn. (2.6.181).



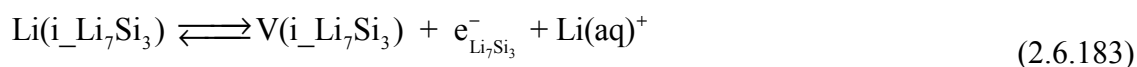
At equilibrium the electrochemical potential of this reaction is zero. Therefore,

$$\Delta G = \frac{4}{11} \mu_{\text{Li}_7\text{Si}_3} + \mu_{\text{Li}(\text{lyte})^+} + \mu_{e_{\text{Li}(0)}^-} - \frac{3}{11} \mu_{\text{Li}_{13}\text{Si}_4} = F(\Phi_m - \Phi_{\text{lyte}})$$

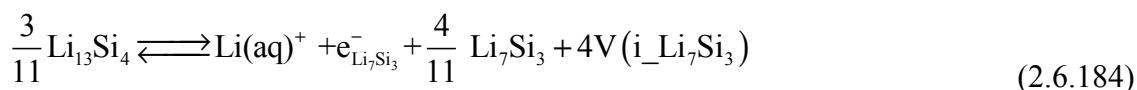
The reactions are now separated into two reactions, which occur on separate surfaces just as we did in Section 2.6.11.2. Now, however, we will identify a particular experimentally identified diffusion mechanism associated the diffusion process in the Li_7Si_3 phase. Diffusion will be assumed to be via an interstitial lattice sites. The main Li_7Si_3 lattice will be assumed to be fully populated. Therefore, the Li_7Si_3 phase will consist of two interrelated linked lattices. Cantera has the capability to model these types of solids with its `LatticePhase` object. On the inner surface the $\text{Li}_{13}\text{Si}_4$ species is transformed into a Li_7Si_3 species. The latter species is less lithiated than the former species. Therefore, in addition to the Li_7Si_3 species that's formed, a concentration of interstitials is postulated to be injected into the interstitial lattice of the Li_7Si_3 . We make the assumption that there is one interstitial site for every matrix site within each solid phase. The following equation sums up the inner reaction.



We assume that the interstitials occupy a different lattice than the Li_7Si_3 , formally. This interstitial lattice consists of two species, $\text{Li}(\text{i_Li}_7\text{Si}_3)$ and $\text{V}(\text{i_Li}_7\text{Si}_3)$ where V is the vacancy. In order to have a mole fraction for $\text{Li}(\text{i})$, which is essential for the thermodynamic consistency of the two surface reaction scheme, there needs to be two species on a lattice. The external complimentary reaction turns into the following form, Rxn. (2.6.183).



The lithium interstitial goes into the electrolyte solution leaving behind an electron and an interstitial vacancy. We have assumed that the electron transfer occurs at the electrolyte/solid interface. If you add up the two reactions, Rxn. (2.6.182) and Rxn. (2.6.183), you end up with something different than the original reaction, Rxn. (2.6.181).



This difference means that we have potentially changed the Gibbs free energy of the electrode reaction by this process. What we've done however does have physical significance. What we've done by adding in an interstitial lattice into the phase is to make the Gibbs free energy of the phase dependent on the Lithium element potential. We've changed the mole fraction of interstitial Li in the Li_7Si_3 by creating more Li_7Si_3 while ejecting a full $\text{Li}(\text{i})$ into the electrolyte. Rxn. (2.6.184) reflects this change in the interstitial lattice concentration and represents real phenomena that occur for non-stoichiometric solids. Experimentally, this effect actually shows up on experimental open circuit plots at the end of the plateau.

What this means however is that the open circuit potential for Rxn. (2.6.184) may be different than Rxn. (2.6.182) if the chemical potential of the vacancy isn't zero. The formula for the

chemical potential of the vacancy is given below, assuming ideal solution behavior on the lattice site.

$$\mu_V(T) = \mu_V^0(T) + RT \ln(X_V) = \mu_V^0(T) + RT \ln(1 - X_{\text{Li}(i)}) \quad (2.6.185)$$

Manipulation of the chemical potential of Li(i_Li7Si3) can make the value of $X_{\text{Li}(i)}$ as small as possible. And, then one can as a rule set the value of $\mu_V^0(T)$ to zero. However, the mixing term is formally non-zero, and will vary as a function of the conditions and Lithium element potential. Therefore, we've opted to set $\mu_V^0(T)$ to a value which sets $\mu_V(T)$ to zero at one temperature and lithium element potential, and let variations in the previous calculations propagate from that condition, hoping changes will be small in nature.

This example has shown that in principle quantities that can be calculated from DFT calculations of defect thermodynamics of solids can be used directly within the Electrode object.

2.6.15 Electrode model with Distributed Treatment of Diffusion

We've started models using the electrode object with a grid in the radial direction for both single phases and for multiple regions. First we start out with the equations for transport of species within the solid phase that account for lattice motion and nonideality of the solid phase. We apply this on a mesh that may be moving as the particle expands and contracts. Essentially this is the treatment that modern implementations of the Newman equation are built on. Notable contributions in this field include Newman, White and Kee. Ralph White had a notable contribution (Zhang and White 2007) within the field where he has tried out various methods for solving the electrode problem.

The initial conservation equation is Eqn. (2.6.186) for neutral molecule transport within an electrode. Note, we have already made the assumption that transport is via neutral molecules. However, this has been relaxed for example by (Colclasure, Smith et al. 2011) when developing models for the SEI layer. In those models, it is not assumed that electroneutrality holds, and therefore a complimentary Gauss' law equation for the electrical potential with the formation of surface space charge layers must be assumed.

$$\frac{\partial C_i}{\partial t} + \nabla \cdot (\mathbf{v}_L C_i) = \frac{1}{r^2} \frac{d}{dr} (r^2 j_{r,i}) \quad \text{where } j_{r,i} = -D \frac{d}{dr} (C^o X_i \gamma_i) \quad (2.6.186)$$

$j_{r,i}$ is the molar flux of species i . C^o is the standard concentration of the phase sites in the current phase. X_i is the mole fraction of species i on the phase sites, while γ_i is the activity coefficient of species i . Eqn. (2.6.186) may be enhanced to support more than one distributed phase. For example this is often done within solid phase systems to describe diffusion through multiple different types of lattices (Swalin 1972) that may be used to describe the

thermodynamics of a solid, as well as the addition of interstitial species that may exist on interstitial phases that may be used to describe diffusion processes.

In this equation \mathbf{v}_L is the material motion of the solid. As the material swells and contracts this motion will be nonzero. There have been several treatments of Lagrangian motion of a solid structure within porous flow frameworks within Sandia (Cairncross, Schunk et al. 1996; Schunk, Sackinger et al. 1998; Schunk 1999; Roach and Schunk 2000; Schunk 2000). These are very instructive to look at. However, none is exactly analogous to the current. This is not necessarily a deformation under an elastic strain. Instead the motion within Eqn. (2.6.186) is a modification to the reference state of the strain-free state, i.e., the reference state before deformation mechanics is applied, due to chemical reactions and solid state diffusion. Note, deformation mechanics as defined within these publications would then be applied on top of the reference state.

The reference state within solids may be clearly identified with an observable quantity. It's associated with the lattice of solids as the lattice gets contorted by swelling phenomena. Note, the lattices are not conserved necessarily within our system as reactions may cause damage to the lattice or we may be interested in growth of interfacial layers which are created by lattice-building reactions involving the electrolyte and interstitial compounds within the electrode (Colclasure, Smith et al. 2011).

The mesh may also move independently of the reference state; this is needed when additional lattice site are created at interfaces. The concentration variables are then calculated on a moving frame of reference that requires the addition of a substantial derivative to the equations. The final result is Eqn. (2.6.187).

$$\frac{\partial C_i}{\partial t} - (\mathbf{v}_s \cdot \nabla C_i) + \nabla \cdot (\mathbf{v}_L C_i) = \frac{1}{r^2} \frac{d}{dr} (r^2 J_{r,i}) \quad (2.6.187)$$

Boundaries between the domains are handled with interfacial kinetics objects. The boundary conditions for moving meshes at interfaces are given by the following equations for the mesh motion (i.e., the distinguishing condition) and the species conservation equation.

$$\mathbf{n} \cdot \mathbf{v}_s C^{T,\alpha} = \sum_{i=1}^N S_i^\alpha \quad (2.6.188)$$

$$\mathbf{n} \cdot \mathbf{J}_i = S_i^\alpha - \mathbf{n} \cdot \mathbf{v}_s C_i \quad (2.6.189)$$

This methodology has been used previously to model the growth of Cu_2S , a corrosion production of Cu and H_2S (Moffat, Sun et al. 2008). This capability is currently under construction.

2.6.16 Initial DAE problem

The battery code has been shown to be problematic in starting up especially when constant current boundary conditions are specified. One issue is that, as currently constructed without inductance terms, the voltage unknowns are algebraic constraints on the system. The equation may be categorized formally as a nilpotency 1 index DAE system (Brenan, Campbell et al. 1989). As such the equation system cannot formally be solved unless consistent initial conditions for the algebraic constraints are imposed at the initial time. And then, on top of this condition is the specification of other parts of the initial condition that must in turn be consistent with the DAE constraints on the system. This latter part is usually identified with the solution of a start-up nonlinear system where parts of the initial time derivative of the solution vector is solved for. We have implemented this alternative non-linear system within the battery code and describe the equations here.

We can divide the unknowns into those that have time derivatives, \mathbf{y}_1 and those that don't, \mathbf{y}_2 . Functions referring to these are \mathbf{f} for the \mathbf{y}_1 unknowns and \mathbf{g} for the \mathbf{y}_2 unknowns. This functional relationship is described in Eqn. (2.6.190).

$$\begin{aligned} \mathbf{0} &= \mathbf{f} \left(\frac{d\mathbf{y}_1}{dt}, \mathbf{y}_1, \mathbf{y}_2 \right) & \mathbf{y} &= \begin{Bmatrix} \mathbf{y}_1 \\ \mathbf{y}_2 \end{Bmatrix} \\ \mathbf{0} &= \mathbf{g} \left(\frac{d\mathbf{y}_1}{dt}, \mathbf{y}_1, \mathbf{y}_2 \right) \end{aligned} \quad (2.6.190)$$

In Eqn. (2.6.190), we note that the \mathbf{y}_2 variables don't have explicit time derivatives.

It's well known that consistent initial conditions are the key to starting DAE problems. This spawns the necessity to solve an additional problem, Eqn. (2.6.191), where the equation unknowns, \mathbf{y}^{DAE} , have been slightly altered to the following form.

$$\begin{aligned} \mathbf{0} &= \mathbf{f}^{DAE} \left(\frac{d\mathbf{y}_1}{dt}, (\mathbf{y}_1^{\text{constant}}), \mathbf{y}_2 \right) & \mathbf{y}^{DAE} &= \begin{Bmatrix} \frac{d\mathbf{y}_1}{dt} \\ \mathbf{y}_2 \end{Bmatrix} \\ \mathbf{0} &= \mathbf{g}^{DAE} \left(\frac{d\mathbf{y}_1}{dt}, (\mathbf{y}_1^{\text{constant}}), \mathbf{y}_2 \right) \end{aligned} \quad (2.6.191)$$

The solution vector is now a combination of time derivatives, the \mathbf{y}_1 equation and the original \mathbf{y}_2 unknowns.

The reformulation from Eqn. (2.6.190) to Eqn. (2.6.191) has significant effects that are not noticed at first hand. For one, the jacobian of the matrix problem no longer becomes singular as

the time step goes to zero. It can be shown that the jacobian of the Newton's method problem that stems from Eqn. (2.6.190) becomes singular as $Vt \rightarrow 0$, even if the nilpotency index of the DAE problem is equal to 1, a very mild problem. Things get much worse if the nilpotency index is greater than 1, such as in the Navier-Stokes equations where the index is 2.

This DAE solution capability may be used whenever there is a step-jump in a constant current boundary condition. This type of boundary condition is frequently used as part of a pulse-testing regimen for a battery. It can be shown that the battery can have multiple solutions with different voltage fields depending on the value of the current boundary condition. Eqn. (2.6.191) is exactly the equation system that determines the solution to this problem.

Numerical experiments have shown, though, that the issues with start-up are not solved with a proper solution of the DAE initial problem. Instead, they are more rooted in the initial selection of the boundary conditions and how that selection affects the eigenvector spectrum away from the actual solution of the problem. When constant current boundary conditions are used as part of the initial problem, a mode where the voltage field immediately starts to diverge often results. This causes the nonlinear solution of the initial time step to fail. This mode may be entirely avoided if the constant voltage boundary conditions are used instead, even if the eventual solution to the nonlinear system is the same.

2.6.17 Root finder used within the 1D code

Currently, the code can stall trying to find a constant current solution when there are no local electrons to grab at the local current conditions. This is because the source term, let alone the jacobian, is not guaranteed to be even continuous at points where the phases are born or are killed off.

The solution to this problem is to wrap the problem in a root finder algorithm based on constant voltage boundary conditions. The root finder then can vary the voltage to find or at least bracket the voltage that yields the desired current. A root finder algorithm doesn't actually require $C1$ continuity, nor even $C0$ continuity if certain requirements on convergence behavior are met, in its function evaluation.

In addition to a root finder combined with the constant voltage B.C., additional algorithm changes are needed for cases where phase deaths and births occur in order to make the function algorithm Lipschitz continuous, over the combined time period of the calculation, a necessary condition for the formal convergence of a time stepping algorithm (Süli 2010). One additional condition is that the time at which the phase deaths occur are calculated as part of the solution procedure. These equations have been explained previously. This circumvents the problems with Lipschitz continuity, because the finite number of points where Lipschitz continuity breaks down occur at the boundaries of the time intervals over which integrations are taking place.

The other additional condition is that an understanding of the overall function's dependence on the independent variable must be supplied to the root finder. For the problem class at hand, the current is always a monotonically changing function of the voltage; the direction of the functional dependence with respect to the independent variable can therefore be supplied to the root finder.

2.6.18 Numerics of Linkage between the 1D electrode Code and the Electrode object

To formulate the equation system we apply a control volume scheme around cell i , and employ a control volume discretization scheme in the time domain as well, to formulate a conservative scheme. Eqn. (2.6.162) results. $V_{i,n+1}$ is the volume of cell i at time $n+1$. $A_{iL,n+1}$ is the surface area of the left boundary of cell i at time $n+1$.

$$\begin{aligned} & \frac{(V_i C_T \phi X_k)_{n+1} - (V_i C_T \phi X_k)_n}{t_{n+1} - t_n} \\ & + n_{iL} \cdot [A_{iL} C_T X_k (\mathbf{v} + \mathbf{V}_k)] + n_{iR} \cdot [A_{iR} C_T X_k (\mathbf{v} + \mathbf{V}_k)] = (V_i w_k)_{n+1} \end{aligned} \quad (2.6.192)$$

In Eqn.(2.6.192), $(\hat{w}_k)_{n+1}$ is the source term for species k evaluated at the conditions pertinent to $t_n < t < t_{n+1}$. The source term is evaluated at the conditions of the external variables, i.e., at $t = t_{n+1}$. But, also represents an integration from conditions at $t = t_n$ to $t = t_{n+1}$ within the internal state of the electrode object. This may involve abrupt transitions in the electrode structure, or it may involve non-uniform source terms with respect to time within the $t = t_n$ to $t = t_{n+1}$ period due to changes in the internal morphology or internal state of the electrode. Keeping track of these changes requires us to use a formulation where we integrate the internal state of the electrode from $t = t_n$ to $t = t_{n+1}$ and use that within Eqn. (2.6.162). This concept is expressed by Eqn. (2.6.193) and(2.6.194), which is a formal representation of the subgrid integration process within the Electrode model.

$$z_{j,n+1} - z_{j,n} = \int_{t_n}^{t_{n+1}} f_j (A^E(t), \mathbf{z}, t) dt \quad (2.6.193)$$

The source term for the numerical model has the following form

$$\hat{w}_{k,n+1} (A_{n+1}^E, \mathbf{z}_{n+1}, t) \rightarrow \frac{\int_{t_n}^{t_{n+1}} w_k (A^E(t), \mathbf{z}, t) dt}{t_{n+1} - t_n} \quad (2.6.194)$$

Eqn. (2.6.194) indicates that we must evaluate an integral in time over a time step to evaluate the source term for applications which use the electrode object. This integration will be tricky, and involve the handling of special cases involving the formation and deletion of phases and

regions of phases, as electrodes go through material transformations. However, we will not deal with the details of electrode models here. But, instead focus on the numerical aspects of error control.

The electrode model represents an integration of a set of time dependent equations, Eqn.(2.6.193), for state variables, z_j , that have a time history, but are not formally part of the solution vector. The integration in Eqn. (2.6.193) is subject to a set of external fields, A^E , that influence the state variables that are part of the solution vector. Initial treatments of the time dependence of A^E have used a constant value of A^E equal to the external field value at t_{n+1} , which is the minimum necessary because these are stiff terms. However, strong reasons for going to a linearly interpolated value of A^E within the global time step have arisen. Eqn. (2.6.193) may be carried out in one or more steps as the need arises for breaking the step up due to phase or morphology changes, for relaxing the nonlinear system in Eqn. (2.6.193) to aid in convergence, or for integrating the equations in Eqn. (2.6.193) with sufficient precision to resolve the time dependence of α_j to a sufficient degree. The last point will be elaborated upon extensively below.

Once we have the independent variables for the electrode calculation determined, Eqn. (2.6.163) is used to calculate the source term, $w_{k,n+1}(A_{n+1}^E, z_{n+1}, t)$ for the global field variables at the continuum level to be used in Eqn. (2.6.162). $w_{k,n+1}$ is the source term at time t_{n+1} according to the backwards Euler approximation of the time derivative used in Eqn. (2.6.162). However, from Eqn. (2.6.163), it represents an integrated quantity over the interval t_n to t_{n+1} that is fully consistent with the change in the state variables, z , over that same interval. Generally, we require C^0 continuity for z over the global interval. We also require piecewise C^1 continuity for z over each subintegration interval within the global step. This means that wherever a break in the slope of z occurs within the subinterval, we must end an integration step at that time. In turn this requirement means that the integration interval will have to be part of the solution unknowns. We require C^1 continuity for A^E within the global integration interval. Step jumps in the value and derivative of A^E are allowed at global integration boundaries, though they have been shown to be linked to problems with local integration startups. The fact that we do not expect C^1 continuity for the solution unknowns within the global integration means that normal canned software such as sundials cannot solve this system of equations.

We do not achieve any extra level of formal time-step accuracy from this splitting treatment, because we still use a constant or linearly varying value of A_{n+1}^E throughout the t_n to t_{n+1} integration and we are still essentially using the backwards Euler method to integrate the equations. There are several advantages nonetheless. First, we achieve a level of separation between the models for the electrode and the 1D models for the cell. z doesn't have to be included in the source term vector for the 1D model. The number of unknowns within z may vary as well from treatment to treatment. We can handle abrupt changes in the electrode structure such as the disappearance of a phase easily within the integration step, by breaking the integration steps up at boundaries where z is discontinuous. Eqn. (2.6.163) leads us to

understand how embedded implicit coupling schemes should be handled in a general way, especially considering when the subgrid model gets to be very expensive.

In order to handle the implicit coupling within the 1D code, a jacobian must be formulated consisting of the variation of $w_{k,n+1}(A_{n+1}, z, t)$ with respect to variables in the 1D code which are the external field variables with the subgrid electrode model, A_{n+1}^E . This is achieved by integrating Eqn. (2.6.163) repeatedly with respect to deltas of each of the A_{n+1}^E variables. Ideally, the fact that there are often nonlinear convergence issues with calculating Eqn. (2.6.193) and that there are phase births and deaths that require time steps to be calculated on the fly means that a policy of applying a uniform time step history to Eqn. (2.6.193) during the formulation of the numerical jacobian cannot be implemented at all times. However, this policy does have appeal for its ability to reduce the noise in the calculation of the jacobian, and its implementation in some form is being considered.

In order to understand the time step truncation errors, predicted vs. corrected values of the A_{n+1}^E variables are calculated. This means that the time step error in these variables are controlled. The time step errors in the α variables are not under global time step error control. These issues are addressed below in the future by establishing a subcycling strategy that seeks to control the time step error within the Eqn. (2.6.163) integration step.

In that context let's develop several principles. Let's provide formulas for the error conditions in several of the formulas

Let $e_{\alpha,n+1}^G$ represent the global error in the computed value of the electrode state variables at t_{n+1} from the integration of Eqn.(2.6.193). Specifically this is equal to

$$e_{z,n+1}^G = \left\| z_{j,n+1} - \tilde{z}_j(t = t_{n+1}) \right\|_{\infty} \quad (2.6.195)$$

Here, \mathcal{Z} is the analytical "true" solution of the equation system evaluated at t_{n+1} , and $z_{j,n+1}$ is the computed solution of the equation system after applying the subintegration process. In Eqn. (2.6.195) we also use the infinity norm in order to ensure equal control of all solution components.

The error in the $e_{z,n+1}^G$ for a backwards-Euler predictor-corrector first order process is given by Eqn. (2.6.196), where β is a coefficient that depends on the solution behavior.

$$e_{z,n+1}^G = \beta(\Delta t) \quad (2.6.196)$$

At each step of the subintegration process, it is common policy to control the local error per unit step to be below a given tolerance, ϵ .

$$le_n < \epsilon(t_{n+1} - t_n)$$

Sometimes another more restrictive formula is used, originally championed by Gear.

$$le_n < \max(\mathcal{E}(t_{n+1} - t_n), \mathcal{E}') \quad (2.6.197)$$

It can be shown (Süli and Myers) that the truncation error, T , for the backwards Euler method is given by

$$T_{n+1} = \frac{\tilde{z}(t_{n+1}) - \tilde{z}(t_n)}{\Delta t_{n+1}} - f(t_{n+1}, \tilde{z}(t_{n+1}))$$

Therefore T_{n+1} is the error one would get if the exact solution were plugged into the discretization equation. Applying Taylor's theorem, it follows that there exists an $\xi_n \in (t_n, t_{n+1})$ such that

$$T_{n+1} = \frac{1}{2} \Delta t_{n+1}^2 \tilde{z}''(\xi_n) \quad (2.6.198)$$

\tilde{z}'' is the second time derivative of the state variables, or the first time derivative of $f(t_{n+1}, \tilde{z})$. Then, it can be shown (Süli 2010) that the local error induced by the local step is equal to

$$le_{n+1} = le_n + (t_{n+1} - t_n) (f(t_n, \tilde{z}) - f(t_n, z_n)) + hT_{n+1} \quad (2.6.199)$$

We may assume that the function is Lipschitz continuous when there are not phase changes taking place. Note, when there are phase changes taking place the function is not Lipschitz continuous, and therefore, most ODE software algorithms for convergence will fail their requirements. Thus, for a given finite region in time and state space, and if there is an L such that

$$|f(t_n, y) - f(t_n, z)| \leq L|y - z| \quad (2.6.200)$$

(this is the Lipschitz continuity requirement), then,

$$le_{n+1} \leq (1 + hL)le_n + hT_{n+1} \quad (2.6.201)$$

By induction, we may now calculate an estimate for the global time step error, assuming that there is a maximum truncation error T and all of the time steps are of the same size (I believe the analysis doesn't change if this is relaxed).

$$\begin{aligned} e_{n+1}^G &\leq \frac{T}{L} \left((1 + hL)^n - 1 \right) + (1 + hL)^n e_n^G \\ &\leq \frac{T}{L} \left(e^{L(t_{n+1}^G - t_n^G)} - 1 \right) + e^{L(t_{n+1}^G - t_n^G)} e_n^G \end{aligned} \quad (2.6.202)$$

We may define the bound on T as

$$T_{n+1} = \frac{1}{2} \Delta t_{n+1}^L M_2 \quad \text{where} \quad M_2 = \frac{1}{2} \Delta t_{n+1}^L \max_{\xi \in (t_n^G, t_{n+1}^G)} (z''(\xi))$$

So that the global bound is

$$e_{n+1}^G \leq \frac{M_2 h}{2L} \left(e^{L(t_{n+1}^G - t_n^G)} - 1 \right) + e^{L(t_{n+1}^G - t_n^G)} |e_n^G| \quad (2.6.203)$$

Eqn. (2.6.203) asserts that the error in the integration can be reduced if the time step values are reduced and that the reduction occurs in a linearly dependent rate with respect to the time step size. This is the expected result for the Backwards Euler method.

At each step we create an estimate for the local truncation error from the predicted versus the corrected value of the state variables, $z_j(t_{n+1})$. We then assign it the value of Eqn. (2.6.197) in the following nondimensional form, Eqn. (2.6.204). Eqn. (2.6.204) becomes the local time step control function for the subgrid integrator within the electrode.

$$\max_j \left| \frac{z_j^c(t_{n+1}) - z_j^p(t_{n+1})}{\max(rtol_j * |z_j^c(t_{n+1})|, atol_j)} \right| < \max\left(\frac{(t_{n+1}^L - t_n^L)}{(t_{n+1}^G - t_n^G)}, 0.01\right) \quad (2.6.204)$$

$rtol_j$ and $atol_j$ are the relative and absolute tolerances on the electrode state variables. In general $rtol_j$ is going to be about the same order of magnitude as the global relative tolerance control for the global state variables. In general $z_j(t_{n+1})$ variables refer to moles of species within a single electrode. $atol_j$ should be set for these species to be equal to no less than 10^{-13} (and probably a couple of orders of magnitude greater) multiplied by the number of total moles of species in each electrode. Anything less leads to round off error issues, especially when phase death and birth issues enter into the mix.

Eqn. (2.6.203) states that the error in the calculation of the state variables is proportional to the average error of the calculation of the predictor-corrector errors in each of the subgrid iterations. This principle will be applied to the numerical analysis routines. For example, if we require 4 digits of accuracy in the calculation of the state variables in going from t_n to t_{n+1} then we will require that each subgrid integration step have four digits of accuracy according to the predictor-corrector algorithm.

Eqn. (2.6.204) states that we will require more accuracy for each intermediate step, when the intermediate step gets smaller in relation to the global step. This is an inevitable result because the errors for each intermediate step are additive at least when formulating a bounds on the error for the global step. Eqn. (2.6.204) also indicates that we cap the correction factor at a factor of 0.01; this is an empirical result. At the point where 100 local steps are taken for each global step, the model for the subgrid iterations starts taking on a life of its own. The fact that the time step

error for each time step is proportional to Δt^2 means that algorithm behind Eqn. (2.6.204) is permissible at least theoretically.

Solution of the nonlinear equation system for each local subgrid time step requires proper control. The accuracy of this operation is usually linked to the accuracy required for the time-discretization error, the theory being that it does not pay to solve the nonlinear problem to a higher accuracy than the amount of time step truncation error inherent in the time integration (Brenan, Campbell et al. 1989). We have learned that this isn't necessarily the case for some subgrid integrations, especially involving systems with nonideal thermodynamics with species with large activity coefficients. In these systems, it has been beneficial to solve the equation system to a higher degree of accuracy than the time step truncation error would indicate.

In solving the nonlinear system, we use Cantera's nonlinear solver. It has the capability to require convergence of both the solution variables and the residual equation to a given level of accuracy. We specify convergence requirements for both of these categories. The solution variables are controlled with the same *atol rtol* requirements as specified in Eqn. (2.6.204). Residual weights are controlled in two ways. Residual equations may have different scales associated with them. Seldom are they actually scaled such that terms of comparable magnitude have order one. Cantera addresses this issue by calculating a row weight scaled value for each residual row by the following formula, Eqn. (2.6.205).

$$rowWtScls[i] = \sum_j |J_{i,j}| wt_j \quad (2.6.205)$$

wt_j is the value of the error weight for the j th solution component. Our first requirement is that the residual not be larger than its *rowWtScls* value.

$$\max_j \left| \frac{res(j)}{rowWtScls_j} \right| < 1.0 \quad (2.6.206)$$

The idea is that the each component of the solution when bounded by its minimum value for variance when multiplied by the jacobian entry, a linearization of the residual, provides a proper scale for the residual. This usually works for a range of problems. However, for some problems involving species with large activity coefficients, Eqn. (2.6.206) turned out not to be stringent enough. In those cases, we employed

$$residScls[i] = \min(rowWtScls[i], residAtol_i + (residRtol) rowWtScls[i]) \quad (2.6.207)$$

residRtol and *residAtol_i* are specified uniquely for each electrode object. We suspect that the error weighting requirements for the species mole fractions for cases with high activity coefficients was insufficient due to the high nonlinearities that created a need to specify the mole fractions to a high level of accuracy in order to reduce the residual to an acceptable value in

these cases. In other words, in order to solve the residual to three digits of accuracy, it was necessary to solve the mole fractions to six digits of accuracy, when dealing with nonideal phases.

The equation system may be interpreted by zeroing in on what it takes to converge the global equation step.

Now, let's start with Eqn. (2.6.208) and describe what it takes to converge this equation and what requirements that may entail on the subgrid iteration.

$$R() = \frac{(V_i C_T \phi X_k)_{n+1} - (V_i C_T \phi X_k)_n}{t_{n+1} - t_n} + n_{iL} \bullet [A_{iL} C_T X_k (\mathbf{v} + \mathbf{V}_k)] + n_{iR} \bullet [A_{iR} C_T X_k (\mathbf{v} + \mathbf{V}_k)] = (V_i w_k)_{n+1} \quad (2.6.208)$$

The residual in Eqn. (2.6.208) is considered converged if it is small compared to the residual weight for that row of the matrix problem. The residual weights, w_i^R , are calculated via the following procedure

For Cantera's nonlinear solver, we define the residual weights as being equal to the residual that will be created when solution delta's marginally satisfy the tolerance requirements used in a linearized newton's method, when the absolute value of the jacobian entries are used, Eqn. (2.6.209).

$$w_i^R = C^R \sum_{j=1}^N |J_{ij}| (w_j^X) \quad (2.6.209)$$

Then, we can be reasonably assured that the residual norm and the solution norm will roughly approach the value of one together as convergence is achieved, if there is not a significant amount of ill-conditioning in the matrix problem. If there is ill-conditioning the solution norm may be significantly larger than the residual norm when the stopping criteria is triggered. We scale the residual weighting factors by an additional factor, C^R , less than one, to reflect the ill-conditioning in the jacobian and partially mitigate this issue (note it can't and shouldn't be fully mitigated). C^R is determined by a procedure that makes the solution norm and the residual norm roughly convergent at the same time.

We will assume that the residual weighting factor is roughly equivalent to the largest component of the residual vector (treated as a summation) multiplied by the relative tolerance of the solution error norm. Then, in order to relax and solve the nonlinear global system at t_{n+1} , the calculation of the residual (and actually each term in the residual will have to be noise free at least up to levels that are on the order of the value of w_i^R). Normally, this is not a problem for terms as their calculation is considered to be noise-free. However, with source terms that come from a subintegration step, the possibility of noise in the calculation of the subgrid terms must be

considered. The noise in the calculation of the integrated quantity must be less than the number of digits requested in the residual evaluation as a prerequisite. Moreover, the same is true for the calculation of the jacobian. Requirements on the stability of the jacobian calculation may be the more stringent and therefore the more important determining factor for success in solving the global system.

Eqn. (2.6.210) contains a rough breakdown of the calculation of the jacobian entries from the source term in Eqn. (2.6.208) calculated by the subgrid Electrode object that will be used in the 1D level.

$$\left. \frac{dS}{dc} \right|_{calc} = \left. \frac{dS}{dc} \right|_{real} + \left. \frac{dS}{dc} \right|_{constE} + noise\left(\frac{dS}{dc}\right) \quad (2.6.210)$$

The first term is the actual jacobian entry if the time integration within the subgrid Electrode object is carried out in a time accurate manner such that there are no errors in the calculation of the numerical jacobian due to time integration within the subgrid iteration. Of course, this not really warranted or desired in practice, but it remains approachable in fact and represents an interesting limit in terms of analysis. The second term represents the deterministic error in the calculation of the jacobian source terms due to an inaccurate time stepping algorithm in the subgrid iteration. For example if the calculation of the subgrid iteration used the same time step history during the numerical differencing of the jacobian entry, then the behavior of the time-step truncation error tolerances within the jacobian may be deterministic and not problematic in terms of creating random noise in the calculation of the jacobian entry. They may also be compatible with the calculation of the residual. In other words, the jacobian may be wrong, but it may not change from iteration to iteration and it would be compatible with the residual leaving the ability to attain a solution, albeit an inaccurate solution, intact. Then, methods may be employed to measure the deterministic component $\left. \frac{dS}{dc} \right|_{constE}$, manage it, and then control its magnitude.

The last term in Eqn. (2.6.210) represents a “nondeterministic” noise component to the calculation of the jacobian entry. Here nondeterministic is meant rather loosely to mean a variable component of error that is due to unaccounted-for variations in the subgrid integration due to nonlinear solver errors, differences in time stepping within the jacobian calculation, hysteresis involving phase death and births within the subgrid iteration, and other issues. The nondeterministic component doesn’t have an analog outside of subgrid integration problems; it’s new. One analog, though, are problems with assuming pseudo-steady state calculations with additional degrees of freedom on surfaces (i.e., MPSalsa’s implementation (Shadid, Salinger et al. 1998)), which is used as part of the function calculations. In that case it was heuristically determined that the pseudo steady state equation had to be solved to a greater degree of accuracy to create stable function evaluations.

The requirement is stated in Eqn. (2.6.211).

$$noise\left(\frac{dS}{dc}\right)wt_c^X < wt_i^R \quad (2.6.211)$$

Eqn. (2.6.211) is a requirement on the last part of the convergence process. It states that the noise in the calculation of the jacobian multiplied by the permissible variation in the solution variable that is allowed under convergence conditions must be less than the permissible change in the residual, which is given by the residual weight. If Eqn. (2.6.211) is not satisfied the global solution process doesn't converge.

But it must also be the case that

$$noise\left(\frac{dS}{dc}\right) < rtol\left(\frac{dS}{dc}\right) + atol\left(\frac{dS}{dc}\right) \quad (2.6.212)$$

In Eqn. (2.6.212), we are saying that the noise in the calculation of the Jacobian must be a factor of *rtol* less than the main jacobian entries that determine the actual value of the global variable C. *rtol* here is the requested number of digits of accuracy in the variable C and is usually a prime determiner in the value of wt_c^X . In particular if you make *rtol* lower, i.e. requesting that there be more accuracy in the calculation of the solution variables, you will make Eqn. (2.6.211) a less stringent requirement, because the variation of the residual about the marginal convergence requirements of the residual is less. However, you'll be making Eqn. (2.6.212) a more stringent requirement in the sense that the noise in the calculation of the solution variables will be larger now than the tolerance requirements allow.

Eqn. (2.6.212) essentially says that we need a certain number of digits of accuracy in the jacobian entries for the nonlinear global system to converge. What does this require for the solution of the integrated source term? Usually, numerical derivatives are taken using deltas in solution variables that are on the order of 10^{-6} . However, in this instance this type of delta is unsustainable, because it is too small to rise above the time step discretization error. Instead a large enough delta that can be gotten away with must be used. The largest numerical delta values that are permissible are related to the size of the error weighting vector. In other words, we only solve the system up to a granularity equal to the error weight vector, so using that granularity in picking a numerical delta is permissible. So, setting numerical relative deltas at values of 10^{-3} are relevant. However, this still means that the source term must be calculated to a relative value of 10^{-6} in order for the jacobian entry to be known to three significant digits.

The goal of 10^{-6} may be achieved in a couple of ways. The first is to ensure that the absolute error is restricted to errors of 10^{-6} . What this essentially means is setting $rtol_j$ to 10^{-6} in Eqn. (2.6.204). This is a very restrictive, but not impossible goal for the integration accuracy of the subgrid method. The alternative is to forego thinking about driving the time step discretization accuracy below 10^{-6} . Instead, the idea would be to ensure that the time step discretization error is relegated to the $\left.\frac{dS}{dc}\right|_{constE}$ term in Eqn. (2.6.210). No effort is made to reduce this term, only

to make it consistent with the residual calculation and stable with respect to its calculation. The noise component is then isolated and reduced in magnitude.

The chief strategy for accomplishing this is to pick a time stepping strategy for the base residual evaluation of the source term in Eqn. (2.6.208). Then, when calculating the jacobian contributions, the same time steps are taken. Therefore, the time step truncation error is the same for all determinations used in the numerical jacobian, at least to an initial approximation. A key issue are the time steps where phase changes occur. Their time values are parts of the solution unknown. In that case, the strategy of identical time steps must slip to one in which only the phase birth/death time steps have differing values. The other issue is that no qualitative changes to the solution trajectories that the numerical delta calculations take that the base residual evaluation doesn't take as well. This is a serious issue and usually leads to global time step truncation error faults or nonconvergence of the nonlinear global step. This occurs in practice often. In order for the eventually, in order for the essential stability requirements of the method are to be made, the system must be analyzed in terms of a coupled system where the subgrid integration step has been relegated to that of the global time step itself. That's the subject of the next section.

Note, an alternative treatment where sensitivities are computed as part of the integration process, an approach that's included in sundials for example, wasn't attempted in this approach. However, it may have significant advantages and should be attempted in the future.

Conceptually the problem may be broken up into the solution of the global equation set and the solution of a local equation set for the subgrid problem. The coupling is fully two-way and stiff compared to the time-scale of physical scale, since the coupling involves Butler-Volmer reactions which are typically close to being equilibrated. However, the coupling is down through a source term, s . The global equations don't explicitly depend on the unknowns from the local equation, n_j^{ll} . They depend on the local equations through a vector of source terms, s .

$$\begin{aligned} \frac{dn_j^{gl}}{dt} &= f_g(n_j^{gl}, V, s(V, n_j^{gl}, n_j^{ll})) && \text{global problem} && (2.6.213) \\ 0 &= g_g(n_j^{gl}, V, s(V, n_j^{gl}, n_j^{ll})) \\ \\ \frac{dn_j^{ll}}{dt} &= f_l(n_j^{gl}, V, n_j^{ll}) && \text{local subgrid problem} \\ s &= s(n_j^{gl}, V, n_j^{ll}) \end{aligned}$$

Eqn. (2.6.213) conceptually describes the problem. One way to understand how to integrate the coupled global and local problem is to consider how the problem would be formulated if the equations were combined into a fully coupled system where all of the unknowns were part of the global solution vector. In this case, presumably, then if the time stepping were handled via the usual $rtol$, $atol$ procedure then the equation system could be solved to a desired tolerance.

The local problem is already solved via an *rtol*, *atol* procedure and usually to a tighter tolerance than the global tolerances by necessity. Therefore, when a solution is found for the global step, that solution has all of the convergence properties of a fully coupled solution, albeit at the global delta time step level. No extra convergence properties are implied by taking tighter steps in the local subgrid problem.

The equation system for the decoupled system appears even more like the coupled system in Eqn. (2.6.213) if the local problem is restricted to being a single step. In that case the problem can almost entirely be recast as the solution of the global linear system via the creation of the Schur complement for the local problem (Golub and Van Loan 1989). Using this analogy, it should be recognized as well that no terms in the jacobian for Eqn. (2.6.213) are actually dropped when formulating the Schur complement, and therefore, the combined problem remains fully coupled even though they are solved in a decoupled process. Solving problems via a Schur complement process has a long and successful history, especially when doing continuation methods such as arc length continuation.

However, when the local subgrid problem is relaxed to allow for multiple local time steps per global time steps the system behavior may be altered dramatically. This point needs to be emphasized. In fact, there is absolutely no proof for why the global jacobian determined by procedure outlined in the previous section, must actually point to a descent direction when multiplied by the current global residual, even if the jacobian is evaluated up to the desired level of accuracy. This conjecture of course is dependent on the level of convergence, and on the norm used in evaluating the global residual convergence process. For example, it's typical for convergence to occur during the initial part of the nonlinear solve. But, final convergence of the process up to the desired tolerances may not occur because the global jacobian essentially points in the wrong direction for just one electrode, and this issue doesn't arise until all other modes in the problem are sufficient converged that the remaining electrode cell's residual contribution stands out.

Therefore, given that these potential coupling problems are guaranteed to disappear when the subgrid time step iterations disappear a coupling strategy has been proposed. The strategy is based on evaluating whether the global jacobian is in fact a producer of a robust descent direction for the global residual (see Dennis and Schnabel (J. E. Dennis and Schnabel 1996) for practical ways to determine algorithms for this procedure). If it is not, then the global time step is reduced until the global jacobian becomes a robust descent direction. Also, the global time step strategy is also informed of the global jacobians being an adequate producer of a descent direction. And, when it is not an adequate producer, then the global time step for the next time step is reduced so that it always remains a good descent direction producer. Additional constraints on the maximum permissible number of local steps per global steps have also been proposed as a practical way to avoid convergence problems arising between the local to global problem.

When the local problem is taking more than one local step per global step, a phenomena has been observed related to the treatment of external variables during intermediate states of the local

problem. Currently, external variables are treated as fully implicitly, and undergo a step jump during intermediate times. Essentially a relaxation process ensues related to the step jump in the global variables, which also includes the allowed delta time step values. The predictor-corrector for the local problem reduces the time step at the beginning of the local problem because the predictor-corrector algorithm fails. However, at the end of the time step the predictor-corrector will increase the delta time because the algorithm suggests that the behavior is well represented. The reason behind this is the step-jump in the external variables. We have proposed but not fully implemented a fix for this behavior by implementing a linear interpolation for all external variables that is implemented at intermediate times of the local subgrid time integration. Using this approach relaxation phenomena over the intermediate time stepping shouldn't occur.

2.6.19 *CanTrilBat Progress*

We have taken the freedom car battery electrodes and have derived thermodynamic formulations for the anode and cathode compounds as a function of the degree of lithiation.

These have been parameterized using the Redlich-Kister model for nonideality in Cantera. Original references for this work are from Karthikeyan et al. (Karthikeyan, Sikha et al. 2008), Smith and Wang (Smith and Wang 2006), and Gu and Wang (Gu and Wang 2000).

The usual method for modeling the interaction process is one based on empiricism. Essentially, the open circuit potential is measured as a function of extent of reaction to calculate the chemical potential of the incremental insertion process. This type of approach is used ubiquitously within the battery modeling literature, either using a model like Redlich-Kister or even just using a calibration curve as in the Battery Design Studio's approach, to calibrate thermodynamics and obtain accurate representations of the open circuit voltage as a function of the extent of reaction. The fact that the intercalation curves are fit means that accurate representations of voltage vs. extent of reaction curves can be produced by battery software. This is a plus. However, these types of models with these fitting approaches then become unspecific to the chemistry mechanism behind the chemical potential curves. Essentially they become a dead end, which can't inform the process of figuring out why the curves change in time or due to damage or fatigue processes. Without specificity concerning site bonding, defect chemistry, and detailed morphology configurations that are behind the curves, no progress can be made concerning these issues beyond some degree of curve watching of these curves (as well as the entropy curve) as a function of cycle number.

A better approach would be to create more advanced models for the intercalation process that involves more specific site identification information. One interesting feature that we found while constructing the model was the severe values of the activity coefficients used within the freedom car models. In fact, some of the models used in Karthikeyan et al. (Karthikeyan, Sikha et al. 2008) exhibited activity coefficient values that could not be represented with double

precision numbers only their logs could be represented. This type of numerical issue is indicative of a species model that is not representative of a physical situation and one that is forced to agree with the data. Typically, if additional species are introduced with appropriate stoichiometries and standard states, the magnitudes of activity coefficients can be reduced significantly. The magnitude and extent of activities are then an indicator of the appropriateness of the speciation model. With that yardstick, it seems that the single species model used in the current literature for intercalation fails substantially, and should be modified substantially to include multiple species with site specific thermodynamics. For example, intercalation in graphite usually occurs through specific planes in the graphite being filled in with a certain periodicity depending on the amount of intercalation. This type of periodicity should be included in more advanced speciation models.

Note, electrode models based on transfer functions solutions (both short time and long time infinite solution formulations) have advantages in terms of understanding and accuracy (Doyle, Fuller et al. 1993; Smith and Wang 2006) . However, they forego any ability to add complexity to the chemistry or transport mechanism within the solid phase. Therefore, we have not pursued these approaches.

We additionally have not included double layer capacitances in the model. These have been shown to be important only at millisecond time scales [15] , and we have not built the infrastructure for modeling the double layer within Cantera yet. Literature treatments of double layer capacitances have focused on adding them with and without added film resistances due to the diffusion layers (Doyle, Newman et al. 1996).

Our initial treatment has focused on putting the models into the Electrode_CSTR object and then adding film resistances to that model.

3 CONCLUSIONS AND ONGOING WORK

This report summarizes progress made under a Laboratory Directed Research and Development project to model thermal abuse in Li-ion batteries. This project developed several notable capabilities. The simulation of electrode-electrolyte interfaces in the presence of an applied voltage remains a major challenge; we have developed techniques that marry an electronic density functional theory program to capture the atomistic energetics involved in chemical reactions induced by the applied voltage with a fluids density functional theory program to describe the bulk response of the electrolyte to the charges in the electrode and the inner Helmholtz plane. In a Li-ion battery, reactions at this interface grow a passivating layer that prevents thermal runaway. We have used solvated density functional theory calculations to develop a chemical mechanism that we have used to drive a number of mesoscale simulation techniques (continuous, KMC, and phase field) to understand the evolution of the microstructure of this passivating layer. Finally, one needs to capture the effect of the passivating layer on the overall battery cell performance, and we have developed techniques based on the Trinos scalable solver library and the Cantera chemical kinetics library to develop a continuum-level description of the battery behavior as the passivating layer forms.

These elements lay the groundwork for predicting how different battery materials determine a battery's tendency to undergo thermal runaway, but more work is required to apply these tools to understand the shortcomings of existing materials and to develop more stable ones. To date, we have only focused on the formation of passivating layers, whereas the reverse process that involves the dissolution of passivating layers is what is central to battery safety. The analyses we have made here will provide a sound foundation for considering these processes, but more work is clearly needed in these areas.

4 REFERENCES

- Abe, T., F. Sagane, et al. (2005). "Lithium-ion transfer at the interface between lithium-ion conductive ceramic electrolyte and liquid electrolyte - a key to enhancing the rate capability of lithium-ion batteries " J. Electrochem. Soc. **152**: A2151.
- Abraham, D. P., E. P. Roth, et al. (2006). "Diagnostic examination of thermally abused high-power lithium-ion cells." J Power Sources **161**(1): 648-657.
- Anderko, A., P. Wang, et al. (2002). "Electrolyte Solutions: from thermodynamic and transport properties models to the simulation of industrial processes." Fluid Phase Equilibria **194-197**: 123-142.
- Andersson, A. M., A. Henningson, et al. (2003). "Electrochemically lithiated graphite characterised by photoelectron spectroscopy." Journal of Power Sources **119**: 522-527.
- Aurbach, D., Y. Einely, et al. (1994). "The Surface Chemistry of Lithium Electrodes in Alkyl Carbonate Solutions]." J Electrochem Soc **141**(1): L1-L3.
- Aurbach, D., Y. Gofer, et al. (1992). "The Behavior of Lithium Electrodes in Propylene and Ethylene Carbonate - The Major Factors that Influence Li Cycling Efficiency." Journal of Electroanalytical Chemistry **339**(1-2): 451-471.
- Bai, P., D. Cogswell, et al. (2011). "Suppression of phase separation in LiFePO₄ Nanoparticles during battery discharge." Nano Lett. **11**: 4890.
- Bard, A. J. and L. R. Faulkner (2001). Electrochemical Methods: Fundamentals and Applications, John Wiley & Sons, Inc.
- Barr, L. W. and A. B. Lidiard (1971). Defects in ionic crystals. . Physical Chemistry - An Advanced Treatise, Jost. **10**: 151-228.
- Bayly, C. I., P. Cieplak, et al. (1993). "A well-behaved electrostatic potential based method using charge restraints for deriving atomic charges: the RESP model." J. Phys. Chem. **97**(40): 10269-10280.
- Becke, A. D. (1993). "Density functional thermochemistry. 3. The role of exact exchange." J Chem Phys **98**: 5648-5652.
- Bedrov, D., G. D. Smith, et al. (2012). Reactions of Singly-Reduced Ethylene Carbonate in Lithium Battery Electrolytes: A Molecular Dynamics Simulation Study Using the ReaxFF. Journal of Physical Chemistry A. **116**: 2978-2985.
- Bengtsson, L. (1999). Phys. Rev. B **46**: 16067.
- Bessler, W. G., J. Warnatz, et al. (2007). "The influence of equilibrium potential on the hydrogen oxidation kinetics of SOFC anodes." Solid State Ionics **77**: 3371 - 3383.
- Bird, J. Stewart, et al. Transport Phenomena.
- Bockris, J. (2001). Modern Electrochemistry 2A: Fundamentals of Electrodictics. New York, NY, Kluwer Academic Publishers.
- Bockris, J. O. M. and S. U. m. Khan (1993). Surface Electrochemistry - a molecular level approach. New York, Plenum Press.
- Bohnen, K. P. and D. M. Kolb (1998). Surf. Sci. **407**: L629.
- Borukhov, I., D. Andelman, et al. (1997). Phys. Rev. Lett. **79**: 435.
- Brenan, K. E., S. L. Campbell, et al. (1989). Numerical Solutions of Initial-Value Problems in Differential-Algebraic Equations. New York, North-Holland.

- Broussely, M., S. Herreyre, et al. (2001). "The electrochemical behavior of Alkali and Alkaline earth metals in nonaqueous battery systems - the solid electrolyte interphase model." J. Power Sources **97-98**: 13.
- Cairncross, R. A., P. R. Schunk, et al. (1996). Drying in Deformable Partially-saturated porous media: sol-gel coatings. Albuquerque, Sandia National Labs.
- Ceperley, D. M. and B. I. Alder (1980). Phys. Rev. Lett. **45**: 566.
- Christensen, J. and J. Newman (2004). "A mathematical model for the lithium-ion negative electrode solid electrolyte interphase." J. Electrochem. Soc. **151**: A1977.
- Christensen, J. and J. Newman (2004). "A Mathematical Model for the Lithium-Ion Negative Electrode Solid Electrolyte Interphase." J. Electrochem. Soc **151**: A1977-A1988.
- Cieplak, P., W. Cornell, et al. (1995). "Application of the multimolecule and multiconformational RESP methodology to biopolymers: Charge derivation for DNA, RNA, and proteins." J. Comput. Chem. **16**(11): 1357-1377.
- Coffee, T. P. and J. M. Heimerl (1981). "Transport Algorithms for Premixed, Laminar Steady-State Flames." Combustion and Flame **43**: 273-289.
- Cogswell, D. and M. Bazant (2012). "Coherency strain and the kinetics of phase separation in LiFePO₄ nanoparticles." ACS Nano **6**: 2215.
- Colclasure, A., K. Smith, et al. (2011). "Modeling detailed chemistry and transport for solid-electrolyte interface (SEI) films in Li-ion batteries." Electrochim. Acta **58**: 33.
- Colclasure, A. M., K. A. Smith, et al. (2011). "Modeling detailed chemistry and transport for solid-electrolyte interface (SEI) films in Li-ion Batteries." Electrochimica Acta **58**: 33-43.
- Curtiss, C. F. and R. B. Bird (1999). "Multicomponent Diffusion." Ind. Eng. Chem. Res. **38**: 2515-2522.
- Curtiss, C. F. and R. B. Bird (2001). "Multicomponent Diffusion (errata)." Ind. Eng. Chem. Research **40**: 1791-1791.
- Doll, J. D. and A. F. Voter (1987). "Recent Developments in the Theory of Surface-Diffusion." Annual Review of Physical Chemistry **38**: 413-431.
- Doughty, D. H. (2005). "Li-ion Battery Abuse Tolerance Testing - An Overview." Proc. AABC.
- Doyle, M., T. F. Fuller, et al. (1993). "Modeling of Galvanostatic Charge and Discharge of the Lithium/Polymer/Insertion Cell." J. Electrochem. Soc **140**(6): 1526 - 1533.
- Doyle, M., J. Newman, et al. (1996). "Comparison of Modeling Predictions with Experiment Data from Plastic Lithium Ion Cells." J. Electrochem. Soc **143**(6): 1890 - 1903.
- Engelhardt, G. and H.-H. Strehblow (1995). "Reducing systems of ion transport equations to systems of equations of multi-component diffusion in non-electrolytic solutions." J. of Electroanalytical Chemistry **394**: 7-15.
- Fang, C. M. and G. A. de Wijs (2006). Chem. Mater. **18**: 1169.
- Feibelman, P. (2001). Phys. Rev. B **64**: 125403.
- Filhol, J.-S. and M. Neurock (2006). Angew. Chem. **118**: 416.
- Frink, L. J. D., A. L. Frischknecht, et al. (2012). "Toward Quantitative Coarse-Grained Models of Lipids with Fluids Density Functional Theory." J. Chem. Theor. Comput. **8**(4): 1393-1408.
- Frisch, M. J., G. W. Trucks, et al. (2004). Gaussian 03 C.02. Wallingford, CT, Gaussian, Inc.

- Fu, C. L. and K.-M. Ho (1989). Phys. Rev. Lett. **63**: 1617.
- Fuller, T. F., M. Doyle, et al. (1994). "Simulation and Optimization of the Dual Lithium Ion Insertion Cell." J. Electrochem. Soc **141**: 1-10.
- Genuchten, R. v. (1978). Calculating the unsaturated hydraulic conductivity with a new closed form analytical model. Princeton, NJ, Princeton University.
- Golub, G. H. and C. F. Van Loan (1989). Matrix Computations, 2nd Ed. Baltimore, Johns Hopkins University Pub.
- Goodwin, D. G. and M. A. Aivazis (1999). A Modular, Object-Oriented Software Package for chemical kinetics and chemical thermodynamics, California Institute of Technology.
- Goodwin, D. G., H. Zhu, et al. (2009). "Modeling Electrochemical Oxidation of Hydrogen on Ni-YSZ Pattern Anodes." J. Electrochem. Soc **156**: B1004-B1021.
- Grechnev, G. E., R. Ahuja, et al. (2002). Phys. Rev. B **65**: 174408.
- Groot, S. R. d. and P. Mazur (1962). Non-Equilibrium Thermodynamics. Amsterdam, North Holland.
- Gu, W. B. and C. Y. Wang (2000). "Thermal-electrochemical modeling of battery systems." JOURNAL OF THE ELECTROCHEMICAL SOCIETY **147**(8): 2910-2922.
- Guyer, J., W. Boettinger, et al. (2004). "Phase field modeling of electrochemistry. II. Kinetics." Phys. Rev. E **69**: 021604.
- H. Zhu, R. J. Kee, et al. (2005). "Modeling Elementary Heterogeneous Chemistry and Electrochemistry in Solid-Oxide Fuel Cells." J. Electrochem. Soc **152**: A2427-A2440.
- Hagberg, A. A., D. A. Schult, et al. (2008). Exploring network structure, dynamics, and function using NetworkX. Proceedings of the 7th Python in Science Conference (SciPy2008), Pasadena, CA.
- Hao, Y. and D. G. Goodwin (2007). "Numerical Modeling of Single-Chamber SOFCs with Hydrocarbon Fuels." J. Electrochem. Soc **154**: B207-b217.
- Hatchard, T. D., D. D. MacNeil, et al. (2001). "Thermal model of cylindrical and prismatic lithium-ion cells." Journal of the Electrochemical Society **148**(7): A755-A761.
- Henderson, D., Ed. (1992). Fundamentals of Inhomogeneous Fluids. New York, Dekker.
- Henderson, D. and D. Boda (2009). "Insights from theory and simulation on the electrical double layer." Phys. Chem. Chem. Phys. **11**(20): 3822-3830.
- Heroux, M. A., A. G. Salinger, et al. (2007). "Parallel segregated Schur complement methods for fluid density functional theories." SIAM J. Sci. Comput. **29**(5): 2059-2077.
- Hodak, M., W. Lu, et al. (2008). J. Chem. Phys. **128**: 014101.
- J. E. Dennis, J. and R. B. Schnabel (1996). Numerical Methods for Unconstrained Optimization and Nonlinear Equations. Philadelphia, PA, SIAM.
- Jensen, K. P. and W. J. Jorgensen (2006). "Halide, ammonium, and alkali metal ion parameters for modeling aqueous solutions." J. Chem. Theory Comput. **2**(6): 1499-1509.
- Jinnouchi, R. and A. B. Anderson (2008). Phys. Rev. B **77**: 245417.
- Karthikeyan, D. K., G. Sikha, et al. (2008). "Thermodynamic model development for lithium intercalation electrodes." Journal of Power Sources: 1398-1407.
- Kim, G. H., A. Pesaran, et al. (2007). "A three-dimensional thermal abuse model for lithium-ion cells." Journal of Power Sources **170**(2): 476-489.

- Kohn, W. and L. J. SHAM (1965). "Self-consistent equations including exchange and correlation effects." *Phys Rev* **140**: 1133-&.
- Lau, K. C., C. H. Turner, et al. (2008). "Kinetic Monte Carlo simulation of the Yttria Stabilized Zirconia (YSZ) fuel cell cathode." *Solid State Ionics* **179**(33-34): 1912-1920.
- Letchworth-Weaver, K. and T. A. Arias (2012). *Phys. Rev. B* **86**: 075140.
- Linstrom, P. J. and W. G. Mallard. "NIST Chemistry WebBook, NIST Standard Reference Database Number 69." Retrieved June, 2012.
- Louie, S. G., S. Froyen, et al. (1982). *Phys. Rev. B* **26**: 1738.
- Lozovoi, A. Y. and A. Alavi (2003). *Phys. Rev. B* **68**: 245416.
- Lozovoi, A. Y., A. Alavi, et al. (2001). *J. Chem. Phys.* **115**: 1661.
- Magyar, R. J., A. E. Mattsson, et al. (2011). *Metallic Systems: A Quantum Chemist's Perspective*. T. Allison and O. Coskuner. Boca Raton, CRC Press Taylor and Francis.
- Mansoori, G. A., N. F. Carnahan, et al. (1971). "Equilibrium Thermodynamic Properties of Mixtures of Hard Spheres." *J. Chem. Phys.* **54**(4): 1523-&.
- Mao, Z., P. D. Vidts, et al. (1994). "Theoretical Analysis of the Discharge Performance of a NiOOH/H₂ Cell." *J. Electrochem. Soc.* **141**: 54 - 64.
- Marten, B., K. Kim, et al. (1996). "New model for calculation of solvation free energies: Correction of self-consistent reaction field continuum dielectric theory for short-range hydrogen-bonding effects." *J Phys Chem* **100**: 11775-11788.
- Martinez, L., R. Andrade, et al. (2009). "PACKMOL: A package for building initial configurations for molecular dynamics simulations." *J. Comput. Chem.* **30**(13): 2157-2164.
- Martinez, M. J. and C. M. Stone (2008). Considerations for Developing Models of MultiphaseFlow in Deformable Porous Media. Albuquerque, NM., Sandia National Labs.
- Martinez, M. J., C. M. Stone, et al. (2011). Computation Thermal, Chemical, Fluid and Solid Mechanics for Geosystems Management, Sandia National Labs.
- Mishra, S. K. and G. Ceder (1999). *Phys. Rev. B* **59**: 6120.
- Moffat, H., A. Sun, et al. (2008). Modeling Pore Corrosion in Normally Open Gold-Plated Copper Connectors. Albuquerque, NM, Sandia National Laboratories.
- Moffat, H. K. (2011). Thermal Runaway in Batteries – Formulations for Electrolyte Transport involving Multicomponent Concentrated Electrolytes. Albuquerque, NM, Sandia National Laboratories.
- Moffat, H. K. (2012). Additional of diffusional resistances into existing Electrode objects that don't have diffusional resistances . *Sandia Memo*. Albuquerque, NM, Sandia National Laboratories.
- Moffat, H. K. (2012). Electrode Morphology and Model Development. Albuquerque, NM, Sandia National Laboratories.
- Moffat, H. K. and C. F. V. Colon (2009). Implementation of Equilibrium Chemistry speciation and chemistry (EQ3 type) Calculations into Cantera or Electrolyte Solution. Albuquerque, NM, Sandia National Labs.
- Moffat, H. K. and J. Hewson (2010). Thermodynamics Properties of Electrodes in Thermal Batteries. Albuquerque, NM, Sandia National Labs.
- Moffat, H. K., J. C. Hewson, et al. (2009). Kinetics of Electrodes in Thermal Batteries.

- Moffat, H. K. and J. S. Hewson (2009). Thermodynamic Properties of Molten Salts, Reconciling reciprocal molten salt representations with ionic-species representations. in prep. Albuquerque, NM, Sandia National Laboratories.
- Neugenbauer, J. and M. Scheffler (1993). Surf. Sci. **287-288**: 572.
- Newman, J. and T. W. Chapman (1973). "Restricted Diffusion in Binary Solutions." AIChE Journal **19**(2): 343-348.
- Newman, J. and K. E. Thomas-Alyea (2004). Electrochemical Systems, Wiley-Interscience.
- Oleksy, A. and J.-P. Hansen (2006). "Towards a microscopic theory of wetting by ionic solutions. I. Surface properties of the semi-primitive model." Molecular Physics **104**(18): 2871-2883.
- Otani, M. and O. Sugino (2006). Phys. Rev. B **73**: 115407.
- Peled, E. (1979). "The Electrochemical-Behavior of Alkali and Alkaline-Earth Metals in Non-Aqueous Battery Systems - the Solid Electrolyte Interphase Model." Journal of the Electrochemical Society **126**(12): 2047-2051.
- Peled, E., D. Golodnitsky, et al. (1997). "Advanced model for solid electrolyte interphase electrodes in liquid and polymer electrolytes." Journal of the Electrochemical Society **144**(8): L208-L210.
- Perdew, J. P., K. Burke, et al. (1996). "Generalized gradient approximation made simple." Physical Review Letters **77**(18): 3865-3868.
- Perdew, J. P. and A. Zunger (1981). Phys. Rev. B **23**: 5048.
- Plimpton, S., C. Battaile, et al. (2009). Crossing the Mesoscale No-Man's Land via Parallel Kinetic Monte Carlo, Sandia National Laboratories.
- Plimpton, S. J. (1995). "Fast parallel algorithms for short-range molecular dynamics." J. Comput. Phys. **117**: 1-19.
- Plimpton, S. J. (2012). LAMMPS Molecular Dynamics Simulator. Albuquerque, NM, Sandia National Laboratories.
- Pornprasertsuk, R., T. Holme, et al. (2009). "Kinetic Monte Carlo Simulations of Solid Oxide Fuel Cell." Journal of the Electrochemical Society **156**(12): B1406-B1416.
- Rappe, A. K. and W. A. G. III (1991). "Charge Equilibration for Molecular Dynamics Simulations." JPC **95**: 3358.
- Reiner, E. S. and C. J. Radke (1990). "Variational approach to the electrostatic free-energy in charged colloidal suspensions. General theory for open systems." J. Chem. Soc. Faraday Trans. **86**(23): 3901-3912.
- Ringnalda, M. N. (2009). Jaguar. New York, NY, Schrodinger, LLC.
- Roach, R. A. and P. R. Schunk (2000). GOMA's capabilities for partially saturated flow in porous media. Albuquerque, Sandia National Labs: 30.
- Roth, E. P. (2008). Abuse Response of 18650 Li-Ion Cells with Different Cathodes Using EC:EMC/LiPF₆ and EC:PC:DMC/LiPF₆ Electrolytes. ECS Transactions. **11**: 19-41.
- Roth, R., R. Evans, et al. (2002). "Fundamental measure theory for hard-sphere mixtures revisited: the White Bear version." J. Phys. Condens. Matter **14**(46): 12063-12078.
- S̄uli, E. (2010). Numerical Solution of Ordinary Differential Equations.
- Sasaki, Y., M. Hosoya, et al. (1997). "Lithium cycling efficiency of ternary solvent electrolytes with ethylene carbonate dimethyl carbonate mixture." J Power Sources **68**(2): 492-496.

- Schultz, P. A. (1999). Phys. Rev. B **60**: 1551.
- Schultz, P. A. (2000). Phys. Rev. Lett. **84**: 1942.
- Schultz, P. A. (2006). Phys. Rev. Lett. **96**: 246401.
- Schultz, P. A. (2012). SeqQuest.
- Schultz, P. A. and O. A. von Lilienfeld (2009). Mater. Sci. Eng. **17**: 084007.
- Schunk, P. R. (1999). Porous Media Capabilities / Tutorial for Goma. User Guidance for saturated porous penetration problems.
- Schunk, P. R. (2000). TALE: An Arbitrary Lagrangian-Eulerian approach to fluid-structure interaction problems. Albuquerque, Sandia National Labs.
- Schunk, P. R., P. A. Sackinger, et al. (1998). GOMA 2.0 - A Full-Newton Finite Element Program for Free and Moving Boundary Problems with Coupled Fluid/Solid Momentum, Energy, Mass, and Chemical Species Transport: User's guide. Albuquerque, Sandia National Labs.
- Shadid, J. N., A. G. Salinger, et al. (1998). MPSalsa version 1.5 : a finite computer program for reacting flow problems. Part 1, Theoretical development. Albuquerque, NM, Sandia National Laboratories. **SAND95-2752**.
- Sharp, K. A. and B. Honig (1990). "Calculating total electrostatic energies with the nonlinear Poisson-Boltzmann equation." J. Phys. Chem. **94**(19): 7684-7692.
- Skulason (2007). Phys. Chem. Chem. Phys. **9**: 3241.
- Smith, K. and C.-Y. Wang (2006). "Solid-state diffusion limitations on pulse operation of a lithium ion cell for hybrid electric vehicles." J. of Power Sources **161**: 628-639.
- Süli, E. (2010). "Numerical Solution of Ordinary Differential Equations." 2012, from <http://people.maths.ox.ac.uk/suli/nsodes.pdf>.
- Süli, E. and D. Myers An Introduction to Numerical Analysis. Cambridge, UK, Cambridge University Press.
- Swalin, R. A. (1972). Thermodynamics of Solids. New York, N.Y., J. Wiley and Sons.
- Udell, K. S. and J. S. Fitch (1985). Heat and mass transfer in capillary porous media considering evaporation, condensation, and non-condensable gas effects. 23rd ASME/AICHE National Heat Transfer Conference. Denver, CO.
- Wang, J., W. Wang, et al. (2006). "Automatic atom type and bond type perception in molecular mechanical calculations." J. Mol. Graph. Mod. **25**(2): 247-260.
- Wang, J., R. M. Wolf, et al. (2004). "Development and testing of a general amber force field." J. Comput. Chem. **25**(9): 1157-1174.
- Wang, Y. and P. Balbuena (2001). "Associations of alkyl carbonates: Intermolecular C-H center dot center dot center dot O interactions." J Phys Chem A **105**(43): 9972-9982.
- Wang, Y. and P. Balbuena (2002). "Associations of lithium alkyl dicarbonates through O center dot center dot center dot Li center dot center dot center dot O interactions." J Phys Chem A **106**(41): 9582-9594.
- Wang, Y. and P. Balbuena (2002). "Theoretical insights into the reductive decompositions of propylene carbonate and vinylene carbonate: Density functional theory studies." J Phys Chem B **106**(17): 4486-4495.

- Wang, Y. and P. Balbuena (2005). "Theoretical studies on cosolvation of Li ion and solvent reductive decomposition in binary mixtures of aliphatic carbonates." Int. J. Quantum Chem. **102**(5): 724-733.
- Watson, E. B. and R. Dohmen (2010). Non-traditional and emerging methods for characterizing diffusion in minerals and mineral aggregates. Diffusion in Minerals and Melts. H. Zhang and D. J. Cherniak. Chantilly, VA, Mineralogical Society of America and Geochemical Society. **72**: 65-105.
- Wu, J. (2006). "Density functional theory for chemical engineering: From capillarity to soft materials." AIChE J. **52**(3): 1169-1193.
- Yamada, Y., Y. Iriyama, et al. (2009). "Kinetics of lithium ion transfer at the interface between graphite and liquid electrolytes: effects of solvent and surface film." Langmuir **25**: 12766.
- Zhang, Q. and R. E. White (2007). "Moving Boundary Model for the Discharge of a LiCoO₂ Electrode." J. Electrochem. Soc **154**: A587-A596.
- Zhuang, G., K. Xu, et al. (2005). "Lithium ethylene dicarbonate identified as the primary product of chemical and electrochemical reduction of EC in 1.2 m LiPF₆/EC : EMC electrolyte." J Phys Chem B **109**(37): 17567-17573.

APPENDIX A: ELECTROSTATIC FREE ENERGY IN TRAMONTO

Here we document the calculation of the electrostatic free energy in our fluids-DFT code, Tramonto, and how it is related to other expressions for the free energy in the literature. We also show results of testing to make sure that the free energy is calculated correctly.

For an electrolyte near a single charged surface, the surface tension is given by

$$\begin{aligned}\gamma &= \frac{\Omega^{ex}}{A} = \frac{1}{A} (\Omega[\rho(z)] - \Omega[\rho_b]) \\ &= F[\rho(z)] - F[\rho_b] - \sum \mu_\alpha \Gamma_\alpha\end{aligned}\tag{A.1}$$

where F is the Helmholtz free energy per unit area and Γ_α is the adsorption of species α . Here Ω is the grand free energy of the system, $\rho(z)$ is the density of all species a distance z from the surface, ρ_b is the bulk density, and μ_α is the chemical potential of species α . The electrostatic mean field term in F is given by Eq. (2.2.6), where $\phi(\mathbf{r})$ is the electrostatic potential and $\rho_c(\mathbf{r})$ is the total charge density. Note that this charge density is the total charge density in all space, which includes both mobile and fixed charges:

$$\rho_c(\mathbf{r}) = \rho^f(\mathbf{r}) + \rho^m(\mathbf{r}) = \rho^f(\mathbf{r}) + \sum_\alpha q_\alpha \rho_\alpha(\mathbf{r})$$

where the q_α are the charges and $\rho_\alpha(\mathbf{r})$ are the densities of the mobile ions in the system. This point is often not made clear in the f-DFT literature, but is crucial to getting the right free energy in the PB limit as we will see below.

A.1. A note about units

In SI units Poisson's equation is given by Eq. (2.2.2). In Tramonto, we use reduced variables $\phi^* = e\phi/kT$ and $x^* = x/d$, where d is the reference length, typically one of the atomic diameters. The dimensionless form of Poisson's equation is then

$$\nabla^2 \phi^* = -\frac{4\pi}{T_{elec}} \sum q_\alpha \rho_\alpha^*$$

where lengths are now in units of x^* , $\rho_\alpha^* = \rho_\alpha d^3$, and the dimensionless temperature T_{elec} is given by

$$T_{elec} = 4\pi kT \epsilon \epsilon_0 d / e^2$$

In the Poisson-Boltzmann limit of point charges, the unit d does not have any physical meaning. In Tramonto, for this case we set $d = 1$. In the literature, typically the Debye length κ is used as the unit of length, where

$$\kappa^2 \equiv \frac{kT \epsilon \epsilon_0}{\sum_\alpha q_\alpha^2 e^2 \rho_\alpha^b} = \frac{T_{elec}}{4\pi d \sum_\alpha q_\alpha^2 \rho_\alpha^b}$$

Note that the d in the denominator is simply $= 1$ when solving Tramonto in the PB limit. One other common measure of length is the Bjerrum length, given by

$$l_B \equiv \frac{e^2}{4\pi kT\epsilon\epsilon_0} = \frac{d}{T_{elec}}$$

So the parameter T_{elec} behaves as the inverse Bjerrum length when $d = 1$.

A.2. Poisson-Boltzmann Limit

In this section, we show that in the Poisson-Boltzmann (PB) limit of a 1:1 electrolyte consisting of point charges near a charged surface, the normal formulation of the electrostatic free energy in the f-DFT as presented in Sec. 2.2.2.4 is the same as the electrostatic free energy derived previously by a different route for a PB system. In particular, we consider an expression for the electrostatic free energy of a PB system developed by Reiner and Radke (Reiner and Radke 1990) and Honig and Sharpe (Sharp and Honig 1990). They find that the surface excess grand free energy is

$$\Omega_{RR}^{ex} = \int_S dr^s \omega_s(r^s) - \int d\mathbf{r} \left\{ \frac{\epsilon\epsilon_0}{2} |\nabla\phi(\mathbf{r})|^2 + (\Pi - \Pi^0) \right\} \quad (\text{A.2})$$

where the osmotic pressure term $(\Pi - \Pi^0)$ is actually just the total adsorption. The first term is integrated over the boundaries. For the case of a surface with constant charge, this term reduces to the surface charge times the potential at the surface. We rewrite Eq. (A.1) in dimensionless units in the DFT manner to find

$$\Omega_{RR}^{ex} = \sigma\phi_s - \int d\mathbf{r} \left\{ \frac{T_{elec}}{8\pi} |\nabla\phi(\mathbf{r})|^2 + \sum_{\alpha} (\rho_{\alpha}(\mathbf{r}) - \rho_{\alpha,b}) \right\} \quad (\text{A.3})$$

where σ is the surface charge density, ϕ_s is the electrostatic potential on the surface, and $\rho_{\alpha,b}$ is the bulk density of species α . Now consider the DFT expression for the free energy of a PB system. In this limit, where the ions are modeled as point charges, the grand free energy functional consists of only the ideal gas (Eq. (2.2.5)) and mean-field electrostatic terms (Eq. (2.2.7)):

$$\Omega[\rho(\mathbf{r})] = \sum_{\alpha} \int d\mathbf{r} \rho_{\alpha}(\mathbf{r}) (\ln \rho_{\alpha}(\mathbf{r}) - 1) + \frac{1}{2} \int d\mathbf{r} \rho_c(\mathbf{r}) \phi(\mathbf{r}) - \sum_{\alpha} \int d\mathbf{r} \mu_{\alpha} \rho_{\alpha}(\mathbf{r}) \quad (\text{A.4})$$

where we are assuming that the external field V^{ext} consists of a single hard charged wall and therefore does not contribute to the last term above. We solve this equation by the usual method, solving the coupled Euler-Lagrange equations and Poisson's equation. Note that formally, Poisson's equation gives the potential ϕ in terms of the total charge density:

$$\nabla^2 \phi(\mathbf{r}) = -\frac{4\pi}{T_{elec}} \rho_c(\mathbf{r})$$

When we have a boundary, we solve this equation using just the mobile charges, and the fixed charges lead to the boundary condition. The boundary conditions for Poisson's equation in the case of a single planar, hard charged wall located at $x=0$ are

$$\begin{aligned} \frac{d\phi}{dx} &= -\frac{4\pi\sigma}{T_{elec}}, \quad x=0 \\ \frac{d\phi}{dx} &\rightarrow 0, \quad x \rightarrow \infty \end{aligned}$$

where σ is the surface charge density.

We note that the chemical potential is simply $\mu_\alpha = \ln \rho_{\alpha,b}$ since the electrostatic contribution to the free energy vanishes in the bulk. From Eqs. (A1) and (A4), the excess surface free energy is then given by

$$\begin{aligned} \Omega[\rho(\mathbf{r})] - \Omega[\rho_b] &= \sum_\alpha \int d\mathbf{r} \rho_\alpha(\mathbf{r}) (\ln \rho_\alpha(\mathbf{r}) - 1) - \sum_\alpha \int d\mathbf{r} \ln \rho_{\alpha,b} \rho_\alpha(\mathbf{r}) + \frac{1}{2} \sigma \phi(0) \\ &+ \frac{1}{2} \sum_\alpha \int d\mathbf{r} q_\alpha \rho_\alpha(\mathbf{r}) \phi(\mathbf{r}) - V \sum_\alpha \rho_{\alpha,b} (\ln \rho_{\alpha,b} - 1) + V \sum_\alpha \ln \rho_{\alpha,b} \rho_{\alpha,b} \\ &= \sum_\alpha \int d\mathbf{r} \left[\rho_\alpha(\mathbf{r}) \ln \frac{\rho_\alpha(\mathbf{r})}{\rho_{\alpha,b}} - \rho_\alpha(\mathbf{r}) + \rho_{\alpha,b} \right] + \frac{1}{2} \sigma \phi(0) \\ &+ \frac{1}{2} \sum_\alpha \int d\mathbf{r} q_\alpha \rho_\alpha(\mathbf{r}) \phi(\mathbf{r}) \end{aligned}$$

where we have split ρ_c into its fixed and mobile parts. Now recall that we are in the PB limit, so we know that the mobile charge density obeys

$$\frac{\rho_\alpha(\mathbf{r})}{\rho_{\alpha,b}} = \exp[-q_\alpha \phi(\mathbf{r})]$$

Plugging this into the first term above and taking the log, we can rewrite the excess surface free energy as

$$\Omega[\rho(\mathbf{r})] - \Omega[\rho_b] = -\sum_\alpha \int d\mathbf{r} [\rho_\alpha(\mathbf{r}) - \rho_{\alpha,b}] - \frac{1}{2} \sum_\alpha \int d\mathbf{r} q_\alpha \rho_\alpha(\mathbf{r}) \phi(\mathbf{r}) + \frac{1}{2} \sigma \phi(0) \quad (\text{A.5})$$

We can now do some standard manipulations on the second term. From Sharp and Honig (Sharp and Honig 1990), an expression of Gauss' law is

$$\frac{1}{2} \int \rho_c(\mathbf{r}) \phi(\mathbf{r}) d\mathbf{r} = \frac{1}{2} \int (\rho^f(\mathbf{r}) + \rho^m(\mathbf{r})) \phi(\mathbf{r}) d\mathbf{r} = \frac{T_{elec}}{2 * 4\pi} \int |\nabla \phi|^2 d\mathbf{r}$$

This comes from noting that we can replace the charge density with $\nabla^2\phi$ from Poisson's equation and then integrating by parts over all space, so

$$\frac{1}{2} \int \rho_c(\mathbf{r})\phi(\mathbf{r})d\mathbf{r} = -\frac{T_{elec}}{8\pi} \int \phi(\mathbf{r})\nabla^2\phi(\mathbf{r})d\mathbf{r} = \frac{T_{elec}}{8\pi} \int |\nabla\phi|^2 d\mathbf{r}$$

So substituting in for ρ^m in Eq. (A.5) we obtain

$$\Omega[\rho(\mathbf{r})] - \Omega[\rho_b] = -\sum_{\alpha} \int d\mathbf{r} [\rho_{\alpha}(\mathbf{r}) - \rho_{\alpha,b}] + \frac{1}{2}\sigma\phi(0) + \frac{1}{2}\sigma\phi(0) - \frac{T_{elec}}{8\pi} \int |\nabla\phi|^2 d\mathbf{r}$$

leading to

$$\Omega[\rho(\mathbf{r})] - \Omega[\rho_b] = -\sum_{\alpha} \int d\mathbf{r} [\rho_{\alpha}(\mathbf{r}) - \rho_{\alpha,b}] + \sigma\phi(0) - \frac{T_{elec}}{8\pi} \int d\mathbf{r} |\nabla\phi(\mathbf{r})|^2$$

This is precisely the Sharp and Honig (or Reiner and Radke) expression for the total free energy of the PB system, Eq. (A.3). We also note that Eq. (A.5) derived here is the same as the second part of Eq. (24) in Sharp and Honig (Sharp and Honig 1990). Thus, the f-DFT reproduces the PB model in the limit of point charges.

A.3. Tests of Electrostatics in Tramonto

4.1.1 A.3.1. Pressure from electrostatic terms

Recall from thermodynamics that the bulk pressure is $-PV = \Omega_b$. In the bulk, $\rho^m = \sum_{\alpha} q_{\alpha}\rho_{\alpha} = 0$ due to charge neutrality, and there are no surfaces since we're in the bulk. Thus, from Eq. (2.2.7) we see that $F_C = 0$ in the bulk. So mean field electrostatics make no contribution to the pressure or to the chemical potential from the mobile ions.

The correlation term F_{corr} in Eq. (2.2.8) likewise makes no contribution to the bulk pressure when the ions have the same size. If the ions have different hard sphere diameters, then F_{corr} does make a contribution to the bulk pressure. Substituting the bulk densities into $P = -\Omega_b/V$, we find

$$P_{corr} = -\frac{\beta}{2} \sum_{\alpha\beta} \rho_{\alpha,b}\rho_{\beta,b} \int d\mathbf{r} \Delta c_{\alpha\beta}(\mathbf{r})$$

This contribution was added to Tramonto in the course of this project, along with the generalization of the correlation terms.

4.1.2 A.3.2. Sum rules

Below we show various results for a 1:1 electrolyte next to a surface with a fixed surface charge density. We check three different sum rules (Henderson 1992). First, for a system between two planar charged surfaces as a function of the distance L between the surfaces, the solvation force sum rule states that the force between the plates $f(L)$ is

$$f(L) = -\frac{1}{A} \left(\frac{\partial \gamma}{\partial L} \right)_{T, \mu} = kT \sum_{\alpha} [\rho_{\alpha}(d_{\alpha}/2; L) - \rho_{\alpha}(d_{\alpha}/2; L = \infty)]$$

where γ is the excess surface free energy from Eq. (A.1). Second, the adsorption sum rule states

$$\Gamma_{\alpha}^{ex} = -\frac{\partial \gamma}{\partial \mu_{\alpha}}$$

where Γ_{α}^{ex} is the excess adsorption of species α . Finally, we have the contact sum rule, which states that the bulk pressure P is given by

$$P = kT \sum_{\alpha} \rho_{\alpha}(0) - \frac{\sigma^2}{2\epsilon\epsilon_0}$$

for a system with a charged hard wall at $x = 0$, with surface charge σ . In the dimensionless Tramonto units, this becomes

$$\beta P = \sum_{\alpha} \rho_{\alpha}^*(0) - \frac{2\pi\sigma^{*2}}{T_{elec}}$$

where $\rho_{\alpha}(0)$ is the contact density, i.e. the density at the charged surface.

We now consider various simple test problems, and verify that they satisfy these sum rules. The pressure sum rule is well obeyed by Tramonto in all cases tested, so below we only consider the force and adsorption sum rules.

4.1.3 A.3.3. PB Limit

We first verify that Tramonto satisfies the sum rules in the PB limit, with just point charges.

4.1.4 A.2.2.1. Problem 1: small surface charges

To test the force and adsorption sum rules requires us to solve the f-DFT equations many times for different values of L and μ_{α} , respectively. To do this we use the continuation methods

available in Tramonto, which can increment the problem size or any continuous variable automatically. For the adsorption sum rule, Fig. A1 shows results using arc-length continuation, going from $\rho_{\pm} d^3 = 0.06$ to $\rho_{\pm} d^3 = 0.066$, with a surface charge density of $\sigma^* = 0.04$. We set $d = 2.8 \text{ \AA}$, $T=298 \text{ K}$, and $\epsilon = 78.5$. We find excellent agreement with the sum rule for both positive and negative species.

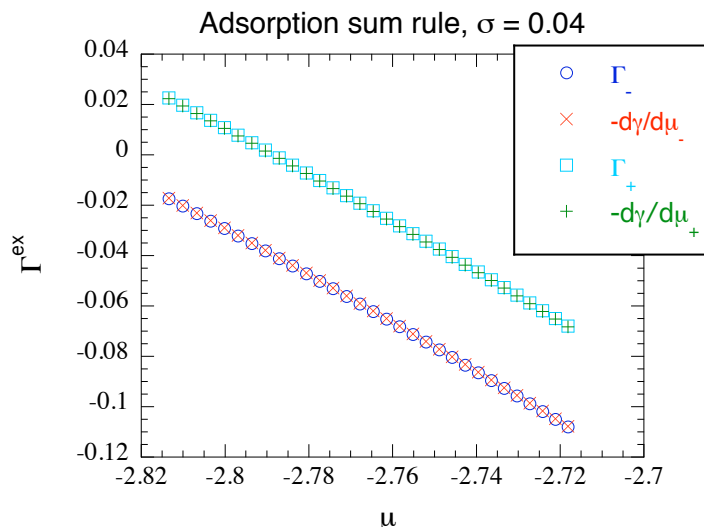


Figure A1. Test of adsorption sum rule in PB limit.

Next consider the solvation force. For the same conditions as in Fig. A1, with a mesh size of $0.02d$, $\rho_{\pm} d^3 = 0.06$, and $\sigma^* = 0.04$, we find perfect agreement for the two sides of the solvation force sum rule, as shown in Fig. A2. Note the log scale on the y-axis. We find equally good agreement for the same parameters but with $d = 4.25 \text{ \AA}$, and also for densities of $\rho_{\pm} d^3 = 0.04$ for the two species and a reduced surface charge density of $\sigma^* = 0.2$.

4.1.5 A.2.2.1. Problem 2: large surface charges

Now we consider a system with a much higher surface charge of $\sigma^* = 1.55$, and with ion densities of $\rho_{\pm} d^3 = 0.0267657$. We again get excellent agreement for the adsorption sum rule as shown in Fig. A3, and for the solvation force, as shown in Fig. A4. We conclude that Tramonto is accurately calculating density profiles and free energies in the PB limit.

A.3.4. RPM model

Now we test the restricted primitive model (RPM), which consists of a 1:1 electrolyte in which the ions have the same sign. The ions are immersed in a background dielectric, without explicit solvent. We check the case where we use the White Bear functional given in Eq. (2.2.6), with $\sigma^*=0.04$, $\rho_{\pm} d^3 = 0.06$, mesh size of $0.02d$, $d = 4.25 \text{ \AA}$, $T = 298 \text{ K}$, and $\epsilon = 78.5$. Calculations are performed in the mean-field limit, i.e. we do not include the correlation term F_{corr} in Eq. (2.2.8). Once again the solvation force sum rule is very well obeyed as shown in Fig. A5. The adsorption sum rule is also well obeyed, as long as one takes a small enough step in μ , so that the free energy γ doesn't change too much and it's therefore possible to get a good estimate of the derivative $d\gamma/d\mu$. We also tested the solvation force sum rule with neutral walls, $\sigma^*=0$, and all other parameters the same. This case, shown in Fig. A6, has a small minimum in the force; both calculation methods give this minimum and again are in perfect agreement.

A.3.5. SPM model

Finally, to test the SPM model where ions have different sizes, we checked the adsorption sum rule and the solvation force sum rule for the system studied by Oleksy and Hansen (Oleksy and Hansen 2006), using parameters from their 2, a 0.1 M NaCl solution, and Fig. 6, a 1M CaCl₂ solution. (density profiles for the 0.1 M NaCl solution as calculated by Tramonto are shown in Fig. 2.2.2). Both the adsorption and solvation force sum rules were also well obeyed for these two systems. We checked using just the mean-field electrostatics, and using the generalized correlation term, and both gave good results. A final example of the excellent agreement is shown in Fig. A7, which shows the force sum rule for the 1M CaCl₂ solution, with a surface charge density of -0.087. This is a stringent test of the theory because it includes divalent ions at high concentration.

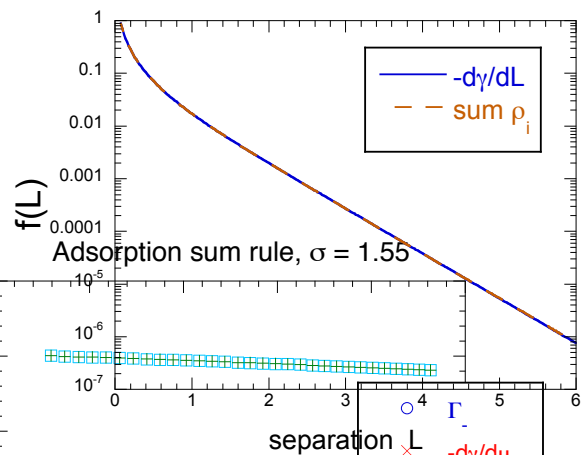


Figure A2. Test of solvation force sum rule in PB limit; $\rho_{\pm} d^3 = 0.06$ and $\sigma^* = 0.04$.

Figure A3. Test of adsorption sum rule in PB limit; $\rho_{\pm} d^3 = 0.0267657$ and $\sigma^* = 1.55$.

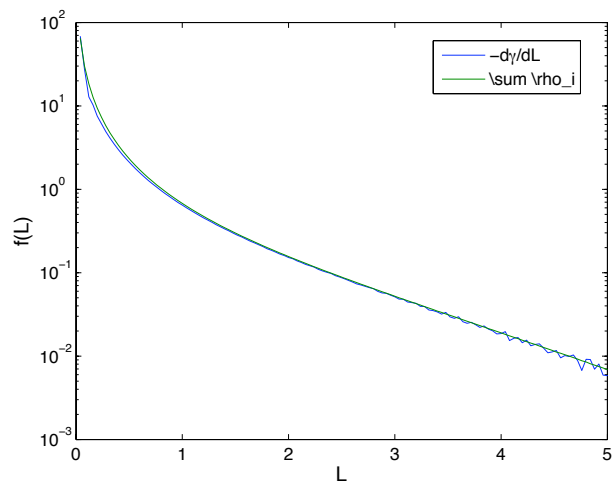


Figure A4. Test of solvation force sum rule in PB limit; $\rho_{\pm}d^3 = 0.0267657$ and $\sigma^* = 1.55$.

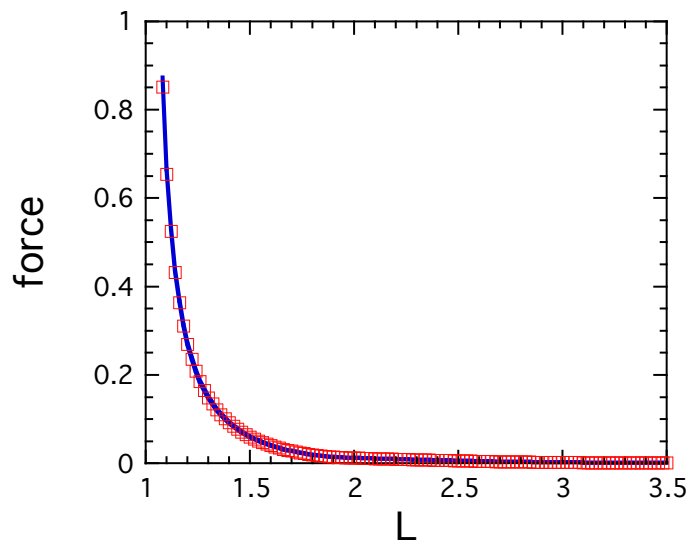


Figure A5. Test of solvation force sum rule for the RPM; $\rho_{\pm}d^3 = 0.06$ and $\sigma^* = 0.04$. The derivative $-(1/A)d\gamma/dL$ is the blue curve and the sum of the contact densities are the red squares.

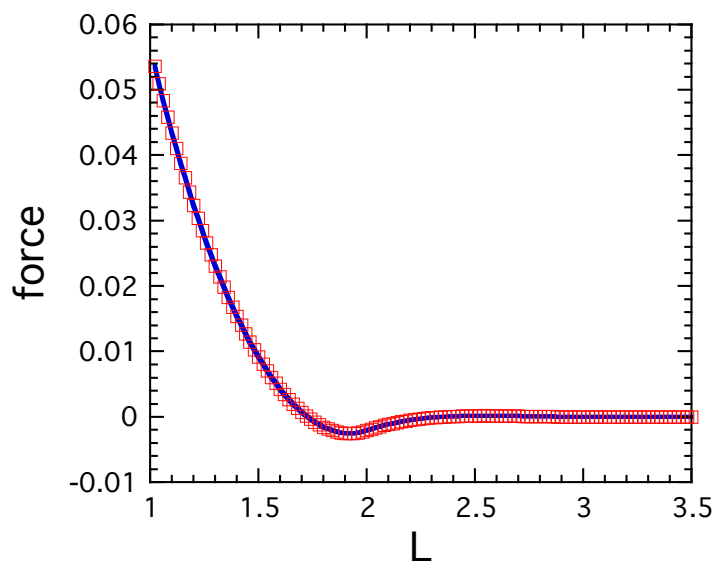


Figure A6. Test of solvation force sum rule for the RPM; $\rho_{\pm}d^3 = 0.06$ and $\sigma^* = 0.0$. The derivative $-(1/A)d\gamma/dL$ is the blue curve and the sum of the contact densities are the red squares.

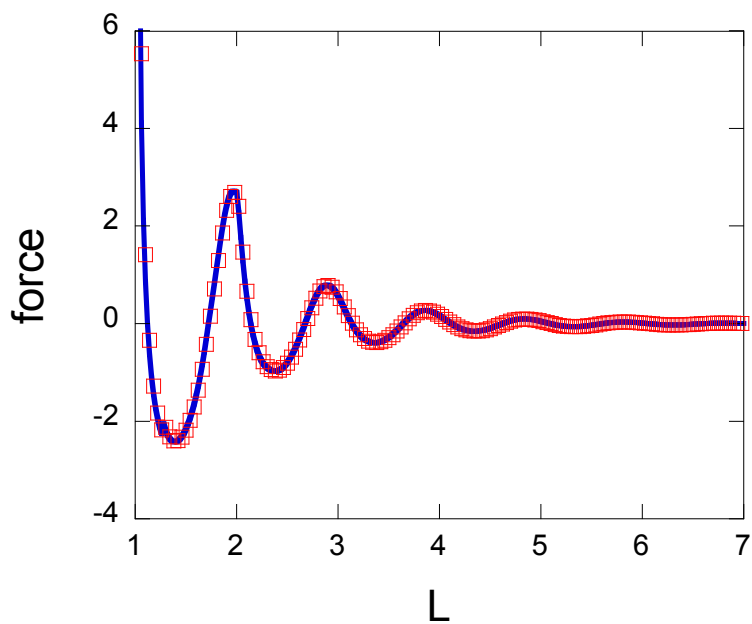


Figure A7. Test of solvation force sum rule for the SPM, for 1M CaCl_2 in water; $\sigma^* = -0.087$. The derivative $-(1/A)d\gamma/dL$ is the blue curve and the sum of the contact densities are the red squares.

DISTRIBUTION

1	MS0359	D. Chavez, LDRD Office	1911
1	MS0613	Christopher Gresham	2540
1	MS0614	David Ingersoll	2546
1	MS0614	Chris Orendorff	2546
1	MS0614	Pete Roth	2546
1	MS0614	Tom Wunsch	2546
1	MS0885	Terry Aselage	1810
1	MS0899	Technical Library	9536 (electronic copy)
1	MS1315	Sean Hearne	1132
1	MS1322	John Aidun	1425
1	MS1415	Kevin Leung	1131
1	MS1415	Nancy Missert	1114
1	MS9161	John Sullivan	8656



Sandia National Laboratories